Gas Phase Air Pollution in Remote and Urban Atmospheres: From the Azores to Beijing

Freya Anne Squires

PhD

University of York

Chemistry

August 2020

Abstract

Gaseous air pollutants can be hazardous to health and contribute to global warming, both directly or via the formation of particulate matter. Understanding atmospheric composition in both remote and urban regions is essential for understanding air pollution and developing methods for mitigating its harmful impacts. In this thesis, measurements of gas-phase pollutants are presented in Beijing, China and over the North Atlantic. Despite being very different, both these atmospheres are polluted. Seasonal differences in air pollution are examined for Beijing comparing measurements made during November–December 2016 and May–June 2017. Meteorology significantly impacts the winter pollution experienced as periods of stagnant weather allow pollution to build up leading to haze events. High O_3 mixing ratios were measured in summertime, with a daytime average of 66.4 ppbv. Large deviations from the O_3-NO-NO_2 photostationary state are presented which cannot be explained solely by the presence of peroxy radicals. Seasonal differences in emissions were also explored. For the first time in Beijing, the eddy-covariance technique was used to quantify emissions of NO_x, CO and aromatic VOCs with traffic found to be the dominant source. NO_x and CO fluxes were then compared to a Chinese emissions inventory, which significantly overestimated emissions for the region, suggesting that proxy-based emissions inventories have positive biases in urban centres. This work provides a useful benchmark of emissions from the city which can help to inform future inventories. The spatial distribution of gas-phase pollutants over the North Atlantic Ocean is explored and it is shown that transport of pollutants from North America impact the atmospheric composition of the region. Measurements were then compared with the GEOS-Chem model which highlighted a systematic underestimation in CO mixing ratios by the model, possibly indicating a missing source of emissions in the inventory used.

Contents

List of Tables

List of Figures

Acknowledgements

I'd first like to thank my supervisors James Lee and Jacqui Hamilton for giving me the opportunity to carry out this PhD and for their support and guidance over the past four years.

I am incredibly grateful to Eiko Nemitz, Ben Langford and Oliver Wild for their advice and guidance when I was doing the emissions analysis for Beijing. Special thanks to the eddy4R team - Stefan Metzger, Natchaya Durden and Dave Durden - for support with my analysis throughout my PhD.

A massive thank you goes to the brilliant people I worked with on the Air Pollution and Human Health Campaign in Beijing. I learnt so much in the field and had a lot of fun along the way. Special thanks to Archit, Jess, Joshi, Ellie and Rob who I first met in Beijing. We have been firm friends ever since and I am certain we will continue to be so! Thanks to all at FAAM for being there at the start of my journey in research and for being a lot of fun to go on fieldwork with.

Huge thanks to everyone who has made my time at WACL so enjoyable - Will, Pete, Stefan, Naomi, Liselotte, Stuart, Marv, Mike, Rachel, Chris, Steve - I'm going to really miss working with you and Friday trips to the pub (well socially-distanced tinnies in a field now thanks to COVID). Special thanks to Shona for picking me up when I was fed up of everything! Thanks to all my lovely friends in York who allowed me to escape all things PhD - Mark, Jack and Katie especially.

Lastly but certainly not least, thank you to Mum, Dad, James and Lorna for being brilliant, for proof reading various drafts, for always encouraging me, for advice and pick-me-up phone calls and letters throughout the PhD. Finally to Graeme; thank you for your LaTeX skills, scientific advice and unwavering love and support throughout.

Declaration

I declare that this thesis is a presentation of original work and I am the sole author. This work has not previously been presented for an award at this, or any other, University. All sources are acknowledged as References. Chapter 4 is based on a peer-reviewed publication of which I am the lead author. Details of this publication are:

Squires, F. A., Nemitz, E., Langford, B., Wild, O., Drysdale, W. S., Acton, W. J. F., Fu, P., Grimmond, C. S. B., Hamilton, J. F., Hewitt, C. N., Hollaway, M., Kotthaus, S., Lee, J., Metzger, S., Pingintha-Durden, N., Shaw, M., Vaughan, A. R., Wang, X., Wu, R., Zhang, Q., and Zhang, Y. Measurements of traffic-dominated pollutant emissions in a Chinese megacity, *Atmospheric Chemistry and Physics*, 20, 8737–8761, 2020, DOI:10.5194/acp-20-8737-2020.

1 Introduction

At the time of writing many countries across the world are in some state of lockdown due to the COVID-19 pandemic. Daily life has changed dramatically and within a very short period of time. For example, in the UK mobility decreased significantly since lockdown was announced on 23 March 2020. Compared to the pre-lockdown period, there was a 70% reduction in vehicle traffic and a 90% reduction in UK rail journeys by mid-April [AQEG, 2020]. Significant reductions in air traffic also occurred; a 94% drop in revenue passenger kilometres (the number of revenue passengers carried multiplied by the distance flown) was reported across the industry in April compared to the previous year [IATA, 2020]. Reductions in activity have led to air quality improvements in cities across the world due to a reduction in emissions [e.g. Mahato et al., 2020, Bao and Zhang, 2020, Li et al., 2020a]. Figure 1.1 shows the reductions in ambient concentrations of nitrogen dioxide (NO_2), a key anthropogenic pollutant, over China during lockdown compared to the period before lockdown.

As well as improvements in air quality as a result of lockdown restrictions, there is some evidence that exposure to air pollution is linked to more serious disease outcomes in coronavirus patients, though it is not possible to say conclusively this is the case. Liang et al. [2020] and Wu et al. [2020] have suggested a link between high concentrations of traffic-related pollutants and COVID-19 mortality, though it is difficult to disentangle air pollution exposure from other factors that could lead to increased severity of the disease. Often the highest air pollution concentrations occur in urban areas where population density is higher, there are higher rates of poverty and public transport is more commonly used, all of which increase the risk factors for disease transmission and severity. Nonetheless, public concern about air pollution is growing.

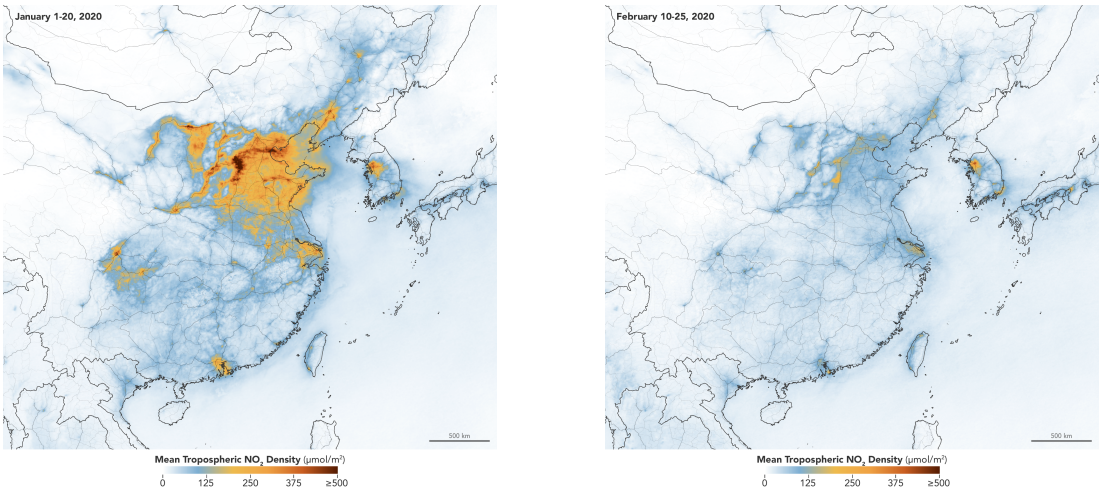

(a) Before lockdown.

(b) During lockdown.

Figure 1.1: Tropospheric NO_2 column density over China before (1 – 20 January 2020) and during (10 – 25 February 2020) lockdown. Data was obtained from the Tropospheric Monitoring Instrument (TROPOMI) on European Space Agency's (ESA's) Sentinel-5 satellite. Image taken from NASA Earth Observatory [2020].

The visible improvements in air quality, as well as heightened awareness of public health issues, are two possible reasons that public concern about air pollution has increased dramatically since the virus outbreak. According to the environmental charity Global Action Plan, 47% of those surveyed were now more concerned about air pollution than during the pre-lockdown period [Client Earth, 2020].

Whilst there currently appears to be heightened awareness and concern about air pollution it is not a new problem. Air pollution has long been recognised as an issue with records dating back to 12th century Egypt [Finlayson-Pitts and Pitts, 2000a]. In fact, the first known instance of air pollution legislation was introduced in 14th century England when Edward I introduced a law banning coal burning when Parliament was in session [Gaffney and Marley, 2009]. Since the mid 18th century, the Industrial Revolution in Europe and North America led to the development of heavy industry and subsequent poor air quality. By the 1850s, higher coal usage was associated with higher death rates from respiratory diseases [Beach and Hanlon, 2017]. During this period a range of legislation was introduced to deal with the "nuisances" of smoke pollution, including changing how furnaces were built to reduce the gases and particles emitted [Heidorn, 1978]. Severe pollution episodes have often acted as driving forces for new environmental legislation. For example, the UK's 1956 Clean Air Act, an important milestone in environmental law, was introduced following severe haze pollution events in London during December 1952 [Brimblecombe, 2006]. Air pollution remains a problem today, though scientific understanding of the complex interactions between pollutants and their impacts on health and climate has developed dramatically since its first records in the 12th century.

1.1 Impacts of air pollution

Air pollution is a global problem. Air is polluted when substances that "substantially alter or degrade the quality of the atmosphere" are present [American Meteorological Society, 2012a]. Studies have shown the devastating impacts air pollution can have with estimates that air pollution causes 4.2 million deaths globally in 2015 [Cohen et al., 2017]. The World Health Organisation (WHO) estimates that 90% of the global population breathes unhealthy, polluted air [World Health Organization, 2016]. Such

Table 1.1: Summary of WHO limits for regulated pollutants.

Pollutant	**WHO Limit**
PM_{10}	50 μg m^{-3} (24-hour mean)
	20 μg m^{-3} (annual mean)
$PM_{2.5}$	25 μg m^{-3} (24-hour mean)
	10μg m^{-3} (annual mean)
O_3	100 μg m^{-3} (8-hour mean)
NO_2	200 μg m^{-3} (1-hour mean)
	40 μg m^{-3} (annual mean)
SO_2	500 μg m^{-3} (10-minute mean)
	20 μg m^{-3} (24-hour mean)

is the impact of air pollution that the United Nations (UN) has called for clean, healthy air to be recognised as a human right [UN Environment Programme, 2019]. Across the world, people are exposed without their consent to hazardous substances which increase their risk of developing diseases and disabilities. The WHO recommends concentrations of certain pollutants be maintained under thresholds to reduce harm to health with regulated pollutants including particulate matter (PM), ozone (O_3), nitrogen dioxide (NO_2) and sulfur dioxide (SO_2). These pollutants are directly harmful to health linked to reduced lung function, chronic obstructive pulmonary disease, asthma and cardiovascular diseases [Kampa and Castanas, 2008]. Table 1.1 summarises the limits set by the WHO for key pollutants [World Health Organization, 2006]. According to the urban air quality database for 2018 (latest available) 49% of cities with more than 100,000 residents in high income countries do not meet these guidelines [World Health Organization, 2018]. Residents in low and middle income countries are worse affected still, with 97% of cities in these countries breaching air quality guidelines. Shaddick et al. [2020] shows that over half of the global population were exposed to air pollution substantially above the WHO guidelines and highlight in many countries there are regions, particularly in Central and Southern Asia and Sub-Saharan Africa, where inhabitants are exposed to increasing levels of pollution.

Aside from dangerous health impacts air pollution is closely linked to climate change. Global climate has been changing at an unprecedented rate since industrialisation driven by increases in ambient concentrations of greenhouse gases (GHGs), like carbon dioxide (CO_2) and methane (CH_4) [Fiore et al., 2015]. The Paris Agreement 2015 was heralded as a historic event in environmental law which set out an international commitment to hold the increase in the global average temperature to "well below 2 °C...and to pursue efforts to limit the temperature increase to 1.5 °C" [UN, 2015]. In 2018 the Intergovernmental Panel on Climate Change (IPCC) published a special report investigating the impacts of a mean global temperature increase of 1.5 °C compared to a larger temperature increase. Global warming of over 1.5 °C increases the likelihood of catastrophic environmental damage, including a rise in sea levels of over 0.8 m by 2100 and irreversible instabilities in Antarctica and the Greenland ice sheet, which could lead to multi-metre sea level rise, destruction of valuable habitats including coral reefs and thawing of permafrost [Allen et al., 2018]. Global warming can also create dangerous feedback loops; for example, thawing of permafrost can accelerate release of CO_2 into the atmosphere, further warming the planet [Schuur et al., 2015]. In order to prevent warming above 1.5 °C there must be rapid action and understanding the mechanics of climate change, including the role of air pollution, is vital.

GHGs act to warm the planet by absorbing and emitting radiation that would otherwise escape to space. Radiative forcing (RF) is used to quantify the warming potential of an atmospheric species with positive RF leading to surface warming and negative RF leading to surface cooling [Stocker et al., 2013]. CO_2 and CH_4 are the most potent climate change gases with an RF of +1.83 W m^{-2} and +0.61 W m^{-2} respectively [Etminan et al., 2016]. As well as air pollutants themselves leading to warming, climate change in turn influences air pollution by altering the severity, length and frequency of precipitation, heat waves and air stagnation events [Jacob and Winner, 2009].

Air pollutants which are hazardous to health and regulated by the WHO can also impact global climate. In particular, changes in tropospheric O_3 have been estimated to have a RF of +0.35 W m^{-2}, making it the third largest contributor to total tropospheric radiative forcing between 1750 and 2011 [Myhre et al., 2013, Iglesias-Suarez et al., 2018]. O_3 is a GHG as well as a harmful air pollutant and is formed from the

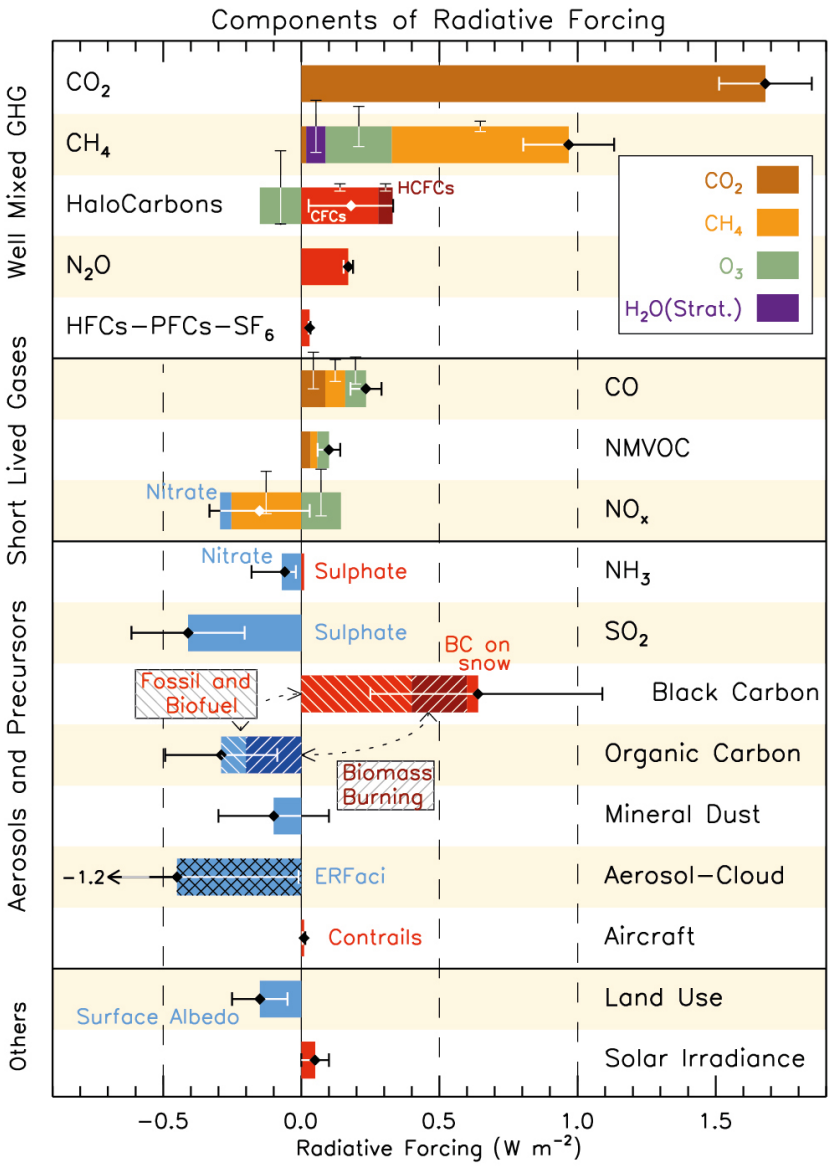

Figure 1.2: Radiative forcing (W m^{-2}) for a range of gases and aerosol species for the period 1750 – 2011. Air pollutants like NO_x and CO influence climate through impacting other species like CH_4 and O_3. Image taken from Myhre et al. [2013].

photochemical reactions of precursor gases. Figure 1.2 presents the radiative forcing of a range of atmospheric species for the period 1750–2011 and shows that some air pollutants have secondary impacts on climate. These pollutants do not act as GHGs directly but influence climate through altering concentrations of GHGs, like O_3 and CH_4, or through aerosol formation. Nitrogen oxides (NO_x) and volatile organic compounds (VOCs) react in the presence of UV radiation to form O_3 and emissions of these O_3 precursors have risen sharply since the pre-industrial era [Lamarque et al., 2010, Hoesly et al., 2018]. Through O_3 formation, NO_x, CO and VOCs have a warming effect. NO_x can also have a cooling impact through CH_4 perturbations as a result of changes to hydroxyl radical mixing ratios [Derwent et al., 2008].

NO_x and VOCs can form particulate matter, with SO_2 also being an important aerosol precursor [Ziemann and Atkinson, 2012]. Aerosols absorb and scatter radiation and affect cloud properties by providing a surface for water vapour to condense. In these ways they impact the radiative balance of the earth and therefore climate. It is generally assumed aerosols have a net-cooling effect however, aerosol impacts on clouds and precipitation are some of the largest sources of uncertainty in climate models [Stocker et al., 2013, Seinfeld et al., 2016]. Unlike for O_3, legislating to reduce aerosol concentrations which would improve public health could have a negative impact on climate. Studies have suggested that reduced aerosol concentrations could lead to climate warming in the short term, modelling alarming increases in temperature of up to 0.8 °C per decade as a result of aerosol mitigation strategies [e.g. Raes and Seinfeld, 2009, Samset et al., 2018, Lelieveld et al., 2019]. However, more recent modelling studies, which took a more holistic approach to emissions reductions scenarios, suggest there is no such trade-off between protecting public health and tackling climate change [Shindell and Smith, 2019]. As aerosol and aerosol precursor emissions have similar fossil-fuel sources, the reduction in aerosol concentrations and resulting cooling impact is negated by the concurrent reduction in CO_2 emissions.

Given the public mood since the outbreak of the COVID-19 pandemic, the urgency of climate change and the devastating health implications of air pollution it is vital air pollution is controlled. Understanding the drivers of air pollution is critical in order to develop successful management strategies to alleviate the catastrophic repercussions of air pollution.

1.2 Meteorology & atmospheric transport

Ambient concentrations of air pollution are dictated by emissions, chemical transformation, transport and deposition [Monks et al., 2009]. Across all spatial and temporal scales meteorology, which dictates vertical and horizontal transport of pollution, can have large impacts on air pollutant concentrations, often to a greater degree than emissions reductions [Grange and Carslaw, 2019]. It is possible to legislate and change behaviours to reduce emissions of pollutants but it is not possible to change the weather! An interesting case study is that of the 2014 Asia-Pacific Economic Cooperation (APEC) conference which took place in Beijing during November. Due to rapid industrialisation and urbanisation Beijing experiences significant air quality problems, with dramatic haze events caused by particulate pollution frequent during winter months [Zheng et al., 2015]. Mean 24-hour concentrations of $PM_{2.5}$ of up to 630 μg m^{-3} were measured in Beijing 2012–2013 during such haze events [Ouyang, 2013], over 25 times greater than the WHO limit (Table 1.1). During the APEC 2014 conference extensive emissions control measures were put in place including factory closures, reductions in traffic volume, the closure of construction sites and operations of coal-fuelled industries paused to reduce the likelihood of the hazardous winter haze events. Similar emissions controls had previously been found to improve air quality in the short term at the 2008 Olympic Games which was also held in Beijing [Wang et al., 2010a]. Emissions reductions were imposed locally (within Beijing) as well as in the surrounding provinces or municipalities; Tianjin, Hebei, Liaoning, Shanxi, Shandong, Henan and Inner Mongolia [Guo et al., 2016]. The relative contributions of meteorology and emissions controls were evaluated and it was found that the emission control measures reduced the $PM_{2.5}$ concentrations in Beijing by 41.3% indicating these measures were effective, but that on average, meteorology played a dominant role in the air quality improvements observed [Liu et al., 2017a]. As mentioned earlier, during the COVID-19 pandemic lockdown in China, emissions of air pollutants decreased (Figure 1.1) however this was not the case for all air pollutants and across the whole of China. Whilst NO_2 emissions were reduced by over 90% in some regions, there were simultaneously extremely high $PM_{2.5}$ concentrations observed in the North China Plain [Le et al., 2020]. Analysis revealed that this enhancement in $PM_{2.5}$

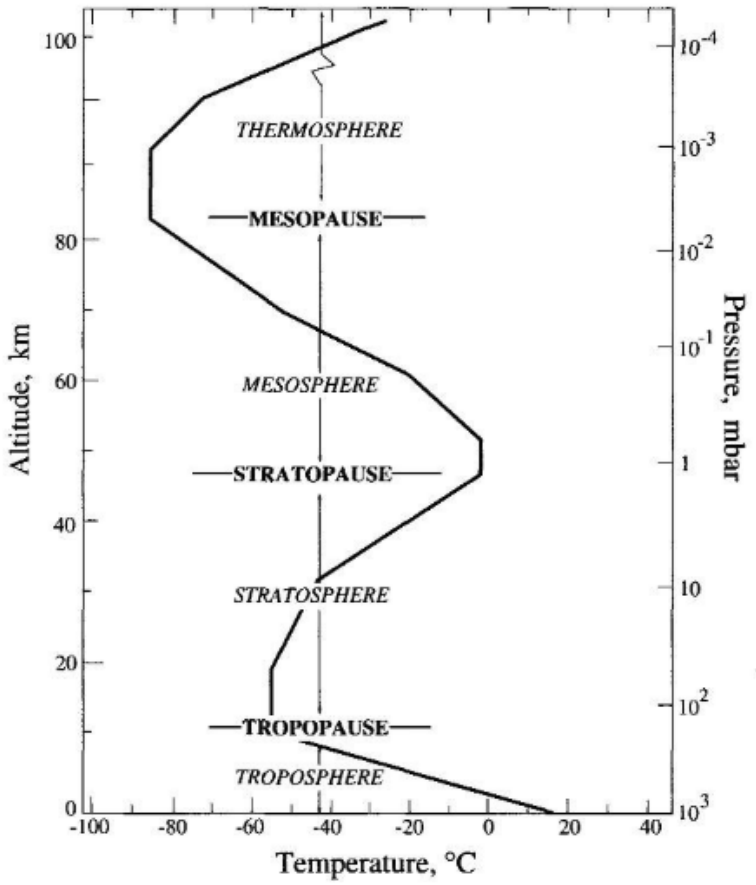

Figure 1.3: Diagram to show the vertical structure and layers of the atmosphere taken from Seinfeld and Pandis [2006]. The typical variation of temperature with altitude is shown.

concentrations was driven by meteorology; relative humidity (RH), was higher than typical for the time of year and created favourable conditions for secondary aerosol formation. Wind speeds also decreased by 20% in Beijing which is favourable for haze formation creating stable conditions with no advection to remove pollution from over the cities.

Figure 1.3 shows the structure of the atmosphere. The troposphere is the lowest layer of Earth's atmosphere extending from the surface to about 10 km upwards. It contains most of the mass (about 90%) of the atmosphere and is where weather occurs [Wayne, 1991]. The lowest part of the troposphere, the boundary layer, is strongly

influenced by its direct contact with the Earth's surface. Heat transfer between the surface and the atmosphere means the depth and turbulence of this layer varies considerably with location and time, both on a seasonal and diurnal scale. During the day, heating means that the boundary layer is usually turbulent and well mixed throughout its vertical extent. A capping layer, often due to a temperature inversion (shown in Figure 1.4) separates the boundary layer from the free troposphere. The depth of this well mixed layer, the mixed layer height (MLH), affects pollutant concentrations as it determines the rate and range of vertical dispersion of pollutants that are formed or emitted on the surface and defines the volume of air that pollution is mixed into [Emeis and Schäfer, 2006].

As well as vertical transport, wind drives atmospheric transport. Low wind speeds in areas where air pollutants are emitted reduce ventilation and hence lead to deterioration of air quality [Grundstrom et al., 2015] on local scales. Larger scale meteorological phenomena have also been shown to drive air quality. Intercontinental pollution transport is driven by the general circulation of the atmosphere and constrained by the MLH [Dentener et al., 2010]. The North Atlantic Oscillation (NAO), an atmospheric pressure system characterised by a region of low pressure centred over Iceland and a region of high pressure centred over the Azores, has been shown to affect pollutant transport and impact air quality [Pope et al., 2018, Grundstrom et al., 2015]. The pressure difference between these two regions dictates the phase of the North Atlantic Oscillation Index (NAOI); when the atmospheric pressure difference is small between the two centres, NAOI is in its negative phase whereas a large pressure difference means NAOI is in its positive phase. During a positive NAOI, strong westerly winds are favoured which typically lead to better air quality over Europe due to increased ventilation. Negative phase NAOIs result in cold and stable air masses over Northern Europe, normally originating from Arctic or Siberian regions. These more stable conditions can lead to pollution building up over Europe.

Atmospheric transport can mean regions without emissions sources become polluted. For example, it is well documented that O_3 pollution is often worse downwind of urban environments owing to reactions of NO_x and VOC emissions [e.g. Xu et al., 2011]. Remote regions which have few local emissions sources can be influenced by atmospheric transport of pollutants from other regions. For example, the Azores in the

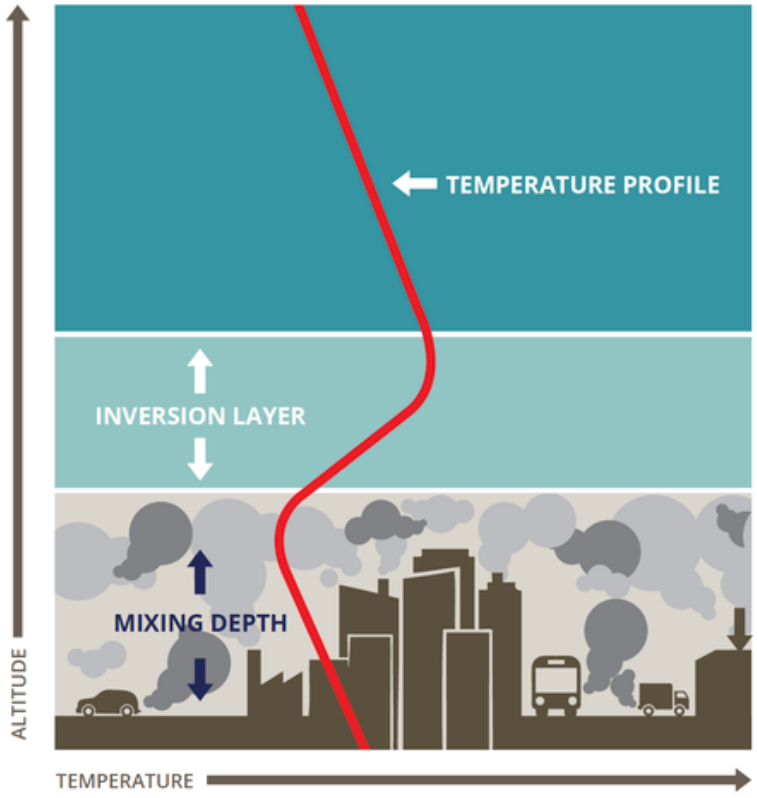

Figure 1.4: Infographic to show how a temperature inversion can "trap" pollution. This phenomenon is particularly common during winter where air in contact with the ground is cold. Warm air rises and stops vertical mixing trapping colder area close to the ground where pollution can build up. Adapted from European Environment Agency [2016].

North Atlantic Ocean is influenced by anthropogenic pollution from North America and biomass burning emissions, which can lead to enhanced CO, oxidised nitrogen and O_3 mixing ratios [Val Martin et al., 2006]. Intercontinental transport can impact regions previously considered 'pristine' environments. For example, the Arctic was considered a pristine area with few local emissions sources but since the 1950s has been affected by haze pollution, the so-called "Arctic haze". This is a result of pollution from anthropogenic activities transported from mid-latitudes and being trapped in the polar region by the stable winter meteorological conditions [Granier et al., 2006].

1.3 Pollutant emissions

Pollutants can be emitted into the atmosphere from natural or anthropogenic sources. Whilst the role of pollutant transport and meteorology has been discussed above, the availability of emissions sources is an important driver of air pollution. For example, for the short-lived pollutant NO_x, there are very few emissions sources in remote atmospheres like remote marine or forest environments. In these environments NO_x mixing ratios tend to be < 1 ppb whereas in urban atmospheres mixing ratios are higher on the order of 10–1000 ppb [von Schneidemesser et al., 2015]. Anthropogenic pollutant emissions are closely linked with economic growth [Li et al., 2019b] as economic prosperity generally brings about growth in vehicle use, power demands and industry. Environmental legislation has led to reductions in ambient concentrations of many directly emitted pollutants, though there is regional variation in the success of policy [Guo et al., 2019].

1.3.1 Overview of global trends in pollutant emissions

NO_x largely originates from fossil fuel combustion processes, for example, during vehicle use or power generation. Global NO_x emissions increased between 1960 and 2013, only very recently reaching their peak [Huang et al., 2017]. The decrease in NO_x emissions has largely been driven by reductions in coal consumption and the implementation of denitration technologies in China [Liu et al., 2016]. In terms of the spatial distribution of NO_x emission sources, emissions from industry are most significant in China and East Asia whereas power generation and vehicle emissions

are more significant in Europe and North America. NO_x from biomass burning is significant in Africa and Australia [Huang et al., 2017].

Observations have shown that global concentrations of CO have been decreasing since 2000 [Yin et al., 2015, Zheng et al., 2019]. CO is emitted from incomplete combustion processes from industry and vehicle emissions. Studies have linked reduced anthropogenic emissions in the northern hemisphere to the downward trend in CO concentrations [Yin et al., 2015, Zheng et al., 2019]. Reductions in CO emissions from the transport sector are likely the dominant cause of this improvement for North America and Europe, with improvements in emissions technology for industry and within the residential sector driving CO emissions reductions in China [Zheng et al., 2019]. Jiang et al. [2017] also highlighted a reduction in biomass burning events was significant for reduced CO emissions.

Global emissions of SO_2 peaked in 1970 [Smith et al., 2011] and decreased by 31% between 1990 and 2015 [Aas et al., 2019]. SO_2 emissions largely originate from fossil fuel burning in industrial processes and power generation [Fioletov et al., 2016], though ships tend to burn fuel with a high sulfur content and emissions from the shipping industry make an increasing contribution to global SO_2 [Smith et al., 2011]. SO_2 was a major air quality problem in the UK during the 1950s due to high levels of coal burning. In London during December 1952 a dramatic pollutant event caused by high particulate and SO_2 pollution, combined with favourable meteorological conditions occurred which is thought to have directly led to 4000 deaths [Thorsheim, 2004]. Developments in emissions technology within the energy sector has largely been responsible for the recent reduction in global SO_2 emissions [Klimont et al., 2013].

Volatile organic compounds (VOCs) are a class of organic compounds sufficiently volatile to exist in the gas-phase. There are numerous natural and anthropogenic sources of VOCs in the atmosphere, including plants and trees as well as traffic, industry and solvents. Some VOCs are directly harmful to health (e.g. benzene [Smith, 2010]) but VOCs can also degrade air quality through formation of O_3 and PM. VOC emissions from traffic have decreased in many regions because of emissions controls technologies, like catalytic converters [Parrish et al., 2016]. As the transportation sector becomes cleaner, an increasing proportion of the VOC emission budget originates from volatile chemical products containing organic solvents (e.g. pesticides, cleaning

agents and personal care products) [McDonald et al., 2018].

1.3.2 Emissions inventories

Emissions inventories provide information about the types and sources of pollution emitted into the atmosphere as well as the magnitude of the emission. Emissions inventories are central to air quality research and are useful tools for policy makers and scientific investigation; inventories can be used to check compliance with environmental law, identify regions which have especially high emissions and evaluate the success of emissions controls over time. Inventories are used as inputs to atmospheric models which are used to improve scientific understanding of air pollution processes in the atmosphere. Access to reliable and accurate emissions inventories is therefore imperative for guiding policy to improve public health and furthering scientific understanding of the air pollutants in the atmosphere. If inventories do not correctly detail pollutant emissions, regardless of the quality of the atmospheric model, the model outcomes will be wrong.

Emissions inventories exist at a range of spatial resolutions. For example, the Emissions Database for Global Atmospheric Research (EDGAR) presents emissions on a global scale [Crippa et al., 2020]. Other emissions inventories exist on national and regional scales for example the National Atmospheric Emissions Inventory (NAEI) in the UK [DEFRA, 2014] and the Multi-resolution Emissions Inventory for China (MEIC, `http://www.meicmodel.org/`) [Qi et al., 2017]. Local inventories can be useful to assess air quality on a city-scale to improve understanding of local conditions [Zhao et al., 2015]. This is especially useful for urban areas with high population density where poor air quality has significant impacts on residents. Emissions inventories can be developed using 'bottom-up' or 'top-down' methods. Bottom-up approaches involve statistical analysis of activity data and emissions factors whereas top-down approaches estimate emissions based on observations [Oda et al., 2019]. Emissions inventories can be associated with large uncertainties due to difficulty estimating emissions and activity factors [e.g. Li et al., 2017b, Cheewaphongphan et al., 2019]. Top-down methodologies often use inverse modelling techniques to scale national emissions statistics or observations to higher resolutions, but developing emissions estimates on sub-national scales can be problematic [Oda et al., 2019]. Spatial

proxies can be used to downscale emissions estimates but these do not often accurately represent emissions at local scales [Zheng et al., 2017].

One way that emissions inventories can be evaluated at local scales is by comparing to directly measured emissions. Using the eddy-covariance (EC) technique, fluxes of pollutants can be quantified and the pollutant flux compared to the emission inventory. Work carried out in London, UK used the EC technique to quantify NO_x flux and highlighted a significant underestimation of NO_x emissions by the NAEI. Measured emissions were on average 80% higher than the inventory suggested [Lee et al., 2015]. Discrepancies were assumed to be caused by unexpectedly high NO_x emissions from diesel vehicles which had not decreased as expected given emissions legislations [Carslaw and Rhys-Tyler, 2013]. A systematic underestimation of NO_x emissions by the NAEI for London was also suggested by a series of airborne eddy covariance measurements [Vaughan et al., 2016]. Karl et al. [2017] calculated NO_x fluxes for Innsbruck, Austria which also showed that NO_x from traffic sources could be considerably underestimated in Europe. Other sets of EC measurements have shown good agreement between inventories and measured emissions. For example, Velasco et al. [2009] showed that a local inventory compared well to measured emissions of CO_2 and selected VOCs in a residential district of Mexico City. Gioli et al. [2015] used long-term EC flux measurements of CO_2 to improve the temporal variability in a local atmospheric inventory, though showed good agreement between annual average CO_2 emissions.

EC fluxes only allow direct comparison to inventories on local scales, typically over a few kilometres, and for evaluation of emissions inventories on larger scales other techniques must be used. The mass balance technique has been used to calculate emissions from aircraft which allows emissions to be quantified over larger areas, for example over a city [e.g. Mays et al., 2009, Cambaliza et al., 2014, Pitt et al., 2019]. O'Shea et al. [2014] measured CO_2, CH_4 and CO fluxes over London using the mass balance technique and compared results with the NAEI. Measured fluxes were found to be at least a factor of 2 larger than emissions given in the annual inventory. As the flux measurement only provided a 'snapshot' of emissions it was difficult to evaluate the emissions inventory given the large degree of temporal variation in emissions. Aircraft mass balance techniques, whilst offering the ability to calculate emissions for city-

scale areas, are often limited as they require the surrounding areas to have negligible emissions sources which is often not a reasonable assumption to make [Pitt et al., 2019].

Inverse modelling is another technique which has been used for the evaluation of emissions inventories at local and regional scales. Essentially inverse modelling attempts to constrain an emissions inventory to observed pollutant concentrations. An atmospheric transport model is used to show how pollutants travel to a measurement site from a source given in the emissions inventory. Emissions can then be optimised in the model to best fit the measured pollutant concentrations. Bergamaschi et al. [2015] used inverse modelling and long-term, continuous measurements from a network of monitoring stations to evaluate GHG emissions for Europe and suggested that emissions inventories underestimate CH_4 emissions by 26–56%. A study over Paris used inverse modelling to show that NO_x emissions were overestimated in urban areas and underestimated in suburban areas of the city [Pison et al., 2007]. Inverse modelling is limited by the number of observations available however. This is especially problematic especially when using inverse modelling at local scales where air quality monitoring stations may be present but local meteorological observations are generally sparse and pollutant backgrounds variable.

Given the variable performance of emissions inventories, it is important to perform such evaluation exercises using techniques like EC flux, inverse modelling or mass balance. Depending on the purpose and scale of the inventory a combination of evaluation techniques may be useful.

1.4 Tropospheric chemistry of air pollutants

Emissions and meteorology have striking impacts on the pollutant concentrations experienced on Earth but pollutant emissions do not build-up in the atmosphere indefinitely. Thousands of tons of pollutant gases are released into and removed from the atmosphere each year. Photochemical reactions initiated by hydroxyl radicals (OH) oxidise pollutant gases [Lelieveld et al., 2004], allowing pollution to be removed from the atmosphere normally via wet- or dry-deposition [Fowler et al., 2009]. Production of the OH radical itself is initiated by the photolysis of O_3 in the presence of water

vapour (reaction R1 and R2) [Wayne, 1991].

$$O_3 + h\nu \longrightarrow O(^1D) + O_2(^1\Delta_g) \tag{R1}$$

$$O(^1D) + H_2O \longrightarrow 2OH \tag{R2}$$

In polluted atmospheres, the photolysis of nitrous acid (HONO) is also an important source of the OH radical (reaction R3) [Harrison, 2018].

$$HONO + h\nu \longrightarrow OH + NO \tag{R3}$$

1.4.1 Tropospheric ozone formation

Nitrogen oxides (NO_x) exists as NO and NO_2 in the atmosphere. In atmospheres with low VOC concentrations NO and NO_2 exist in equilibrium with O_3 according to reactions R4–R6 below. This equilibrium is known as the photostationary state (PSS). NO_2 is photolysed at $\lambda < 420$ nm, producing NO and an oxygen atom, $O(^3P)$. $O(^3P)$ reacts with O_2 to form O_3. This is the only significant source of O_3 within the troposphere [Monks et al., 2015]. O_3 reacts rapidly with NO, so there is no net formation or destruction of O_3, summarised in Figure 1.5A.

$$NO_2 + h\nu \longrightarrow NO + O(^3P) \tag{R4}$$

$$O(^3P) + O_2 + M \longrightarrow O_3 + M \tag{R5}$$

$$O_3 + NO \longrightarrow NO_2 + O_2 \tag{R6}$$

In the presence of CO or VOCs however (figure 1.5B) the PSS is perturbed. VOCs are oxidised by OH to form reactive peroxy radical intermediates (RO_2 or HO_2) shown in reactions R7 and R8:

$$VOC + OH \xrightarrow{O_2} RO_2 + H_2O \tag{R7}$$

$$CO + OH \xrightarrow{O_2} HO_2 + CO_2 \tag{R8}$$

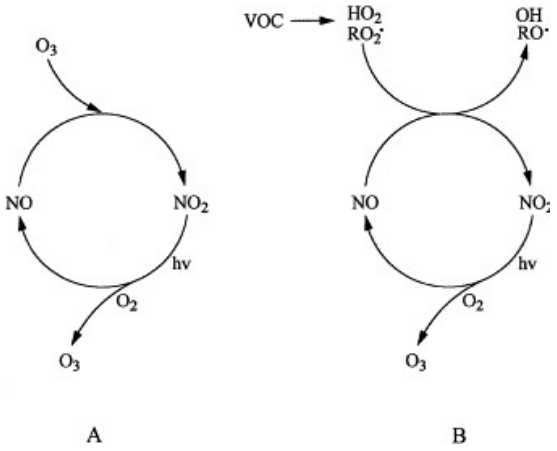

Figure 1.5: Schematic showing the interconversion of NO and NO_2 and O_3 formation in the absence of VOCs (A) and in the presence of VOCs (B). Figure taken from Atkinson [2000].

RO_2 or HO_2 can then react with NO to form NO_2 (reactions R9 and R10), in place of the O_3 molecule (shown earlier in reaction R6). O_3 is then generated according to reactions R4 and R5 but because an O_3 molecule is not used up when generating NO_2 as in the absence of VOCs, there is net O_3 production [Atkinson, 2000].

$$RO_2 + NO \xrightarrow{O_2} secondary\,VOC + HO_2 + NO_2 \tag{R9}$$

$$HO_2 + NO \longrightarrow OH + NO_2 \tag{R10}$$

O_3 production is a non-linear process with respect to NO_x concentrations [Monks et al., 2015]. This is due in part to the rapid reaction between O_3 and NO (reaction R6) so at high NO concentrations, O_3 is titrated by NO. Observations in urban areas, where NO concentrations are typically high due to plentiful emissions sources, show that O_3 concentrations can decrease when NO is over a threshold concentration [e.g. Tiwari et al., 2015]. At low VOC/NO_x ratios, NO_2 can compete with VOCs for reaction with OH to form nitric acid, HNO_3 (reaction R11) so NO_2 and a radical are removed from the system without formation of an O_3 molecule. HNO_3 is removed easily from the atmosphere by wet- or dry- deposition.

$$NO_2 + OH + M \longrightarrow HNO_3 + M \tag{R11}$$

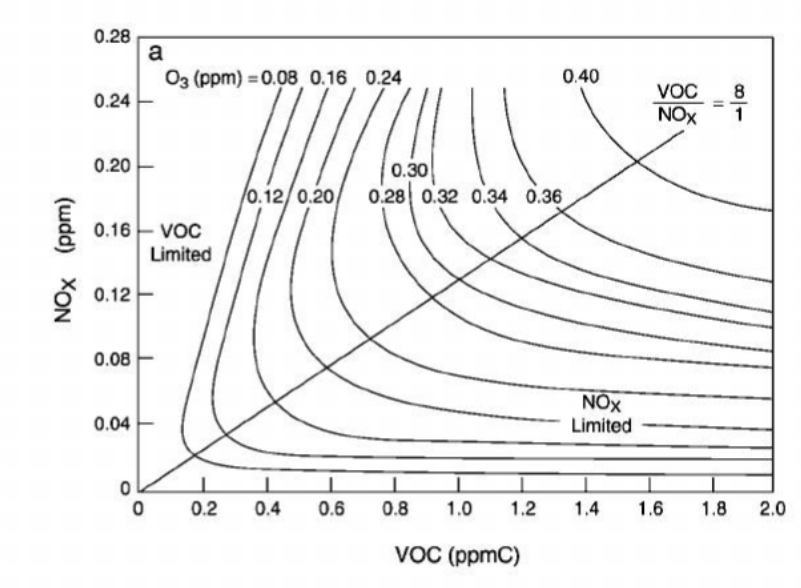

Figure 1.6: A typical O_3 isopleth, taken from Finlayson-Pitts and Pitts [2000b].

Figure 1.6 shows a typical O_3 isopleth, representing the non-linear relationship between concentrations of NO_x, VOCs and O_3. The sensitivity of O_3 formation to VOC or NO_x can be described as a "VOC limited" regime or "NO_x limited" regime. Figure 1.6 shows that in the NO_x limited part of the isopleth, increasing NO_x concentrations whilst VOC concentrations remain constant, increases O_3 concentrations. In contrast, the VOC limited part of the isopleth shows that moving along a line of increasing VOC concentrations and constant NO_x emissions increases O_3 concentrations.

1.4.2 Nitrogen oxides

As well as being the major route to O_3 formation in the troposphere, NO_x reacts to form other nitrogen species. The lifetime of NO_x in the troposphere is dictated by the chemical composition of the air, usually by loss of NO_x via formation of alkyl nitrates or HNO_3 via reaction with OH (reaction R11) and is non-linearly dependent on NO_x

concentration [Laughner and Cohen, 2019]. Generally speaking though, the lifetime of NO_x is short, on the order of a few hours to a few days [Monks et al., 2015], in the troposphere. In remote atmospheres, where there are no direct emissions sources, NO_x present in the atmosphere is usually released from other molecules which have longer lifetimes and can be transported over long distances. For example, peroxyacetyl nitrate (PAN, $CH_3C(O)OONO_2$) is a pollutant formed from the reaction of NO_2 with the peroxyacetyl radical (shown in reaction R12) [Fischer et al., 2014], itself formed from the oxidation of non-methane VOCs (NMVOCs).

$$CH_3C(O)OO + NO_2 + M \rightleftharpoons PAN + M \tag{R12}$$

Traditionally, it has been assumed that NO_x in marine atmospheres is formed from the transport and successive thermal decomposition of organic nitrates, such as PAN, originating in continental regions. Formation of HNO_3 (reaction R11) then removes NO_x from the system. A balance between these two processes was assumed to maintain the low NO_x mixing ratios observed but more recently, the role of particulate nitrate (p-NO_3) has been considered to be a significant source of NO_x in oceanic atmospheres. Reed et al. [2017] suggest that long-term observations of NO_x at the Cape Verde Atmospheric Observatory (CVAO), positioned on the north-eastern side of São Vicente (one of 10 islands in the Cape Verde archipelago) indicate photolysis of p-NO_3 plays a critical role in NO_x formation. Long-term measurements from CVAO show a consistent diurnal cycle with peak concentrations in the daytime ($\sim$ 15 pptv higher than at night), indicative of an in-situ, photolytic source. If the traditional view of NO_x formation is accepted, it would be expected that NO_x concentrations would decrease over the day due to reaction with OH. Ye et al. [2016] present further evidence for p-NO_3 as an in-situ source of NO_x. Rather than acting as a sink of NO_x, HNO_3 could act as a reservoir species that regenerates NO_x. Photolysis is enhanced by up to 4 orders of magnitude when adsorbed onto a surface, for example sea salt particles [Zhou et al., 2003, Baergen and Donaldson, 2013].

1.4.3 Carbon monoxide

Carbon monoxide (CO) is a major sink of OH and therefore influences the oxidising capacity of the atmosphere, accounting for around 40% of the removal of OH in the

troposphere [Lelieveld et al., 2016]. CO impacts global radiative forcing indirectly in this way by reducing OH concentrations and increasing O_3 and CH_4 abundances [Fiore et al., 2012]. As well as leading to O_3 formation in the troposphere, CO competes for the OH radical (reaction R13), the major CH_4 sink and therefore increases CH_4 lifetimes [Fiore et al., 2015]. CO contributes to tropospheric O_3 formation via the formation of HO_2 (reactions R13 and R34).

$$CO + OH \longrightarrow CO_2 + H \tag{R13}$$

$$H + O_2 + M \longrightarrow HO_2 + M \tag{R14}$$

The global average lifetime of CO is approximately 2 months [Novelli et al., 1998], but its lifetime is dependent on OH abundance. As such a great degree of spatial and temporal variability in CO lifetimes; CO lifetimes are approximately 10 days near the tropics due to higher OH abundance and over a year in the polar regions [WMO, 2018]. Compared to NO_x however it exists on timescales long enough to be transported over longer distances away from emissions sources, influencing atmospheric composition and chemistry of other regions. This makes CO an ideal tracer of transport of global and regional pollutants from biomass burning and anthropogenic activities [e.g. Stohl et al., 2003, Sodemann et al., 2011, Panagi et al., 2020].

1.4.4 Volatile organic compounds

Volatile organic compounds (VOCs) are important for O_3 formation, discussed in section 1.4.1, and can also be oxidised to form secondary organic aerosol (SOA). As emissions technologies improve secondary particulates comprise an increasing component of particulate matter [Air Quality Expert Group, 2012, Guo et al., 2014, Duan et al., 2020]. The chemistry of VOCs is complex due to the wide variety of emitted compounds with different structures and functional groups and hence different chemical properties [Mellouki et al., 2015]. As a result of the differences in reactivity, different VOCs have different O_3 formation potentials. For example, aldehydes (which contain a carbonyl group) were found to have higher O_3 formation potentials than other VOCs, accounting for 40% of total O_3 formation for a study in Beijing [Duan et al., 2008]. Atmospheric lifetimes vary greatly for VOCs as a result of different reactivity ranging

from minutes to years depending on atmospheric composition [Atkinson and Arey, 2003].

Saturated hydrocarbons like alkanes can react with OH or NO_3 radicals or Cl atoms through abstraction of a H atom [Stockwell et al., 2012]. This leads to the formation of peroxy radicals which leads to tropospheric O_3 production (presented in section 1.4.1). Saturated hydrocarbons that are larger or have a greater degree of branching produce more stable radicals and therefore are more reactive to OH. For unsaturated hydrocarbons, like alkenes, OH can react through addition of OH across the double bond [Atkinson, 2000] e.g. for 1-butene:

$$CH_3CH_2CH = CH_2 + OH + M \longrightarrow CH_3CH_2\dot{C}HCH_2OH + M \qquad \text{(R15)}$$

This hydroxyalkyl radical can then react with O_2 to form a hydroxyalkyl peroxy radical which can contribute to tropospheric O_3 formation as per the reaction scheme in section 1.4.1. Aromatic hydrocarbons predominantly react with OH, first via H abstraction from a C–H bond, then by radical addition of OH to the aromatic ring [Atkinson, 2000].

1.5 Thesis Outline

This thesis presents work carried out in Beijing, China; a megacity with a population of over 20 million, and over the remote North Atlantic Ocean. Both of these atmospheres can be described as polluted, though to different degrees. The work in this thesis explores the atmospheric composition of both environments and demonstrates the role of emissions, meteorology and chemistry in determining the atmospheric composition observed.

Chapter 2 outlines the principles of operation for the measurement of gas-phase pollutants; O_3, NO_x, NO_y, CO and SO_2 and describes the measurement site and instrument set-up. Measurements were carried out during two field campaigns in Beijing, as part of the Air Pollution and Human Health-Beijing project. Fieldwork took place during November–December 2016 and May–June 2017. An uncertainty analysis is carried out for the measurements made during the two field campaigns.

Chapter 3 presents details of gas-phase pollutants measured in Beijing. Seasonal differences in pollutant mixing ratios are presented and possible drivers for these differences suggested. An analysis of the NO_x-O_3 chemistry is carried out, with particular focus on any reasons for deviations from the photostationary state.

Chapter 4 presents emissions measurements made using the EC technique in Beijing. Emissions of NO_x, CO and some aromatic VOCs were quantified for the first time using this technique, the dominant source of which was determined to be vehicle emissions. The seasonal differences between emissions are discussed and the measured emissions are compared to a Chinese emissions inventory. It was found that for the emissions measured, the inventory considerably overestimates emissions.

Chapter 5 presents airborne measurements of gas-phase air pollutants made over the North Atlantic Ocean. The spatial distribution of pollutants is examined and pollutant ratios and trajectory analysis used to classify some air masses sampled during flights. Measurement data is compared with the GEOS-Chem model.

Chapter 6 summarises the main findings of this work.

2 Experimental

THIS chapter discusses the methods used during two field campaigns in Beijing, China as part of the Air Pollution and Human Health-Beijing (APHH) project. An overview of the techniques used to obtain measurements presented in this thesis is given and an uncertainty analysis carried out.

2.1 A note on terminology used in this thesis

The term 'mixing ratio' is used throughout this thesis to refer to the molar fraction of a substance in air. This can also be referred to as 'amount fraction' (short for amount of substance fraction), but given the prevalence of mixing ratio within the atmospheric science community, it is used in this work instead. The units of gaseous mixing ratios are defined as:

- ppm = μmol mol^{-1} = 10^{-6} mole of substance per mole of air
- ppb = nmol mo^{-1} = 10^{-9} mole of substance per mole of air
- ppt = pmol mol^{-1} = 10^{-12} mole of substance per mole of air

2.2 The measurement site in Beijing, China.

Measurements were taken at the Institute of Atmospheric Physics (IAP), Chinese Academy of Sciences (39°58'28"N, 116°22'16"E) in central Beijing, shown in Fig. 2.1. The site is between the third and fourth ring roads and surrounding land use can

be characterised as urban, being mainly residential with some busy (two and three lane dual-carriageway) roads nearby. The Jingzang Highway is approximately 400 m east of the site. Buildings surrounding the tower are predominantly 15–30 m in height, but with some almost 100 m tall within 500 m to the south of the tower. The site is in a 'green' area with some park space and a canal close by. In terms of the wider area, Beijing is situated at the northern tip of the North China Plain. The city itself and areas to the south are reasonably flat. Beijing is surrounded by the Yanshan mountain ranges to the north and the Xishan mountain ranges to the west.

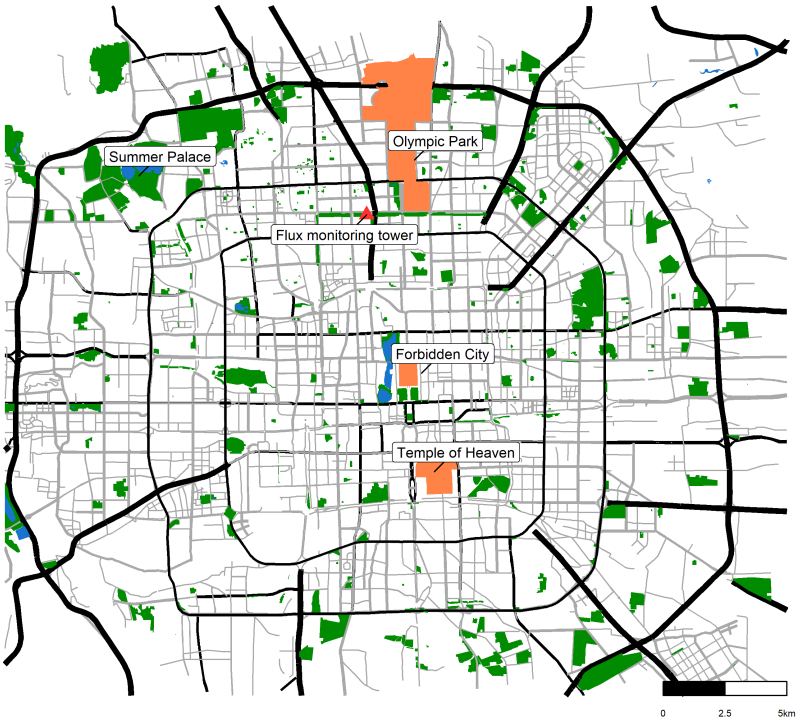

Figure 2.1: Measurement site position is shown by the red triangle between the third and fourth ring roads. Key landmarks of Beijing are highlighted in orange with major roads shown in black and smaller roads in grey. Parks are shown in green and water in blue. Surrounding land use is mainly residential with many restaurants within a few hundred meters of the site with the Jingzang Highway close by. Map was built using data from © OpenStreetMap contributors 2019. Distributed under a Creative Commons BY-SA License.

2.3 Gas-phase air quality instrumentation

This section describes the measurement of O_3, NO, NO_2, NO_y, SO_2 and CO with instrumentation shown in Fig. 2.2.

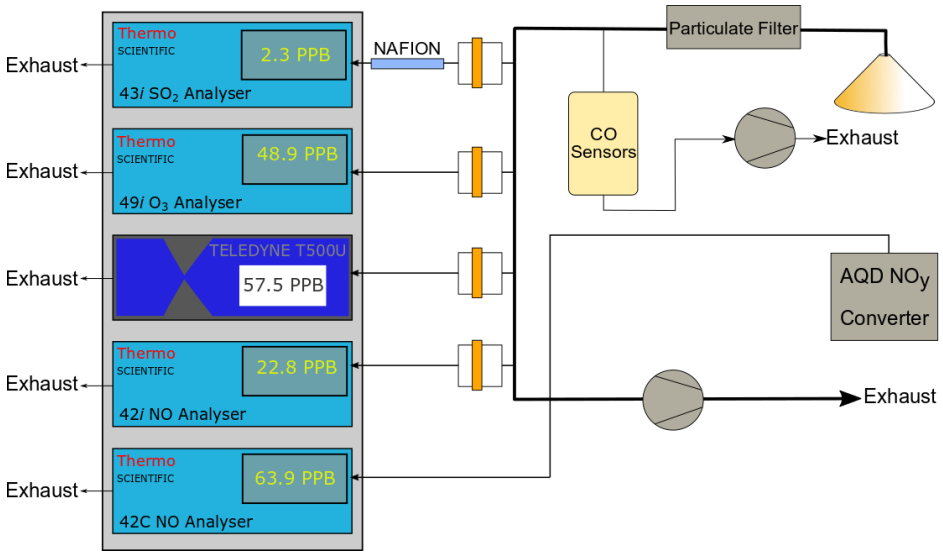

Figure 2.2: Flow schematic for the air quality instrumentation deployed during the winter and summer field campaigns in Beijing. All measurements shared a manifold line apart from the NO_y measurement which had a dedicated sample inlet.

Air quality instrumentation was housed in a modified shipping container laboratory at the IAP site, to make measurements of gas-phase pollutants: NO, NO_2, NO_y, O_3, CO and SO_2. A vacuum pump sampled ambient air at a rate of approximately 30 SLPM from an elevated inlet at 8 m. All gas lines were heated and insulated to minimise condensation within the line. A filter was installed at the inlet of the manifold to remove any particles and changed regularly to ensure sufficient flow rates were maintained. Each instrument drew from the sample manifold as shown in Fig. 2.2, apart from the NO_y measurement which had a dedicated sample inlet.

Measurement of ozone

O_3 was measured using a Thermo Scientific Model 49*i* UV photometer which exploits the absorption of O_3 in the UV range. O_3 absorbs light at a wavelength of 254 nm

[Parrish and Fehsenfeld, 2000] with the degree of absorption being proportional to concentration as per the Beer-Lambert law:

$$\frac{I}{I_0} = e^{-KLC} \tag{2.1}$$

Where I is the intensity of UV light emitted by O_3 in the sample gas, I_0 is the intensity of UV light emitted by the reference gas, K is the molecular absorption coefficient of O_3, L is the length of the cell (38 cm) and C is the mixing ratio in ppm. The instrument itself has two separate cells, into which monochromatic light at 254 nm is shone. Sample gas alternates between reference and sample modes which allows continuous O_3 measurements and compensates for fluctuations in instrument conditions e.g. lamp intensity. Air is sampled at a rate of 1 SLPM and split into two streams. One gas stream passes through an ozone scrubber, removing any ambient O_3 creating a reference sample whilst the second stream passes unaltered into the sample cell. Two detectors measure the UV light intensities in the two cells and the O_3 mixing ratio is calculated according to equation 2.1. Given that few other atmospheric species absorb at this wavelength there are minimal interferences.

Measurement of nitrogen oxide

Nitrogen oxide was measured by chemiluminescence with a Thermo Scientific Model 42*i* NO_x analyser which quantifies NO through its reaction with O_3 and subsequent light emission from the decay of excited state NO_2 produced [Drummond et al., 1985]. The instrument sampled ambient air from the sample manifold at a rate of 1 SLPM. The sample is directed to a reaction chamber where any NO in the sample reacts with O_3. The O_3 is generated from ambient O_2 by an internal silent discharge ozonator sampling dry ambient air from a separate inlet. On reaction with O_3, NO reacts to produce excited NO_2* molecules which produce infra-red light emission when the molecules decay to the ground state. Simply, the reaction is:

$$NO + O_3 \longrightarrow NO_2 + O_2 + h\nu \tag{R16}$$

The resulting luminescence is detected by a photomultiplier tube (PMT) which produces a photocurrent proportional to the number of photons emitted. The chemiluminescence technique will be discussed in more detail in section 2.5.

Measurement of nitrogen dioxide

NO_2 was measured directly, using a Teledyne Model T500U Cavity Attenuated Phase Shift (CAPS) spectrometer. This instrument operates as an optical absorption spectrometer, exploiting the strong absorbance of NO_2 at 450 nm (as per the Beer Lambert Law, equation 2.1). A light emitting diode (LED) emits light at a wavelength of 450 nm into a measurement cell which has high-reflectivity mirrors at either end of the cell to increase the path length of the light. When NO_2 is present and light is absorbed, there is a shift in the phase of light detected by the photodiode detector compared to the phase of the incident light. This phase shift is proportional to absorption so increases with amount of NO_2 [Kebabian et al., 2005]. This method is advantageous as there are no interferences from reactive nitrogen species due to the wavelength used as have been reported for NO_2 measurements in chemiluminescence systems. Many commercial chemiluminescence systems use a non-selective catalytic converter to reduce NO_2 to NO, allowing detection as for NO, which also convert reactive nitrogen species like HNO_3 and PAN [Dunlea et al., 2007, Ge et al., 2013].

Measurement of total reactive nitrogen

Odd nitrogen, NO_y (the sum of NO_x + HONO + HNO_3 + HO_2NO_2 + NO_3 + $2N_2O_5$ + PAN + other organic nitrates + aerosol nitrate...) was measured using a Thermo Scientific Model 42*C* NO_x analyser with a molybdenum mesh catalyst heated to approximately 350 °C located at the sample inlet. The molybdenum converter reduces NO_y compounds to NO, which is then measured via the chemiluminescence reaction with O_3. The Mo surface is oxidised to MoO_2 and MoO_3 as NO_y is reduced. The difference between NO_y and NO_x mixing ratios quantifies non-NO_x reactive nitrogen compounds termed NO_z. This method has been shown in other studies to have a high conversion efficiency ($> 90\%$) for NO_y species at ambient mixing ratios [Fehsenfeld et al., 1987, Williams et al., 1998]. For analysis presented in this thesis it is assumed that the conversion efficiency of NO_y by the molybdenum converter is 100% which has been calibrated using NO_2.

Measurement of sulfur dioxide

SO_2 was measured using a Thermo Scientific 43*i* fluorescence spectrometer. SO_2 molecules absorb UV light at wavelengths 190–230 nm (equation R17) with emission from electronically excited SO_2* molecules occurring at 240–420 nm (equation R18), as they decay back to the ground state [Okabe et al., 1973].

$$SO_2 + h\nu_1 \longrightarrow {SO_2}^* \tag{R17}$$

$${SO_2}^* \longrightarrow SO_2 + h\nu_2 \tag{R18}$$

The intensity of light emission is proportional to SO_2 concentration. Air is drawn into the instrument at a rate of 1 SLPM, via a nafion drier, to remove water vapour from the sample stream which can weaken the fluorescence signal by providing an alternative path back to the ground state through quenching. Fluorescence systems can suffer from interferences with hydrocarbons being highly fluorescent at UV wavelengths which can cause misleading enhancements in SO_2 signal. To eliminate this interference, the sample passes through a hydrocarbon 'kicker' before entering the reaction cell, through which hydrocarbons are removed from the sample stream by application of differential pressure across a partially permeable membrane. SO_2 molecules pass through unaltered. A UV flash lamp, pulsed at a rate of 10 Hz, emits UV light for the excitation of SO_2 molecules. The UV light from the lamp is focused through a condensing lens onto a series of mirrors which selectively reflect wavelengths of light required for excitation of SO_2 (wavelengths 190–230 nm). Fluorescence is then detected by a PMT.

Measurement of carbon monoxide

CO measurements were made using 6 clustered electrochemical sensors (Alphasense Ltd.) encased in a 2×3 formation. Ambient air was supplied from the manifold line to the sensors at a flow rate of 1.5 SLPM via a metal bellows pump. The sensors performed well when compared to a reference CO instrument (Aero-Laser AL5002 vacuum UV analyser) described in section 2.6. It was found that through clustering the sensors, rather than having individual sensors, the performance was improved through

eliminating random drift observed for individual sensors [Smith et al., 2017]. The electrochemical sensors use a three electrode system; the working electrode which is coated with a high surface area catalyst, a counter electrode and a reference electrode [Mead et al., 2013]. When CO comes into contact with the working electrode it undergoes a redox reaction, generating a current at the working electrode which is balanced by reaction at the counter electrode. This changes the potential of the counter electrode whereas the potential of the working electrode is fixed through the reference electrode which is maintained at a constant potential. A potential difference is therefore generated between the working and counter electrodes which forms the output signal of the sensor. Because the rate of diffusion of the CO gas into the sensor is slower than the rate of reaction of the gas at the electrode the potential difference generated is proportional to CO concentration [Stetter and Li, 2008].

2.3.1 Calibration of air quality instrumentation

All instruments were calibrated regularly throughout the measurement period, at least once every week, but more frequently during the summer campaign when temperatures were warmer and laboratory conditions less stable. A 'zero' or background calibration was carried out for the NO, NO_2, NO_y, SO_2 and O_3 instruments using a Sofnofil/charcoal trap. Sample gas passes through Sofnofil beads first then activated charcoal. Activated charcoal removes NO_2, SO_2 and O_3 as the molecules adsorb onto the charcoal surface. NO is oxidised to NO_2 by the Sofnofil, which contains potassium permanganate as the oxidising agent and is then removed by the activated charcoal as NO_2. The background signal of the CO sensors was determined by calibration with a BTCA zero air standard. Span (high mixing ratio) calibrations were carried out using gas standards. Both the Thermo Scientific 42i (NO measurement) and 42C (NO_y measurement) were calibrated by overflowing the inlet with a 100 ppbv NO in nitrogen standard, traceable to the National Physical Laboratory (NPL) NO scale. The NO_2 instrument was calibrated using a 73 ppbv NO_2 in nitrogen standard (BOC). The SO_2 instrument was calibrated using a 1 ppm SO_2 standard (BOC). CO sensors were calibrated frequently throughout the campaign using a BOC 1 ppm CO in synthetic air standard.

2.4 Measurement of NO_x and CO fluxes

2.4.1 Instrument set-up

In order to quantify pollutant flux, high time resolution data is required to capture the rapid changes that result from the turbulent transport of pollution. 5 Hz measurements of NO_x and CO mixing ratios were made at the IAP site at which there is a 325 m tall meteorological tower. NO_x and CO instrumentation was housed in a temporary shipping container laboratory located at the base of the tower and sample lines from an inlet platform at an elevation of 102 m ran down the tower to the laboratory.

2.5 NO_x chemiluminescence measurements

Chemiluminescence is a well documented technique for the measurements of nitrogen oxides which has been used extensively in remote and polluted environments [Lee et al., 2009, Reed et al., 2017, Karl et al., 2017]. The key principles behind the measurement technique are explored here.

NO is detected through the reaction with excess O_3 to form excited state NO_2 (reaction R19), which emits a photon on decaying to the ground state (reaction R20). Light at a wavelength of > 600 nm is emitted with an intensity proportional to the concentration of NO [Kley and McFarland, 1980].

$$NO + O_3 \longrightarrow {NO_2}^* + O_2 \tag{R19}$$

$${NO_2}^* \longrightarrow NO_2 + h\nu \tag{R20}$$

The measurement of NO_2 is slightly more complex. For detection by chemiluminescence, NO_2 must first be reduced to NO. One way to achieve this is through catalytic reduction e.g. a molybdenum converter, as is used in some commercially available NO_x measurement systems. The high conversion efficiency of the Mo converter has made this option attractive in the past, however other reactive nitrogen species (NO_z) are also reduced to NO leading to overestimation of NO_2 concentrations [Dunlea et al., 2007]. Another more specific method is to photolytically convert NO_2 to NO [Kley

and McFarland, 1980, Ryerson et al., 2000], shown in reaction R21.

$$NO_2 + h\nu \longrightarrow NO + O \tag{R21}$$

NO_2 is photolysed at wavelengths below 400 nm. A range of converters have been used to photolyse NO_2 to NO, for example mercury lamps, Xenon arc lamps and UV-LEDs [Sadanaga et al., 2010]. Those with broadband light sources (e.g. mercury and Xenon arc lamps) are associated with low conversion efficiencies and given these emit radiation at shorter and longer wavelengths than required for NO_2 photolysis they are affected by interferences from other species, e.g. HNO_3, at wavelengths below 350 nm [Buhr, 2007]. Pollack et al. [2010] evaluated the performance of three types of photolytic converter and showed that blue light converter (BLC) with $\lambda = 395$ nm had a smaller spectral overlap with interfering compounds compared to those operating at a shorter wavelength of 365 nm.

2.5.1 The AQD NO_x chemiluminescence detector

5 Hz NO_x mixing ratios were measured in Beijing using a dual channel chemiluminescence analyser (Air Quality Design Inc., Golden, Colorado, USA). The two channels enable simultaneous measurements of NO and NO_2. A flow schematic is shown in Fig. 2.3.

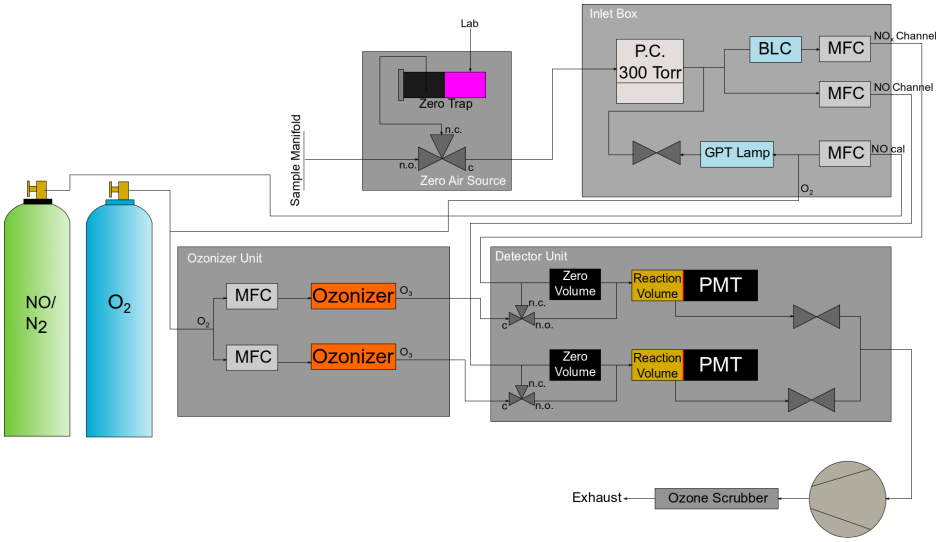

Figure 2.3: Flow diagram for the Air Quality Design Inc. (AQD) NO_x Chemiluminescence Analyser.

Ambient air enters the system via the inlet box, and is pressure controlled at 300 Torr by an MKS 640 pressure controller before being split into two channels; the NO channel and the NO_x channel. Both channels are mass flow controlled using a mass flow controller (MFC, MKS Instruments, Type 1179A), maintaining flow in each channel at 1500 sccm. In effect, the two channels are identical with the same components and the same path lengths apart from a photolytic converter in the NO_x channel which converts NO_2 to NO. The photolytic converter used is supplied by Air Quality Design Inc. (AQD) and has a high conversion efficiency compared to traditional photolytic converters that use broadband light sources [Buhr, 2007]. The converter is comprised of two UV-LED arrays at either side of a highly reflective Teflon block through which the sample gas flows. The volume of the converter is 10 mL, giving a residence time of 0.12 s. To remove heat generated by the UV-LEDs, and prevent thermal decomposition of reactive nitrogen species that could lead to a falsely high NO_2 reading [Reed et al., 2016], the converter is Peltier cooled to below 35 °C. The wavelength of light produced by the UV-LED arrays is 395 nm which provides good spectral overlap with the NO_2 quantum yield and cross section, and limited overlap with the spectra of other potentially interfering species [Pollack et al., 2010] including

HONO, shown in Fig. 2.4. In the NO channel an extra length of PFA tubing with a volume of 10 mL is included so that there is no lag between the two channels.

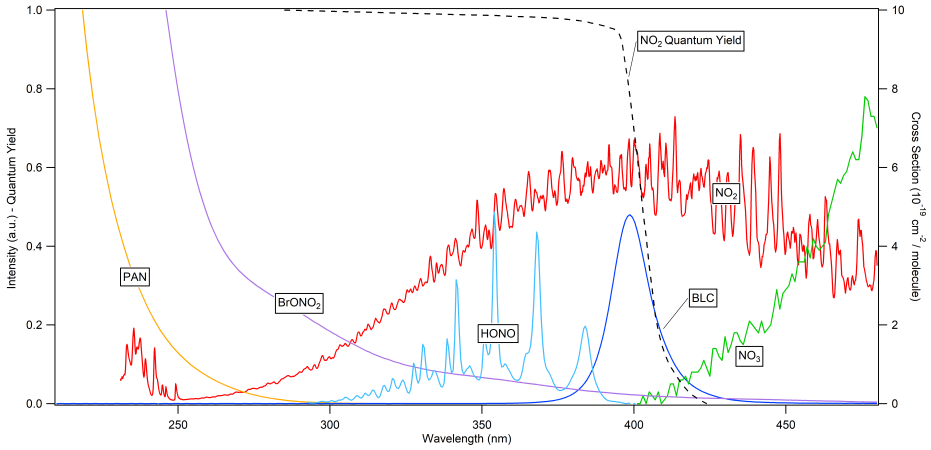

Figure 2.4: Absorption cross section (red) and quantum yield (dashed black) of NO_2, presented with the average spectral output of BLC lamps (dark blue) used in a similar instrument discussed in Reed et al. [2016]. The absorption cross spectra for NO_3 radicals (green), HONO (light blue), BrONO2 (lilac) and PAN (yellow) are also shown to show that these species are not interferences for the BLC. Figure adapted from Reed et al. [2016].

Gas in the two channels is then fed into the detector unit, which houses the reaction cells where the ambient sample in each channel reacts with excess O_3 generated in the ozonizer units (described below). Two reaction vessels (241 mL, stainless steel with gold coating) sit in front of two PMTs (Hamamatsu, R2257P). The signal detected by the PMTs is the sum of chemiluminescence from the NO + O_3 reaction, the "dark current" from thermionic emissions of the PMT and from any interference e.g. other gas-phase reactions or from illumination of chamber walls [Drummond et al., 1985]. In order to minimise quenching of the excited NO_2 molecules by other molecules, and therefore maximise the chemiluminescence signal, the reaction cell is maintained at a low pressure of 10 Torr. Other atmospheric molecules (such as alkenes) can react with O_3 but these emit photons between 400 and 600 nm. This signal is negated by the presence of a red transmission filter in front of the PMT which only transmits photons with a wavelength longer than 600 nm [Drummond et al., 1985]. To minimise the

dark current signal the PMT is cooled to below -15 °C by Peltier coolers but it is still necessary to quantify this background signal. In order to do this the instrument is "zeroed" at regular intervals (once every hour for 2 minutes during instrument operation in Beijing). When the instrument is in zero mode the O_3 generated in the ozonizer unit is diverted to a zero volume (180 mL, PFA) to mix with the sample before reaching the reaction volume. This means that the chemiluminescent reaction occurs in the zero volume rather than the reaction chamber and no chemiluminescence is detected by the PMTs. The counts measured are due to background signal.

The ozonizer unit supplies a constant flow of O_3 to the detector unit. O_2 gas from a cylinder is supplied to two "ozonizers" which generate O_3 by corona discharge. A high voltage is applied across the surface of a glass tube through which the O_2 gas flows, splitting O_2 molecules, forming two unstable O^- atoms. These unstable O^- atoms then react with other O_2 molecules forming O_3.

A scroll pump (Edwards nXDS20) is used to pull the sample air through both channels. An O_3 scrubber (Ozone Solutions) is used to remove O_3 from the exhaust stream, with a removal efficiency of 99.9%.

2.5.2 AQD NO_x calibrations

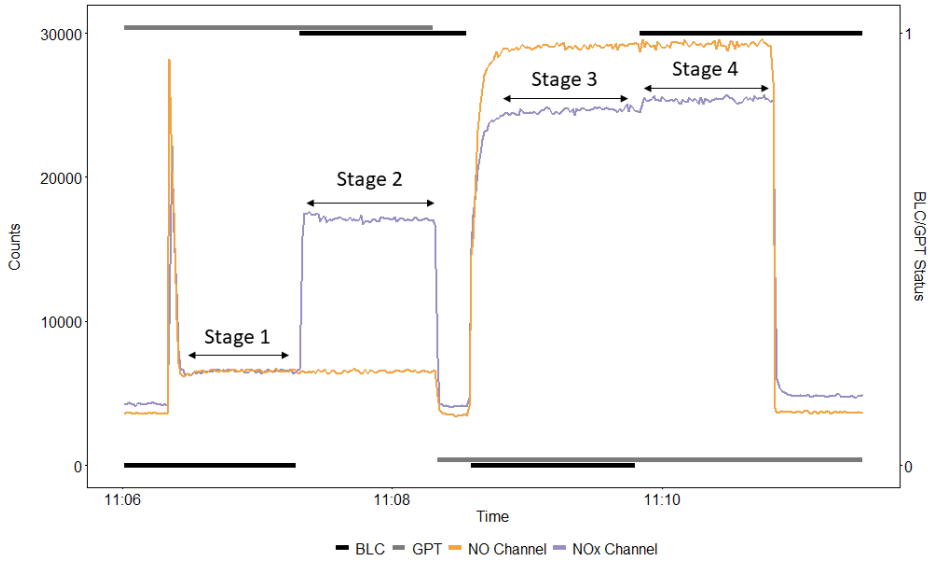

Figure 2.5: Example calibration sequence for the AQD NO_x analyser showing the four stages of the calibration. When the BLC or GPT signal is 1 they are switched on and when the signal is 0 they are off. Note that the GPT trace in grey has been offset slightly from the BLC trace so it can be seen clearly.

Regular calibrations were carried out during the field campaigns in Beijing approximately every 2–3 days. To calibrate the sensitivity of each channel to NO a flow of 10 sccm of a 1 ppmv NO calibration standard was added to a scrubbed ambient air flow of 3000 sccm to give a NO mixing ratio of approximately 3000 pptv. By adding the calibration gas to ambient air, channel sensitivities are calculated in air which has the same humidity as the sample. Water vapour acts as a quencher of the NO_2 excited state so sensitivity can be affected by changes in humidity. The stages of the calibration can be seen in Fig. 2.5. The scrubbed air is supplied through a Sofnofil/activated charcoal scrubber sampling air from inside the laboratory. The conversion efficiency of the photolytic converter is calibrated by gas phase titration (GPT), where O_3 is added to the sampled NO calibration gas in the titration cell to create a known mixing ratio of NO_2. The GPT cell consists of a mercury pen lamp which generates UV light converting O_3

from O_2 (fed to the cell from the O_2 cylinder) and oxidising 60–80% of the NO into NO_2.

Calculating conversion efficiency

Figure 2.5 shows an example calibration sequence for the AQD NO_x analyser. During stage 1 the GPT lamp is on, so NO from the calibration cylinder is converted to NO_2. As the BLC in the NO_x channel is off, only NO which has not been titrated is measured. During stage 2, the GPT lamp remains on and the BLC switches on corresponding to a signal increase. The NO_x channel is now measuring NO, as per stage 1 with the addition of the titrated NO_2 created in the GPT. Any small amount of NO_2 in the calibration standard will also be measured at this stage. During stage 3, both the BLC and GPT are off so the NO_x channel signal is solely from NO in the calibration standard. During the final stage of the calibration the BLC is turned on again to allow measurement of any NO_2 in the cylinder, corresponding to a small increase in counts. Conversion efficiency is then calculated from the mean counts at each stage in the calibration, according to equation 2.2. The subscripted numbers correspond to the different stages of the calibration.

$$C.E. = 1 - \frac{NO_xCounts_{(4)} - NO_xCounts_{(2)}}{NO_xCounts_{(3)} - NO_xCounts_{(1)}} \tag{2.2}$$

As instrument conversion efficiency deteriorated over the course of the two campaigns, conversion efficiencies were linearly interpolated between each calibration and applied to raw data. Conversion efficiencies varied between 0.9 and 0.5 over the two campaigns.

Calculating channel sensitivity

Sensitivity to NO is calculated during the third stage of the calibration shown in Fig. 2.5. The sensitivity of each channel is equal to the increase in counts caused by the calibration gas during NO calibration (untitrated) divided by the mixing ratio of the diluted calibration gas. The median sensitivity for the NO channel was determined to be 4.97 Hz $pptv^{-1}$ during the APHH winter and summer measurement campaigns. The NO_x channel sensitivity was slightly lower at 4.53 Hz $pptv^{-1}$. The channel sensitivities

remained consistent during the two campaigns. NO and NO_2 mixing ratios are then calculated from raw PMT counts using equations 2.3 and 2.4 respectively.

$$NO(pptv) = \frac{NO\ Counts_{measure\ mode} - NO\ Counts_{zero\ mode}}{NO\ sensitivity} \tag{2.3}$$

$$NO_2(pptv) = \frac{\left(\frac{NO_X\ Counts_{measure\ mode} - NO_X\ Counts_{zero\ mode}}{NO_X\ sensitivity}\right) - NO\ (pptv)}{C.E.} \tag{2.4}$$

2.6 Carbon monoxide measurements

CO was measured using a resonance fluorescence technique where the fluorescence from excited state CO to its ground state is at a similar wavelength as the exciting radiation. Vacuum ultra-violet (VUV) fluorescence is used to excite the fourth positive bands of CO at 150 nm and was first described by Volz and Kley [1985]. CO is excited by filtered radiation from a resonance lamp according to reaction R22 and relaxes to its ground state via fluorescence (equation R23). Excited CO molecules can also be deactivated by quenching, which can be minimised by maintaining a low pressure inside the instrument fluorescence chamber (equation R24).

$$CO(X^1\Sigma, v'' = 0) + h\nu \longrightarrow CO(A^1\Pi, v') \tag{R22}$$

$$CO(A^1\Pi, v') \longrightarrow CO(X^1\Sigma, v'' = 0) + h\nu \tag{R23}$$

$$CO(A^1\Pi, v') + M \longrightarrow CO(X^1\Sigma, v'' = 0) + M \tag{R24}$$

The instrument used was an Aerolaser AL5002 CO monitor described by Gerbig et al. [1996, 1999]. Figure 2.6 shows the flow system for the instrument.

2.6.1 The AeroLaser AL5002 CO monitor

The AeroLaser instrument comprises a resonance lamp and optical filter, fluorescence chamber and PMT to measure CO fluorescence. The resonance lamp is used to generate VUV radiation at approximately 150 nm. A mixture of 0.25% CO_2 in Ar is

required to operate the lamp and is supplied from a cylinder. The light generated is collimated with a parabolic mirror and then filtered using dielectric mirrors which have a bandwidth of approximately 10 nm centred at 150 nm. The entire optical path between the lamp and the fluorescence chamber is flushed with high purity N_2 (N6.0) to avoid absorption by molecular oxygen and impurities, especially CO [Gerbig et al., 1999] Given the volume of the optical path is small, a low flow of N_2 gas is required (approximately 35 mL min^{-1}). Ambient air is drawn into the fluorescence chamber, via an external nafion drier, using a scroll pump. The filtered light from the resonance lamp is directed into the fluorescence chamber where fluorescence from atmospheric CO is viewed at a right angle by a PMT with suprasil windows, thus only measuring fluorescence from CO in the ambient sample and not that from the lamp. The fluorescence of CO is distributed in the range 145–220 nm [Volz and Kley, 1985] so to maximise the ratio of resonance fluorescence to scattered light the PMT detects light in the between 160 nm and 190 nm. This, along with the filtering of the resonance lamp and the PMT angle minimises the signal from scattered light. The AeroLaser instrument has a fast time response (less than 0.1 s) making it appropriate for the fast measurements required for calculating fluxes.

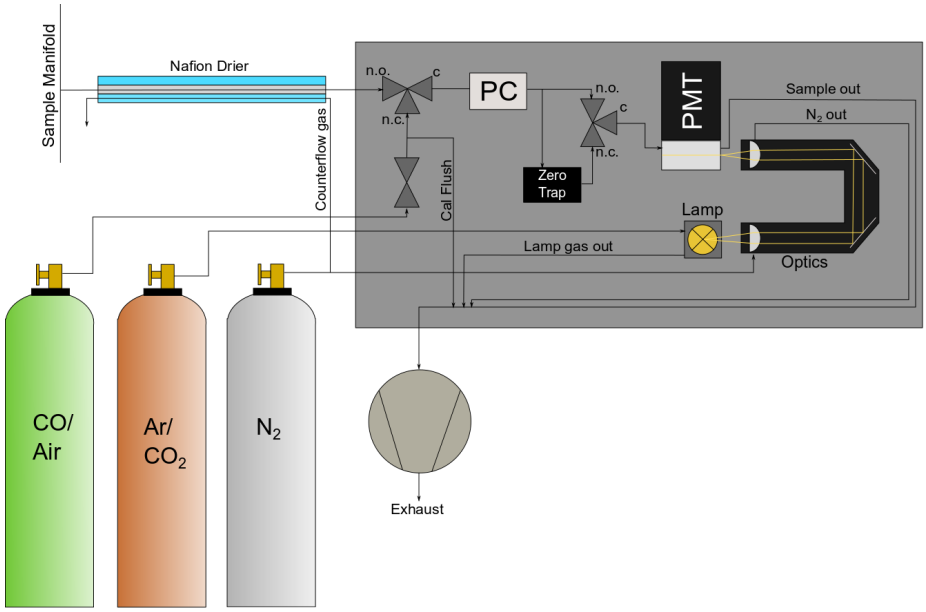

Figure 2.6: Flow diagram for the AL5002 CO Monitor adapted from the AeroLaser AL5002 Manual v1.27 (http://www.aero-laser.de).

2.6.2 Calibration of the AL5002 CO analyser

The AL5002 CO analyser was calibrated at regular intervals during the APHH winter and summer campaigns to determine the sensitivity of the instrument. Each calibration takes approximately 90 seconds. The instrument was calibrated using a 1 ppmv gas standard to determine instrument sensitivity (Hz $ppbv^{-1}$). The calibration starts with the stabilisation of the calibration standard, by flushing the gas through the internal lines before allowing the standard gas to enter the fluorescence chamber. The signal is averaged and sensitivity calculated. The background signal (Hz), i.e. signal when CO mixing ratio is 0 ppbv, was determined by passing the calibration gas through an internal Hopcalite scrubber which quantitatively removes CO to mixing ratios $<$ 1 ppbv by oxidising CO to CO_2. Instrument calibrations are automatically applied to the data as they are performed. The instrument has been shown to have a linear response to CO mixing ratios from $<$ 1 ppb to 100 ppmv CO [Gerbig et al., 1999].

2.7 Instrument uncertainties

When reporting a measurement it is necessary to quantify the uncertainty or 'doubt' associated with that measurement. This is essential as it allows an assessment of the reliability or quality of the measurement to be made. It is important to note that uncertainty is different from error, where error is the difference between the measured value and the 'true' value and is generally corrected by applying calibration factors. When an uncertainty is normally distributed it can be reported as an expanded uncertainty by applying a coverage factor, k. The expanded uncertainty gives the range which the result of a measurement can then be expected to fall within at a given confidence interval. A k of 2 is applied in this analysis which equates to a confidence level of 95%, the level recommended by the World Meteorological Organisation [World Meteorological Organization, 2018]. The uncertainty associated with a measurement can be estimated in two ways; 'Type A' uncertainties are estimated using statistical methods and 'Type B' which are estimated by any other means e.g. calibration certificates and manufacturers specifications [Bureau International des Poids et Mesures, 2008]. Instrument uncertainties are first discussed for the flux instrumentation and then for air quality instrumentation.

Estimating uncertainty of the AQD NO_x analyser measurements

Sources of uncertainty for the AQD NO_x analyser were identified and include instrument precision, uncertainty due to the calibration factors applied, uncertainty in the calibration cylinder mixing ratio, variable instrument flows, instrument drift and NO and NO_2 artefacts. The instrument precision in this analysis refers to the minimum signal that can be reliably recorded by the detector and is related to the signal-to-noise ratio. The instrument precision of the AQD NO_x analyser was determined from the zero count variability which is determined by the photon-counting precision of the detector [Lee et al., 2009]. Photon-counting rates are best described by a Poisson distribution [Mandel, 1958] but at high photon counting rates can be described by a Gaussian distribution [Lee et al., 2009]. The background photon counting rates for the campaigns in Beijing ranged between 6000 Hz and 8000 Hz for the two channels and can therefore be described by a Gaussian distribution. To evaluate precision the anal-

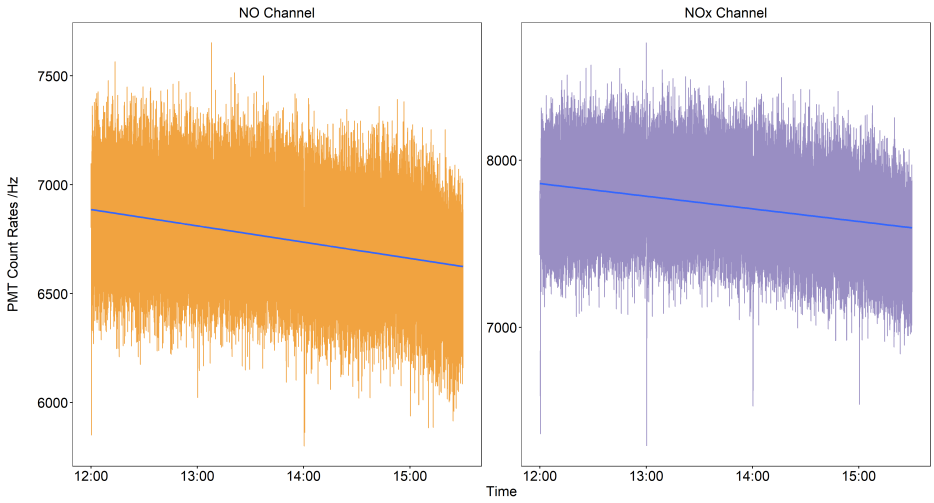

Figure 2.7: Data to show the response of the AQD NO_x analyser to 'zero' or NO_x-free air. Data is presented at a frequency of 5 Hz. A slight downward trend (shown by the blue line) was observed which was removed prior to calculating the precision of the NO and NO_2 measurements.

yser was set to sample zero air from a Pure Air Generator (ECO PHYSICS, PAG 003) for 3.5 hours. There was a slight downwards trend during the period sampling zero air shown in Fig. 2.7. This trend was removed from the data and detrended counts were converted to a mixing ratio by dividing by the channel sensitivities, giving the frequency distribution of zero measurements, shown in Fig. 2.8. The 1σ standard deviation was 37.7 pptv for the NO channel and 45.6 pptv for the NO_x channel for 5 Hz data.

The uncertainty due to the calibration cylinder is a 'Type B' uncertainty and taken to be 0.5% from the calibration certificate of the NO/N_2 cylinder (NPL). The uncertainty due to the calibration factors applied is calculated using statistics (type A) and was evaluated from calibration data from the two campaigns. Six calibrations, three from the winter campaign and three from the summer campaign, were selected to calculate the uncertainty in the calibration factors. The time of the calibrations selected were evenly spread over the campaigns. For each calibration the relative uncertainty in sensitivity, $u_{sens.}/sens.$, was calculated according to equation 2.5, where SE_{x3} is the standard error of the counts measured during stage 3 of the calibration (shown in figure

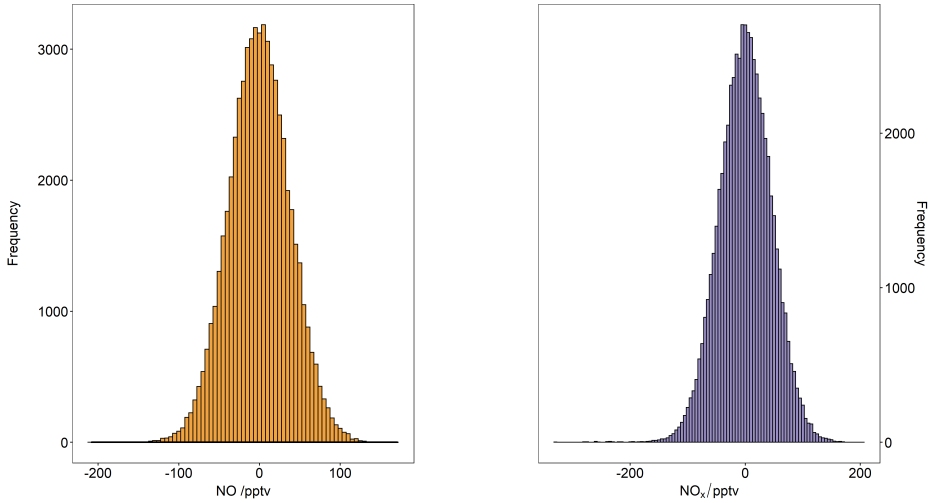

Figure 2.8: Frequency distributions of NO and NO_x mixing ratios for 3.5 hours of zero air measurements showing that the response of the detectors is normally distributed.

2.5) and $\bar{x}_3$ is the mean counts measured during stage 3 of the calibration. The mean 1σ u_{sens} was found to be 0.09% for the NO channel and 0.13% for the NO_x channel across the two campaigns.

$$\frac{u_{sens.}}{sens.} = \sqrt{\left(\frac{SE_{x_3}}{\bar{x}_3}\right)^2} \tag{2.5}$$

The relative uncertainty in the conversion efficiency calibration, $u_{C.E.}/C.E.$, was determined using equation 2.6, where $SE_{(x_n)}$ is standard error of the counts, $\bar{x_n}$ is the mean counts and n denotes the stage of the calibration as described in figure 2.5.

$$\frac{u_{C.E.}}{C.E.} = \sqrt{\left(\frac{SE_{(x_4)} - SE_{(x_2)}}{\bar{x}_4 - \bar{x}_2}\right)^2 + \left(\frac{SE_{(x_3)} - SE_{(x_1)}}{\bar{x}_3 - \bar{x}_1)}\right)^2} \tag{2.6}$$

The mean $1\sigma u_{C.E.}$ was found to be 2.2% for the calibrations evaluated over the two campaigns.

Uncertainty due to variability in instrument flows was taken to be the uncertainty of the mass flow controllers in the instrument. There were 3 mass flow controllers in the AQD NO_x analyser, one for each channel and one to control the flow of the calibration gas, all with a reported uncertainty of 1%. These individual uncertainties were combined through error propagation to give a 1σ uncertainty for the NO measurement

of 1.5% with a precision of 37.7 pptv and a 1σ uncertainty for the NO_2 measurement of 2.9% with a precision of 45.6 pptv. The uncertainty in the NO_2 measurement is larger than for the NO measurement as it is affected by uncertainties in both channels.

Uncertainty due to instrument drift is expected to be small because linear interpolation between the regular (hourly) background measurements was performed. As such it is not considered when combining uncertainties for the NO_x analyser. No NO or NO_2 artefacts were applied for NO_x measurements in Beijing and are not expected to be important at the mixing ratios measured for the city because the artefact to NO_x ratio is low. Artefacts are caused by "fake" NO signal and are not removed by subtraction of the signal observed during the pre-chamber zeroes [Drummond et al., 1985]. Artefacts have been determined for a near-identical instrument deployed in Cape Verde where the low NO_x mixing ratios measured make the NO_x artefact a significant source of uncertainty. Artefacts for NO and NO_2 were found to be < 10 pptv [Lee et al., 2009, Andersen et al., 2020] and so are not incorporated into the combined uncertainty for the NO_x analyser. By applying a coverage factor, k, of 2 the expanded uncertainty becomes 3.0% with a precision of 75.4 pptv and 5.8% with a precision of 91.2 pptv for NO and NO_2 respectively. Table 2.1 summarises the sources and value of individual uncertainties. To put the uncertainty values into context, uncertainties are given in ppbv for a range of NO_x mixing ratios in Table 2.2.

Estimating uncertainty for the AL5002 CO analyser

The precision of the CO instrument at 5 Hz was evaluated using the zero count statistics during the background calibration of the instrument. As for the calibration uncertainties associated with the AQD NO_x analyser, six calibrations spread over the two campaigns (three from the winter campaign and three from the summer campaign) were selected for analysis. For each background calibration a standard deviation was calculated and converted to a mixing ratio by applying the sensitivity calculated for that calibration. The precision of the instruments during the two campaigns was taken as the pooled standard deviation (equation 2.7, where s is standard deviation and n is the number of observations made per calibration), of the six background calibrations. The resulting 1σ precision of the AL5002 CO Analyser was determined to be 5.2 ppbv

Table 2.1: Summary of Uncertainties associated with the AQD NO_x Analyser

Source of Uncertainty	**2σ Uncertainty**
Cylinder	1.10%
MFC (NO Channel)	2%
MFC (NO_x Channel)	2%
MFC (Calibration Flow)	2%
NO_2 Conversion Efficiency	4.4%
Sensitivity of NO Channel	0.18%
Sensitivity of NO_x Channel	0.26%
Precision of NO measurement*	7.54%
Precision of NO_2 measurement*	9.12%

**Precision reported as a percentage of 100 ppbv NO or NO_x at a 5 Hz measurement frequency.*

Table 2.2: Combined uncertainties for the AQD NO_x analyser for a range of mixing ratios measured at 5 Hz.

NO /ppbv	**2σ NO Uncertainty / ppbv**
0.1	0.08
1	0.11
10	0.38
100	3.08
NO_2 /ppbv	**2σ NO_2 Uncertainty / ppbv**
0.1	0.10
1	0.15
10	0.67
100	5.89

Table 2.3: Combined uncertainties for the AL5002 CO analyser for a range of mixing ratios measured at 5 Hz.

CO /ppbv	2σ CO Uncertainty / ppbv
100	14.8
500	32.4
1000	54.4
2000	98.4
5000	230.4

for 5 Hz data.

$$s_{pooled} = \sqrt{\frac{(n_1-1)s_1^2 + (n_2-1)s_2^2 + ...}{n_1 + n_2 + ...}} \tag{2.7}$$

The uncertainty of the AL5002 CO Analyser was determined statistically from the pooled standard deviation of the six calibrations where the instrument sampled the calibration standard. Unlike the standard deviation associated with the zero calibration, where it was assumed that the variability in signal was due solely to detector counting, variability in the calibration signal represents additional instrument uncertainties. The uncertainty associated with the cylinder mixing ratio is assumed not to contribute to variability in calibration signal, as whilst the absolute mixing ratio has an associated uncertainty, the mixing ratio should be constant. Absolute standard deviations were converted to relative standard deviations (or the coefficient of variance) by dividing by the mean mixing ratio measured during the calibration. The pooled standard deviation representing uncertainty of the AL5002 CO analyser was 2.0% (1σ). The total uncertainty of the CO measurements is due to the instrument precision, uncertainty of the instrument and the uncertainty associated with the CO calibration cylinder which was reported as 1%. Bell [2001] suggests that uncertainties reported on calibration certificates can be assumed to be normally distributed and it is assumed that 1% is a 1σ uncertainty. The combined 2σ uncertainty associated with the AL5002 CO analyser was estimated to be 4.4% with a precision of 10.4 ppbv for 5 Hz data. Table 2.3 summarises uncertainties in ppbv for a range of mixing ratios.

Table 2.4: 2σ Uncertainties for the AQI instruments.

Instrument	**2σ Uncertainty**	**2σ Precision /ppb***
O_3, TEi49i	4.04%	0.28
NO, TEi42i-TL	4.58%	0.03
NO_y, TEi42C	4.73%	0.05
SO_2, TEi43i	3.12%	0.03
NO_2, CAPS, T500U	5.72%	0.04
CO Sensors	9.14%	2.14

**Precision given for 15 minute averaging time.*

Estimating uncertainty for the gas phase air quality instruments

Uncertainty was estimated for each of the air quality instruments described in section 2.3. As for the AQD NO_x and the AL5002 CO analysers, precision was determined for the air quality instruments using data from the zero measurements. For each zero calibration performed in the field the standard deviation of the measurements was calculated. The pooled standard deviation was then calculated according to equation 2.7. The standard deviation calculated from the zero calibrations corresponds to the 1σ precision of the instruments at the averaging time of the data (in this case 1 minute). In the analysis presented in Chapter 3, however, the data was 15 minute averaged which improves the signal-to-noise ratio, and hence the precision, by a factor of $1/\sqrt{n}$ where n is the number of samples averaged. The uncertainty of the instruments was determined as for the AL5002 CO analyser from the standard deviations of the span calibrations. Standard deviations were converted from mixing ratios to percentages by dividing by the mean mixing ratio recorded during each calibration and multiplying by 100 and combined using equation 2.7.

Uncertainty in the calibration cylinders are another source of uncertainty for the measurements described in section 2.3. For the SO_2 and CO measurements these were taken to be 1%, as quoted on the calibration cylinder certificate. For NO, NO_y and NO_2 the calibration cylinders used were first measured on the AQD NO_x so that these

cylinders are traceable to the NPL NO standard. This is especially important as NO_2 standards are not typically stable and degrade over relatively short periods of time. The uncertainty of the NO, NO_y and NO_2 calibration standard is therefore taken to be the uncertainty of the NO and NO_2 measurements of the AQD NO_x analyser. A mixing ratio of 100.4 ppbv was measured by the AQD NO_x analyser for the NO calibration standard and 72.9 ppbv for the NO_2 calibration standard. The uncertainty due to precision of the NO and NO_2 measurements of the AQD NO_x analyser is very small when averaged over minutes as was done in order to determine the mixing ratio of NO and NO_2 in the calibration standards. These are therefore not included in the uncertainty calculation for the calibration cylinders with the 1σ uncertainty taken to be 1.5% for the NO calibration cylinder and 2.9% for the NO_2 cylinder.

An additional source of uncertainty affecting measurements of NO, NO_2, NO_y and O_3 is the contribution from the reaction of O_3 and NO in the sample inlet line. NO and O_3 react to form NO_2 and so the NO_2 mixing ratios are overestimated and NO mixing ratios underestimated. The NO mixing ratio prior to reaction with O_3 in the sample manifold can be calculated according to:

$$[NO]_0 = [NO]_t \times e^{k_{O_3} t} \tag{2.8}$$

Where $[NO]_0$ is the mixing ratio at t_0, the time before the sample gas enters the manifold line, $[NO]_t$ is the measured NO mixing ratio, k_{O_3} is the rate of the reaction between NO and O_3 multiplied by the measured O_3 mixing ratio and t is the residence time in the sample inlet. k was taken to be 1.9×10^{-14} cm^3 $molecule^{-1}$ s^{-1} at 298 K [Atkinson et al., 2004]. The residence time in the sample inlet was calculated to be 1.02 s, assuming a flow rate of 30 SLPM and an inlet length of 8 m for $\frac{1}{2}$" O.D. (9 mm I.D.) tubing. This is an overestimation of the true residence time as the 8 m length is measured from the sample inlet outside the container to the manifold pump and instrumentation sampled part way off the manifold line. NO_y is measured as NO, and once converted the NO can react with O_3 in the sample line so $[NO_y]_0$ was calculated as for $[NO]_0$. Given that the rate of loss of NO to O_3 is equal to the rate of formation of NO_2, the NO_2 mixing ratio at t_0, $[NO_2]_0$ can be calculated according to:

$$[NO_2]_0 = [NO_2]_t - ([NO]_0 - [NO]_t) \tag{2.9}$$

The O_3 mixing ratio at t_0, $[O_3]_0$ can be calculated in the same way according to:

$$[O_3]_0 = [O_3]_t \times e^{k_{NO}t} \tag{2.10}$$

For each 15 minute averaging period the difference between measured mixing ratio (at time t) and mixing ratio at t_0 were calculated as a percentage of the measured value. The uncertainty due to the reaction of O_3 and NO was taken to be the standard deviation of the differences. This led to a 1σ uncertainty of 1.70%, 0.18%, 1.71% and 2.02% for the NO, NO_2, NO_y and O_3 measurements respectively as a result of O_3 and NO reactions in the sample line. The instrument uncertainties and calibration standard uncertainties are summed in quadrature to give combined uncertainties, which are presented in Table 2.4.

Gas Phase Air Pollution in Beijing

3

3.1 Introduction

CHINA'S economy has rapidly grown as a result of economic reforms which began in 1978. Between 1978–2018 the mean growth in gross domestic product (GDP) has been 9.5% year^{-1} [World Bank, 2020]. This rapid economic growth has led to an explosion in population which has been predominantly concentrated in urban areas including megacities. Megacities are defined by the United Nations (UN) as a "metropolitan area with a total population of more than 10 million people" [United Nations' Department Of Economic and Social Affairs: Population Division, 2016]. In 1978, before economic reforms, just 17.9% of China's total population lived in urban areas. This had increased to 59.2% in 2018 according to the UN [United Nations, Department of Economic and Social Affairs, Population Division, 2019]. Beijing itself became a megacity in 2000 when population reached 10.3 million people and at the start of 2016 it was estimated that the population was approaching 22 million [Beijing Municipal Bureau of Statistics, 2016].

An inevitable consequence of economic development and population growth is a degradation of air quality. Increases in energy consumption, motor vehicle use, construction and industrial waste have contributed to China's air pollution. Air pollution is one of the leading contributors to the global burden of disease causing an estimated 4.2 million deaths globally in 2015 [Cohen et al., 2017]. Around 1.1 million premature deaths in China were attributable to air pollution in 2015 with 21.8 million disability-adjusted life-years (DALYs) lost. As well as severe impacts on physical health, poor

air quality has profound effects on mental health and well being and detrimental economic impacts. Studies have indicated a link between poor air quality and increased instances of dementia [Carey et al., 2018]. Annual economic losses due to air pollution in China were estimated to account for approximately 1.2% of the nation's GDP based on disease cost.

Tackling poor air quality in China has been challenging. Despite the establishment of a legal framework to control pollution in the late 20th century [Feng and Liao, 2016], pollution control strategies were not widely enforced until the start of the 21st century. Zhang et al. [2012] outlined that controlling air pollution had been a secondary priority to economic growth. China's economic success had been driven by energy intensive construction of highways, railways and cities and by expansion of heavy industries like pig-iron and cement production. Between 2005–2010 vehicle production increased by 220% and coal usage rose by 44% [Zhang et al., 2012]. Environmental protection was further hindered by a decentralised system of environmental enforcement with little cooperation between local governments. To address this, in 2013 the Chinese government introduced the "Air Pollution Prevention and Control Action Plan" to combat severe air pollution and improve public health. Some key features of the legislation included improving industrial emissions standards, upgrading industrial boilers, promoting use of natural gas and electricity instead of coal within the residential sector, strengthening vehicle emissions standards and removing older vehicles from the Chinese vehicle fleet. Reductions of $PM_{2.5}$ by 25% were mandated in Beijing and the surrounding region by 2017 [Jin et al., 2016].

The impacts of legislation are reflected in the ambient concentrations of air pollutants and have had some positive outcomes. In general, up until 2005 the effectiveness of pollution control measures was limited [Jin et al., 2016] and concentrations of air pollutants increased over China during the early 2000s, though longer term measurements of pollutants are sparse [Xue et al., 2019]. Gas-phase pollutants like NO_2, SO_2 and O_3 are identified by the World Health Organisation (WHO) as harmful to human health which has set exposure thresholds for these pollutants. As such these compounds have been relatively well monitored in many countries for some time. WHO also offers guidelines on particulate matter (PM) limits and so important precursor species are also widely monitored. This allows insight into long-term trends of air

quality over China.

In terms of NO_x, China's emissions increased by 70% between 1995 and 2004 [Zhang et al., 2007]. Satellite observations of NO_2 column densities provide useful data about trends in NO_x concentrations. Liu et al. [2016] report that between 2005 and 2011 NO_2 emissions increased by 53% for the whole of China, attributed for the most part to increasing fuel consumption with coal the dominant fuel type. An estimated three quarters of all electricity in China was generated by coal in 2016 [International Energy Agency, 2016]. After 2012 however, a combination of the installation of power plant de-nitration devices and vehicle emissions controls has led to a 32% decrease in NO_2 emissions [Liu et al., 2016, Krotkov et al., 2016, Miyazaki et al., 2017]. Whilst nationwide, the upward trend of NO_x emissions in China is slowing or being reversed, this is not the picture for all regions of China due to discrepancies in how new emission legislation is implemented [Liu et al., 2016]. It tends to be more economically developed regions, including the Pearl River Delta, Shanghai and Beijing, where a decreasing trend in NO_2 levels has been observed [Gu et al., 2013, Jin and Holloway, 2015, Duncan et al., 2016]. From monitoring stations across China no downward trend was observed in NO_2 concentrations between 2015–2017 and the percentage of the stations that comply with the WHO's annual mean guideline of 40 μg m^{-3} had declined, from 71% in 2015 to 66% in 2017 [Silver et al., 2018].

SO_2 concentrations peaked over the North China Plain in 2007 when concentrations were the highest in the world but dropped to less than half of its 2005 levels in 2015 [Krotkov et al., 2016]. This occurred despite increases in coal combustion across China as a result of legislation mandating the use of desulfurisation technologies. SO_2 continued to decrease at a rate of 10.3% $year^{-1}$ across China between 2015–2017 [Silver et al., 2018]. CO concentrations have also declined over China between 2005–2016. Using observations of tropospheric CO columns, Zheng et al. [2018] showed that there was a -1% to -2% $year^{-1}$ trend in CO over eastern China. The study concluded that improvements in combustion efficiency and strengthened air pollution control were responsible for 92% of China's emissions reductions over this period.

In the Pearl River Delta region of China Wang et al. [2016] reported $PM_{2.5}$ concentrations rose between 2000–2005 and then decreased between 2005–2010. Trends in $PM_{2.5}$ have been assessed using satellite retrievals of aerosol optical depth. Ma et al.

[2016] investigated trends in $PM_{2.5}$ between 2004–2013 and found that concentrations increased over China between 2004–2007 and decreased thereafter. Between 2015–2017 Silver et al. [2018] reported that $PM_{2.5}$ had decreased by 7.2% $year^{-1}$ across China using data from air quality monitoring stations.

The situation for secondary pollutants like secondary organic aerosol and O_3 is more complex. These pollutants cannot be reduced directly by emissions controls but instead have non-linear dependencies on emissions of precursor species. Satellite observations show O_3 concentrations have been increasing across China at a rate of 7% per year between 2005–2010 [Verstraeten et al., 2015]. It is thought that reductions in ambient $PM_{2.5}$ could be at least partly responsible for increases in O_3 concentrations [Li et al., 2019a], highlighting the challenges facing legislators when designing air quality controls.

3.1.1 Air quality in Beijing

Megacities and surrounding regions bear the brunt of poor air quality. Studies have shown that the health impacts of poor air quality are greater in denser urban areas like megacities with higher pollutant exposure levels for residents [Zhou et al., 2018a, Carozzi and Roth, 2019]. Beijing itself has frequently been in the headlines as a result of the dramatic pollution events that occur there.

Beijing experiences severe haze episodes, usually during the winter months. The frequency of haze events has increased over past decades with heavy pollution periods occurring in January 2013, December 2015 and December 2016 being particularly notable. In January 2013 the maximum daily $PM_{2.5}$ in Beijing reached 500 μg m^{-3} [Cai et al., 2017]. These haze episodes are heavily influenced by local meteorology; the concentration of aerosol increases rapidly when the back trajectories of the air mass swing from the north west to the south in a process termed "sawtooth cycles" [Jia et al., 2008]. As aerosol concentration increases the airmass tends to become more humid and particle size decreases. Haze formation during these "sawtooth cycles" has also been reported by Li et al. [2017a] during December 2015. Analysis of back trajectories indicated that each stage of haze formation was driven by sudden changes in wind speed, indicating the significance of meteorology in the evolution of haze episodes. Clean air brought in from the north west, associated with higher wind speeds, led to

the end of these haze episodes and a sharp reduction in air pollutant concentrations. This distinctive meteorological phenomenon occurs in Beijing as a result of the East Asian Winter Monsoon, itself driven by temperature differences between the Pacific Ocean and Asian continent [Chen et al., 1992]. Moreover, Beijing's surrounding landscape influences its air quality; the mountain ranges which surround Beijing enable the efficient transportation of non-local pollutants into the city [Xu et al., 2017]. Cai et al. [2017] predicts that increasing temperatures due to climate change could increase the frequency of haze events by altering circulation patterns in the region.

Beijing has adopted a very intensive set of air quality control measures called the Clean Air Action Plan since 2013. Control measures taken can be classified into seven categories; coal-fired boiler control, clean fuels in the residential sector, optimization of the industrial structure, improvements in end-of-pipe control, vehicle emission control, fugitive dust control and integrated treatment of volatile organic compounds (VOCs). The impacts of this plan have been positive with emissions reductions for all major air pollutants. Cheng et al. [2019] estimates that Beijing's anthropogenic emissions decreased by 83.6% for SO_2, 42.9% for NO_x , 42.4% for VOCs and 54.7% for $PM_{2.5}$ as a result of the plan. Air quality monitoring stations across Beijing measure CO, NO_2, SO_2 and O_3 and ambient concentrations measured reflect the impact of legislation. Figure 3.1 shows the location of the air quality monitoring stations across Beijing. For all sites in the air quality network there was a mean annual decrease of 5.2% between 2013–2017 for CO. SO_2 showed a larger decrease of 16.1% year^{-1} and NO_2 showed the smallest trend of the three directly emitted pollutants with a mean decrease of 1.5% year^{-1}.

Whilst the decreases in concentrations of directly emitted pollutants is a positive story, O_3 concentrations are increasing over Beijing, as for China as a whole. O_3 concentrations over Beijing increased by approximately 2% year^{-1} between 1995–2005 [Ding et al., 2008]. Data from air quality monitoring stations across Beijing show an increasing trend in O_3 concentrations at a rate of about 5% year^{-1} between 2013 and 2017. Figure 3.2 shows the de-seasonalised trend in measured O_3. All stations within the sixth ring road, apart from Dongsi, showed an increasing trend in mean O_3 concentration ranging from 4.38–19.32% year^{-1}, indicating worsening photochemical pollution within the city. Stations outside of the sixth ring road, further away from

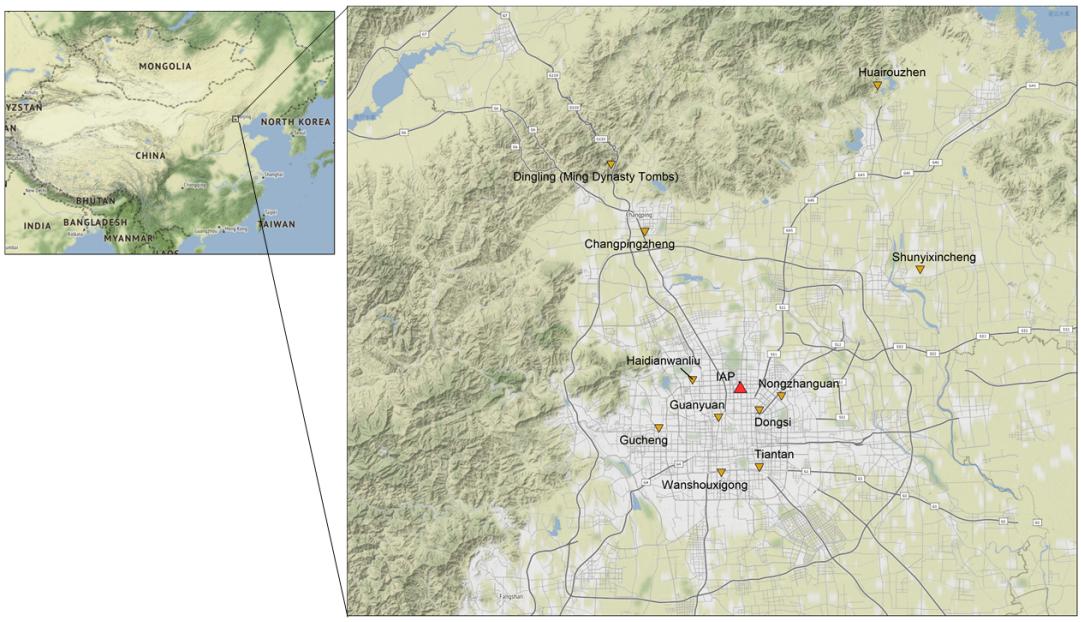

Figure 3.1: Map to show locations of air quality monitoring stations around Beijing. The measurement site is shown by the red triangle labelled 'IAP'.

O_3 precursor emission sources, generally showed a negative trend apart from Dingling which experienced a mean increase of 2.84% year^{-1}.

3.1.2 The "Air Pollution and Human Health-Beijing" Campaign

The Air Pollution and Human Health-Beijing (APHH) in a Chinese megacity program was funded to address air quality problems experienced in Beijing by improving understanding of pollution sources, atmospheric processes and health impacts. An overview of the campaign can be found in Shi et al. [2019]. The APHH project has several research themes including AIRPRO (the integrated study of AIR Pollution PROcesses in Beijing) which aimed to inform understanding of the processes by which pollutants are transformed or removed through transport, chemical reactions and photolysis in Beijing. Measurements of key gas-phase pollutants were made to investigate local in-situ chemical processing of air pollution during two intensive field campaigns in central Beijing as part of the APHH project, the first in November–December 2016 and the second during May–June 2017, to contrast winter and summertime processes.

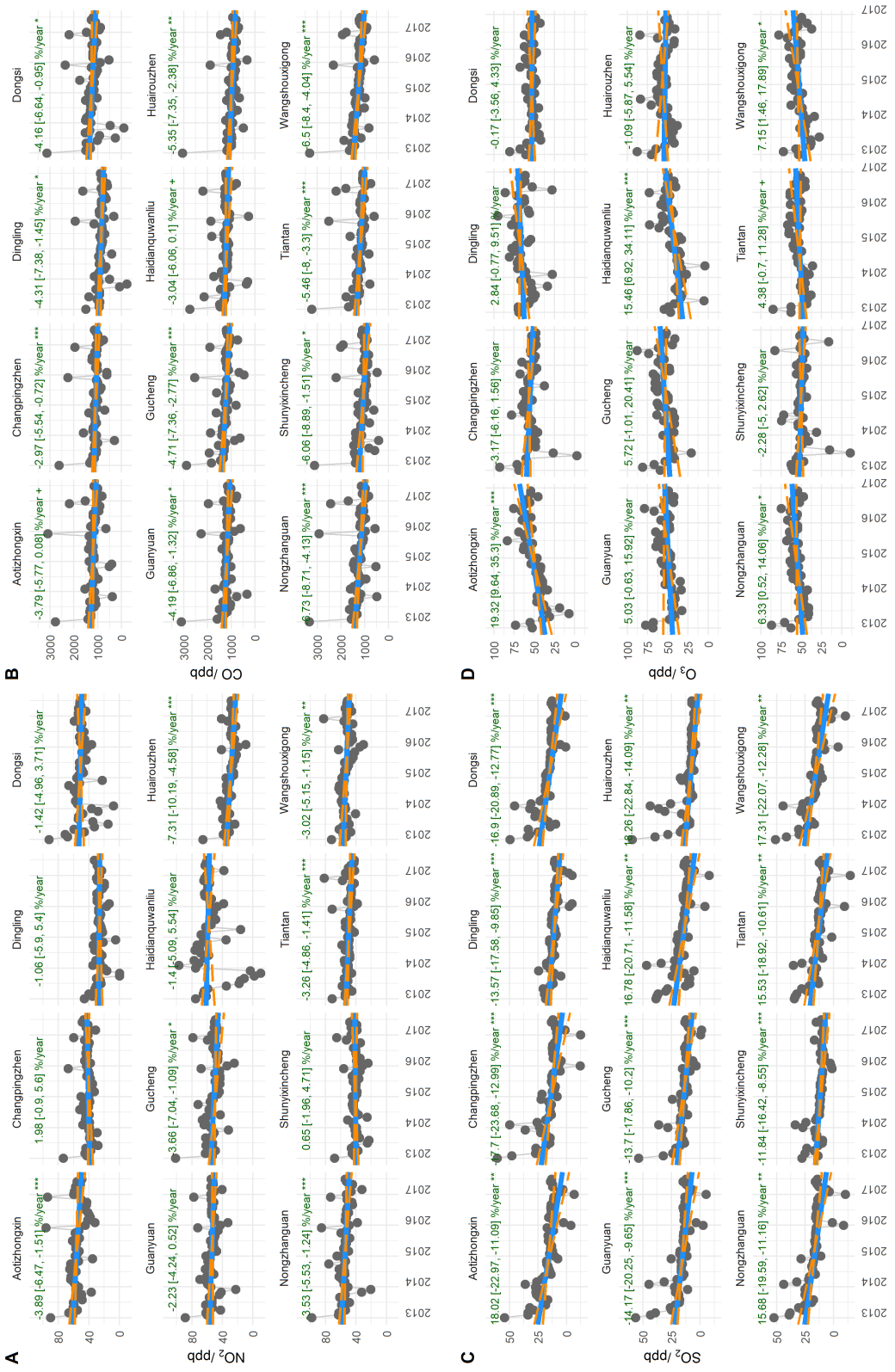

Figure 3.2: Trends in NO_2 (panel A), CO (panel B), SO_2 (panel C) and O_3 mixing ratios (panel D) measured by the air quality network in Beijing. Trends have been calculated using the Theil-Sen technique in Openair. Grey points show measurement data with the blue solid line showing the fit and orange dashed lines the error in the fit.

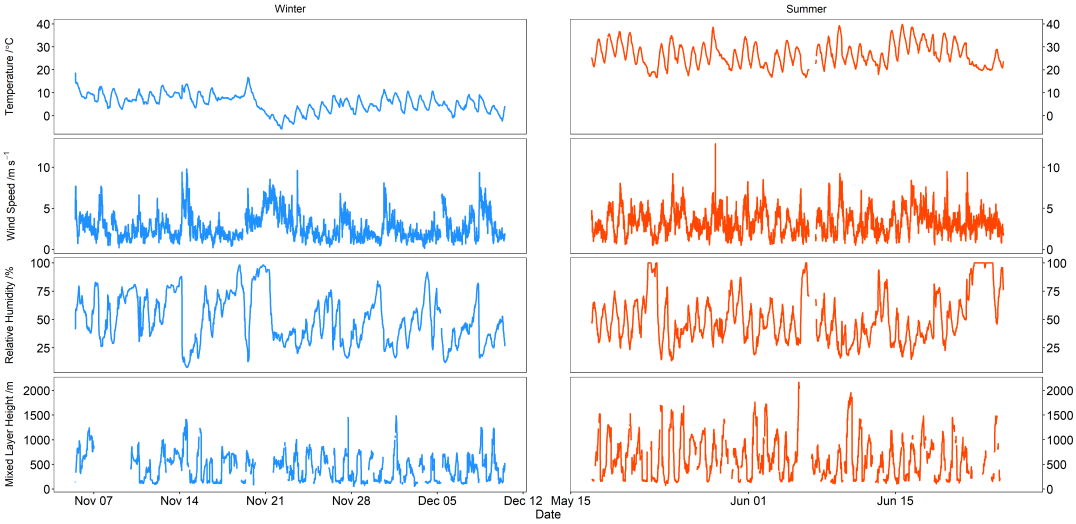

Figure 3.3: Temperature (top panels), wind speed (second panels), relative humidity (third panels) and mixed layer height (lower panels) measurements from the winter and summer campaigns. Data is 15 minute averaged.

3.1.3 Meteorological conditions during the APHH campaigns

Meteorological data is presented in Figs. 3.3–3.5 for the two campaigns. Temperature and relative humidity data was obtained from a weather station located on top of a shipping container housing air quality instrumentation (discussed in Chapter 2). Wind data was obtained from a sonic anemometer located on a platform at 102 m up a meteorological tower at the measurement site. Mixed layer height was measured throughout both campaigns using a celiometer (Vaisala CL31) and determined using the CABAM algorithm [Kotthaus and Grimmond, 2018].

As expected temperatures were higher in summer than winter. Mean daily maximum temperature for summer was 31.1 °C (occurring around 15:00) compared to a mean daily maximum temperature of 8.6 °C (occurring at 14:00) during the winter campaign. Solar intensity is greater during the summer campaign than for the winter campaign due to the higher solar elevation angle (72.9° at solar noon for the midpoint in the summer campaign compared to 29.7° for the midpoint in the winter campaign). Relative humidity, was on average, very similar for the two campaigns with mean relative humidity being 50.3% across the whole winter campaign and 50.9% across the

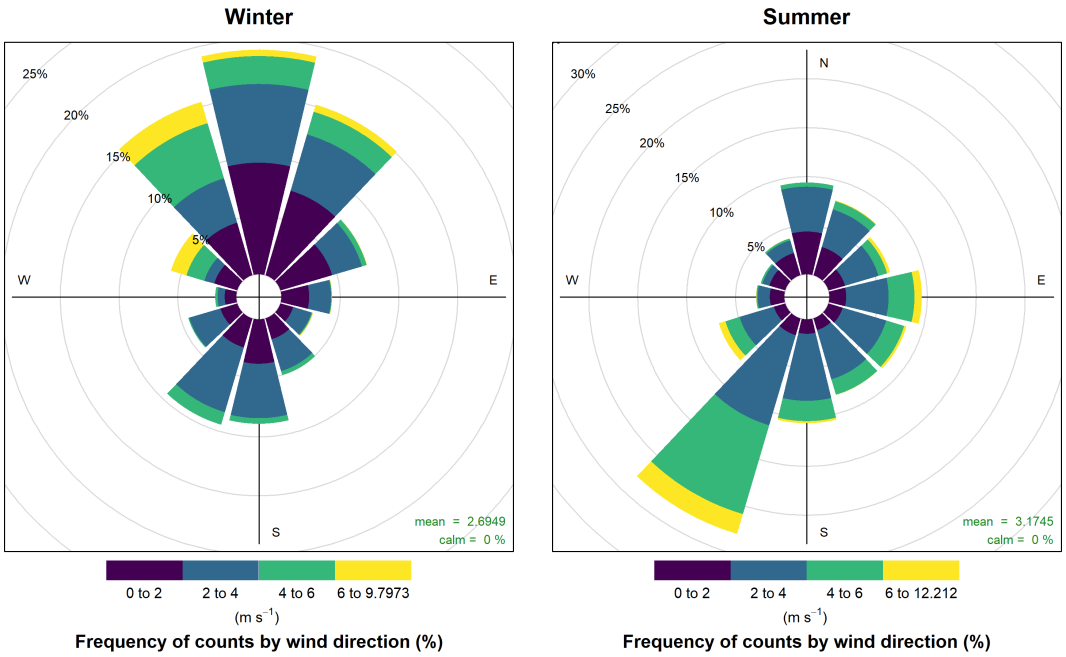

Figure 3.4: Wind roses averaged over the winter campaign (left hand panel) and the summer campaign (right hand panel). Wind direction is averaged into 30° segments and wind speed shown by the colours on the wedges. Note that the scales are different between winter and summer.

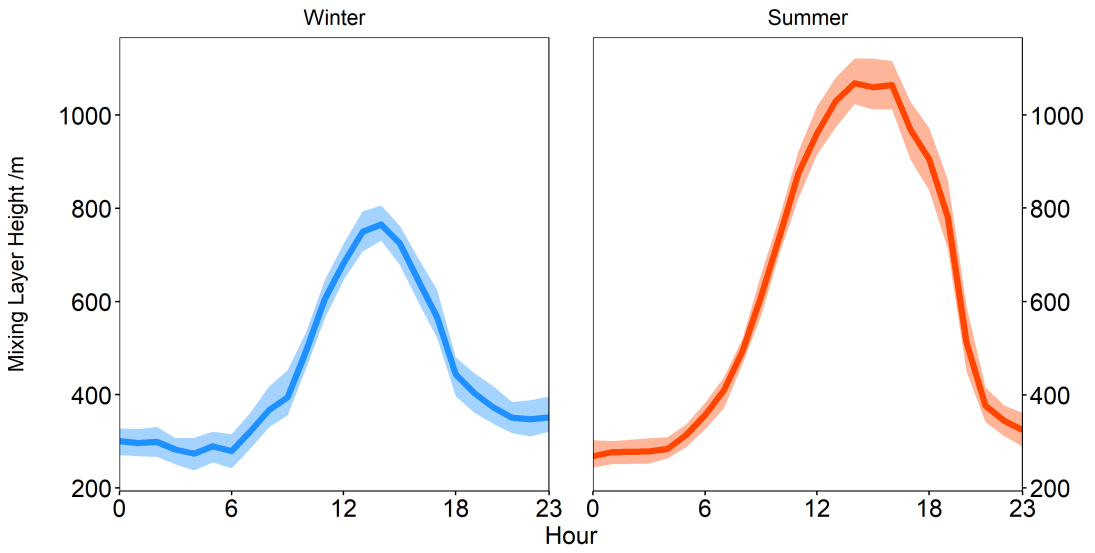

Figure 3.5: Diurnal variation in MLH for the winter and summer campaigns. The solid line represent the mean diurnal variation with shaded areas corresponding to the 95% confidence intervals about the mean.

summer campaign. Relative humidity in winter was more variable than for summer with very dry periods (e.g. 14/11/2016). These fluctuations in relative humidity during the winter correspond to sudden changes in wind speed indicating the influence of different air masses. Wind speeds during the winter campaign were characterised by stagnant periods with low wind speeds followed by periods of mixing by stronger winds. During the summer, conditions were more consistent with a diurnal cycle in relative humidity clear for summer. Dominant wind directions varied between the winter and summer campaign (shown in Fig. 3.4) which show that during the winter northerly winds dominated. These tended to be associated with higher wind speeds compared to winds from other directions. During the summer campaign southerly wind directions were more frequently observed, with south westerly being dominant. A wider range of wind speeds were observed during the summer compared to the winter.

Mixed layer height (MLH) can drive pollutant concentrations in the troposphere by determining the effective volume pollution is “trapped” within. Diurnal variation in MLH for the winter and summer campaigns is presented in Fig. 3.5. During the winter campaign the MLH was stable in the early hours of the morning (00:00–06:00

with a mean height of 290 m) until it started to increase after 06:00 as temperatures increased. Daily mean maximum height was 765 m at 14:00. The MLH contracted again as the temperature cooled. MLH in summer also expanded and contracted in line with temperature. Overnight the MLH in summer was the same as for the winter (290 m between 00:00–05:00) but started to expand after 05:00 and reached a mean daily maximum height of 1070 m at 14:00, approximately 300 m higher than in the winter.

3.2 Overview of air pollutant measurements during the winter and summer campaigns

3.2.1 Seasonal differences in air pollutants

Table 3.1: Table summarising key statistics for gaseous pollutants measured in Beijing.

	Winter					Summer				
	Mean	**Median**	**S.D.**	**Min**	**Max**	**Mean**	**Median**	**S.D.**	**Min**	**Max**
NO /ppb	40.5	22.8	45.8	0.066	220	3.86	0.678	9.10	0.0166	87.1
NO_2 /ppb	36.4	36.0	17.1	5.39	88.0	20.2	17.6	11.3	4.22	64.9
O_3 /ppb	8.79	4.18	8.98	0.05	33.3	54.7	49.7	36.2	0.222	176
CO /ppb	1408	1226	856	90.0	4379	534	492	258	41.6	2103
SO_2 /ppb	5.37	4.57	4.09	0.04	19.1	2.43	1.44	2.58	4×10^{-4}	14.3
T /°C	5.68	6.05	3.90	-5.76	18.17	36.7	26.3	5.06	16.6	39.6
RH /%	50.3	47.3	21.5	7.76	98.0	50.9	46.3	21.5	14.1	100
WS /m s^{-1}	2.70	2.25	1.49	0.391	8.72	3.17	3.04	1.41	0.667	7.86

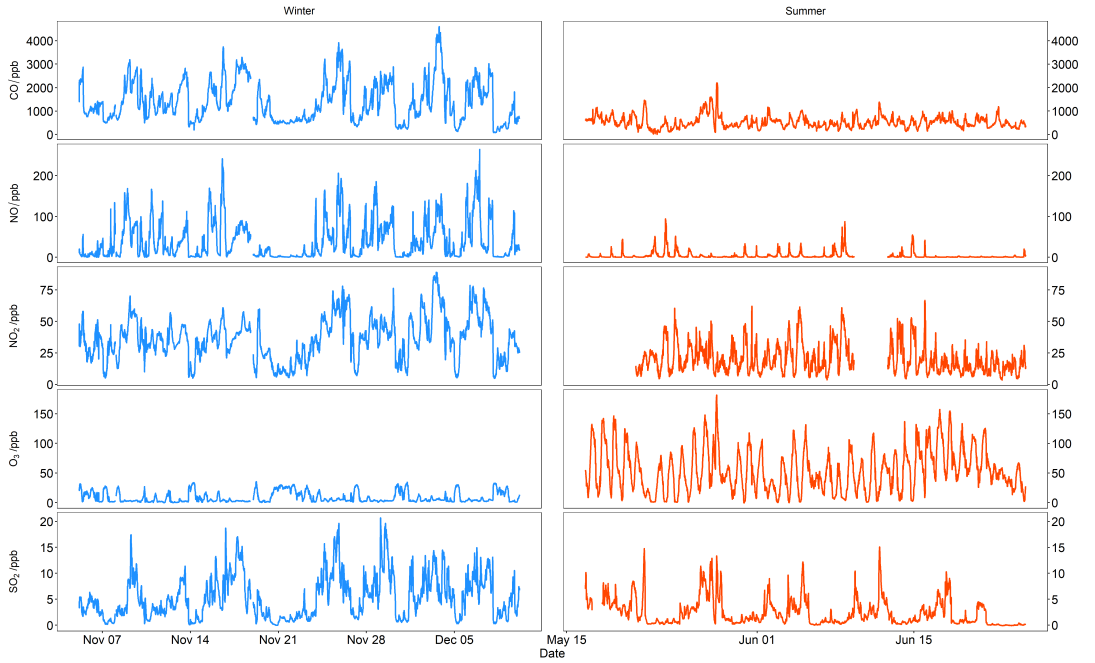

Figure 3.6: Time series data for CO, NO_x O_3 and SO_2 for the winter (LHS) and summer (RHS) campaigns. Data is 15 minute averaged.

Figure 3.6 presents time series data for CO, NO, NO_2, O_3 and SO_2. Generally, higher pollutant mixing ratios (apart from O_3) were measured during the winter campaign, though there was a several-day period (21/11/2016–24/11/2016) during which mixing ratios well below the campaign average were measured. During the summertime a diurnal pattern was clear for O_3 and NO_2, though there is greater variability in CO and SO_2 mixing ratios. Taking the mean mixing ratios (Table 3.1) the greatest seasonal difference was for NO which was 10.5 times higher in winter than summer. The seasonal dependence of NO_2, CO and SO_2 is less, with mean wintertime mixing ratios measured between 1.8–2.6 times higher than the mean summertime mixing ratios.

Diurnal variation for CO, NO, NO_2, O_3 and SO_2 mixing ratios alongside MLH for the two campaigns is shown in Fig. 3.7. Measured mixing ratios are a result of a balance between emissions, vertical mixing, transport from other regions and chemistry. Wintertime mixing ratios are therefore generally higher than those experienced in summertime as anthropogenic emissions are higher due to increased energy demands, combustion inefficiencies due to colder temperatures, slower chemical destruction due

to weaker solar radiation and weaker vertical mixing. NO_x, CO and SO_2 are emitted from industrial processes, power plants and domestic heating whilst vehicle emissions are also sources of NO_x and CO [Monks et al., 2009]. Diurnal trends in these primary pollutants reveal the relationship between factors controlling mixing ratios. As temperature increases through the day the MLH is lifted to its maximum height at 14:00 due to convection and most primary pollutant mixing ratios decreased to a minimum at this time. The MLH tended to be stable and low overnight which had the effect of concentrating pollutants.

CO mixing ratios in winter were high during the nighttime (here defined as between 20:00–06:00), with a mean value of 1554 ppb $\pm$ 949 ppb compared to 1306 ppb $\pm$ 784 ppb during the daytime (06:00–19:00). During the daytime, CO peaked at 06:00 and between 18:00–19:00 in the winter. This was most likely due to emissions, probably from vehicles as these times correspond to peak traffic density across Beijing [Jing et al., 2016]. For summer, CO mixing ratios peaked between 06:00–07:00, due to the rush hour, with a small enhancement at 10:00, indicating an increase in emissions at this time. CO mixing ratios then decreased to a minima at 14:00 before increasing steadily to 21:00 as the MLH contracted.

Diurnal variation in NO mixing ratios during the winter was similar to that for CO. NO mixing ratios were also higher overnight than during the day (50.0 ppbv $\pm$ 52.7 ppbv at night and 34.0 ppbv $\pm$ 40.7 ppbv in the day). A peak in NO mixing ratio occurred at 07:00, likely due to emissions from rush-hour traffic, and decreased to its minima at 14:00 as for CO. There was a small enhancement in NO at 19:00. During the summer, NO mixing ratios peak between 04:00–07:00 and then steadily decreased throughout the day reaching mixing ratios of less than 500 pptv after 17:00. Mean mixing ratios were 3.2 ppbv $\pm$ 6.2 ppbv during the daytime and 4.8 ppbv $\pm$ 12.7 ppbv during the nighttime. During summer, daytime NO mixing ratios were low which was probably due to the reaction of NO with high levels of O_3, though this photochemistry will be explored in detail later in the chapter (section 3.3).

The mean nighttime NO_2 mixing ratio was 38.6 ppbv $\pm$ 16.1 ppbv compared to 34.8 ppbv $\pm$ 17.9 ppbv during the daytime. NO_2 peaked at 07:00 and 19:00 during the day, the same as for NO though the morning peak in NO_2 mixing ratio is smaller than the evening peak, which was the opposite to NO. For summer, NO_2 mixing ratios

show a similar diurnal trend to that for CO; peaked between 06:00–07:00, decreased to its minima at 14:00 after which NO_2 steadily increased till 20:00.

SO_2 mixing ratios during winter were higher at night similar to the other pollutants already discussed, with a mean nighttime value of 5.6 ppbv $\pm$ 4.5 ppbv compared to 5.2 ppbv $\pm$ 3.9 ppbv during the daytime. SO_2 mixing ratios peaked in the morning at 09:00, later than observed for CO or NO_x. This could suggest that from around 06:00 there was a significant increase in SO_2 emissions as mixing ratios increased despite the increase in effective volume they were being emitted into. Alternatively, the increase in SO_2 mixing ratio observed could be due to mixing of SO_2 which has been transported above the boundary layer, into the surface layer as turbulence increases. SO_2 mixing ratios reached a minimum at 18:00, later than for NO_x and CO, with a small peak at 19:00. For summer, daytime mixing ratios were slightly higher than at night; 2.5 ppbv $\pm$ 2.7 ppbv compared to 2.3 ppbv $\pm$ 2.4 ppbv at night. The diurnal profile is most similar to that of NO in the summer. SO_2 mixing ratios increased in the early hours of the morning, presumably due to a build up of pollution overnight and peaked between 06:00–07:00. After this, MLH effects dominated and SO_2 decreased until reaching a minimum at 20:00. SO_2 mixing ratios did not increase as the boundary layer contracts, possibly as there were no further emissions or the most significant SO_2 emissions occurred in the morning.

O_3 is a secondary pollutant formed through photochemical reactions of precursor species. As expected, the diurnal trend in O_3 was closely linked to solar radiation, peaking at the same time where the MLH was at its highest for both campaigns. This is due to faster photochemistry with increased solar radiation combined with reduced amounts of pollutant species (i.e. NO) resulting in less titration of O_3. O_3 mixing ratios were much higher in the summer than in the winter due to higher solar radiation; mean daytime O_3 mixing ratios were 10.6 ppb $\pm$ 9.9 ppb in the winter and 66.4 ppb $\pm$ 37.9 ppb in the summer. During the summer campaign half of the campaign days breached the WHO's 8-hourly health limit for O_3.

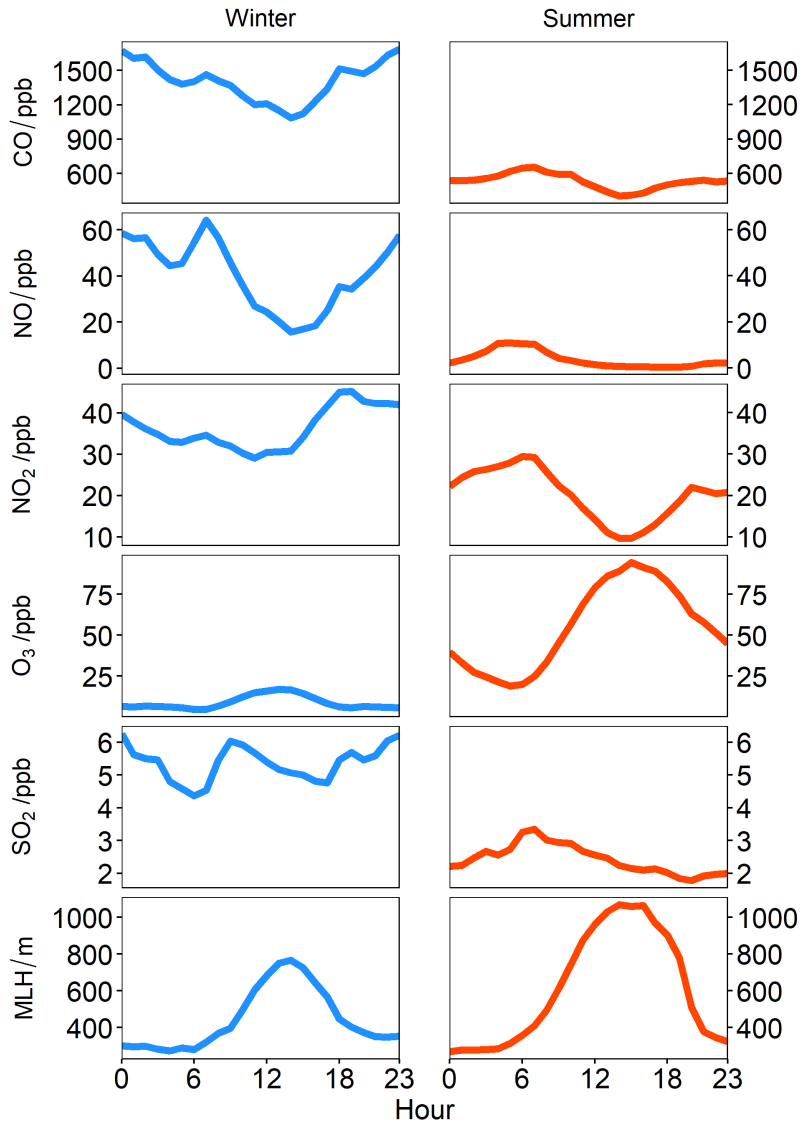

Figure 3.7: Diurnal variation for mean gas-phase pollutant mixing ratios and MLH for the winter and the summer campaigns.

3.2.2 Correlations between directly emitted pollutants

Correlations of NO_x, CO and SO_2 were investigated to see if these differed between the two campaigns. Correlations were stronger between all primary pollutants during the winter campaign compared to the summer campaign. NO_x and CO exhibited the

strongest correlation of the winter campaign with $R^2 = 0.73$. These species are typically emitted from vehicle sources so this could suggest that local sources are more significant in the winter than the summer campaign. SO_2 is usually a marker of industrial combustion processes, along with NO_x and CO, and is not typically emitted in city centres. In winter, there was a positive correlation between SO_2 and CO ($R^2 = 0.51$) suggesting some regional influence from an industrial or power source. CO has a longer atmospheric lifetime than NO_x which may explain its stronger correlation with SO_2 (R^2 for SO_2 and NO_x correlation = 0.36). That said, SO_2 is also a marker of coal burning which whilst banned by the Clean Air Act since 2013, markers of coal burning have been observed in a series of flux measurements made during the APHH campaigns suggesting that there could be a local source of SO_2 [Langford, 2020]. In the summer, NO_x was very weakly correlated with CO ($R^2 = 0.10$) and not correlated with SO_2 ($R^2 < 1 \times 10^{-4}$). This was possibly due to higher rates of photochemistry in the summer removing and transforming NO_x. The correlation between CO and SO_2 during the summer ($R^2 = 0.50$) was similar to winter suggesting the influence of a regional industrial source remains for the summer campaign.

In order to investigate the relationships between these primary pollutants further the correlations were investigated for different wind quadrants, shown in Figs. 3.8 and 3.9. For winter, Fig. 3.8 the strongest correlation between NO_x and CO were seen for northerly ($R^2 = 0.81$ between 315°–45°) and westerly ($R^2 = 0.77$ between 225°–315°) wind directions, suggesting the influence of local roads in these directions. NO_x was best correlated with SO_2 when wind directions were from the north, though correlations were poorer than those with CO. CO and SO_2 were most strongly correlated when associated with northerly and westerly wind directions, as for NO_x, probably due to these wind directions being the dominant experienced during the winter campaign (see Fig. 3.4). For the summer, correlations between NO_x and CO were weaker than for the winter in all wind directions, with air masses from the west showing the strongest relationship ($R^2 = 0.32$). Very little correlation was observed between NO_x and SO_2 (all $R^2 < 0.1$). A strong correlation was observed between SO_2 and CO with easterly winds ($R^2 = 0.63$) suggesting there could be an industrial source east of the site.

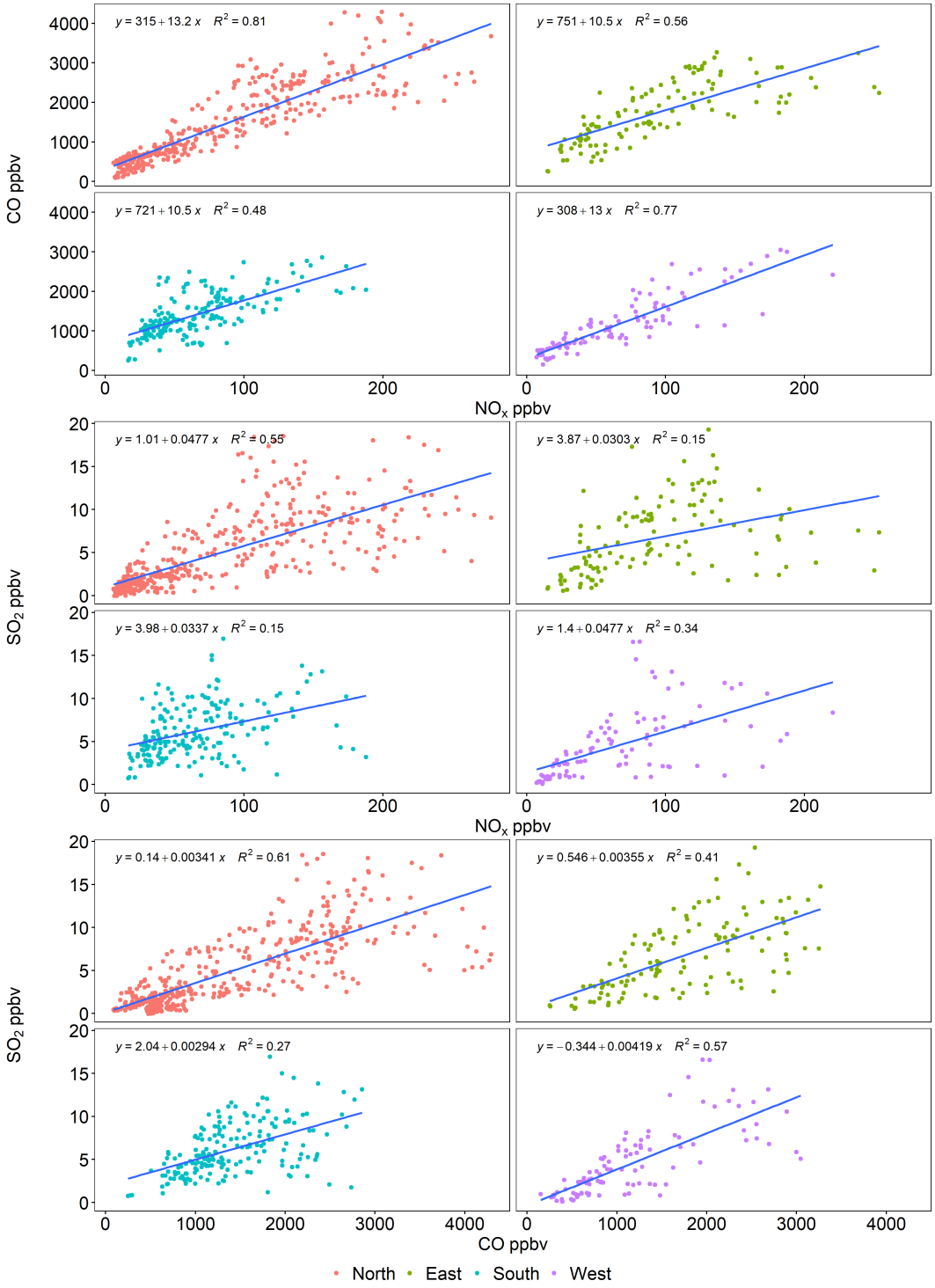

Figure 3.8: Correlations of primary pollutants separated by wind direction during the winter campaign. Data is hour averaged. The wind quadrants are defined as; North = 315°–45°, East = 45°–135°, South = 135°–225° and West = 225°–315°.

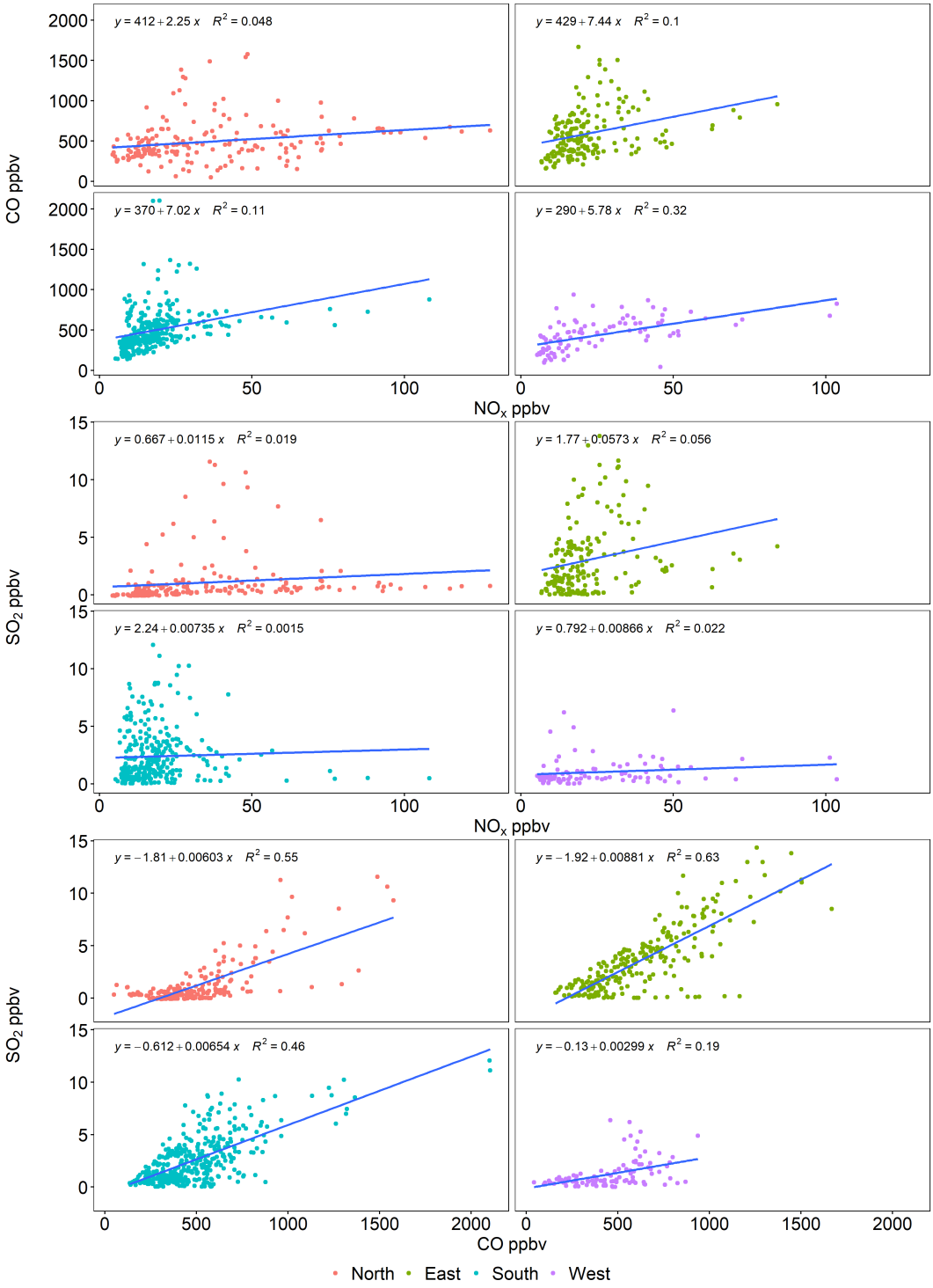

Figure 3.9: Correlations of primary pollutants separated by wind direction during the summer campaign. Data is hour averaged. The wind quadrants are defined as; North = 315°–45°, East = 45°–135°, South = 135°–225° and West = 225°–315°.

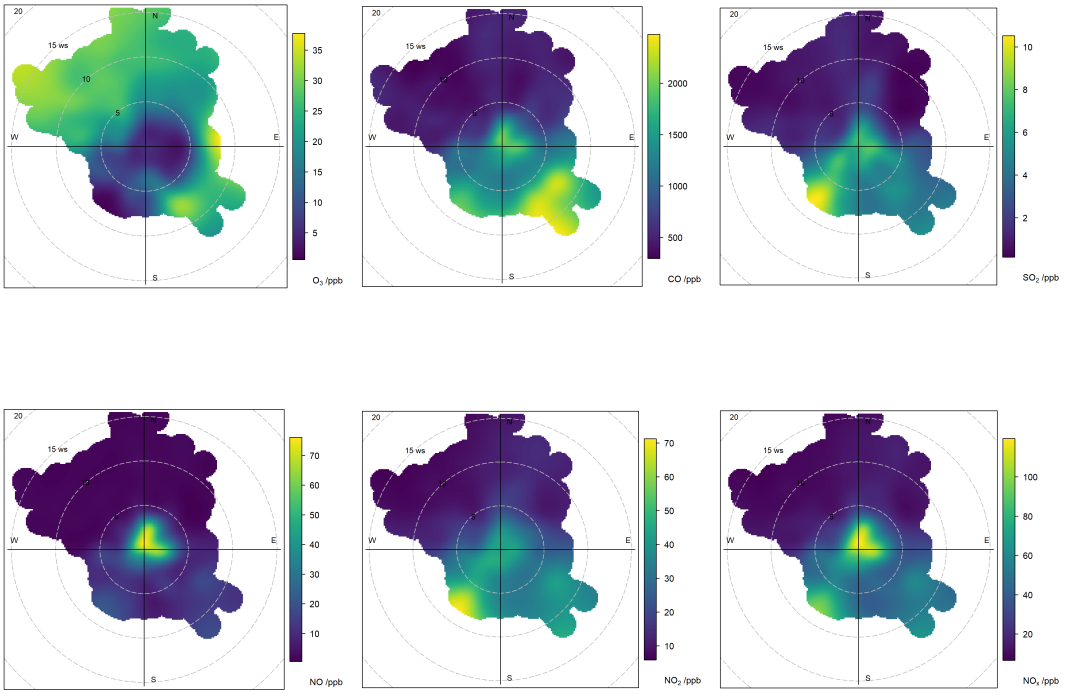

Figure 3.10: Polar plots showing the relationship between mixing ratios of O_3, CO, SO_2, NO, NO_2 and NO_x and wind direction during the winter campaign.

3.2.3 Meteorological impacts on pollutants

The winter campaign

The relationship between pollutant mixing ratio, wind direction and wind speed is shown for the winter campaign in Fig. 3.10. In these plots wind speed can be thought of as a proxy for distance as higher wind speeds mean pollutants can be transported to the site over greater distances. In general during the winter campaign primary pollutant mixing ratios (NO_2, NO_x, CO and SO_2) were lower for northerly wind direction sectors. O_3 mixing ratios show the opposite trend due to reduced titration with NO_x. The highest primary pollutant mixing ratios in winter were observed when there were southerly winds. South of the measurement site is the centre of Beijing where traffic density is higher and there are more pollution sources. Mountains surround Beijing to

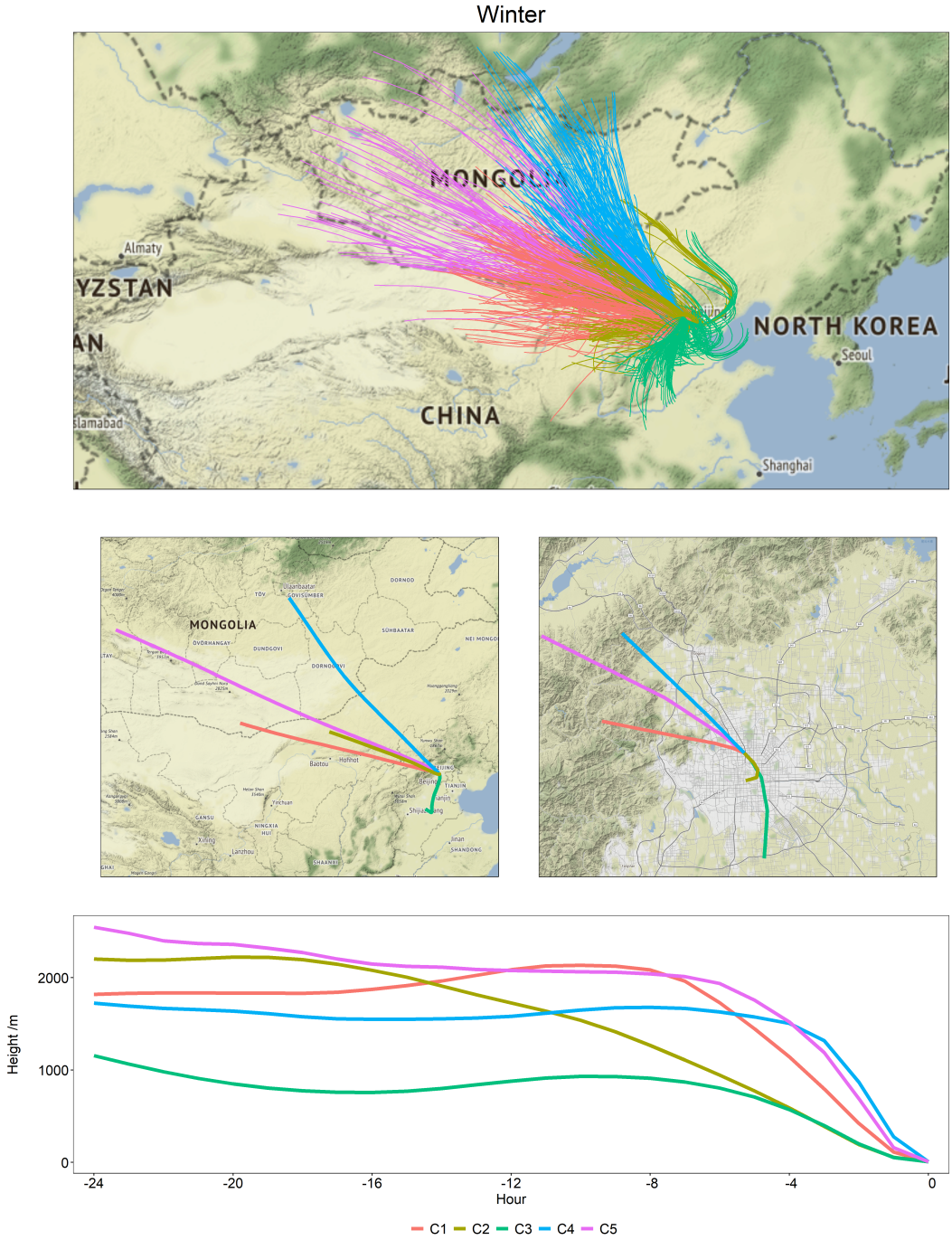

Figure 3.11: HYSPLIT back trajectories for the winter campaign. The top panel shows all trajectories that were run for the campaign coloured by cluster determined using Openair for R, the left hand middle panel shows the mean trajectory for each cluster and the right hand middle panel shows the last 5 hours of the mean trajectory path and the lower panel shows the mean travelling height.

the north west and north (shown in Fig. 3.1) which enhance pollutant mixing ratios by acting to accumulate pollution when wind directions came from the south. There were some "hot spots" for pollution to the south-west for SO_2, CO, NO_2 and NO_x and to the south-east for CO. O_3 also showed some enhancements to the east and south-east of the measurement site, possibly indicating low levels of photochemical O_3 production. NO mixing ratios were highest when the wind speed was lowest indicating a local source likely from vehicle exhausts on roads close to the measurement site. NO is oxidised rapidly to NO_2 after being emitted and therefore NO which is emitted further from the site is transported as NO_2 accounting for higher NO_2 emissions when wind speeds are higher.

These polar plots can give insights into processes occurring on local scales but not about long range transport. The influence of long-range transport on pollution can be investigated by calculating backward trajectories. Figure 3.11 shows 24 hour backwards trajectories calculated using the HYSPLIT model [Stein et al., 2016] using 6-hourly archive meteorological data from the NCEP Global Data Assimilation System (GDAS) ($1^\circ \times 1^\circ$). The IAP site (39.97 N, 16.37 E) was set as the end point of the trajectory with a height of 8 m above ground level (the height of the inlet) and trajectories were calculated hourly. Individual trajectories were then grouped into 5 clusters, shown in Fig. 3.11 using the OpenAir package [Carslaw and Ropkins, 2012]. Table 3.2 summarises the mean mixing ratios associated with each trajectory grouping.

During the winter campaign, clusters 1–3 were associated with the highest primary pollutant emissions. Cluster 3 indicates slow moving air masses that originated south of the measurement site and had a low travelling height (mean 745 m) meaning that these air masses could have spent time within the boundary layer. Cluster 3 was associated with the highest mean CO and SO_2 mixing ratios (1829 ppbv and 7.47 ppbv respectively). Data taken from the Emissions Database for Global Atmospheric Research (EDGAR), shown in Fig. 3.12, indicate high CO emissions which are fairly homogeneous for Beijing and extending south of the city. Emissions of SO_2 indicate numerous SO_2 point sources to the south of Beijing. For this cluster O_3 mixing ratios were lowest presumably due to titration with high amounts of primary pollutants and limited mixing of free tropospheric air due to the low travelling height of the trajectory. Clusters 1 and 2 both originated west/north-west of the site. Using EDGAR

Table 3.2: Mean travelling height, pollutant mixing ratios and pollutant ratios associated with each 24 hour backwards trajectory cluster.

	C1	C2	C3	C4	C5
WINTER					
% contribution	27.0	19.0	18.0	23.5	12.4
Height /m	1624	1481	745	1455	1880
NO /ppb	54.2	42.7	45.3	19.2	46.8
NO_2 /ppb	42.0	41.1	35.4	24.5	39.2
NO_x /ppb	96.2	83.8	83.6	43.7	86.0
CO /ppb	1702	1576	1829	726	1404
SO_2 /ppb	6.78	6.42	7.47	2.38	4.37
O_3 /ppb	6.69	6.10	5.48	14.9	8.88
NO_x/NO_y	0.91	0.88	0.88	0.99	0.93
NO/NO_2	1.14	0.95	1.03	0.53	0.99
SUMMER					
% contribution	18.1	27.7	23.8	23.0	7.5
Height /m	1083	529	617	1877	899
NO/ppb	4.01	2.27	1.77	7.78	1.93
NO_2 /ppb	20.7	21.4	17.6	21.9	15.9
NO_x /ppb	24.7	23.5	19.5	29.7	17.8
CO /ppb	537	632	573	389	492
SO_2 /ppb	1.68	3.67	2.67	1.13	2.74
O_3 /ppb	56.7	70.5	46.6	45.3	49.4
NO_x/NO_y	0.70	0.70	0.73	0.75	0.76
NO/NO_2	0.12	0.06	0.08	0.26	0.11

data there appears to be lower emissions in this region compared to south of Beijing. There are several major roads in this area which could explain why the highest NO and NO_2 mixing ratios were observed in cluster 1. Cluster 2 spends longer at lower altitudes compared to cluster 1, so it may be expected that this cluster should have higher mixing ratios of primary pollutants but the trajectory lies more to the north where emissions are lower. Cluster 5 also has high amounts of pollutants (though generally less than clusters 1–3) following a similar path to cluster 2 but travelling at a higher altitude and is more influenced by cleaner mountainous regions and air over Mongolia where emissions are lower. The second highest O_3 mixing ratios are observed for this cluster. Cluster 4 has the lowest amounts of all pollutants apart from O_3 originating north of the site where emissions are low over the mountains.

The summer campaign

Figure 3.13 shows the local impacts of surface wind on pollutant mixing ratio during the summer campaign as described for Fig. 3.10. For the summer campaign O_3 mixing ratios were more consistent for all wind directions compared to winter, indicating that O_3 was reasonably well mixed over the city during summer. O_3 was enhanced at higher wind speeds in most directions indicating that O_3 was formed as it was transported to the site from primary emissions in the city and wider region. O_3 mixing ratios were lowest close to the site (lowest wind speeds and northerly wind direction), where mixing ratios of NO, NO_2 and NO_x were highest indicating O_3 titration from local emissions. There were enhancements in SO_2 and CO east and south-east of the site possibly indicating an industrial source east of the site. There is a coal-fired power station east of the measurement site in the Chaoyang District of Beijing though this has largely been retired since March 2017 and remains on standby. The district of Tianjin, a major industrial centre in China lies south east of Beijing.

The back trajectory clusters are presented in Fig. 3.14. Cluster 2 represents air masses that originated south of the measurement site, which predominantly travelled within the boundary layer. The highest mean mixing ratios of CO and SO_2 were also observed in these air masses which was also observed during the winter campaign due to high levels of emissions in south Beijing and beyond. Interestingly, O_3 mixing ratios associated with these air masses were also highest, indicating that O_3 is being directly

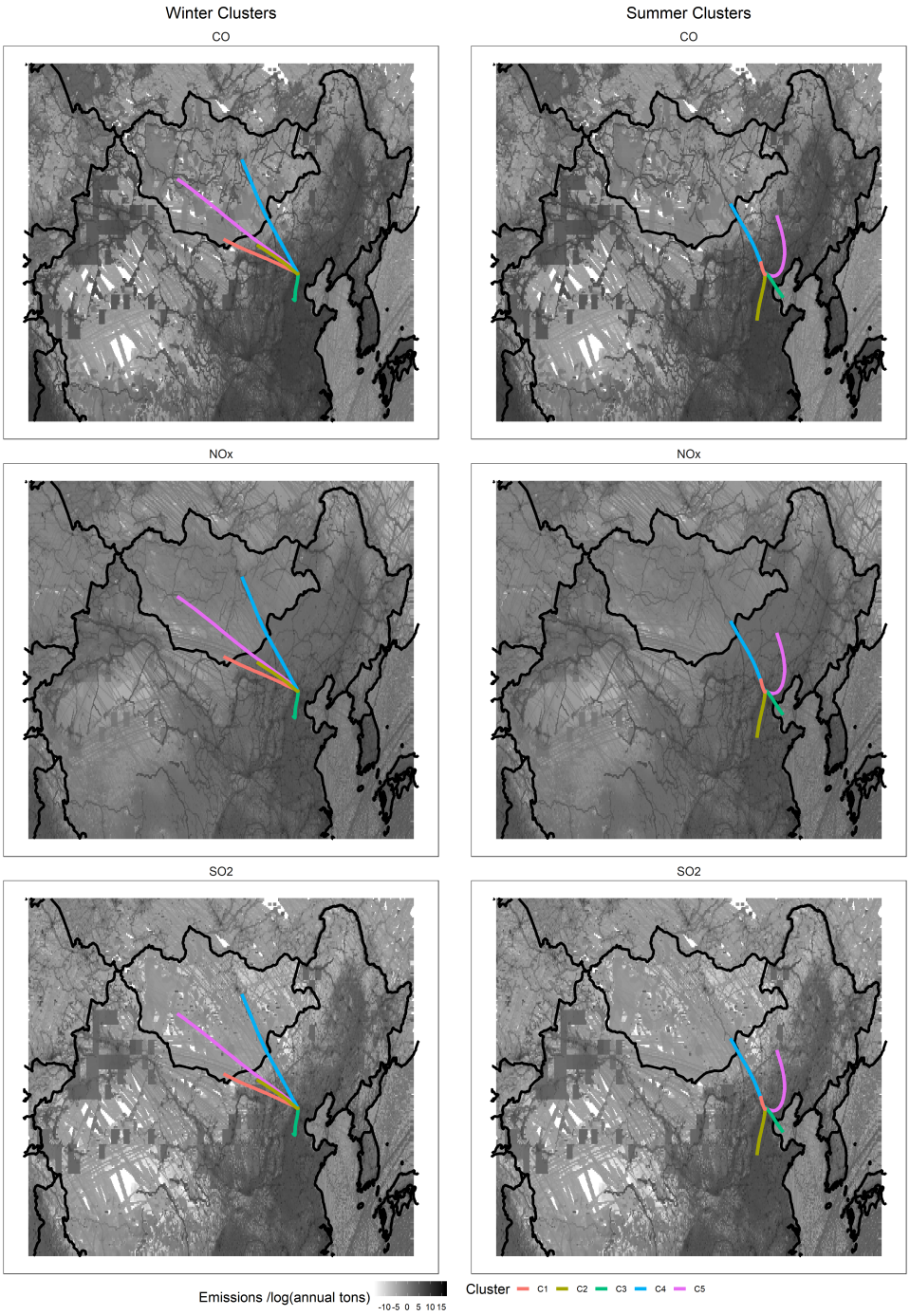

Figure 3.12: Annual emissions for CO, NO_x and SO_2 are shown for a region around Beijing from 2015 (the most recent publicly available emissions from EDGAR). The mean trajectory paths, coloured by cluster are overlaid with the left hand column showing the winter campaign trajectories and the right hand column showing the summer campaign trajectories.

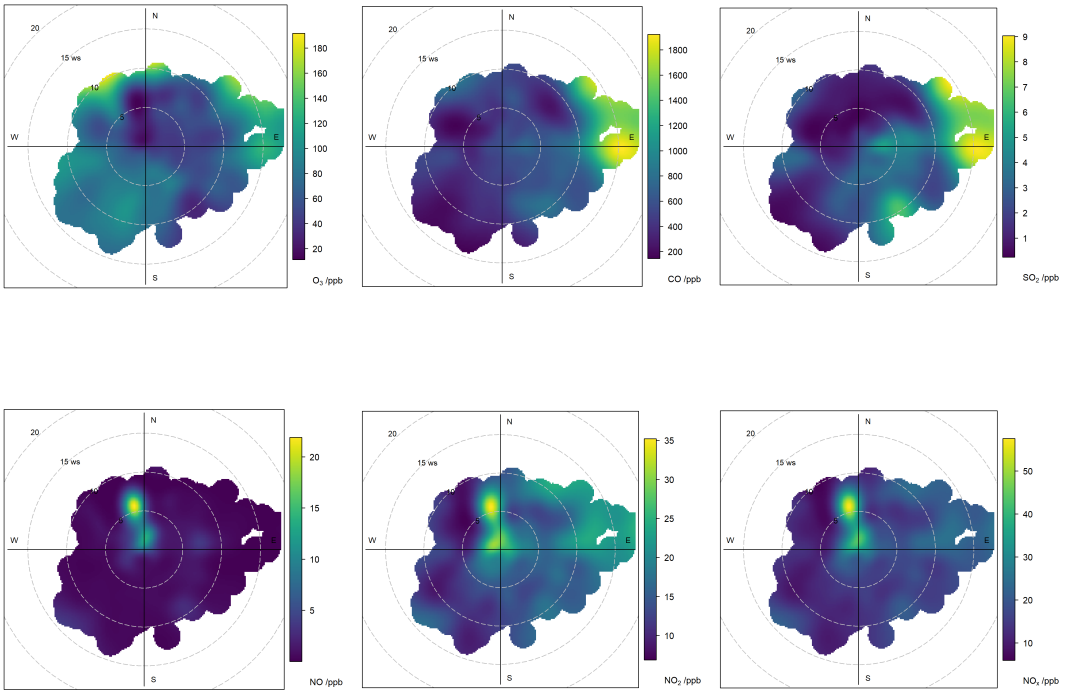

Figure 3.13: Polar plots showing the relationship between mixing ratios of O_3, CO, SO_2, NO, NO_2 and NO_x and wind directions during the summer campaign.

formed in these air masses. This is unlike the case in winter where the influence of free tropospheric air from north of the site led to the highest mixing ratios of O_3. Whilst examining VOC data is beyond the scope of this work, it is likely anthropogenic VOC concentrations are also enhanced in these air masses given CO and SO_2 are tracers for industry. Cluster 1 represents slow moving air masses that have spent the 24 hours over Beijing which has the second highest mean O_3 mixing ratio. Mixing ratios of CO and SO_2 are lower than for cluster 2 probably due to the higher travelling height of these air masses, though given the high levels of O_3 it is likely in-situ O_3 production is still occurring. O_3 mixing ratios are broadly similar for clusters 3–5. The highest NO_x mixing ratios were associated with clusters 4 and 1 which originated north west of the measurement site, which was also observed during the winter campaign, probably due to the presence of major roads in this region. Cluster 3 originates east of the site covering some coastal area. Figures 3.13 and 3.12 indicate some SO_2 point sources in this direction and CO emissions are consistently high east of the site, corresponding to the observed high CO and relatively high SO_2 mixing ratios for this cluster. NO_x mixing ratios are relatively low for this cluster however. Cluster 5 is associated with low NO_x air masses with moderate CO and SO_2 mixing ratios probably influenced by emission sources east and south of the measurement site during the final hours of the air mass journey.

3.2.4 $[NO_x]/[NO_y]$ Ratios

The ratio of NO_x to total reactive nitrogen, NO_y, can provide some information about how photochemically processed an air mass is. This is because the majority of NO_y is emitted as NO_x and then further oxidised to form other reactive nitrogen species. Generally, daytime values of $[NO_x]/[NO_y] < 0.3$ indicate highly processed air masses and $[NO_x]/[NO_y] > 0.3$ are representative of air masses with fresher emissions [Trainer et al., 1993, Chin et al., 1994]. Mean diurnal variation in the $[NO_x]/[NO_y]$ ratio is shown in Fig. 3.15 for the winter and summer campaigns. The $[NO_x]/[NO_y]$ ratio for the winter campaign ranged between 0.88–0.95 indicating that most NO_y is present as NO_x and that local emissions dominate the NO_y budget. Overnight the $[NO_x]/[NO_y]$ ratios are stable around 0.92 and increase to its maximum value of 0.81 at 07:00 due to an increase in NO_x emissions due to morning rush-hour traffic emissions. The

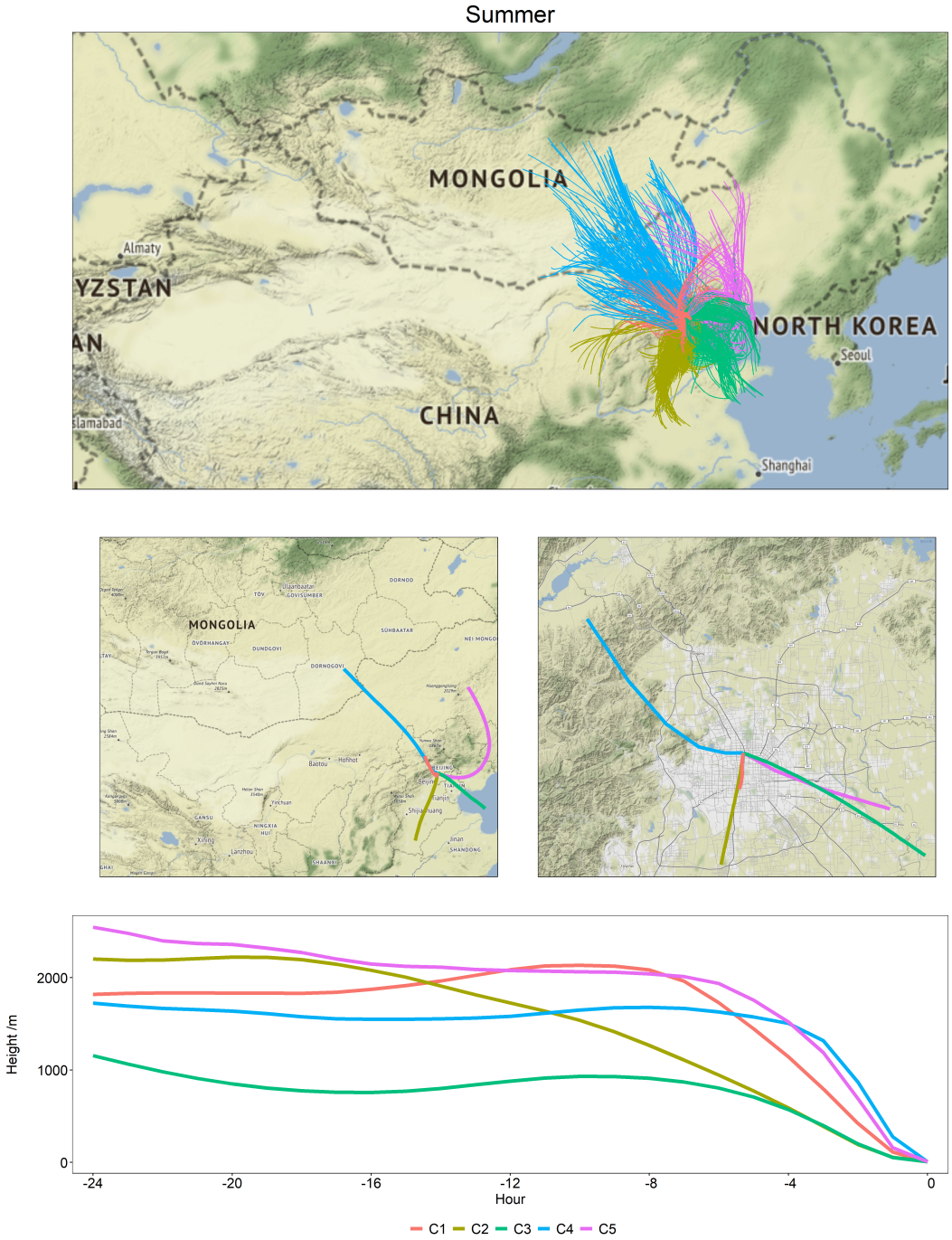

Figure 3.14: HYSPLIT back trajectories for the summer campaign. The top panel shows all trajectories that were run for the campaign coloured by cluster determined using Openair for R, the left hand middle panel shows the mean trajectory for each cluster and the right hand middle panel shows the last 5 hours of the mean trajectory path and the lower panel shows the mean travelling height.

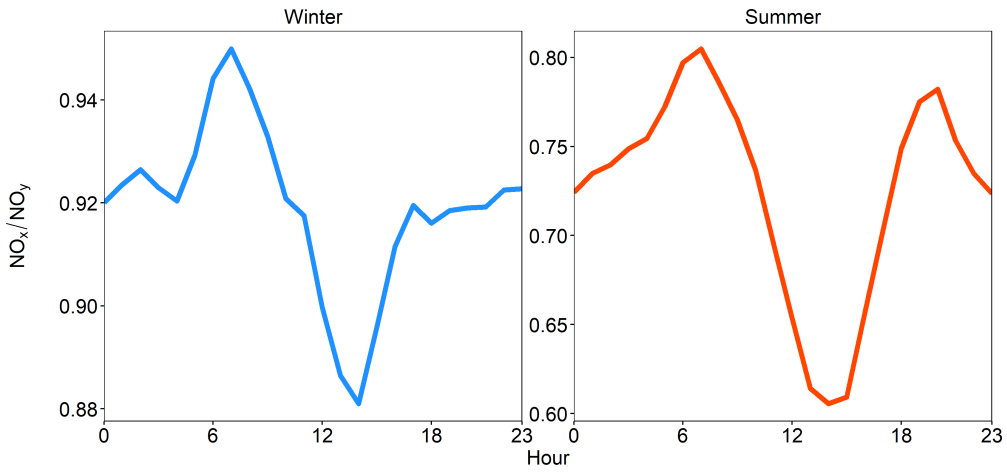

Figure 3.15: Diurnal variation in NO_x/NO_y ratios for the winter and summer campaigns.

$[NO_x]/[NO_y]$ ratios decrease to a minima during the day at 14:00 when solar radiation is at its peak due to the photochemical oxidation of NO_x. For the summer campaign, the mean diurnal variation in the $[NO_x]/[NO_y]$ ratio ranged between 0.60–0.80 with its minimum value at 13:00–15:00 and maximum at 07:00 as for the winter campaign. These values still indicate that most NO_y is in the form of NO_x highlighting the importance of local emissions in Beijing however there is still more photochemical processing of the air masses above the city in summer compared to winter. Photochemistry during the summer will be faster due to increased solar radiation. Looking at the $[NO_x]/[NO_y]$ ratios by cluster (Table 3.2) for the winter seems to indicate that the slower moving clusters which have spent more time over Beijing within the boundary layer have lower NO_x/NO_y ratios indicating more chemical processing than for the longer, higher trajectories. Overall however the difference between ratios is small. The same is true for the summer campaign, where all clusters have similar ratios. Again the shorter, slower moving trajectories that have spent more time within the boundary layer have lower ratios.

3.2.5 Ozone production efficiencies

Due to the non-linear relationship between O_3 and its precursors, O_3 is a difficult pollutant to control. The ozone production efficiency (OPE) is defined as the number of O_3 molecules produced for each NO_x molecule oxidised and is a useful method for assessing O_3 production and developing control strategies. O_3 is often correlated with the products of NO_x oxidation and therefore OPE can be calculated from the observed ratio of NO_x oxidation products and O_3 [Trainer et al., 1993]. NO_z ($=NO_y - NO_x$) corresponds to NO_x oxidation products (e.g. HNO_3, PAN). Previous studies have used odd oxygen (O_x), the sum of O_3 and NO_2, in linear regression analysis to calculate OPE as this quantity is better conserved than O_3 as O_x is not affected by the $O_3 + NO \longrightarrow NO_2$ titration reaction [Lin et al., 2011, Kleinman et al., 2002]. Mixing ratios of O_3 and NO_y experience strong diurnal cycles due to the influence of the planetary boundary layer, photochemical activity and emissions. For the calculation of OPE, data was filtered to select periods where the boundary layer was fully developed and that were photochemically active (i.e. $j(NO_2) > 0.001$), as outlined by Trainer et al. [1993]. During the winter campaign, data was selected between 12:00–14:00 when observed MLH was at its maximum and $NO_x/NO_y > 0.9$. During the summer, data between 13:00–17:00 was used during which NO_x/NO_y was stable below 0.7. OPE was calculated for each day during the winter and summer campaigns and shown in Fig. 3.16.

During the winter campaign OPE was negative for nearly half (47%) of the days, indicating O_3 destruction by NO_x from local emissions, but the mean OPE was 1.1 ppb ppb^{-1} $\pm$ 3.5 ppb ppb^{-1}. This implies that there is still some photochemical production of O_3 during the winter campaign despite the weaker solar radiation and higher NO_x mixing ratios. For summer, OPE was higher as expected, with a mean value of 4.0 ppb ppb^{-1} $\pm$ 5.7 ppb ppb^{-1}. These values compare to those previously calculated for Beijing. Lin et al. [2011] reported a mean OPE of 1.1 ppb ppb^{-1} $\pm$ 1.6 ppb ppb^{-1} at an urban site in Beijing from measurements taken between November 2007–March 2008. Previous values for urban regions of Beijing during the summer vary between 4–20 [Sun et al., 2011, Ge et al., 2013, Wang et al., 2018a]. Sillman [1995] suggested that OPE < 7 indicated that O_3 formation is VOC limited.

Other studies have suggested that Beijing is largely a VOC limited regime [Sun

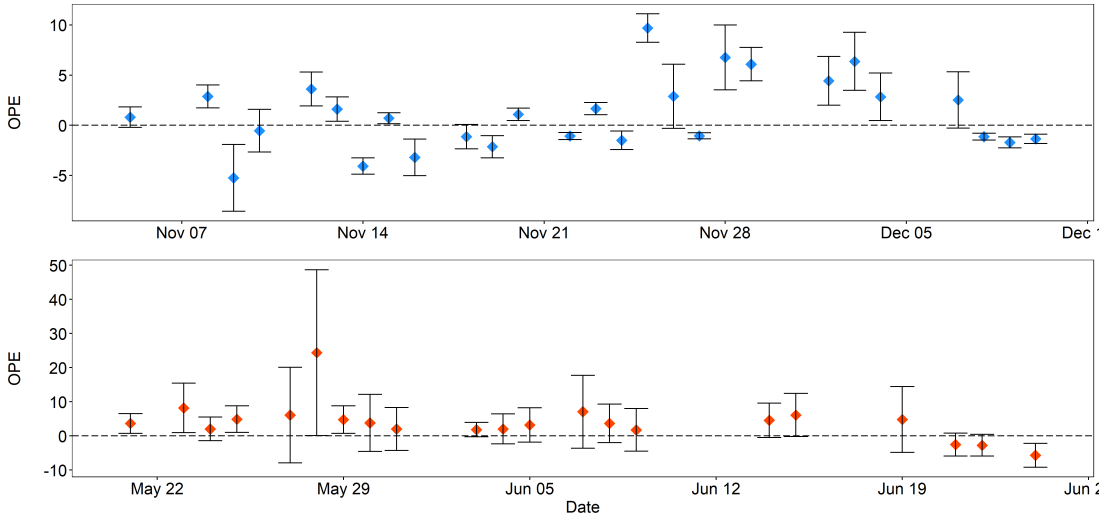

Figure 3.16: Time series of OPE calculated for each day of the winter and summer campaigns. Error bars indicate the residual standard error of the linear fit.

et al., 2011, Tan et al., 2019] though on days with high O_3 mixing ratios, O_3 production became sensitive to NO_x. Sun et al. [2011] reported an OPE value of 20.2 on a day during which O_3 mixing ratios exceeded 100 ppb. The highest OPE calculated during the summer campaign was 24.4 ppb ppb^{-1} and occurred on a day where O_3 mixing ratios were over 160 ppb (15 minute average). Whilst the O_3 formation regime can transition between being sensitive to VOCs and sensitive to NO_x, the mean OPE values calculated are under 7 suggesting that measures to control VOC emissions in Beijing would be most effective to reduce O_3. As different VOC functionality changes their O_3 formation potential, it is useful to design O_3 control strategies which tackle the most important VOCs for O_3 formation. Recent work showed that aromatics and alkenes were the VOC classes with the largest O_3 formation potentials in Beijing and therefore should be targeted in order to reduce O_3 pollution in the city [Li et al., 2020b].

3.3 Chemistry during the summer campaign

3.3.1 HO_2 and RO_2 chemistry

The low NO mixing ratios observed in Beijing during the summer campaign have significant impacts on the chemistry of the peroxy radicals (HO_2 or RO_2). In atmospheres with high NO mixing ratios peroxy radicals formed from VOC oxidation predominantly react with NO to form NO_2, which leads to O_3 formation and alkoxy radicals. However, when mixing ratios of NO are low ([NO]$<$ 1 ppbv), the photostationary state no longer holds because the lifetime of peroxy radical species are longer than 1 second ($\tau_{(HO_2)}$= 45 s at [NO]= 100 pptv). Therefore, other peroxy radical reactions become more favourable e.g. peroxy radicals may react with other peroxy radicals (HO_2 or RO_2) or isomerisation/autoxidation process may occur. Autoxidation refers to intramolecular hydrogen shift reactions to form highly oxidised molecules. These reactions are typically slow but can occur when radical lifetimes are long (on the scale of 10–100 s) and become more favourable with increasing temperature due to an increase in isomerisation rates. The highly oxidised molecules formed are generally less volatile and can effectively partition into the aerosol phase to make ssecondary organic aerosol (SOA) [Ehn et al., 2014], a significant component of particulate matter which is hazardous to public health.

Newland et al. [2020] shows that as a result of the low NO mixing ratios observed during the summer campaign in Beijing oxidation products typically observed in remote regions like rainforests can form. Large emissions of isoprene were observed during the summer campaign [Acton et al., 2020]. Isoprene is oxidised by OH radicals to form ISOPOO which under high NO mixing ratios, typically observed in the morning, reacts with NO to form isoprene hydroxy-nitrate. As NO levels decrease, reactions with peroxy radicals become more favourable and so called ‘low-NO’ products form; ISOPOOH and IEPOX. The extreme low NO mixing ratios observed highlight that it is overly simplistic to think of urban atmospheres as ‘high NO’ environments.

3.3.2 Deviations from the photostationary state during the summer campaign

Tropospheric O_3 is an important atmospheric species as it influences the oxidising capacity of the troposphere and is a harmful air pollutant. In air masses with very low levels of VOCs the reactions that form O_3 are in equilibrium, known as the photostationary equilibrium:

$$NO_2 + h\nu \longrightarrow NO + O(^3P) \tag{R25}$$

$$O(^3P) + O_2 + M \longrightarrow O_3 + M \tag{R26}$$

$$O_3 + NO \longrightarrow NO_2 + O_2 \tag{R27}$$

There is no net O_3 formation for reactions R25–R27. The photostationary state expression can therefore be defined as:

$$\phi = \frac{j(NO_2)[NO_2]}{k_{R27}[NO][O_3]} \tag{3.1}$$

k_{R27} is taken to be 1.9×10^{-14} cm^3 molecule^{-1} s^{-1} [Atkinson et al., 2004] and ϕ will be 1 if the photostationary state holds. The assumption of a photochemical equilibrium only holds true when competing reactions (e.g. between NO_x and VOCs or peroxy radicals) can be ignored. Given that Beijing is an urban area with high NO_x levels, it is expected that the photostationary state will hold, as at higher NO_x mixing ratios (above 1 ppbv) other oxidants are suppressed, with the OH radical reacting preferentially with NO_2 to form HNO_3 [Carpenter et al., 1998]. Time series data for ϕ for the winter and summer campaigns were calculated using Equation 3.1 and are presented in Figs. 3.17 and 3.19. Only $j(NO_2)$ values greater than 0.001 were used so nighttime data is disregarded for the calculation.

During the winter campaign, ϕ ranged between 0.15–4.04. Figure 3.17 shows that for the majority of cases deviation from $\phi = 1$ are negative which is indicative of fresh NO_x emissions perturbing the photostationary state [Chate et al., 2014]. Figure 3.18 shows a negative correlation between NO_x mixing ratios and ϕ calculated, so when there are high amounts of NO_x ϕ is low. As discussed previously in this chapter there

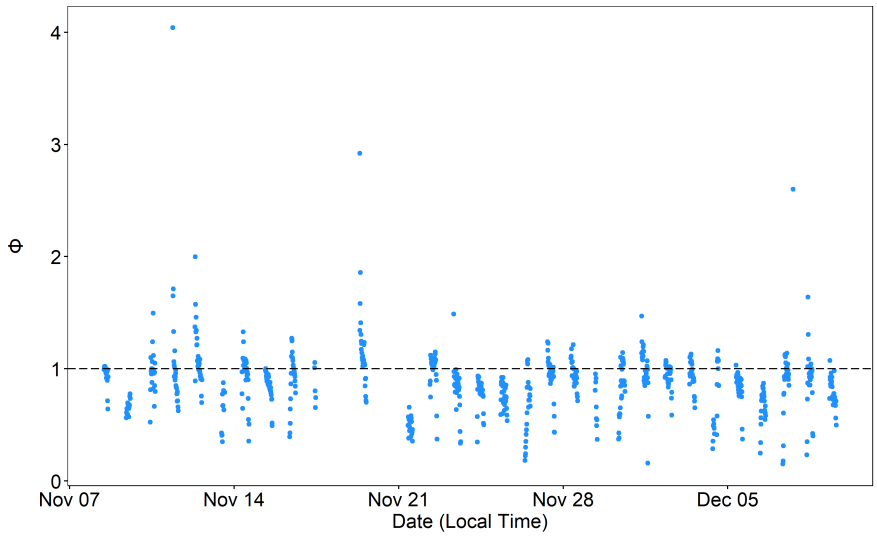

Figure 3.17: Time series of ϕ for the winter campaigns. Negative deviations from unity dominate indicate any perturbation of the photostationary state is due to fresh NO emissions.

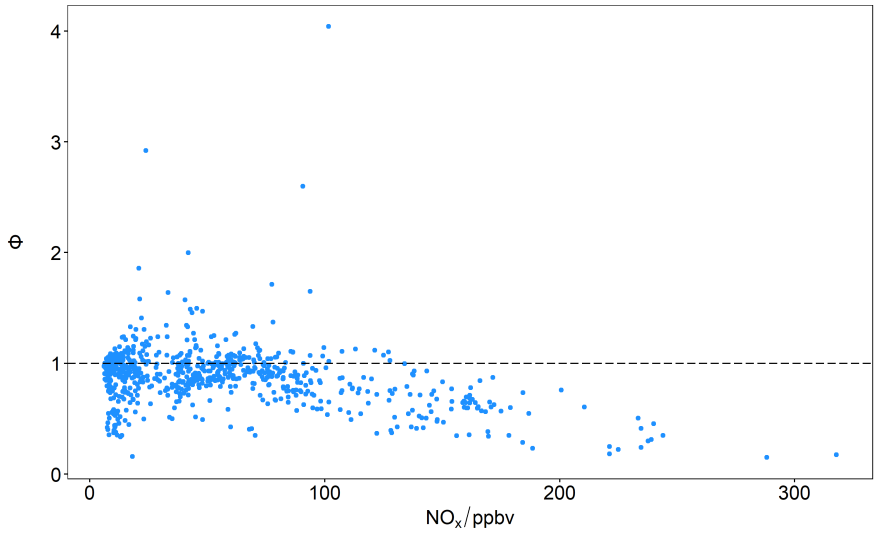

Figure 3.18: ϕ as a function of NO_x mixing ratio during the winter campaign. In general, higher NO_x mixing ratios result in ϕ values below 1.

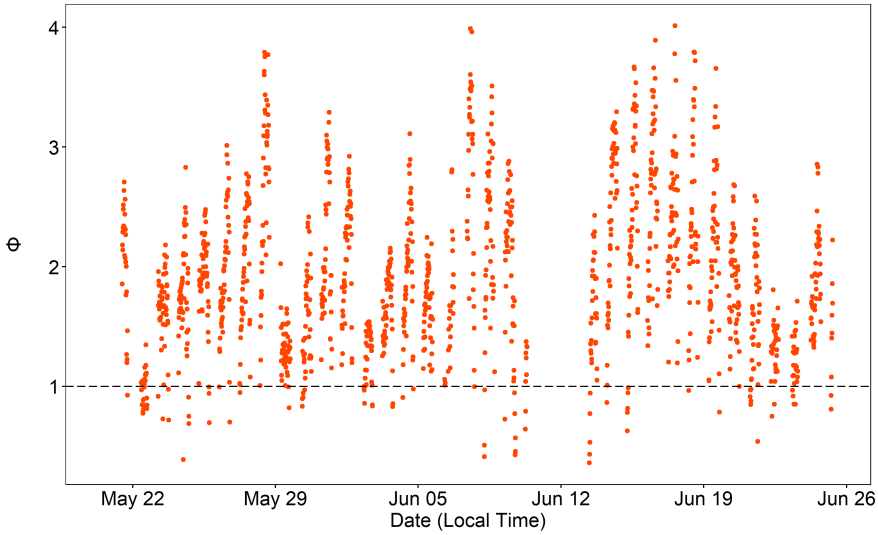

Figure 3.19: Time series of ϕ for the summer campaign.

are numerous roads close to the measurement site which are hot spots for NO emission which are likely responsible for these perturbations in PSS.

Figure 3.19 shows the calculated ϕ values for the summer campaign. For summer, ϕ ranges between 0.36–4.01 but, in contrast to winter, has mainly positive deviations from the photostationary state. Figure 3.19 shows that the largest positive deviations occur when NO_x mixing ratios are low. The diurnal variation in ϕ is shown in Fig. 3.21. The highest deviations from unity occur between 13:00–15:00, when NO mixing ratios are on average below 1 ppbv (see Fig. 3.7). ϕ deviates positively from unity when another chemical process converts NO to NO_2 so O_3 is not the sole oxidant. The O_3 molecule in reaction R27 can be substituted by the presence of hydroperoxy or peroxy radicals, HO_2 or RO_2:

$$NO + HO_2 \longrightarrow NO_2 + OH \tag{R28}$$

$$NO + RO_2 \longrightarrow NO_2 + RO \tag{R29}$$

This reaction will take place preferentially to the reaction of the radical and O_3 (below) when mixing ratios of NO are above a threshold amount (around 30 pptv).

$$O_3 + HO_2 \longrightarrow 2O_2 + OH \tag{R30}$$

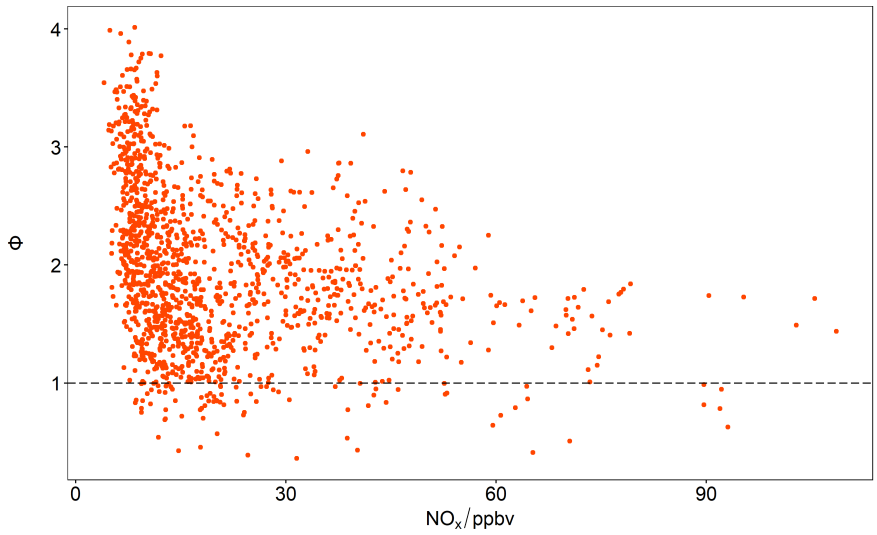

Figure 3.20: ϕ as a function of NO_x mixing ratio for the summer campaign.

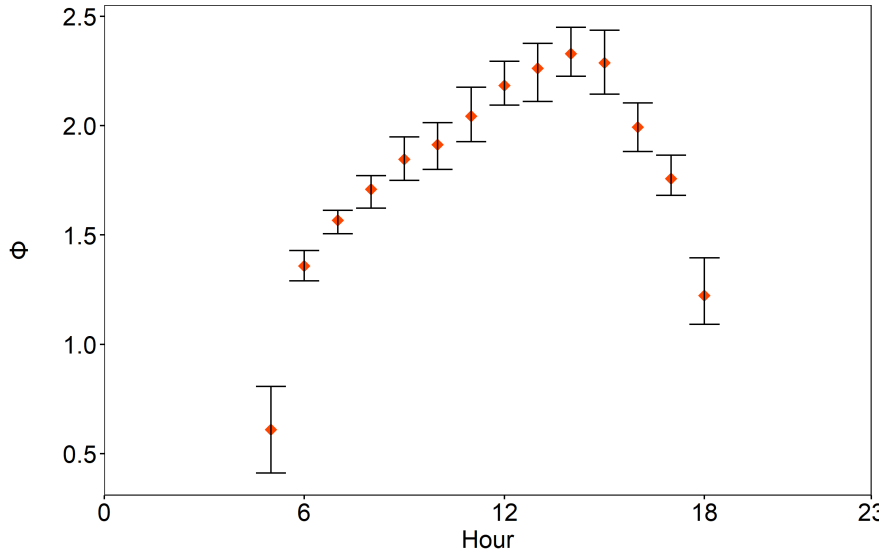

Figure 3.21: Diurnal variation in ϕ for the summer campaign. Mean ϕ is presented with error bars representing the 5^{th} and 95^{th} percentiles.

HO_2, in turn, can be formed from reactions of OH with CO or O_3 (reactions R31 and R32) and from the photolysis of formaldehyde (reactions R33–R35) [Stone et al., 2012].

$$CO + OH + O_2 \longrightarrow HO_2 + CO_2 + H_2O \tag{R31}$$

$$OH + O_3 \longrightarrow HO_2 + O_2 \tag{R32}$$

$$HCHO + hv \longrightarrow H + HCO \tag{R33}$$

$$H + O_2 + M \longrightarrow HO_2 + M \tag{R34}$$

$$HCO + O_2 \longrightarrow HO_2 + CO \tag{R35}$$

RO_2 is formed from the oxidation of hydrocarbons e.g.:

$$RH + OH \longrightarrow R + H_2O \tag{R36}$$

$$R + O_2 + M \longrightarrow RO_2 + M \tag{R37}$$

If HO_2 or RO_2 are perturbing the photostationary state, then the photostationary state expression can be modified as shown in Carpenter et al. [1998].

$$\frac{[NO_2]}{[NO]} = \frac{k_{R26} + k_{R28}[HO_2] + \Sigma k_{R29}[RO_2]}{j(NO_2)} \tag{3.2}$$

Which can be simplified to:

$$[HO_2] + [RO_2] = (\phi - 1)\frac{k_{R27}[O_3]}{k_{R29}} \tag{3.3}$$

By solving equation 3.3 the amount of total peroxy radicals (PO_2=HO_2+RO_2) required to make $\phi = 1$ can be calculated. k_{R29} was taken to be 9.0×10^{-12} cm^3 $molecule^{-1}$ s^{-1}, based on an average of rate coefficients for different R groups at 298 K [Jenkin et al., 2019]. Figure 3.22 shows a time series of peroxy radical mixing ratios calculated assuming that $\phi = 1$ along with the measured PO_2 mixing ratio. PO_2 mixing

ratios calculated assuming PSS conditions are significantly larger than those measured, with the most significant discrepancy occurring between 14:00–16:00, when calculated mixing ratios are on average 9.9 times greater than those measured. This discrepancy is not likely to be explained by a systematic underestimation of PO_2 mixing ratios in the measurement. PO_2 is measured via conversion to and subsequent detection of OH. Reported interferences on the measurement technique mean that HO_2 mixing ratios are more likely to be overpredicted than underpredicted. Its detection relies on conversion of HO_2 into OH via NO and it has been found that some complex RO_2 could convert on a timescale quick enough to interfere with the HO_2 measurement [Fuchs et al., 2011, Whalley et al., 2013]. This interference has been lowered by decreasing the amount of NO added to the sample [Whalley et al., 2013]. Whalley et al. [2018] reports that sensitivity to some more complex RO_2 species may be low due to reduced conversion efficiency, though given the large difference between measured and calculated values, this is not likely to account for the discrepancy observed.

The sensitivity to the rate constant was investigated by substituting k_{R29} for the range of values presented for different types of RO_2 in Jenkin et al. [2019]. In Beijing, isoprene was found to be important for OH reactivity [Bryant et al., 2020] so k_{R29} was substituted for the isoprene-derived rate constant of 8.8×10^{-12} cm^3 $molecule^{-1}$ s^{-1} given in Jenkin et al. [2019]. This was found to slightly worsen the agreement, with calculated peroxy radical mixing ratios being overestimated by a factor of 10.1 between 14:00–16:00. The higher rate constants associated with acyl peroxy radicals ($k = 20$–34×10^{-12} cm^3 $molecule^{-1}$ s^{-1}) were found to best improve the agreement between the measured PO_2 and calculated PO_2 mixing ratios. For a k_{R29} value of 34×10^{-12} cm^3 $molecule^{-1}$ s^{-1} calculated PO_2 are a factor of 2–3 times higher than the measured mixing ratios between 14:00 and 16:00. In order to match measured and calculated PO_2 mixing ratios during the afternoon however, k_{R29} would have to be adjusted to around 1×10^{-10} cm^3 $molecule^{-1}$ s^{-1}.

The large discrepancy between the amount of PO_2 calculated to make $\phi = 1$ and the measured PO_2 indicates another process is driving deviations from the photostationary state. Values of ϕ and $[PO_2]_{PSS}/[PO_2]_{Measured}$ grouped by trajectory cluster are presented in 3.3. The largest discrepancy between predicted and measured PO_2 is associated with air masses from clusters 1 and 4. Figure 3.14 shows that these two

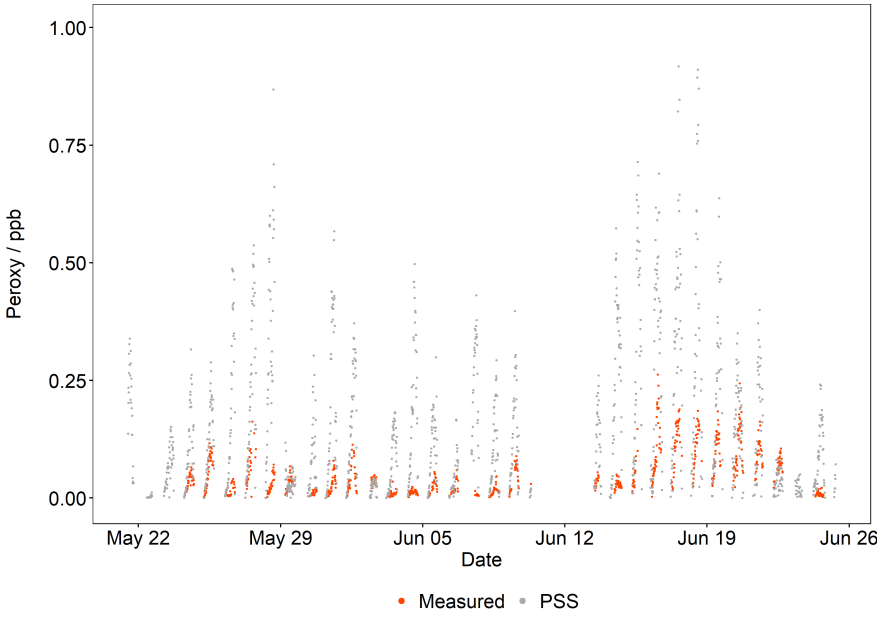

Figure 3.22: Calculated peroxy mixing ratios (dark grey) compared to measured peroxy radical mixing ratios (orange) for the summer campaign. Only data for $\phi > 1$ is presented.

Table 3.3: Summary of ϕ and $[PO_2]_{PSS}/[PO_2]_{Measured}$ ratio for each cluster shown in Fig. 3.14.

	C1	C2	C3	C4	C5
ϕ	2.0	2.1	1.6	2.0	1.6
Ratio	7.5	5.0	4.4	8.6	7.3

clusters follow a very similar trajectory but mean travelling heights are quite different and only becoming similar in the last four hours of the air parcel's journey. The trajectory originates north west of the measurement site and is associated with the highest NO mixing ratios. This is surprising as clusters 1 and 4 are associated with the two highest NO mixing ratios (Table 3.2) and overall there are larger deviations from the PSS when NO mixing ratios are lower.

In order to investigate whether there is some physical process driving deviations from the photostationary state ϕ was compared with wind direction, wind speed, temperature, relative humidity and j_{NO_2} and regression analysis carried out. No correlation was observed between ϕ and wind direction ($R^2 = 0.002$) and wind speed ($R^2 = 0.005$). There was a stronger correlation with temperature ($R^2 = 0.2$) and negative correlation with RH ($R^2 = 0.1$). A strong correlation between ϕ and j_{NO_2} was calculated with R^2 equal to 0.8. This indicates that solar radiation controls the chemical process that causes deviations from the photostationary state. Similarly correlations between $[PO_2]_{PSS}/[PO_2]_{Measured}$ showed little correlation with wind speed and wind direction (R^2 values of 0.0008 and 0.001 respectively). Both correlations were negative. R^2 values of 0.05 and 0.02 were obtained for temperature and RH, with correlation with RH being negative.

The correlation between ϕ and j_{NO_2} indicates that any deviations from the PSS are driven by a process influenced by solar radiation. Mannschreck et al. [2004] concluded that local forests and vegetation caused deviations from the PSS by reducing the photolysis of NO_2 due to lower light penetration through forest canopies increasing NO_2/NO ratios. In the study, a correlation between wind sector and deviations from ϕ was observed in the directions where there were coniferous forests. For Beijing, no

such correlation between ϕ and wind direction was observed. Hollaway et al. [2019] showed that j_{NO_2} was reduced by up to 66% due to haze pollution in the summer. If deviations from the photostationary state were due to reductions in j_{NO_2} however, we would see a negative correlation between j_{NO_2} and ϕ whereas we see a correlation that is strongly positive.

Rather than a meteorological driver for deviations from ϕ it is possible that there is another unknown oxidant acting to titrate NO in the afternoon. Halogenated compounds are known to influence the oxidising capacity of the atmosphere. For example, the reaction rate of Cl with some VOCs is around 200 times greater than the respective reactions with OH and hence can be a significant contributor to overall oxidation rates [Le Breton et al., 2018]. Halogen oxides (XO) can form from the reaction of X and O_3 and go on to oxidise NO e.g. for chlorine:

$$ClO + NO \rightarrow NO_2 + Cl \tag{R38}$$

Reactive Cl originates in the atmosphere from a range of sources, including HCl, sea salt aerosol and gaseous Cl containing species e.g. nitryl chloride ($ClNO_2$) which photolyse to release Cl. Liu et al. [2017b] showed correlations between Cl_2 and SO_2 suggesting that Cl_2 can originate from power generation facilities that burn coal. Studies for other urban areas also indicate an anthropogenic source of Cl can lead to the formation of $ClNO_2$ [Mielke et al., 2011]. $ClNO_2$ forms via the reaction of NO_3 and Cl during the night when NO_3 concentrations are significant. Upon sunrise $ClNO_2$ readily photolyses releasing highly reactive Cl radicals. Measurements of $ClNO_2$ were made in London in 2012 with concentrations peaking directly before sunrise before being photolysed. It was concluded that Cl atoms were the dominant oxidant for alkanes in the early morning, significantly influencing the oxidative capacity of the atmosphere [Bannan et al., 2015].

High levels of $ClNO_2$ have been reported for Chinese megacities. Tham et al. [2016] reported mixing ratios of 2070 pptv (1 minute averaged measurement) in a plume from Tianjin in the North China Plain and $ClNO_2$ continued to increase for four hours after sunlight. It was thought that $ClNO_2$ could be produced by reactions between Cl^- containing aerosol and NO_x from coal fired power plants during the night and the mixing of the nocturnal boundary layer (NBL) in the morning would lead to enhancements of $ClNO_2$ in the morning. For Beijing, mixing ratios of reactive

molecular Cl and $ClNO_2$ reached up to 1 ppbv and 1.4 ppbv respectively in Beijing [Zhou et al., 2018b]. Laboratory studies have shown production of $ClNO_2$ can occur through the heterogeneous uptake of N_2O_5 on Cl-containing aerosol [Finlayson-Pitts et al., 1989]. Particulate Cl mixing ratios measured during the summer campaign were found vary between 76–300 ppt during a mean diurnal cycle, with an average of 85 ppt between 14:00 and 16:00. During the summer campaign the mean diurnal variation in $ClNO_2$ showed that mixing ratios were lowest in the afternoon, with approximately 10 ppt being measured between 14:00 and 16:00. $ClNO_2$ peaked at 21:00 and remained elevated through the nighttime.

Given that $ClNO_2$ photolyses readily in the morning and its lowest mixing ratios were reported when deviations from the photostationary state are the highest, $ClNO_2$ may not be the dominant source of an additional oxidant but Cl could still be an important oxidant, indicated by the particulate chloride measurements. Assuming a source of reactive Cl which forms ClO, it is possible to calculate the amount of halogen required to make ϕ equal to 1. If we assume the additional oxidation is due to chlorine oxides equation 3.2 becomes [Ma et al., 2017]:

$$\phi_{ext} = \frac{j(NO_2)[NO_2]}{k_{R27}[NO][O_3] + k_{R29}[HO_2 + RO_2][NO] + k_{R38}[ClO][NO]} \tag{3.4}$$

This equation can be rearranged to give chlorine oxide:

$$[ClO] = \frac{1}{k_{R38}} \left(\frac{j(NO_2)[NO_2]}{[NO]} - (k_{R27}[O_3] - k_{R29}[HO_2 + RO_2]) \right) \tag{3.5}$$

Assuming any halogen reactivity is due to solely Cl, the mean mixing ratio of ClO required to make $\phi = 1$ was 112 ppt with 240 ppt needed between 14:00–16:00. The rate constant for reaction R38 was taken to be 1.7×10^{-11} cm^3 $molecule^{-1}$ s^{-1} [IUPAC, 2013]. Ma et al. [2017] observed deviations from the photostationary state for Kaiping in the Pearl River Delta of China and calculated a mean mixing ratio of ClO of 118 pptv would be required to make ϕ unity, similar to the value obtained for Beijing. At the time of writing no measurements of ClO are available for the summer campaign to compare to but up to 240 pptv of ClO does not seem likely. However, the deviations from the photostationary state could indicate that halogen chemistry has a role to play in Beijing.

3.4 Conclusions

Beijing experiences severe air quality problems as a result of rapid economic growth and an increase in the urban population. Air quality controls have been successful in some aspects (reductions in SO_2 in particular) but other air pollutants, such as O_3, are still increasing highlighting the challenges of managing air pollution. Large scale measurement campaigns can provide useful information about how atmospheric composition is changing and provide a basis for recommendations for air pollution control strategies. Measurements of gas-phase pollutants; O_3, CO, NO_x and SO_2, made as part of two intensive field campaigns have been summarised in this chapter.

All pollutant mixing ratios were higher during the winter campaign than the summer campaign, with the exception of O_3. The high mixing ratios observed were attributed to enhanced emissions, weaker vertical mixing and, at times, stagnant conditions. The impacts of meteorology were clearly observed during the winter with periods of high and low mixing ratios linked to distinctive weather patterns as a result of the East Asian Monsoon. Good correlation between CO and SO_2 for the two campaigns hinted at a common industrial source that is transported to Beijing with strong correlations between NO_x and CO during winter highlighting the dominance of traffic emissions on measured pollutants. Understanding and quantifying emissions is important to effectively implement pollution control strategies and the emissions of Beijing will be explored in Chapter 4.

During the summer campaign, O_3 mixing ratios were high enough to be considered hazardous to health with half of the days during the campaign breaching the 8 hourly limit set by the WHO, highlighting an urgent need to understand the relationship between O_3 and its precursor emissions. High OPE values were calculated during the summer showing that Beijing is a photochemically active environment. This mean OPE value calculated for winter and summer (1.1 ppb ppb^{-1} $\pm$ 3.5 ppb ppb^{-1} and 4.0 ppb ppb^{-1} $\pm$ 5.7 ppb ppb^{-1} respectively) suggests that O_3 formation is VOC limited for the city, which is in line with previous studies. Future air quality measurement strategies should target VOC species to reduce O_3 pollution.

NO mixing ratios were low during the afternoon for the summer campaign due to titration with O_3 and regularly fell below 500 pptv. This had profound impacts on

atmospheric chemistry and highlights the importance of making NO measurements. NO_2 measurements are the only NO_x measurements required for public health monitoring, but this does not show the whole picture. The low NO mixing ratios observed lead to peroxy radical reactions becoming more favourable and are linked to deviations from the photostationary state. Deviations from the photostationary state are driven by photochemistry and possibly indicate the presence of an unknown oxidant in Beijing.

Measurements of traffic dominated pollutant emissions in a Chinese megacity

4

4.1 Introduction

RAPID development and population growth has led to an ever increasing number of "megacities", defined by the United Nations (UN) as a "metropolitan area with a total population of more than 10 million people" [United Nations' Department Of Economic and Social Affairs: Population Division, 2016]. In addition to being home to a large population, megacities are typically associated with high levels of industrialisation and extensive transportation networks making air pollution a common problem. Beijing is one such city that regularly experiences significant air quality problems. High levels of particulate matter (PM) in Beijing during winter months have been widely reported. In 2017, annual $PM_{2.5}$ (PM with a diameter less than 2.5 μm) concentrations reached 58 μg m^{-3}, approximately six times greater than the World Health Organisation (WHO) guideline [Ministry of Ecology and Environment, the People's Republic of China, 2018]. During the summer, concentrations of ozone, O_3, a major component of photochemical smog, regularly exceeded the WHO 8-hour mean limit of 100 μg m^{-3} in Beijing. Both PM and O_3 have detrimental impacts on public health and both are formed in the atmosphere from reactions by precursor emissions that include nitrogen oxides (NO_x), carbon monoxide (CO) and volatile

organic compounds (VOCs). Secondary aerosols have been shown to comprise a large fraction of fine particulate matter in Beijing [Guo et al., 2014, Duan et al., 2020].

China is the largest NO_x emitter globally and is estimated to contribute as much as 18% to global NO_x emissions [European Database For Global Atmospheric Research, 2000–2012] while Beijing itself is reported to have annual mean NO_2 concentrations 16 μg m^{-3} higher than the national average [Ministry of Ecology and Environment, the People's Republic of China, 2018]. At high concentrations, NO_2 is a respiratory irritant [Strand et al., 1998, Tunnicliffe et al., 1994]. CO is a harmful air pollutant produced from incomplete combustion processes including those used in power generation and from vehicle engines. Liu et al. [2018] concluded that there is an association between short-term exposure to ambient CO and increased cardiovascular disease mortality, especially coronary heart disease mortality. For both these pollutants, traffic emissions tend to be the dominant source in megacities.

In order to manage air quality it is vital that legislators have a clear understanding of pollutant emissions to guide abatement strategies. Models of atmospheric chemistry provide an important mechanism to predict the efficacy of abatement measures on future air quality yet these predictions are only as certain as the emission inventories upon which they are based. For example, previous studies have highlighted large discrepancies between emissions inventories and measured emissions for UK cities both for NO_x [Lee et al., 2015, Vaughan et al., 2016] and VOCs [Langford et al., 2010, Valach et al., 2015]. In addition to discrepancies in magnitude, the sources of emissions are not always correctly identified in inventories. Karl et al. [2018] indicates via emission measurements that a large, unidentified source of oxygenated VOCs is not represented in emissions inventories and that actual non-methane VOC (NMVOC) emissions could be significantly higher than those used in most models. As new emissions controls are introduced and emissions technologies improve the main sources of pollutant emissions will change. McDonald et al. [2018] showed that an increasing proportion of the VOC emission budget is from volatile chemical products containing organic solvents (e.g. pesticides, cleaning agents and personal care products) as the transportation sector becomes cleaner. Inventories in China are associated with large uncertainties and are rapidly changing in response to economic development and new environmental regulations. Saikawa et al. [2017] reviewed and compared five dif-

ferent emissions inventories for China and found large disagreements between them. Thus there is a critical need for reliable field measurements in order to further improve the emission estimates and reduce the uncertainty of inventories at local and regional scales [Zhao et al., 2017].

Given this pressing need for measurements of pollutant emissions, fluxes of NO_x, CO and commonly co-emitted VOCs (benzene, toluene, C_2-benzenes and C_3-benzenes) were calculated using the eddy-covariance (EC) technique for an urban area in Beijing. To the knowledge of the authors, this is the first time these emissions have been directly quantified in Beijing. This work was carried out as part of the Air Pollution and Human Health-Beijing (APHH) project and an overview of this campaign can be found in Shi et al. [2019].

4.2 Methodology

A more detailed description of the measurement location and the techniques used to measure NO_x and CO concentration is described in detail Chapter 2.

4.2.1 Site description

Measurements were taken from an inlet part-way up a 325 m meteorological tower at the Institute of Atmospheric Physics (IAP), Chinese Academy of Sciences (39°58'28"N, 116°22'16"E) in central Beijing. The site is between the third and fourth ring roads and surrounding land use can be characterised as urban, being mainly residential with some busy (two and three lane dual-carriageway) roads nearby. The Jingzang Highway is approximately 400 m east of the site. Building heights surrounding the tower are predominantly 15–30 m in height, but with some almost 100 m tall within 500 m to the south of the tower. The site is in a 'green' area with some park space and a canal close by. Measurements were made over two field campaigns; the winter campaign from 05 November 2016 – 11 December 2016 and the summer campaign from 22 May 2017 – 25 June 2017 to allow a seasonal comparison of emissions.

Instrumentation was housed in a temporary shipping container laboratory located at the base of the tower. Sample lines from an inlet platform at an elevation of 102 m ran down the tower to the laboratory. Air for sampling was drawn down a $\frac{1}{2}$" O.D. (I.D.

9 mm) perfluoroalkoxy (PFA) tube at a rate of approximately 95 L min^{-1} resulting in an inlet pressure of 44 kPa. This ensured turbulent flow was maintained (Reynolds Number $\approx$ 7000) and attenuation of signals along the $\sim$ 120 m sample line were minimised. Particles were removed from the airflow via a 90 mm Teflon filter mounted near the inlet which was changed at 24 hour intervals. The inlet of the tube comprised of a custom built, 32 mm diameter, stainless steel manifold cap with gauze to prevent larger debris entering the tube. The manifold was mounted 82 cm vertically below a sonic anemometer (Model HS-50, Gill Instruments) which measured the three wind components, *u*, *v* and *w* data at a rate of 10 Hz. During the winter campaign it was orientated NW from the tower and during the summer campaign towards the SE to measure the main wind direction without obstructions. However, analysis of the turbulence characteristics did not suggest that the open structure of the tower affected the measurements even when the flow came through the tower. This may be due to the size of the eddy-motions at this measurement height.

4.2.2 Instrumental description

NO_x sampling and measurement

Concentrations of NO_x were measured using a dual-channel chemiluminescence instrument (Air Quality Designs Inc., Colorado). The instrument is similar to that described in Lee et al. [2009], but modified to enable high time resolution data to be collected with a residence time of 0.12 s inside the photolytic conversion cell. NO was measured directly by chemiluminescence from the reaction of NO and O_3 in one channel. The second channel measures total NO_x via photolytic conversion of NO_2 to NO, at a wavelength of 395 nm, and then by chemiluminescence reaction with O_3, as per the direct measurement of NO. Instrument data were recorded at a frequency of 5 Hz.

The NO_x instrument was calibrated regularly (every 2–3 days) throughout the campaign using NO gas standards traceable to the UK National Physical Laboratory (NPL) NO scale. The instrument was calibrated via standard addition of a small flow of NO calibration gas to a flow of NO_x-free ambient air (NO_x was removed using a Sofnofil/charcoal trap). The sensitivities of the NO and NO_x channels were calcu-

lated by direct addition of the diluted NO calibration gas. The NO_2-NO conversion efficiency within the NO_x channel was calculated by gas-phase titration of the diluted NO calibration gas with O_3 to create a known quantity of NO_2. During the calibration cycle, an instrument zero was quantified by diversion of sample flow to 'zero volumes' so that the chemiluminescence reaction was completed before the gas reached the detectors. Zero measurements were scheduled to occur for 15 seconds every hour through the normal operating schedule.

CO sampling and measurement

CO was measured using a resonance fluorescent instrument (Model AL5002, Aerolaser GmbH, Germany). Flows were adjusted to reduce cell lag times so data could be recorded at 5 Hz to match the NO_x data acquisition rate. Details of the unmodified system are described by Gerbig et al. [1996, 1999]. The CO instrument was calibrated regularly (every 2–3 days) throughout the campaign as for the NO_x instrument using a 1 ppm CO in synthetic air standard. Previous urban flux measurements with this type of instrumentation have been presented for UK cities by Famulari et al. [2010], Harrison et al. [2012], Helfter et al. [2016].

4.2.3 VOC sampling and measurement

VOCs were measured using a Proton Transfer Reaction Time-of-Flight Mass Spectrometer (PTR-ToF-MS). The PTR-ToF-MS (PTR-MS 2000, Ionicon Analytik, Innsbruck, Austria) was installed at the base of the tower and sampled from the common inlet line at 30 sccm. The instrument was operated with a 5 Hz measurement frequency. The drift tube maintained at 60 °C, with a pressure of 1.9 mbar and 490 V applied across it. This gave an E/N (the ratio between electric field strength and buffer gas density) of 120 Td in the drift tube. This set up is described in more detail by Acton et al. [2020].

The PTR-ToF-MS was calibrated twice a week during both the winter and summer campaigns using a VOC standard containing methanol, acetonitrile, ethanol, 1,3-butadiene, acetone, isoprene, butenone, butan-2-one, benzene, toluene, m-xylene and 1,2,4-trimethylbenzene at 1 ppmv (NPL, Teddington, UK). The standard was dynamically diluted in zero air to provide a six point calibration. In the winter campaign the in-

strument was also calibrated using two Ionicon standards the first containing methanol, acetonitrile, acetaldehyde, ethanol, acrolein, acetone, isoprene, crotonaldehyde, butan-2-one, benzene, toluene, o-xylene, chlorobenzene, α-pinene and 1,2-dichlorobenzene at 1 ppmv each and the second made up of formaldehyde, acetaldehyde, acrolein, propanal, crotonaldehyde, butanal, pentanal, hexanal, heptanal and octanal at 1 ppmv, nonanal at 600 ppbv and decanal at 500 ppbv. The background signal was corrected for by sampling a zero air standard for 5 minutes every hour. Background mixing ratios were subtracted from subtracted from measurement data to give corrected mixing ratios. PTR-ToF-MS data was processed using PTRViewer (Ionicon Analytik).

4.2.4 Data processing

Prior to the calculation of pollutant fluxes, the raw data were scaled to take account of calibrations. The sensitivity within each channel of the NO_x chemiluminescence instrument remained consistent throughout the winter and summer campaigns so data were scaled using median sensitivity values. The conversion efficiency of the NO_x channel gradually deteriorated over the two campaigns and so NO_2 data were scaled using linearly interpolated conversion efficiency values. As highlighted in Fig. 4.1, the NO_2 calibration was applied in two stages, the first during pre-processing and the second following lag correction. During the pre-processing stage the channel sensitivities (counts $pptv^{-1}$) determined by field calibration are applied to both the NO and NO_x channels to give NO (pptv) and a term referred to as converted NO_x channel counts 'NO_c'. NO_2 is then calculated from the difference between the time-lagged corrected NO_c and NO divided by conversion efficiency. The time lag correction is described below. For CO concentration data, the instrument sensitivity following each calibration was directly applied and the sensitivity remained consistent for the duration of the two campaigns.

Concentration data were coupled with wind data reported by the sonic anemometer by sub-sampling the wind data to match the 5 Hz concentration data. Data were then despiked prior to flux calculation as per the method described in Brock [1986] and Starkenburg et al. [2016]. Following despiking, the lag time between vertical wind velocity measured in-situ on the tower and the pollutant concentrations, measured on the ground, was calculated. The lag time correction was determined by maximisation

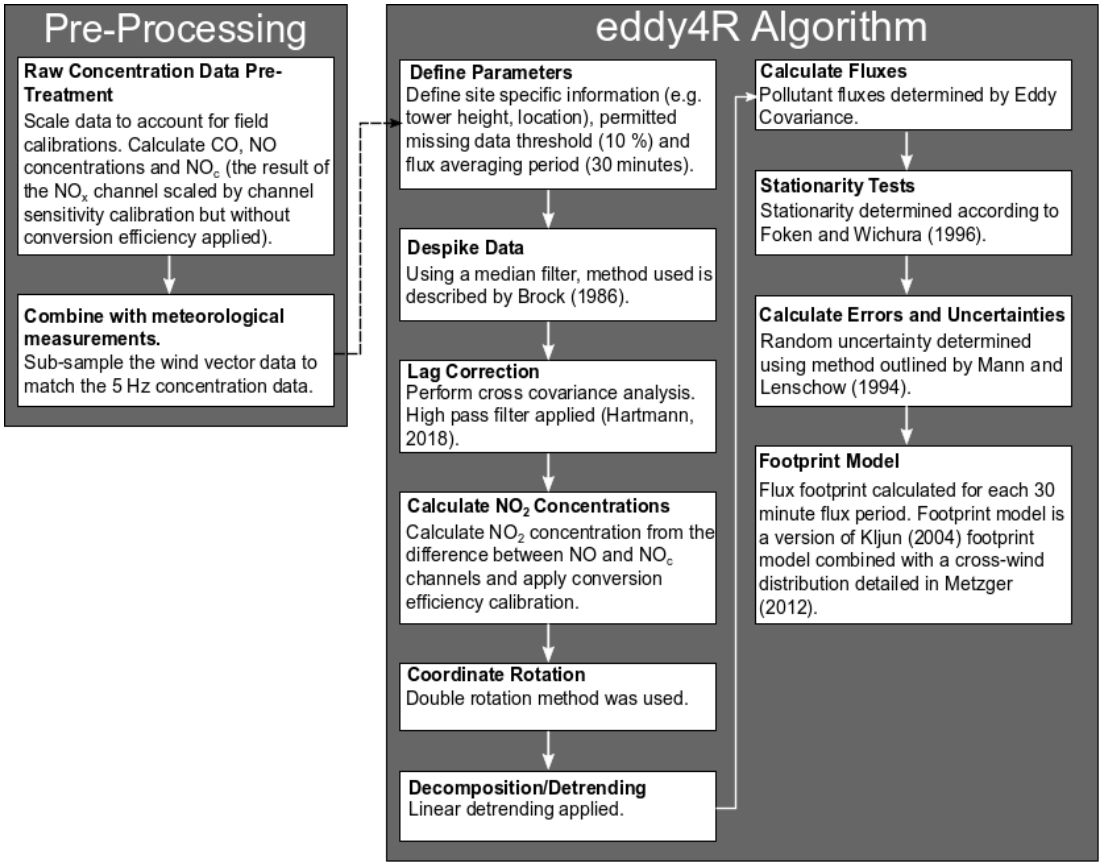

Figure 4.1: Workflow schematic summarising the data processing steps required for calculation of NO_x and CO fluxes.

of the cross-covariance between pollutant concentration and the vertical wind component. When determining the lag time for each species a high-pass filter [Hartmann et al., 2018] was used which improves the precision of the determined lag time by an order of magnitude. The median lag time was then calculated for each species during each campaign. The lag time between the concentration and vertical wind speed during the winter campaign was found to be 9.6 s $\pm$ 0.4 s, 10.0 s $\pm$ 0.4 s, 10.2 s $\pm$ 0.3 s for NO, NO_2 and CO respectively. For the summer campaign lag times were calculated as 9.4 s $\pm$ 0.4 s, 9.8 s $\pm$ 0.3 s and 10.6 s $\pm$ 0.5 s. Because there was no discernible pattern or trend in the lag times and to prevent the flux bias that cross-covariance maximisation can introduce when fluxes are small [Langford et al., 2015], the final fluxes were calculated by applying the median lag time value for each campaign to all flux

periods. Lag time correction was performed using the same method for the PTR-ToF-MS VOC concentrations. Lag times were calculated for isoprene (summer data) and benzene (winter data) within a 5–15 s window and these values were then applied to all compounds. Where the lag time was found to be outside of the 5–15 s range a standard lag time of 9 s was applied.

4.2.5 Flux calculations

The flux, F, of each species, which can be defined as the vertical transport of a pollutant per unit area per unit time, was then calculated using the EC method [Lee et al., 2004]:

$$F \approx \overline{w'c'} \tag{4.1}$$

where w' is instantaneous change in vertical wind speed (i.e. $w' = w - \bar{w}$, where overbars denote averages) and c' is instantaneous change in pollutant concentration. The flux was calculated over a 30 minute averaging period and quantified using the eddy4R family of R-packages [Metzger et al., 2017] with a customized EC workflow template to suit the requirements of this study. Figure 4.1 shows the key steps involved in the calculation of pollutant fluxes. Random uncertainty was calculated using the method outlined by Mann and Lenschow [1994]. The flux limit of detection was taken to be twice the random error. It should be noted that, due to the high measurement height, 30 minute fluxes might be an underestimation of the 'true' flux as the averaging period may not capture low frequency contributions. To quantify the effect, a comparison between 30 minute, 60 minute and 120 minute averaging intervals was carried out for a week-long period of the summer campaign which indicated 30 minute fluxes were 93% of the 60 minute fluxes whilst 120 minutes fluxes were considered too long an averaging periods for sufficient temporal resolution. Additionally increasing the length of averaging time introduces more non-stationary periods into the data. The 30 minute flux is therefore a compromise between capturing the entirety of the flux by keeping the low frequency flux loss small (7%) and having sufficient temporal resolution to relate the measurements to real-world processes. Fluctuations in temperature and humidity can impact fluxes by causing variation in air density [Webb et al., 1980]. For closed path systems, such as those used in this study, air density variations caused by sensible-heat flux are negligible however variations due to latent heat flux may need

to be corrected for. For CO fluxes, samples were passed through a dryer negating the need for this correction, however latent heat flux could have an impact on the NO_x fluxes [Moravek et al., 2019]. The magnitude of the correction is proportional to the concentration/flux ratio which for reactive species, like NO_x, is small. The effect of latent heat flux on NO_x fluxes was found to be significantly less than 1% throughout the campaigns and so the WPL correction was not applied [Pattey et al., 1992]. The effect of high-frequency spectral loss on NO_x and CO fluxes was investigated using a wavelet-based methodology [Nordbo and Katul, 2013]. Spectral losses were found to be less than 3% and so were not corrected for.

Corrections and filtering

There are numerous assumptions made when calculating EC fluxes, all of which can introduce uncertainties in the derived quantity. Further conditions need to be met for the measured flux to be representative of surface flux. Assumptions include but are not limited to, the flux being fully turbulent with all transport done by eddy transfer, the terrain being homogeneous, measurements being made within the boundary layer, air density fluctuations being negligible and conditions remaining stationary. A common method to deal with periods of low turbulence, during which the flux at the measurement height may not reflect the surface flux, is to filter the data based on a friction velocity (u_*) threshold. Friction velocity accounts for shear stress in the turbulent boundary layer, and can be calculated from the instantaneous wind components u', v' and w' [Foken, 2017]. Concepts for u_* filtering were originally developed by the community measuring CO_2 exchange with vegetation. Here, incorrect application of u_* filtering can lead to a "double-counting" of flux as described in Aubinet [2008]. In addition, by filtering out low-turbulence cases (low u_* values) the data set can become biased with little information about nighttime and winter periods. Whilst for CO_2 exchange with vegetation fairly robust parametrisations exist that can be used to gap-fill periods of low turbulence, no such information is yet available for urban fluxes. Liu et al. [2012] therefore argue against applying u_* filtering for the IAP site during a similar analysis of CO_2 fluxes, and suggest more errors could be introduced through filtering than not. Thus u_* filtering was also not applied to the data presented here, unless otherwise stated. Approximately 29% of winter fluxes and 11% of summer fluxes

were associated with u_* values below 0.175 m s^{-1}. Average fluxes as a function of u_* values are presented in Fig. 4.2 and the effect of u_* filtering on diurnal variation is shown in Fig. 4.3. These show the maximum possible effect of low turbulence on fluxes. Because low turbulence is correlated with nighttime conditions during which emission activity is reduced, an increasingly stringent u_* filter preferentially removes periods during which the surface flux is smaller than the average. This may result in an increase in the average nighttime flux that does not necessarily reflect suppression of the flux by lack of turbulence.

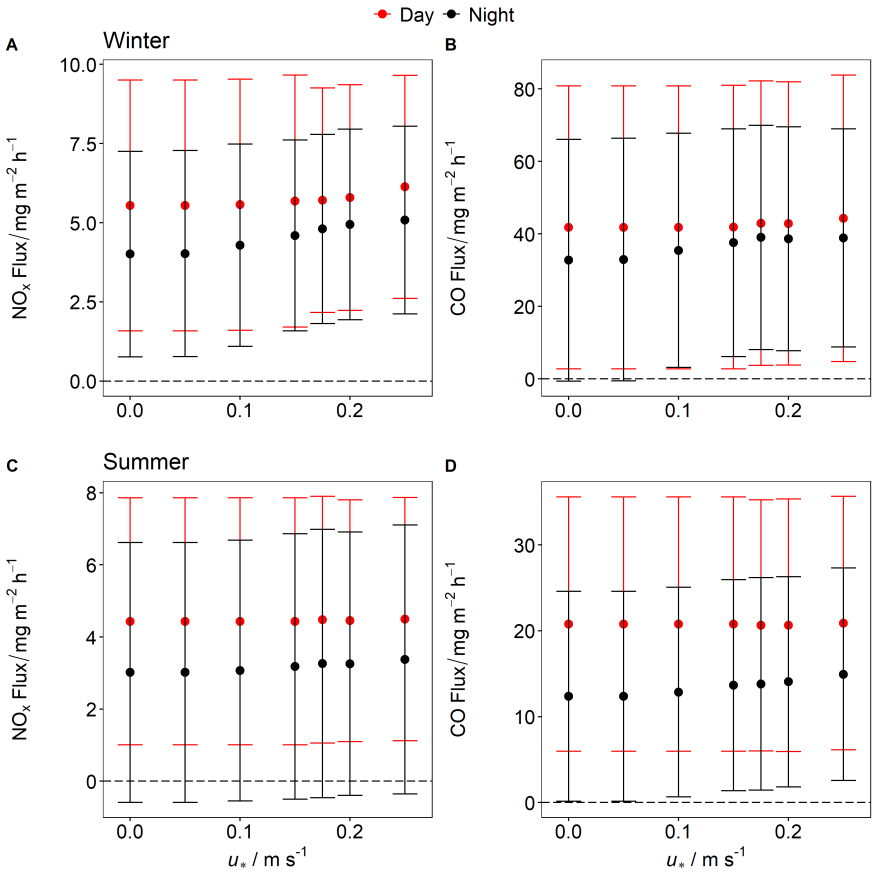

Figure 4.2: Mean NO_x and CO fluxes as a function of different u_* thresholds. Error bars show $\pm$ 1 standard deviation.

Stationarity is another important consideration for flux data. Stationarity is when the flux is statistically invariant over the averaging period and is quantified using the

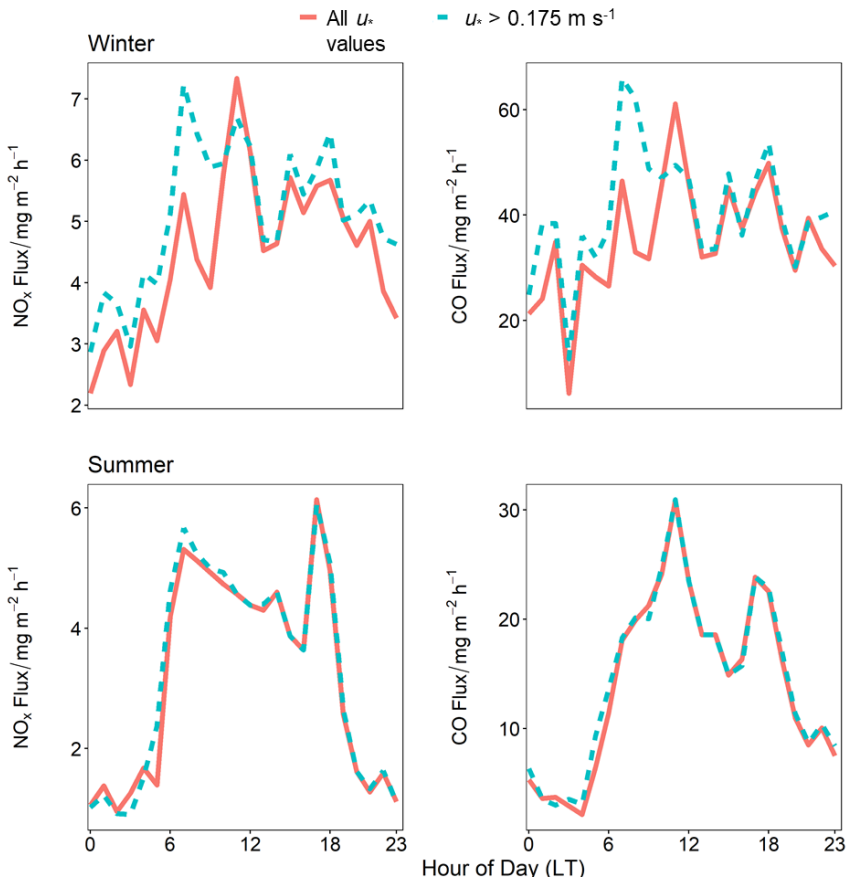

Figure 4.3: Comparison between diurnal variation in NO_x and CO fluxes for all u_* values and for u_* values over 0.175.

method described in Foken and Wichura [1996]. The stationarity criterion is likely not to be met when fluxes are small and subject to a large random uncertainty; this is irrespective of whether the conditions are actually non-stationary. As a result this filter tends to remove the smallest fluxes and can bias flux results [e.g. Nemitz et al., 2018]. A broad stationarity filter of 60% was applied to all flux data presented in any average diurnals, though non-stationary data is presented and highlighted in time series plots. This stationarity filter was used as a more rigorous filter of 30%, commonly used within the CO_2 flux community, removed a large proportion of the data. During the winter campaign 23% of NO_x fluxes and 22% of CO fluxes were non-stationary under this more rigorous criterion. During the summer campaign these proportions were

16% of NO_x fluxes and 39% of CO fluxes. The 60% threshold used was determined to be appropriate as it falls within the stationarity range recommended for "general use", such as using diurnal averages to interpret trends [Foken et al., 2004]. Further to these corrections, any periods where the boundary layer was within 30 m above the measurement height were removed from the data. Boundary layer height was measured throughout both campaigns using a celiometer (Vaisala CL31). The data are analysed using the CABAM algorithm [Kotthaus and Grimmond, 2018].

It was also important to consider storage effects; due to the build-up or dilution of the pollutants below the measurement height. Build-up can occur during periods of low turbulence e.g. during the night and this accumulation reduces the flux at the measurement height with respect to the emission at the ground [Finnigan, 2006]. As conditions become more turbulent the accumulated pollutant concentration gets diluted again and the measured flux contains a component that originates from the stored material rather than emission. Gas concentration profile measurements can be used to allow detection of build-ups by providing data for computing a storage term below measurement height, z_m. In this case, the storage flux, F_s, at time, t, was calculated according to the following equation, where C is concentration and T is flux averaging interval [Andreae and Schimel, 1990]:

$$F_s(t) = \frac{C(t+\frac{T}{2}) - C(t-\frac{T}{2})}{T} \times z_m \tag{4.2}$$

The validity of calculating the storage flux at a single measurement height was evaluated by comparing CO_2 concentration measurements made at the measurement height and CO_2 concentration profile measurements made at three different heights on the tower. By comparing the evolution of the CO_2 concentration at the single measurement height with the CO_2 profile measurements, it was determined that calculating storage flux using the single concentration at the measurement height was a reasonable approximation of the storage within the column. It should be noted that this storage correction to some extent takes care of the flux suppression at low turbulence, except for the interaction with advection and chemistry.

Throughout, this chapter focuses on the analysis of total NO_x flux rather than NO and NO_2 flux separately. Whilst the two compounds undergo rapid interconversion the total should be conserved at the time-scale that governs the transport from the surface to the measurement height; the major loss route for NO_x is HNO_3 formation

through reaction with the hydroxyl (OH) radical. This loss is assumed to be negligible between ground emission and sampling at the tower inlet. Calculation of Deardorff velocity suggests that on average the time taken for a parcel of air to reach the 102 m measurement point is ~ 68 s [Deardorff, 1970]. Assuming average OH concentrations of 1×10^6 molecule cm^{-3} it is estimated that less than 1% reacts with OH at this timescale.

4.2.6 Footprint model

A flux footprint is the area surrounding the measurement tower that contributes to a measured flux based on factors such as wind speed, wind direction, atmospheric stability and surface roughness. A statistical flux footprint model can be used to quantify the flux contribution of each cell of an emission grid relative to the distance away from the measurement position in all directions, creating a weighing matrix that estimates the ground influence of a particular cell contributing to the observed emission flux. A footprint was calculated for each half hour flux period at 100 m resolution. The footprint model used is based on Kljun et al. [2004] with a cross-wind distribution detailed in Metzger et al. [2012]. Surface roughness values were taken from Liu et al. [2012] and taken to be 2.5 m, 3.0 m, 5.3 m and 2.8 m for the NE, SE, SW, and NW wind quadrants respectively. Figure 4.4 shows the average footprint for the winter and summer campaigns with the 30%, 60% and 90% cumulative contributions to the measured flux represented by the contours.

For both campaigns the 90% contribution to the measured flux extended as far as 7 km from the measurement site for some averaging periods, however, as shown in Fig. 4.4 on average 90% of the contribution to measured emissions was from within 2 km of the tower. Figure 4.4 shows the difference in areas of influence covered during the winter and summer campaigns due to differences in dominant wind directions. During the winter, the measured fluxes were predominantly from the north-west encompassing Beitucheng West Road and a block of predominantly commercial buildings and restaurants. The mean footprint maxima, the distance away from the tower at which the maximum contribution to the measured flux occurs, falls 0.26 km away from the tower in winter. In summer, the fluxes were mostly influenced by areas to the north east and east of the tower, encompassing the Jingzang Expressway. The mean footprint

maxima for summer was also 0.26 km away from the site.

Figure 4.4: The mean flux footprints for the winter and summer campaigns. The site is shown by the red triangle in the centre of the map. Each square is 100 m^2 and the brighter colours indicate a greater influence on measured emission for a particular area. The white rings show the areas contributing 30%, 60% and 90% to the flux total with inner ring representing the 30% contribution and outer ring representing 90% contribution. The 90% of the influence from the footprint extends up to 2 km away from the tower with maximum contribution 0.26 km away from the tower. Map was built using data from © OpenStreetMap contributors 2019. Distributed under a Creative Commons BY-SA License.

4.2.7 Inventory

The measured pollutant fluxes were compared with the Multi-resolution Emissions Inventory for China (MEIC, Qi et al. [2017], `http://www.meicmodel.org/`, last access: 19 May 2020) to evaluate how well the inventory describes the diurnal evolution of pollutants and their absolute magnitude. MEIC emissions are available at 0.25×0.25 degree resolution and were downscaled to 3×3 km resolution on a sector by sector basis following the approach of Zheng et al. [2017]. MEIC considers five emission source sectors; power plants, industry, transport, residential, and agricultural.

Agricultural emissions are not relevant within our flux footprint so were not included in this work. Emissions are available on a monthly basis, and are assumed to be the same each day of the month, and a diurnal cycle appropriate to Chinese sources is applied to each emission sector. Example emissions for Beijing are presented in Fig. 4.5 for November. The NO_x and CO emission predicted by the inventory are calculated from the multiplication of each footprint matrix by the MEIC grid. In order to match the scales of the footprint matrix and the inventory, a pseudo 100 m $\times$ 100 m MEIC grid was created by splitting the 3 km resolution inventory into smaller 100 m $\times$ 100 m grid squares, each with the same emission value.

Figure 4.5: MEIC inventory emission grids for NO_x and CO for November. Map was built using data from © OpenStreetMap contributors 2019. Distributed under a Creative Commons BY-SA License.

4.3 Results & discussion

Statistics for NO_x and CO fluxes and concentrations presented in this work are shown in Table 4.1. Figure 4.6 shows a time series of measured NO_x and CO fluxes during the winter and summer measurement campaigns where dark coloured traces highlight data which does not meet the 60% stationarity criteria. For winter, 3.5% of NO_x fluxes and 8.2% of CO fluxes were non-stationary. In summer, slightly fewer measurements did not meet the stationarity criteria with 3.1% of NO_x fluxes and 7.3% of CO fluxes falling

Table 4.1: Summary table for NO_x and CO fluxes and concentrations. Data presented is for fluxes which are within 60% stationarity criteria for all u_* values.

	Winter		**Summer**	
Concentration (mg m^{-3})	**NO_x**	**CO**	**NO_x**	**CO**
Mean	0.103	1.41	0.0310	0.502
Median	0.0839	1.01	0.0213	0.429
Percentiles				
5th	0.0154	0.268	0.00810	0.210
95th	0.252	3.60	0.0876	0.998
Standard Deviation	0.0776	1.16	0.0278	0.267
Flux (mg m^{-2} h^{-1})				
Mean	4.41	34.7	3.55	15.2
Median	4.14	32.0	2.45	12.4
Percentiles				
5th	-1.24	-27.0	-0.0139	-2.15
95th	10.6	103	11.5	42.9
Standard Deviation	3.86	40.1	3.69	14.4

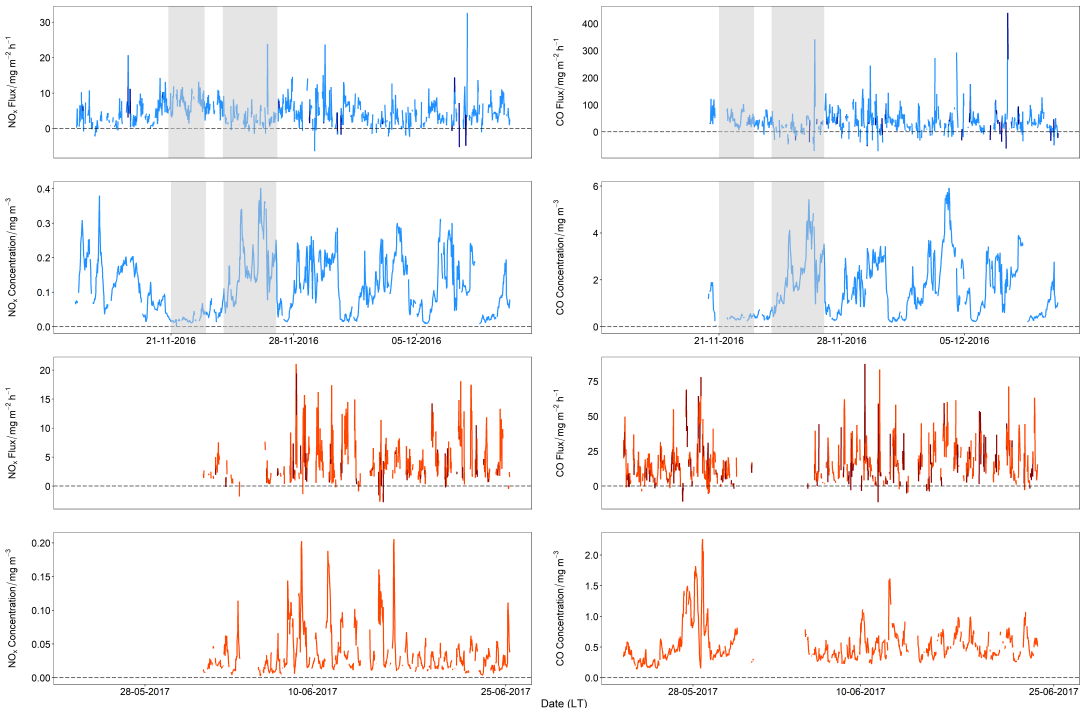

Figure 4.6: Time series data for 30 minute averaged NO_x and CO fluxes for the winter (blue trace) and summer (orange trace) campaigns with fluxes outside of the 60% stationarity criteria shown in darker colours. Gaps in the time series are due to instrument problems. The two contrasting periods discussed in section 4.3.2 are highlighted in grey.

outside the 60% stationarity limits. The mean flux for NO_x during the winter measurement period was 4.4 mg m^{-2} h^{-1}±3.9 mg m^{-2} h^{-1} and 3.6 mg m^{-2} h^{-1} ±3.7 mg m^{-2} h^{-1} for the summer measurement period. For CO, there was a larger difference between the two seasons with the mean flux calculated as 35 mg m^{-2} h^{-1} ±40 mg m^{-2} h^{-1} for winter and 15 mg m^{-2} h^{-1} ±14 mg m^{-2} h^{-1} in summer. Some of the calculated fluxes were negative, corresponding to deposition to the surface, however, as expected in an urban environment, the net flux was strongly positive indicating emission. The average NO_x fluxes for the winter and summer periods were similar suggesting an emission source that did not change much between seasons. In contrast the average CO flux was over double in the winter compared to the summer indicating an additional source in the winter.

When considering previous literature, the NO_x fluxes measured in Beijing were low compared to London, UK where net emissions were in the range of 10.8 mg m^{-2} h^{-1}–14.4 mg m^{-2} h^{-1} [Lee et al., 2015]. A study investigating NO_x fluxes across 13 urban locations in Norfolk, Virginia reported values in the range of 18–28 mg m^{-2} h^{-1}, up to 8 times higher than those measured in Beijing [Marr et al., 2013]. Fluxes measured in Beijing were similar to those measured in Innsbruck at a roadside site in July–October, 2015 where NO_x fluxes of 2.5–5.2 mg m^{-2} h^{-1} were reported [Karl et al., 2017]. For CO, measured fluxes in central London were 2–3 times lower than those measured in Beijing. Average winter (December–February) CO flux was reported to be 12.5 mg m^{-2} h^{-1} ±3.4 mg m^{-2} h^{-1} and average summer (June–July) CO flux was reported to be 4.0 mg m^{-2} h^{-1} ±0.1 mg m^{-2} h^{-1}, for the measurement period September 2011 – December 2014 [Helfter et al., 2016]. NO_x emissions are likely to be lower in Beijing than for other cities as the majority of road vehicles in Beijing are light-duty gasoline vehicles (LDGVs) which made up to 93% of the vehicle fleet in Beijing in 2013 [Yang et al., 2015] compared to other cities which have a higher proportion of diesel vehicles. However, because fluxes vary spatially within each city, care needs to be taken when comparing measurement datasets as the type of the location within the city needs to be considered.

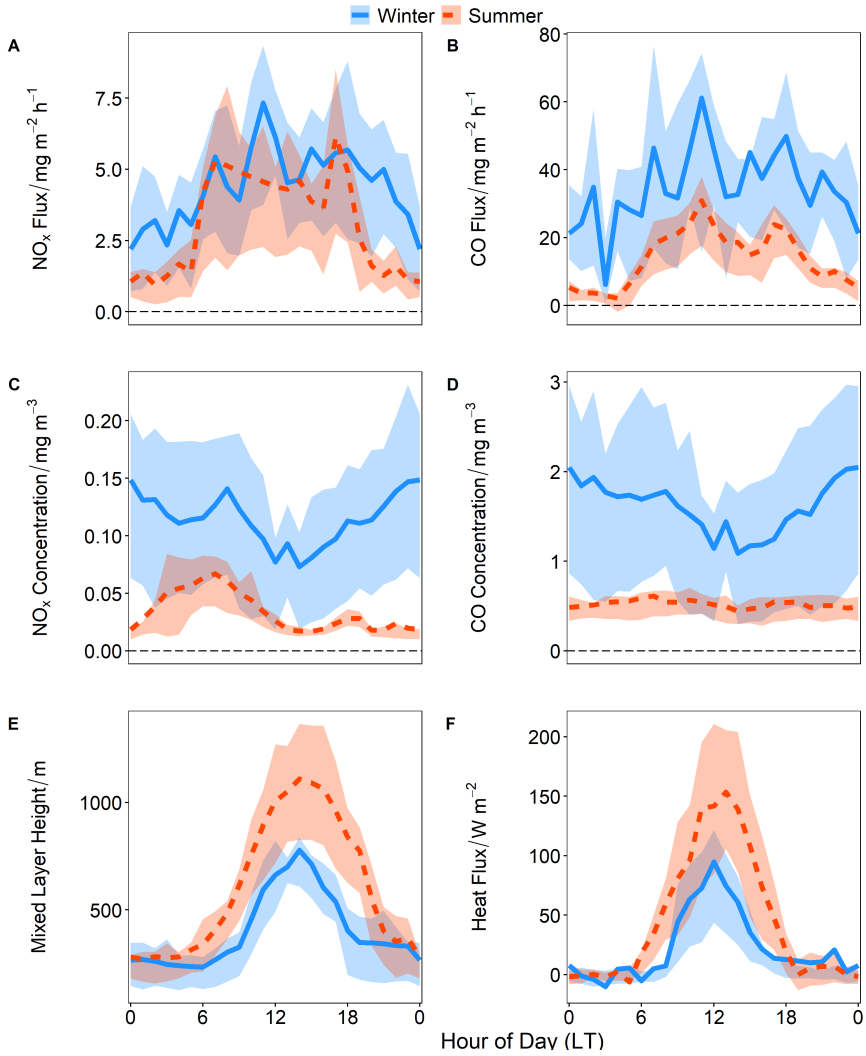

Figure 4.7: Average diurnal profiles for A) NO_x flux, B) CO flux, C) NO_x concentration, D) CO concentration and E) mixed layer height and F) heat flux. Blue, solid lines are for measurements taken during the winter campaign and the orange, dashed lines are measurements taken during the summer campaign. The shaded areas represent the 25^{th} and 75^{th} percentiles. For the NO_x and CO fluxes, only stationary data has been used but no u_* filtering has been applied when doing the diurnal averaging, as described in section 4.2.5.

4.3.1 Average diurnal cycles

Figure 4.7 shows the mean diurnal profile for both campaigns for pollutant fluxes, concentrations and mixed layer height. Diurnal profiles are a useful way to visualise flux data, as time of day may indicate processes responsible for emissions. During the winter campaign, the NO_x fluxes were lower during the early hours of the morning (between 00:00–05:00) ranging between 1.9 mg m^{-2} h^{-1} and 3.6 mg m^{-2} h^{-1}. After 06:00, the NO_x fluxes increased and remained elevated, though variable, throughout the day with a mean daytime value (06:00–18:00) of 5.1 mg m^{-2} h^{-1}. The NO_x fluxes decreased again in the evening. The daily variability in CO fluxes followed a similar pattern to NO_x. The mean daytime CO flux was 38 mg m^{-2} h^{-1}, and was lower during the night (19:00–05:00) with a mean nighttime value of 29 mg m^{-2} h^{-1}. Concentrations are influenced by meteorology and long range transport as well as local emissions (in this study local emissions refer to emissions from within the flux footprint). NO_x and CO concentrations remained constant during the night due to stability in the mixed layer height. When NO_x and CO emissions increased after 05:00, this enhancement in flux was reflected in the concentration data with a small peak in NO_x and CO concentrations around 06:00, though the effect is masked as the mixed layer height begins to increase. Concentrations decreased to their minima at 15:00 when the mixed layer height reached its highest point and increase again when the mixed layer height contracted over night.

Fluxes were lower during the summer campaign than during the winter. The mean nighttime flux was less than 1.6 mg m^{-2} h^{-1} for NO_x and 6.5 mg m^{-2} h^{-1} for CO. Emissions rapidly increased after 05:00 and started to decrease at around 17:00. Daytime emissions for NO_x were fairly consistent with a mean value of 4.6 mg m^{-2} h^{-1}. The first of two distinct peaks in the observed NO_x fluxes occurred at 07:00, where emissions reached 5.4 mg m^{-2} h^{-1} and the second occurred at 17:00 with a slightly higher value of 6.3 mg m^{-2} h^{-1}. The daytime profile for CO showed two distinct peaks in emissions; the first peak occurred at 11:00 with CO emissions around 30 mg m^{-2} h^{-1} and the second at 17:00, when CO fluxes were around 24 mg m^{-2} h^{-1}. Between these times the CO emissions dipped with a minimum daytime value of 16 mg m^{-2} h^{-1} at 14:00–15:00. The influence of local emissions on concentration is more clearly observed during the summer campaign; the peaks in NO_x and CO fluxes at 17:00 occurred at the same time

as an enhancement in NO_x and CO concentration. Both NO_x and CO concentrations reached their daytime minima at 14:00–15:00 when the mixed layer height was at its peak.

Given that the NO_x emissions were fairly consistent between the two seasons it is likely that the major sources of NO_x do not vary significantly over the year. In urban areas, vehicular emissions tend to be a dominant source of NO_x [Parrish et al., 2009, von Schneidemesser et al., 2010, Borbon et al., 2013] and previous studies measuring NO_x fluxes have attributed emissions to vehicles [Lee et al., 2015, Vaughan et al., 2016]. Diurnal variation in summer NO_x emissions agree well with previously reported diurnal variation in Beijing's traffic flow. Jing et al. [2016] showed that traffic flow (vehicle number per hour) begins to increase from 05:00 in the morning, corresponding to the observed increase in NO_x emissions. As would be expected, peak traffic flow coincided with lowest average vehicle speeds and occurred at 08:00 and 18:00. NO_x emissions are dependent on fuel type, engine type, combustion temperature, vehicle speed, engine load and exhaust after-treatment technology. It is known that "stop - start" driving conditions and idling can enhance NO_x emissions compared to driving at steady speeds and observations indicated that there are peaks in NO_x emissions during these rush hour periods. Beijing has attempted to reduce emissions through traffic management as well as by imposing emissions reduction regulations; for example yellow label vehicles, vehicles which do not meet the China I emissions standard have been forbidden from entering Beijing since 2014 [Yang et al., 2015]. One management strategy imposed restrictions on heavy duty vehicles (HDVs) entering the city (past the sixth ring road) and only permits non-local vehicles to enter between 00:00–06:00. HDVs, particularly those using diesel fuel, are thought to be responsible for 85% of NO_x emissions, whilst light-duty vehicles (LDVs) are considered responsible for more than half of CO emissions [Yang et al., 2015]. Nighttime emissions of NO_x and CO during both seasons could be attributed to HDVs making up an unusually high proportion of the vehicle fleet. CO emissions for summer also suggested a strong daytime traffic influence, although the peak at 11:00 may indicate an additional source, possibly relating to cooking given the time of day. Cooking was identified as a major contributor to the organic PM flux in aerosol flux measurements made during the same measurement period [Langford, 2020]. NO_x and CO fluxes

measured during the winter also indicated some traffic influence, although the trend is less clearly resolved than for the summer measurements. Winter NO_x emissions had a peak of 6.0 mg m^{-2} h^{-1} at 07:00 and there was a broader evening peak of similar magnitude between 17:00–18:00. NO_x flux peaked at 11:00 at 6.7 mg m^{-2} h^{-1}. CO flux was more variable; there was a small peak around the time of the morning rush hour though this was not as clearly resolved as it is for NO_x. CO flux peaked at 11:00 and in the evening though the profile showed greater short term variability for NO_x.

The difference between the winter and summer diurnal averages was more significant for CO than for NO_x with larger CO emissions in the winter than the summer throughout the day. This may be in part due to an additional source unique to winter, for example domestic heating. Local heating sources are likely to be reasonably consistent throughout the day which may go some way to explaining why the relative difference between nighttime and daytime emissions is smaller than for NO_x. Local heating sources also appear to contribute to the NO_x emissions measured, albeit to a lesser degree than for CO. The rush hour peaks that were clearly observed in NO_x flux during the summer campaign are masked somewhat in the winter and the peak was broader in the evening which could be due to increased residential emissions throughout the day. It is possible that additional emissions from the residential sector were not the only reason for the difference in magnitude of winter and summer CO emissions however. Strong seasonal variability in the fluxes of CO has been observed for London as another megacity where CO emissions measured in summer were 69% lower than in winter [Helfter et al., 2016]. In this case, higher winter CO emissions were attributed mainly to vehicle cold starts and reduced fuel combustion efficiency due to colder ambient temperatures. It should be noted that this study took place in a temperate, developed city and Beijing needs more winter heating which until recently, was primarily from coal. Indeed, Langford [2020] identified signatures of coal and solid fuel combustion within the flux footprint of the measurement although residential heating is overwhelmingly dominated by district heating in this area of Beijing.

4.3.2 Impact of local emissions on air quality

The average diurnal profiles in Fig. 4.7 highlight the relationship between emissions, mixed layer height and concentrations. Whilst emissions and concentrations seem to

be closely linked when averaged over the whole campaigns, there are periods where local emissions do not drive concentrations. During the winter months Beijing experiences a frequent cycling between "polluted" and "clean" days and this phenomenon has been termed "sawtooth cycles". During winter pollutants build up during near stagnant periods with SE wind flow being trapped by the mountain range in the NW. These are then advected out of the city when wind speed increases and the direction switches to the NW resulting in sharp reductions in atmospheric concentrations [Jia et al., 2008, Li et al., 2017a]. This distinctive meteorological phenomenon occurs in Beijing as a result of the East Asian Winter Monsoon, itself driven by temperature differences between the Pacific Ocean and Asian continent [Chen et al., 1992]. This cycling was observed during the winter field campaign and can be seen in NO_x and CO concentrations highlighted in Fig. 4.6. During the period 21 November 2016 – 23 November 2016 average daytime concentrations of 0.020 mg m^{-3} and 0.35 mg m^{-3} for NO_x and CO respectively were observed. On the following three days, 24 November 2016 – 27 November 2016, higher concentrations of 0.13 mg m^{-3} of NO_x and 1.7 mg m^{-3} of CO were measured, a more than five-fold increase in average daytime concentrations compared with the "clean" period. Corresponding increases and decreases in pollutant flux were not clearly observed however (Fig. 4.6). Figure 4.8 shows the distribution of the NO_x and CO fluxes and concentrations over the "clean" and "polluted" days. Despite the higher concentrations during the polluted period the measured flux is slightly lower. During the polluted period more deposition flux occurred; 13% of NO_x fluxes and 23% of CO fluxes (associated with u_* values over 0.175 m s^{-1}) were negative whereas no deposition fluxes were measured during the clean period.

Figure 4.9 shows two flux footprints; one averaged for the clean period and one for the polluted period. Satellite images and Open Street Map data (openstreetmap.org) shows that these footprints cover very similar land use areas; predominantly residential with busy roads so it is expected that the emissions would be similar for these areas, consistent with the variability in the measured flux. This indicates concentrations were more affected by meteorology, driving the accumulation at the city scale, or transport from regions outside Beijing than local emissions. There was not a significant contrast between mean mixed layer heights between the two periods. A mean height of 464 m (including nighttime and daytime) with a daytime maxima of 811 m for the clean

period was measured. For the polluted period the mean mixed layer height was 434 m with a daytime maxima of 822 m. Wind speeds were much lower during the polluted period with a mean wind speed of 1.9 m s^{-1} compared to 6.0 m s^{-1} for the clean period. These more stagnant conditions cause emissions to build up before being advected out of the city when wind speeds increase once again. Additionally, the higher wind speeds experienced during the "clean" period mean the city is influenced by air masses from further away. To the north-west, the dominant wind direction for the "clean" period, there is less industrial activity compared to the south of the measurement site towards the centre of Beijing, so these air masses are also likely to be less polluted.

4.3.3 Dependence on wind direction

Examining the relationship between diurnal flux and wind direction can give further information about emission sources. Figure 4.10 shows the average diurnal emission NO_x and CO flux plotted as a function of wind direction for both the winter and summer campaigns. Hour of day is represented by the radial scale between the inner and outer rings and starts at 00:00 in the inner side of the ring to 23:00 on the outer side of the ring.

For the winter campaign there appears to have been an enhancement in flux when there is a northerly wind direction. For NO_x the emission was largest throughout the afternoon hours but for CO peaks are more distinct, with an enhancement at midday and again between 16:00–20:00. Within the flux footprint, to the north of the site are residential areas, Beitucheng West Road (a busy traffic route) as well as some university buildings and a hospital. Further north (approximately 1 km from the tower) is the fourth ring road. The largest NO_x fluxes were observed between 16:00–20:00 when the wind direction was westerly. Within this wind sector lies Beitaipingzhuang Road, about 0.65 km from the tower and Xueyuan Road which links the third and fourth ring roads slightly further to the west and just under 2 km away from the tower.

During the summer campaign, there was an enhancement in the daytime flux of CO and NO_x with an easterly wind, indicating an emission source to the east of the site; probably the Jingzang Highway just 0.35 km east of the site as shown in Fig. 2.1. There are also some daytime enhancements in NO_x and CO emissions from the south of the measurement site towards central Beijing. For CO, enhancements to the south

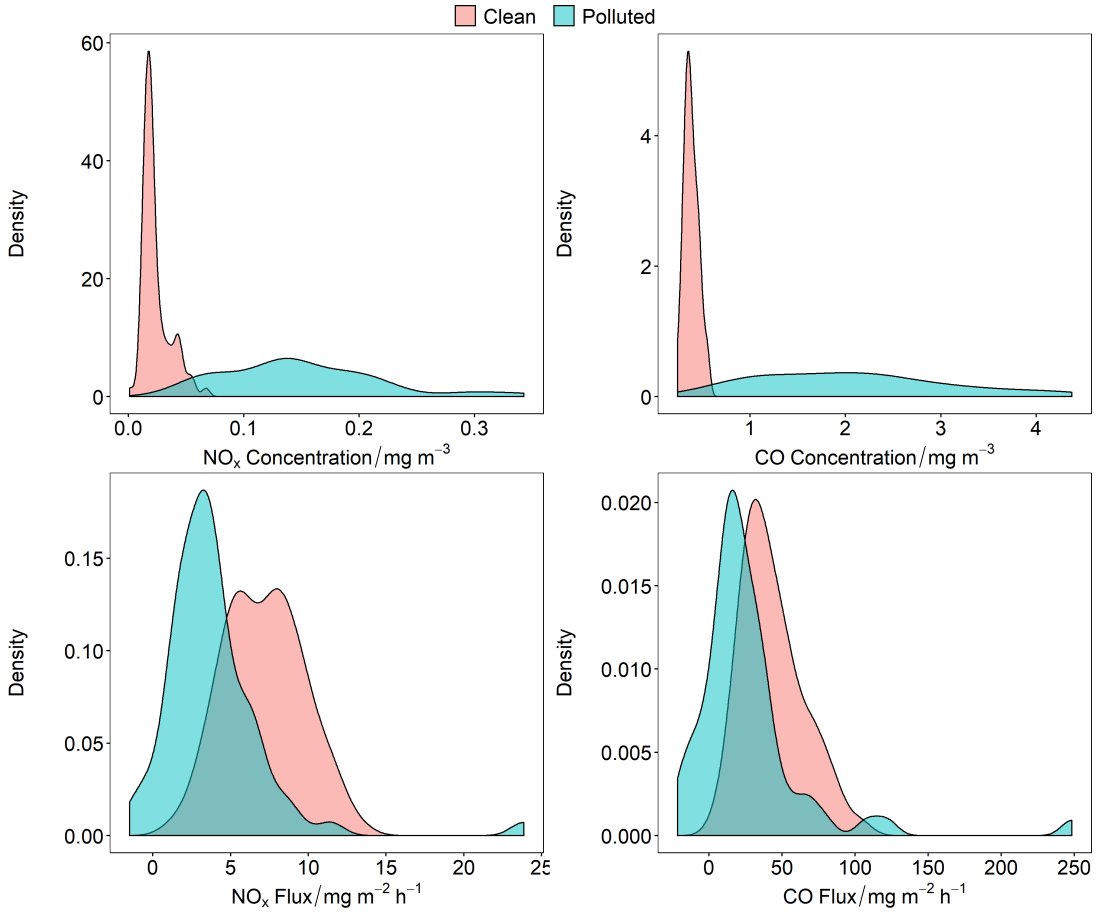

Figure 4.8: The probability density function for NO_x and CO concentrations and fluxes during the "clean" period (21 November 2016 – 23 Novemeber 2016) and "polluted" period (24 November 2016 – 27 November 2016). Only fluxes for which u_* values are over 0.175 m s^{-1} and which meet the 60% stationarity criteria are presented to allow a valid comparison.

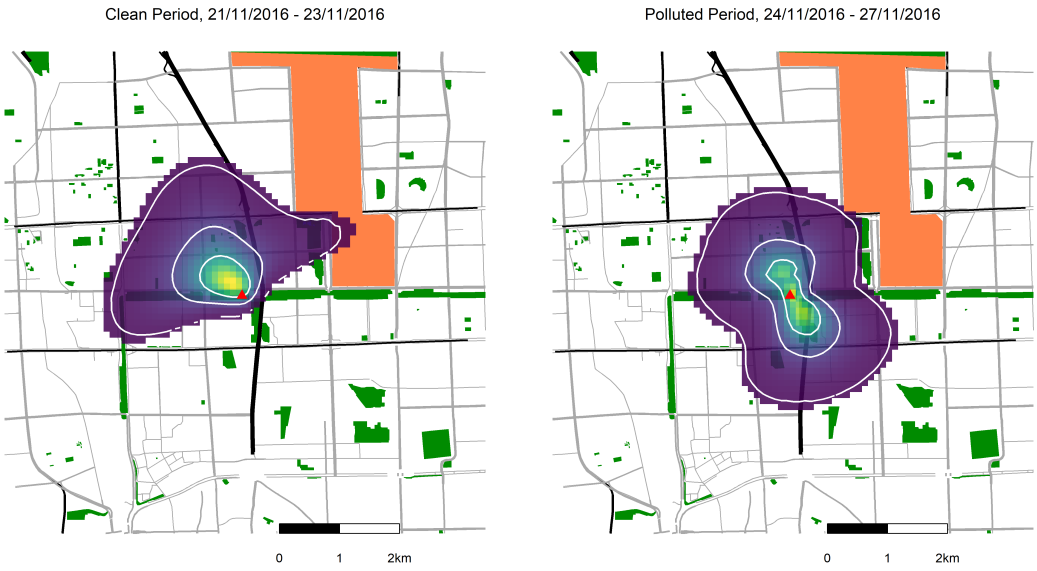

Figure 4.9: Average footprints for the "clean" period, 21 November 2016 – 23 November 2016 (left) and the "polluted" period, 24 November 2016 – 27 November 2016 (right). Map was built using data from © OpenStreetMap contributors 2019. Distributed under a Creative Commons BY-SA License.

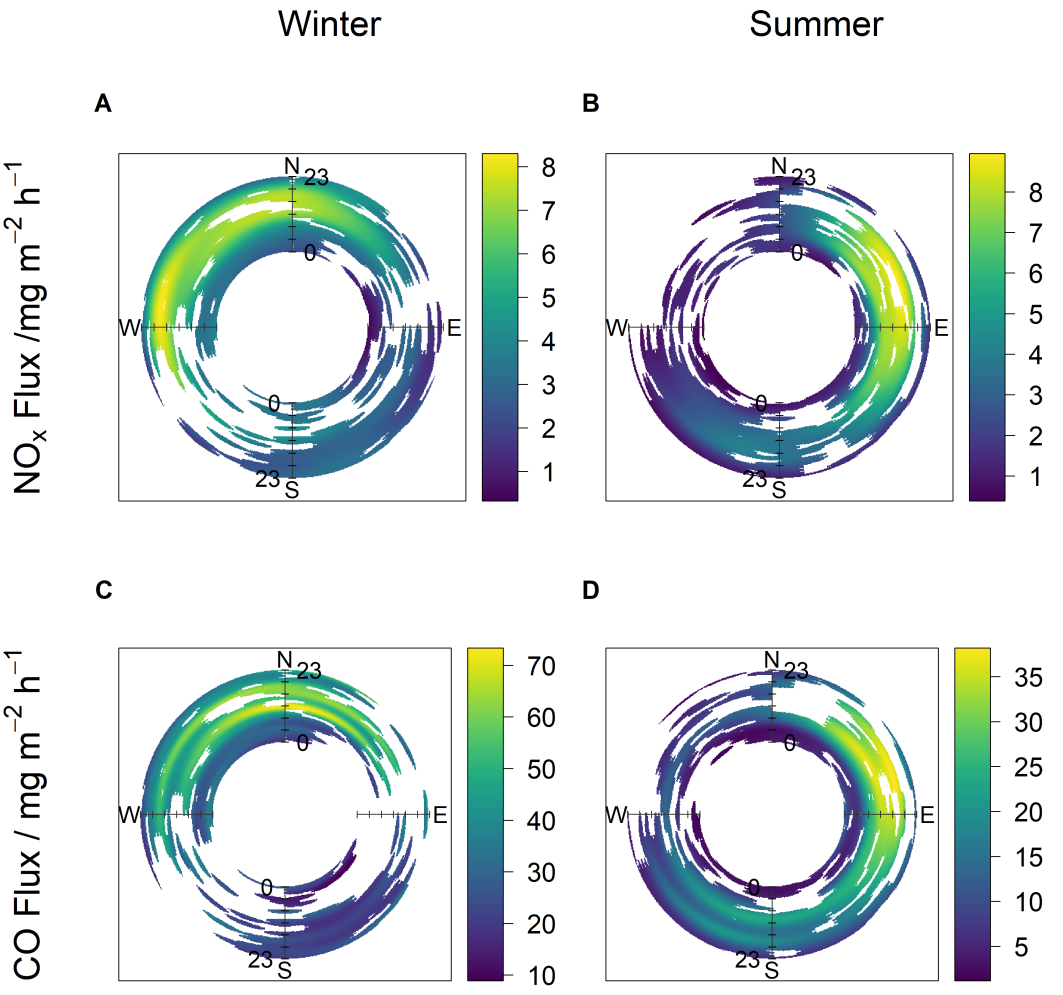

Figure 4.10: Polar annulus plots for NO_x and CO fluxes for both campaigns, showing the relationship between mean diurnal flux and wind direction. 0–23 refers to hour of day and the colour scale shows flux in mg m^{-2} h^{-1}.

show two quite distinct enhancement periods in the morning and evening, suggesting these emissions are from vehicles. It is unlikely that there were any significant seasonal change in traffic density on roads surrounding the measurement site. The change from a westerly influence observed during the winter to an easterly influence in summer is due to changes in the dominant wind direction. Beijing's wind patterns are quite different during the winter and the summer. There is a noticeable absence of easterly winds in the winter and the mean flux footprints (Fig. 4.4) highlight the difference in regions contributing to the observed flux.

4.3.4 Comparison with VOC flux

Aromatic hydrocarbons, including benzene, C_2-benzene, C_3-benzene and toluene are components of gasoline fuel and are typically emitted from combustion and evaporation of fuels and solvents in urban environments [Caplain et al., 2006, Langford et al., 2009]. Table 4.2 summarises the fluxes and concentrations measured during the APHH-Beijing measurement campaigns. Concentrations were significantly greater during the winter season while emissions were higher during the summer for all four hydrocarbon species. During the summer, toluene fluxes were the largest (0.31 mg m^{-2} h^{-1}), followed by C_2-benzene (0.24 mg m^{-2} h^{-1}) then C_3-benzene (0.15 mg m^{-2} h^{-1}) and the flux of benzene being the smallest (0.10 mg m^{-2} h^{-1}). Diurnal variation of VOCs for winter and summer is shown in Fig. 4.11. The uncertainty in the diurnal averages makes drawing conclusions about variations between daytime and nighttime difficult, although there are some indications that summertime trends at least may mimic those of CO and NO_x. During summer, fluxes of all four species followed a very similar diurnal trend with generally higher emissions in the daytime compared to the nighttime. A smaller early morning peak was observed at 08:00, slightly later than the morning peak in NO_x emissions which reached their maximum at 07:00. Emissions increased again in the afternoon for toluene, C_2-benzene and C_3-benzene peaking between 15:00–16:00. Benzene remained fairly constant throughout the afternoon with a mean emission of 0.076 mg m^{-2} h^{-1}. The peak during the night corresponds to a one-off event measured on the 29/05/2017 at 03:30. During the winter, C_2-benzene fluxes were the largest (0.073 mg m^{-2} h^{-1}), followed by the toluene flux (0.064 mg m^{-2} h^{-1}), then benzene (0.012 mg m^{-2} h^{-1}) with the flux of C_3-benzene

Table 4.2: Summary table for VOC concentrations and fluxes measured by PTR-ToF-MS. Data presented is for fluxes which are within 60% stationarity criteria for all u_* values.

	Winter				Summer			
Conc (mg m^{-3})	**Benzene**	**Toluene**	**C_2-Benzene**	**C_3-Benzene**	**Benzene**	**Toluene**	**C_2-Benzene**	**C_3-Benzene**
Mean	0.00703	0.00808	0.00975	0.00258	0.00186	0.00257	0.00390	0.00127
Median	0.00532	0.00620	0.00688	0.00198	0.00173	0.00227	0.00336	0.00113
Percentiles								
5th	0.000910	0.00100	0.00121	0.000431	0.000860	0.00113	0.00166	0.000572
95th	0.0190	0.0225	0.0299	0.00658	0.00346	0.00502	0.00794	0.00245
Standard Deviation	0.00618	0.00707	0.00969	0.00198	0.000864	0.00227	0.00237	0.000677
Flux (mg m^{-2} h^{-1})								
Mean	0.0121	0.0640	0.0730	0.00357	0.101	0.307	0.236	0.148
Median	0.0197	0.00861	0.00656	0.00354	0.0858	0.197	0.131	0.0995
Percentiles								
5th	-0.296	-0.209	-0.270	-0.0662	0.0180	0.137	-0.0166	0.0207
95th	0.195	0.427	0.692	0.0737	0.237	0.872	0.941	0.479
Standard Deviation	0.184	0.249	0.286	0.0455	0.0736	0.363	0.374	0.151

flux (0.0036 mg m^{-2} h^{-1}) being the smallest. There was no clear difference between nighttime and daytime emissions for all species.

Table 4.3 summarises previous urban flux measurements to allow the VOC fluxes from Beijing to be put into context. The benzene fluxes measured in Beijing during summer fall into the range of those reported in Table 4.3 and are most similar to values reported for large cities in the UK. Toluene fluxes and C_2-benzene fluxes measured during the summer in Beijing are also similar to the mean fluxes measured in UK cities where vehicular emissions were found to dominate aromatic fluxes. However, it should be noted that previous measurements over London were all made with a quadrupole PTR-MS instrument, which, unlike the time-of-flight instrument used in the present study, is restricted to a unit mass resolution. This means that the benzene, toluene and C_2-benzene signals may have included contributions from other compounds and therefore is likely to be an overestimate of the true C_2-benzene emission. The VOC flux values reported for Mexico City are much greater than those measured in Beijing for both seasons. Karl et al. [2009] reported an influence from evaporative emissions from the northern industrial district but there is no industrial emission source within the flux footprint for the Beijing measurements. This, along with a more modern vehicle fleet subject to stricter emissions regulation in Beijing may explain the larger discrepancy between these two cities. Fluxes measured in Helsinki are lower than emissions measured in the summer but comparable to those measured during the winter.

Emissions of all four species were higher in summer than in winter, although the statistical significance of all but C_3-benzene is somewhat uncertain. This is the opposite to the trend observed for NO_x and CO emissions, most likely driven by higher evaporation rates due to higher temperatures. The mean daytime temperature was 281 K during the winter campaign and 305 K during the summer campaign. Comparing VOC fluxes to NO_x and CO fluxes in the summer, emissions of C_2-benzene and C_3-benzene started to increase in the early hours of the morning (05:00) as observed for NO_x and CO, indicating a rapid release of emissions from a new source, such as traffic emissions. This is true for toluene and benzene, although the relative difference between night and day emissions is less pronounced. All four hydrocarbon species showed an enhancement during the mid-morning during the summer, like CO, probably due to an additional contribution from residential and cooking emissions from

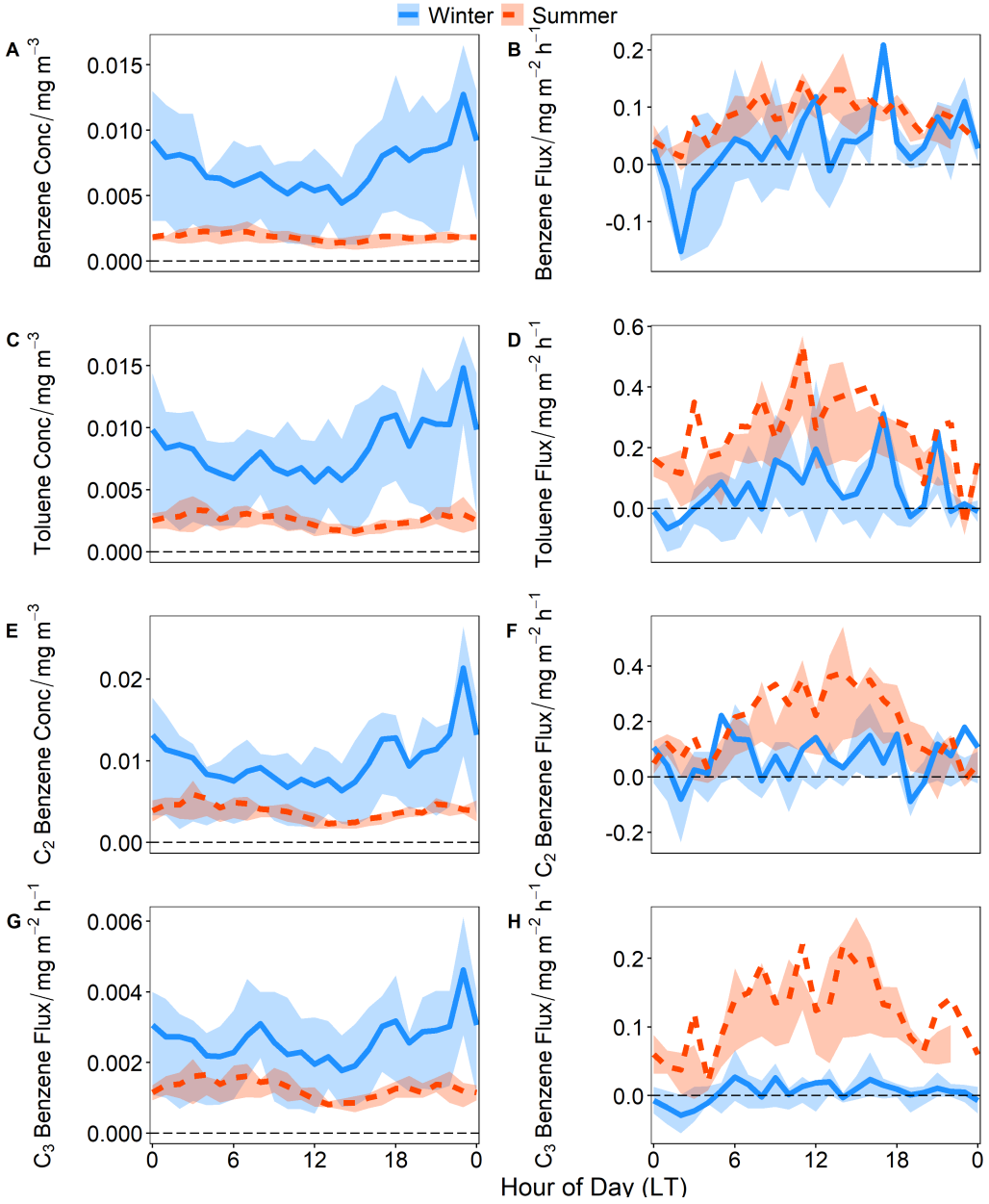

Figure 4.11: Diurnal profiles for A) benzene concentration, B) benzene flux, C) toluene concentration, D) toluene flux, E) C_2-benzene concentration, F) C_2-benzene flux, G) C_3-benzene concentration and H) C_3-benzene flux measured by PTR-ToF-MS. Blue, solid lines are for measurements taken during the winter campaign and the orange, dashed lines are measurements taken during the summer campaign. The shaded areas represent the 25th and 75th percentiles to give an idea of the spread of the data. Only stationary data has been used but no u_* filtering has been applied when doing the diurnal averaging.

Table 4.3: Summary of mean VOC fluxes measured in various urban or semi-urban locations.

Species	**Mean Flux (mg m^{-2} h^{-1})**	**Location and Year**	**Reference**
Benzene	0.0121	Beijing, November–December 2016	*This study*
	0.101	Beijing, May–June 2017	*This study*
	4.7*	Mexico City, March–April 2006	Karl et al. [2009]
	0.396	Mexico City, March 2006	Velasco et al. [2009]
	0.12	Manchester, June 2006	Langford et al. [2009]
	0.15	London, October 2006	Langford et al. [2010]
	0.17	Houston, May–July 2008	Park et al. [2010]
	0.09	London, August–December 2012	Valach et al. [2015]
	0.02	Helsinki (urban background), January 2013 – September 2014	Rantala et al. [2016]
	0.07*	Central London, July 2013	Vaughan et al. [2017]
	0.02	Innsbruck, July–October 2015	Karl et al. [2018]
Toluene	0.0640	Beijing, November–December 2016	*This study*
	0.307	Beijing (May–June 2017)	*This study*
	0.83	Mexico City, April 2003	Velasco et al. [2005]
	14.1*	Mexico City, March–April 2006	Karl et al. [2009]
	3.1	Mexico City, March 2006	Velasco et al. [2009]
	0.28	Manchester, June 2006	Langford et al. [2009]
	0.58	Houston, May–July 2008	Park et al. [2010]
	0.41	London, August–December 2012	Valach et al. [2015]
	0.051	Helsinki (urban background), January 2013 – September 2014	Rantala et al. [2016]
	0.24*	Central London, July 2013	Vaughan et al. [2017]
	0.08	Innsbruck, July–October 2015	Karl et al. [2018]
C_2-Benzene	0.0730	Beijing, November–December 2016	*This study*
	0.236	Beijing, May–June 2017	*This study*
	0.468	Mexico City, April 2003	Velasco et al. [2005]
	1.3	Mexico City, March 2006	Velasco et al. [2009]
	0.32	Manchester, June 2006	Langford et al. [2009]
	0.28	London, October 2006	Langford et al. [2010]
	0.059	Helsinki (urban background), January 2013 – September 2014	Rantala et al. [2016]
	0.32*	Central London, July 2013	Vaughan et al. [2017]

**Measured from an aircraft.*

local restaurants. There is possibly a winter contribution from evening rush hour traffic to the benzene and toluene emissions that mirrors that observed in the CO and NO_x emissions at 17:00, though this is not clearly observed during the summer campaign. During the summer, the emissions of all four species are elevated in the afternoon (between 13:00–18:00) when temperatures are highest. These emissions are likely enhanced by evaporation which masks the evening rush hour traffic contribution. There is a strong correlation between total VOC flux and heat flux in summer ($r = 0.83$) compared to the winter ($r = 0.35$).

The ratio of benzene to toluene (B/T) is often used to gauge the photochemical age of an air mass as the two species have different atmospheric lifetimes due to their different reactivity with the OH radical. Heeb et al. [2000] reported B/T concentration ratios between 0.41–0.83 for primary exhaust emissions. As an air mass ages, the ratio increases as toluene is more reactive than benzene. For Beijing, the median B/T concentration ratio in the winter was 0.89 and 0.73 for the summer at the upper end of the expected range for primary exhaust emissions. Barletta et al. [2005] reported a roadside B/T value of 0.6 for Beijing, however vehicle fleet and fuel types are rapidly changing in response to legislation so this measurement may not be representative for the measurement period of this work. The difference in B/T concentration ratios does however indicate that VOC sources are changing between winter and summer as the change in ratio cannot be explained by expected changes in atmospheric oxidation rates caused by seasonal differences in temperature. Langford et al. [2009] points out that temperature can impact B/T ratios as reactivity rates increase with warmer temperatures but if temperature was driving the seasonal difference it would be expected that the B/T ratio measured during summer is higher than during winter. It is likely that additional sources such as domestic burning and cooking are present in winter; Barletta et al. [2005] reports that higher B/T concentration ratios are associated with natural gas and biomass combustion, which supports the hypothesis that these type of emission sources could be leading to an increased B/T concentration ratio in the winter. The B/T flux ratio should reflect better the ratio of the two pollutants in emissions sources as flux ratios are confined to the area of the flux footprint rather than being influenced by a wider area [Karl et al., 2009]. The median B/T flux ratios were 0.72 for the winter campaign and 0.31 for the summer campaign, further suggesting a change

in emission source between the two seasons. The B/T flux ratio for summer is lower than expected for primary exhaust emissions though similar values have been reported for vehicles without catalytic converters [Heeb et al., 2000] and given higher temperatures, emissions from other sources such as solvent evaporation, may affect this ratio. Indeed, Karl et al. [2009] showed that fuel evaporative losses typically have a higher toluene fraction, leading to lower B/T ratios. The strong VOC-heat flux correlation and the low B/T ratio observed during the summer campaign suggests fuel evaporative loss is a source of aromatic VOC emissions in Beijing.

4.3.5 Comparison with an emissions inventory

The measured NO_x and CO fluxes were compared to the high-resolution (3 km $\times$ 3 km) MEIC v1.3 inventory with a base year of 2013. The comparison of VOC emissions with an emissions inventory is beyond the scope of this work. A direct comparison of the diurnal variation in measured emissions and that in the inventory indicates that NO_x and CO emissions are grossly overestimated throughout the day for both campaigns. Total NO_x emissions are overestimated by a factor of 3.8–17 (mean overestimation of 9.9 throughout the day) in the winter and 4.2–25 (mean = 11) in the summer. For CO, winter emissions were between 1.6–9.7 (mean = 4.8) times larger in the inventory than those measured and summer emissions between 5.2–21 (mean = 10) times larger.

Part of the discrepancy between the inventory and measured emissions may be due to the comparison of observations (made in 2016/2017) with an older inventory (base year 2013). China's NO_x emissions have rapidly changed in the past three decades. Liu et al. [2016] report that between 2005 and 2011 NO_2 emissions increased by 53% for the whole of China, attributed for the most part to increasing fuel consumption with coal the dominant fuel type. An estimated three-quarters of all electricity in China was generated by coal in 2016 [International Energy Agency, 2016]. After 2012 however, a combination of the installation of power plant de-nitration devices and vehicle emissions controls has led to a 32% decrease in NO_2 emissions [Liu et al., 2016, Krotkov et al., 2016, Miyazaki et al., 2017]. In Beijing, NO_x emissions are decreasing thanks to numerous air pollution control measures implemented since 2000; polluting industries and power plants have been relocated outside of the city, stricter emissions standards for industrial and domestic boilers have been introduced and the fuel type shifted from

coal to gas [Wang et al., 2010b]. Since the introduction of the "Clean Air Action Plan" in Beijing in 2013, 900,000 households in Beijing have converted from using coal to cleaner technologies like gas or electricity. The burning of biomass, such as wood and crops, was completely forbidden by the end of 2016 [Cheng et al., 2019]. The impact of the emissions controls has been predicted to reduce emissions of NO_x and VOCs by 43% and 42% respectively between 2013–2017 in Beijing [Cheng et al., 2019]. Most significant for NO_x emissions however is the stringent vehicle control measures introduced within the last decade, accounting for 47% of the total reduction in emissions for the city.

CO emissions have also been declining in Beijing over the past two decades by an average rate of 1.14% $year^{-1}$ [Wang et al., 2018b]. Zheng et al. [2018] highlight a reduction in inefficient domestic stoves and improvements in emissions standards for vehicles as being dominant forces for the observed reduction in CO emissions. For VOCs, vehicle emission controls were another significant contributor to the reduction with 16.1% of the reduction attributed to new controls. Improvements in management of solvent use (e.g. use of high-solid and waterborne paints instead of solvent based ones) dominated the reduction in VOC emissions contributing 49.3% to the total reduction in Beijing. Emissions between 2013–2016 were predicted to reduce by 30% for NO_x and 35% for VOCs [Cheng et al., 2019, Biggart et al., 2020].

These estimated changes were applied to the inventory leading to reductions in emissions of 30% in the winter and 43% for the summer for both species. No emissions reductions were presented for CO alone but given that its expected sources are similar to NO_x the same reduction factor was applied to the CO inventory emissions. The mean diurnal profiles for the lowered inventory estimates are presented in Fig. 4.12, with measured emissions shown by the black dashed line. With the expected reduction considered, NO_x is still overestimated by a factor of 2.7–12 (mean = 7.0) in the winter and 2.4–14 (mean = 6.8) times in the summer. Similarly, CO emissions are still overestimated for both seasons with inventory CO emissions 1.1–6.8 (mean = 3.4) times larger than the measured CO emission for the winter campaign. For summer, the inventory overestimated CO emissions by a factor of 2.9–12 (mean = 5.6) times. The closest agreements between inventory and measurements were during the nighttime in all cases. Applying these reductions does obviously improve the inventory compari-

son, compared with the original, however large overestimations remain. Examination of the flux footprint suggests that the majority of measured emissions are coming from transportation and residential sources. The inventory supports this for CO, suggesting that transportation is the largest contributing sector, followed by the residential sector. However, for NO_x the inventory also suggests that there is a large industrial source, contributing up to 60% to the total emissions for the winter campaign and 52% for the summer campaign. No obvious industrial sources could be identified within the flux footprint for this study. Zheng et al. [2017] observed a decoupling between real world emissions and the spatial proxies used to develop and downscale inventories as polluting industries are moved out of urban centres. The methods used to allocate emissions in the MEIC inventory appear to result in emissions being overestimated in the urban area of Beijing; spatial proxies such as population density and gross domestic product (GDP) are used to scale down national emissions statistics. This method tends to overestimate emissions in urban centres and underestimate emissions in rural areas and so even if this comparison only considered the residential and transport sectors, NO_x and CO emissions would still be overestimated by the inventory. Just considering these two sectors, NO_x emissions are overestimated by a factor 1.6–5.1 (mean = 3.3) for winter and 1.9–8.5 (mean = 3.7) for summer. CO emissions are overestimated by 1.1–6.5 (mean = 3.1) in winter and 2.7–12 (mean = 5.2) in summer. The sensitivity of the inventory to location was tested by shifting the inventory grid 3 km in each direction (north, east, south and west) and it was found that this had little impact on the comparison with the inventory still overestimating emissions for all directions.

The inventory did capture some of the general diurnal variation in emissions. Figure 4.13 shows the normalised diurnal variation for the transportation and residential sectors, calculated relative to one another assuming these sectors are the only emission sectors. The diurnal variation in measured emissions normalised by the daily average is overlaid. For NO_x and CO emissions in the winter (Fig. 4.13, panels A and B) the sum of the residential and transportation emissions captures the time of the morning rush hour peak at 07:00 and the evening enhancement in emissions in the mid-afternoon to evening due to a combination of increased residential and traffic activity. Residential emissions are predicted in the inventory to increase between 11:00–12:00 which was observed in the measurements, though to a greater extent than the inventory suggests.

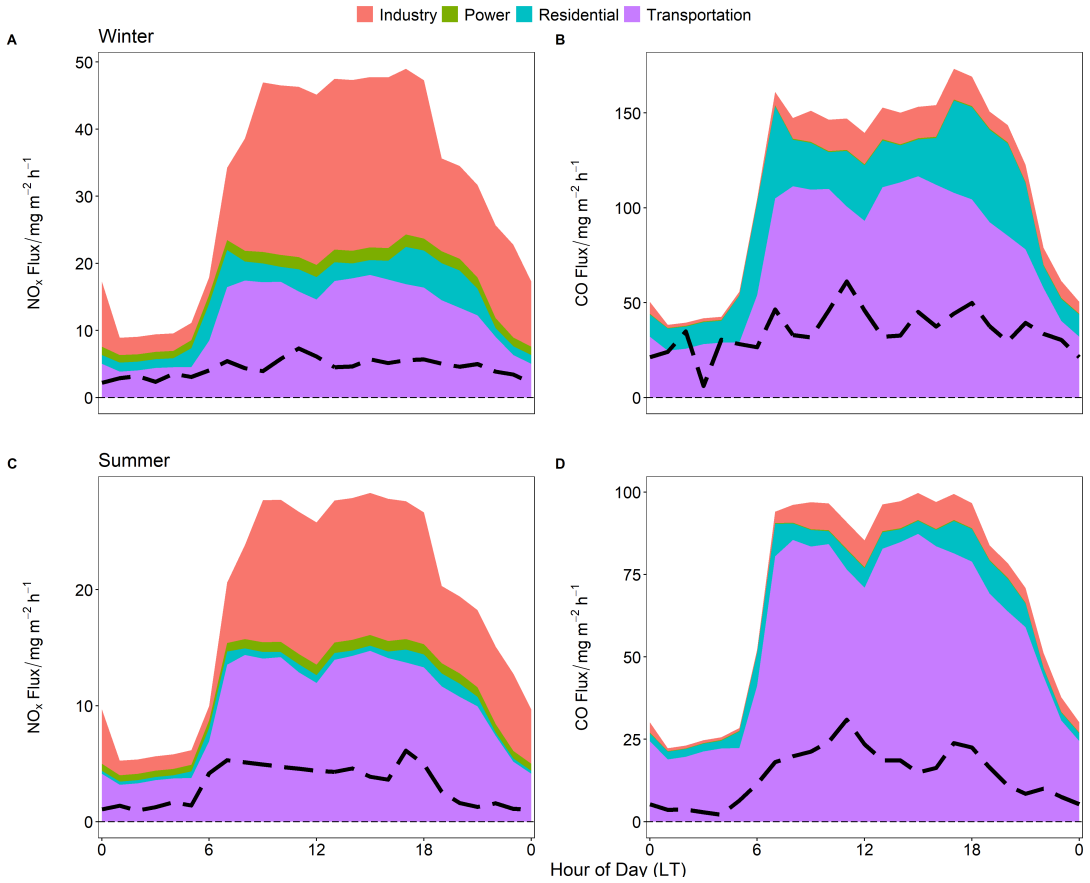

Figure 4.12: Measured diurnal trend (dashed black line) and predicted diurnal trend using the MEIC inventory (filled areas by sector) for NO_x and CO emissions. MEIC inventory data has been reduced by 30% for comparison with the winter 2016 campaign and by 43% for comparison with the summer 2017 campaigns to take account of expected emissions reductions indicated in Cheng et al. [2019]. Panels A and B show emissions for the winter campaign and panels C and D show emissions from the summer campaign.

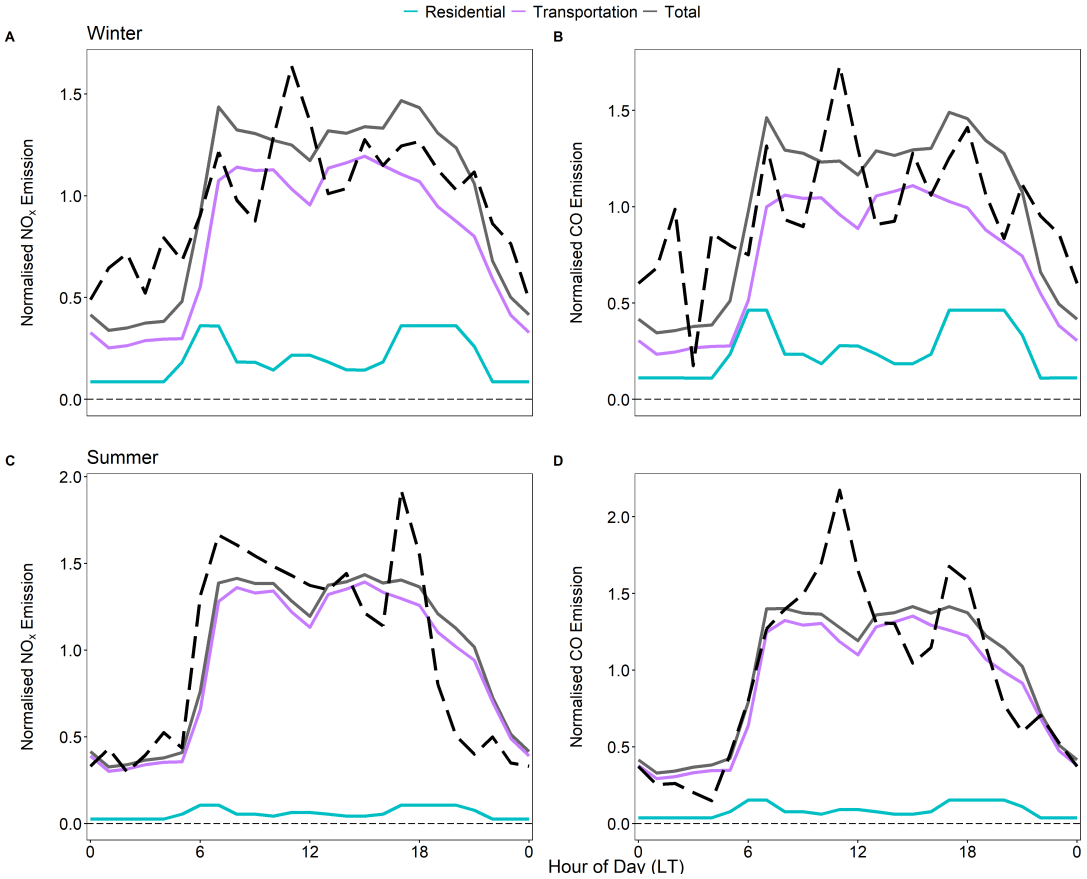

Figure 4.13: Comparison of normalised diurnal variation in NO_x and CO emission predicted by the MEIC inventory and measured flux. The normalised emission has been calculated for the inventory by dividing hourly sector emission by the mean daily sector emission. Given there are no clear industrial or power generation emission sources within the flux footprint, only the residential (blue solid line) and transportation (purple solid line) sectors have been presented. The normalised diurnal variation for these sectors have been multiplied by the normalised diurnal variation for the sum of the residential and transportation sectors (grey solid line) to reflect the relative contributions of the two sectors. Normalised diurnal variation in the measured emission has been calculated by dividing mean hourly emission by mean daily emission (black dashed line). Panels A and B show data for NO_x and CO from the winter campaign and panels C and D for the summer.

Looking at the summer data for NO_x (Fig. 4.13, panel C), the increase in emissions after 05:00 when traffic density increased was well captured for NO_x though the measurements suggested a slightly quicker increase in emission than suggested by the inventory. The minimum daytime emission predicted by the inventory occurred at 12:00 where there was a dip in emissions from transportation though this was not reflected in the measurements where there was an almost constant decrease in NO_x emissions until the evening rush hour peak at 17:00. The evening rush hour peak for NO_x in summer was much more distinct than the inventory suggests and NO_x emissions decrease rapidly after 18:00, earlier than the inventory predicts. NO_x emissions from residential sources in the inventory showed a small enhancement around midday which was not clearly observed in the measurements, suggesting traffic related emissions dominate here. For CO in summer (Fig. 4.13 panel D), the increase in measured emissions after 05:00 matches the rate of increase predicted by the inventory very well. After 07:00 the inventory predicted CO emissions would not increase further which was not reflected in the measured emissions. Emissions from the residential sector are predicted to increase between 11:00–12:00 reflecting emissions from cooking activities. Within the flux footprint there were several restaurants including barbecue restaurants where food was cooked over open coals. This is not likely to be included in the inventory but would explain the increase in measured CO emissions before lunchtime as food is prepared. As with NO_x emissions, the evening rush hour peak in measured CO emissions was narrower and began to decrease earlier than suggested by the inventory.

The inventory suggests that total emissions are higher in winter than in summer; NO_x emissions from the residential and transportation sectors are between 1.3–1.7 times larger and for CO emissions from these two sectors are between 1.5–2.0 times larger. The inventory performs relatively well capturing the measured seasonal difference for emissions of both species. The seasonal difference in NO_x emissions are slightly overestimated (measured emissions were on average 1.2 times greater in winter compared to summer) and the inventory underestimates the seasonal difference in CO emissions (measured emissions were on average 2.3 times higher in winter than summer). For both NO_x and CO the inventory suggests that seasonal variation is driven by increased residential sector emissions, which are predicted to be 5 times higher in winter than summer.

4.4 Summary

NO_x, CO and aromatic VOC emissions have been quantified for the first time during two contrasting seasons for an area of central Beijing. The magnitude of NO_x emissions were found to be similar during the winter and summer periods whilst the fluxes of CO showed a greater seasonal dependence with winter emissions being over 2 times greater than CO emissions measured during summer. The dominant source for NO_x and CO emissions is traffic with influence from residential emissions. The diurnal variation in aromatic VOC fluxes also suggested traffic and residential sources, though evaporative effects due to higher summer temperatures meant emissions were greater in the summer than the winter. The NO_x and CO fluxes presented in this work provide good evidence that proxy-based inventories can overestimate emissions for urban centres as suggested by Zheng et al. [2017]. When developing inventories at an urban scale future work should look carefully at up-to-date proxies or at deriving emissions by bottom-up approaches in order to correctly predict the magnitude of emissions. When comparing the diurnal variation in inventory and measurement the inventory performed relatively well capturing morning and evening rush hour peaks. The inventory also attributed traffic and residential emissions as the major source of NO_x and CO emissions which was supported by analysis in this work. This set of pollutant flux measurements can provide a useful basis for developing these high resolution urban inventories which are at an appropriate scale to assess public health impacts of pollution.

Trace Gas Measurements over the North Atlantic Ocean

5

5.1 The North Atlantic climate system and why it matters

THE NORTH ATLANTIC region plays a central role in global climate system. The Atlantic Ocean transports heat from the southern hemisphere and the tropics to the northern hemisphere and in doing so acts to maintain the mean climate state. The North Atlantic Ocean is unique in that it exhibits variation in sea surface temperatures (SSTs) over multidecadal time scales, termed Atlantic multidecadal variability (AMV). AMV has been linked to a range of climate impacts including rainfall anomalies across Africa, Europe and North America, Greenland ice sheet melt, hurricane activity and sea level changes [Knight et al., 2006, Buckley and Marshall, 2016]. In some cases the magnitude of these impacts is such that the AMV can dominate over the impacts of longer-term climate change, albeit on shorter time scales [Sutton et al., 2018]. Given these significant impacts, understanding the processes that drive AMV and ensuring models are skilful in predicting AMV is a major challenge. Uncertainty in how North Atlantic temperatures will change in the future is a major uncertainty in climate modelling especially for Europe [Woollings et al., 2012]. The importance of this climate system means it is critical to understand the processes driving AMV in order to predict it.

A climate system consists of five main components; the atmosphere, the hydrosphere, the cryosphere, the lithosphere and the biosphere [Stocker et al., 2013]. The

relationship between these is complex with all parts interacting, which makes determining the drivers of AMV difficult. It is generally thought that AMV is related to changes in the strength of ocean circulation, specifically the Atlantic meridional overturning circulation (AMOC) [Ba et al., 2014]. Variability in the North Atlantic Oscillation (NAO), which refers to variability in atmospheric pressure over the North Atlantic region, is thought to be a driver of the AMOC and therefore also influences AMV [Eden and Willebrand, 2001, Robson et al., 2012]. Common features of the NAO include regions of high pressure centred over the Azores and regions of lower pressures centred over Iceland, which regularly cycles in a "see-saw" type pattern. When the NAO is in positive phase there is a greater than usual pressure difference between the two regions. The positive NAO phase is associated with mild, stormy and wet winter conditions in northern Europe. When the NAO is in negative phase (there is a weaker pressure difference than usual between the two regions) Europe tends to experience colder, drier winters. Given the interactions between all aspects of the North Atlantic climate system predicting the variability is challenging, made more so by a sparsity of observations in the region [Robson et al., 2018].

One key element of the North Atlantic climate system is the atmosphere and the role of external forces like changes in greenhouse gas (GHG) emissions. By altering radiative forcing these factors can affect atmospheric circulation and the NAO, hence impacting on the North Atlantic climate system. Booth et al. [2012] proposed a link between AMV and changes in atmospheric composition. Using an Earth system climate model the authors showed how aerosol emissions and volcanic activity could explain North Atlantic SST variability between 1860–2005. It follows that understanding the composition of the atmosphere over the North Atlantic is useful for understanding aerosol formation which may in turn affect SST. Changes in O_3 and CH_4 mixing ratios over the North Atlantic can also affect radiative balance through action as GHGs. Amounts of these pollutants can change due to enhanced emissions of GHG species (or precursor emissions in the case of O_3) and due to transport from other regions. The phase of the NAO plays an important role in pollutant transport and can impact air quality; when the NAO is in positive phase, strong westerlies can act to transport European pollution away from their anthropogenic source regions, whereas when the NAO is in negative phase more stable meteorological conditions cause pol-

lution to build up over the source regions [Pope et al., 2018]. The exception to this is for O_3 as during the positive phase of the NAO there is an increased rate of transport of O_3 rich air from North America to Europe [Robson et al., 2018].

5.1.1 Recent changes in atmospheric composition over the North Atlantic.

Emissions of pollutants are not only important in terms of influencing local air quality but also have the potential to impact remote regions like the North Atlantic due to transport. Indeed, following an airborne measurement campaign investigating the transport of O_3 and precursor emissions to the Atlantic, Lewis et al. [2007] concluded that the remote region was polluted. Transport of pollutants from North America have been observed over the North Atlantic region [Parrish et al., 1998, Honrath et al., 2004, Lewis et al., 2007, Kumar et al., 2013] and less frequently transport from Europe and Africa [Zhang et al., 2017]. Emissions from biomass burning from forest fires have also been shown to impact atmospheric composition over the North Atlantic. Lapina et al. [2006] showed that CO and O_3 mixing ratios were enhanced in air masses associated with fires. Val Martin et al. [2008] showed that transport of polluted air masses from North America leads to enhancements in NO_x over the North Atlantic throughout the year.

In the northern hemisphere, tropospheric O_3 levels have increased at a rate of 1–5 ppb decade^{-1} equating to $> 100\%$ increase since the 1950s [Cooper et al., 2014]. Satellite observations from the Ozone Monitoring Instrument (OMI) show that tropospheric O_3 concentrations at the northern mid-latitudes exceed those in the southern hemisphere by 19% on an annual basis, generally thought to be because anthropogenic emissions are greater in the northern hemisphere than the south, with approximately 90% of the global population and 90% of anthropogenic NO_x emissions [Cooper et al., 2010, Horowitz et al., 2003]. Observations of O_3 concentrations show a spring maximum for northern hemisphere, though the drivers of this phenomenon are not well understood [Monks, 2000]. Long-term observatories such as Mace Head (located on the west coast of Ireland) offer an insight into changes O_3 mixing ratios over the North Atlantic where increases in baseline O_3 mixing ratios of 0.25 ppb year^{-1} between 1987 and 2012 have been reported, though episodic peak O_3 levels have declined steadily

[Derwent et al., 2018].

Unlike in urban areas, direct emissions of NO_x are practically non-existent in the remote oceanic atmosphere, though emissions from shipping may have some impact [Lawrence and Crutzen, 1999, Kasibhatla et al., 2000, Beirle et al., 2004]. For the North Atlantic, observations at Pico Mountain Observatory in the Azores have shown that NO_x transported in anthropogenic plumes from North America causes year-round enhancements in NO_x, as well as larger enhancements in boreal wildfire plumes.

CO is also transported from North America to the North Atlantic. Downward trends in CO mixing ratios measured at Pico Mountain Observatory have been reported at a rate of 0.31 ppbv $year^{-1}$ between 2001 and 2011 which is thought to be driven by a decline in anthropogenic emissions from North America [Kumar et al., 2013].

Atmospheric methane (CH_4) concentrations have been increasing globally since pre-industrialisation as a result of increasing emissions from human agriculture and increased fossil fuel usage [Turner et al., 2019]. As methane has a lifetime of around 10 years in the troposphere it is relatively well mixed and trends in total column CH_4 show a strong increase over the North Atlantic, consistent with global methane trends [Robson et al., 2018, Nisbet et al., 2016].

5.1.2 Measurements from atmospheric research aircraft

Atmospheric Research Aircraft (ARA) are indispensable research tools which allow the study of the atmosphere in unique ways. The manoeuvrability of aircraft offer the chance to sample regions inaccessible by other means, provide large spatial coverage in a short time scale, tracking of meteorological phenomena as well as an ability to respond rapidly to civil contingency events thus providing near real time data as situations unfold. Such is the worth of ARA that investment in the technologies is increasing and an impressive global fleet of ARA are available [Schumann et al., 2013]. These aircraft complement a worldwide network of ground-based and satellite atmospheric monitoring systems allowing a more complete understanding of the atmosphere.

The UK's ARA is a BAe-146-301 (shown in Fig. 5.1) managed by the Facility for Airborne Atmospheric Measurements (FAAM) and has been in service since 2004. The FAAM aircraft is capable of carrying a 4 tonne instrument load, and can operate at altitudes between 50 and 35000 ft (15–10600 m) [McBeath, 2014] allowing the study

Figure 5.1: The UK's atmospheric research aircraft, a modified BAe-146-301 four engine jet, landing at Cranfield Airport.

of the troposphere and boundary layer processes. A wide range of instrumentation is fitted on the ARA including measurements of key meteorological parameters including temperature, humidity, wind speed and direction as well as a range of in-situ trace gas measurements including CO, O_3, NO_x, CO_2 and CH_4. The core principles of operation of the instrumentation of CO, O_3, and NO_x are described in Chapter 2, as they are the same type of analysers as those used for work in Beijing. Greenhouse gases (GHGs), CO_2 and CH_4 were measured using IR absorption spectroscopy (Fast Greenhouse Gas Analyser, Los Gatos Research) and the instrument is described in detail in O'Shea et al. [2013].

Numerous scientific campaigns have deployed aircraft to study atmospheric processes. A key role of ARA, is rapid response to civil contingency events and the UK's ARA has been called on to make measurements in such cases, for example the 2010 Eyjafjallajökull eruption. Between 14 April 2010 and 21 May 2010, the eruption of the Icelandic volcano, Eyjafjallajökull, caused extensive disruption to the aviation industry, with an estimated cost of $320 million per day [Turnbull et al., 2012]. The

FAAM ARA was deployed to investigate the volcanic ash clouds around the UK and validate volcanic ash dispersion forecasts and was instrumental in re-opening airspace. The FAAM ARA was also called upon to quantify the flow rate of an uncontrolled gas leak from the Total Elgin gas platform which was leaking between 25th March and 16th May 2012 [Lee et al., 2018]. Whilst ARA have this ability to rapidly respond to events, where direct access is impossible or dangerous, the FAAM ARA is usually used for scheduled atmospheric research. One example is the Intercontinental Transport of Ozone and Precursors (ITOP) campaign which happened in 2004 and is of particular relevance to this work as it studied atmospheric composition of the North Atlantic region, highlighting the role of pollution transport in affecting chemical composition.

5.2 The ACSIS Campaign

The North Atlantic Climate System Integrated Study (ACSIS), is an ongoing project (2016–2021), and was established in order to increase understanding of changes occurring in the North Atlantic region. ACSIS aims to study all aspects of the North Atlantic climate system and consider their interactions with a view to enhancing the capability to detect, attribute and predict changes in the climate system [Sutton et al., 2018]. In-situ measurements from ground-based stations, like from the observatories in Sao Vincente, Cape Verde and Penlee Point, Cornwall, UK provide useful information improving understanding of atmospheric composition change near the surface, however measurements made from the ARA allow a more complete picture of the atmosphere to be composed. ARA missions as part of ACSIS provide the longest record of composition change in the lower free troposphere over the North Atlantic [Sutton et al., 2018].

In this chapter, data from the first four campaigns are reported, referred to throughout ACSIS 1, ACSIS 2, ACSIS 3 and ACSIS 4. Table 5.1 summarises the dates, location and flight numbers for each campaign. There is a total of 20 flights comprising of nearly 80 hours of measurement data. Measurements were made from approximately 50 m over the sea surface to 7600 m with aircraft position ranges are given for each flight in Table 5.1. ACSIS 1, 2 and 4 were predominantly based out of the Azores, whilst flights for ACSIS 3 were based out of Cork, Ireland. Figure 5.2 summarises

Table 5.1: Summary of timings and location for ACSIS 1–4 flights.

Campaign	Flight Numbers	Dates	Take Off–Landing Times (UTC)	Latitude Range	Longitude Range	Description
ACSIS 1	B996	13/02/2017	09:19:31–13:03:40	41.2–52.8	-9.04– -1.17	East Midlands–Porto
	B998	14/02/2017	12:59:40–17:15:45	38.7–39.1	-37.5– -27.0	Lajes–Lajes (West of Azores)
	B999	15/02/2017	11:55:18–16:39:40	38.7–39.1	-38.1– -26.9	Lajes–Lajes (West of Azores)
	C001	16/02/2017	09:48:22–13:01:05	38.7–41.4	-27.1– -8.67	Lajes–Porto (East of Azores)
	C002	16/02/2017	14:32:27–17:29:17	38.7–52.2	-27.1– -0.490	Porto–Cranfield
ACSIS 2	C066	19/10/2017	10:56:21–13:59:24	41.2–52.1	-9.00– -0.610	Cranfield to Porto
	C067	20/10/2017	08:17:08–12:26:06	38.6–41.3	-27.1– -8.62	Porto to Lajes (East of Azores)
	C068	20/10/2017	14:21:08–17:58:55	38.7–39.1	-36.0– -27.0	Lajes to Lajes (West of Azores)
	C069	22/10/2017	11:04:13–15:49:29	30.5–39.1	-28.6– -26.9	Lajes to Lajes (South of Azores)
	C070	23/10/2017	08:32:59–12:14:43	36.6–52.0	-27.1– -8.49	Lajes to Cork (North of Azores)
	C071	23/10/2017	14:06:20–15:54:43	50.2–52.2	-8.50– -0.474	Cork to Cranfield
ACSIS 3	C103	14/05/2018	11:53:27–15:08:23	41.0–52.4	-9.00– -0.285	Cranfield to Porto
	C105	17/05/2018	08:55:25–12:40:07	50.4–52.0	-20.1– -8.45	Cork to Cork (West Ireland)
	C106	17/05/2018	14:23:00–16:12:17	50.1–52.4	-8.45– -0.451	Cork to Cranfield
ACSIS 4	C139	19/02/2019	09:04:35–12:32:21	40.9–52.4	-9.00– -0.410	Cranfield to Porto
	C140	19/02/2019	14:21:39–18:10:18	38.8–41.4	-27.2– -8.677	Porto to Lajes (East of Azores)
	C142	20/02/2019	15:28:36–19:10:52	38.8–39.6	-36.3– -27.1	Lajes to Lajes (West of Azores)
	C143	21/02/2019	10:44:25–15:24:48	30.5–38.9	-28.6– -27.1	Lajes to Lajes (South Azores)
	C144	22/02/2019	09:38:52–13:04:06	38.8–52.0	-27.2– -8.49	Lajes to Cork (North East of Azores)
	C145	22/02/2019	14:22:31–16:02:52	50.3–52.1	-9.33– -0.571	Cork to Cranfield

the locations of the first four ACSIS campaigns, with flight tracks coloured by altitude. 'Quicklook' files showing a time series of the flight, a flight track and profile information have been generated for all flights and are presented in Appendix A.

5.2.1 Meteorology during the ACSIS campaigns

Figure 5.3 shows how the NAO has changed since 1950, with positive phase NAO shown in red and negative phase NAO in blue. For all four ACSIS campaigns the NAO was in the positive phase though to different magnitudes. The NAO was 1.0 for ACSIS 1 (February 2017), 0.19 for ACSIS 2 (October 2017), 2.12 for ACSIS 3 (May 2018) and 0.29 for ACSIS 4 (February 2019). In order to determine where the air masses sampled during the four ACSIS campaigns were coming from, 96 hour HYSPLIT back trajectories were run for the mid-point of each straight level run with the results presented in Fig. 5.4. All four campaigns were influenced by air passing over North America, with air masses originating west of the Azores dominating. The strong dominance of westerly wind is expected for positive NAO values. There was also influence from air masses from Europe and south of the UK on some of the most easterly flights from the UK or Ireland.

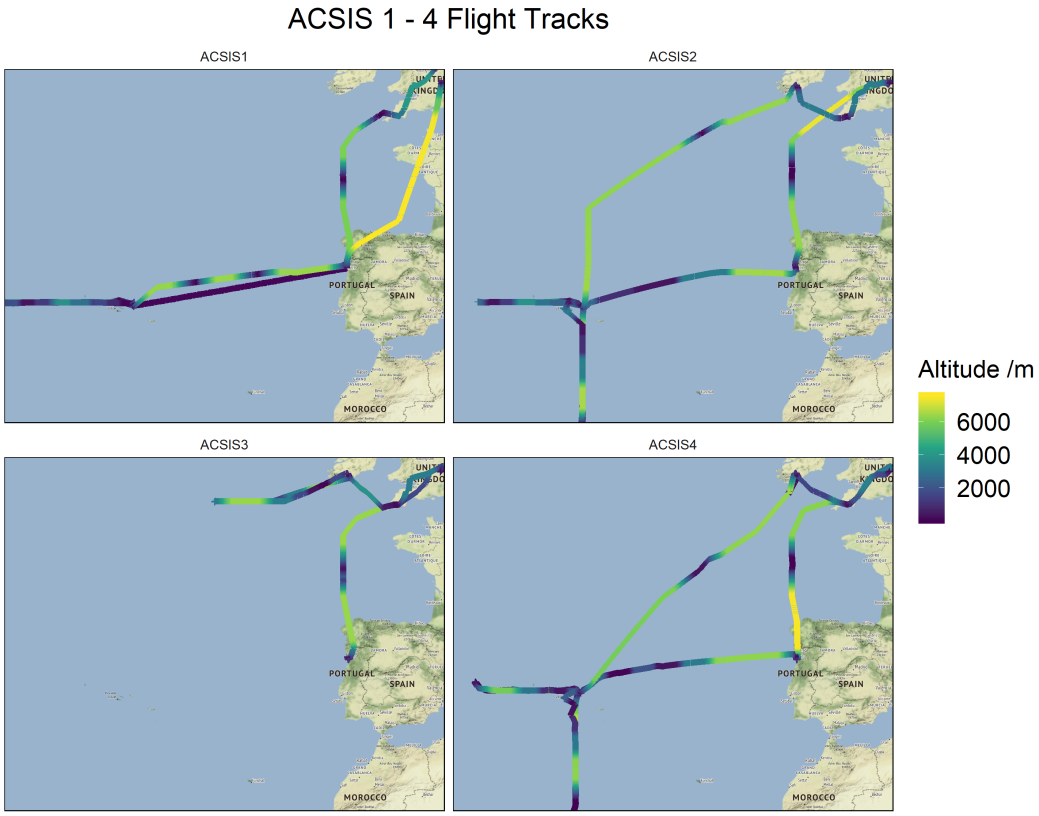

Figure 5.2: Locations of the 20 flights completed as part of the first four ACSIS campaigns. Flight tracks are coloured by altitude.

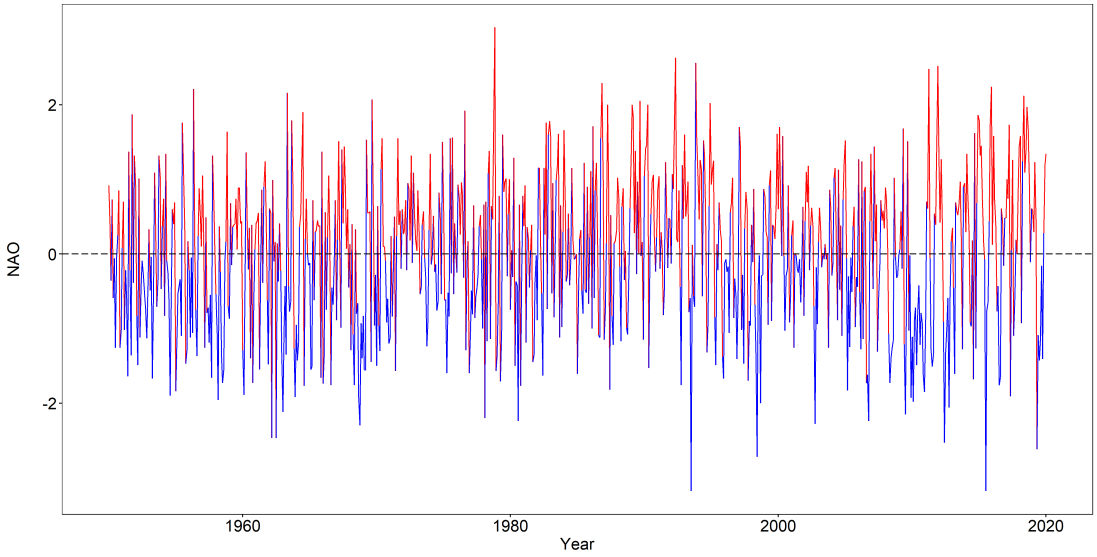

Figure 5.3: Time series of the NAO values since 1950. Data is taken from National Oceanic and Atmospheric Administration [2020].

5.3 Vertical distribution of pollutants

Figure 5.5 shows the vertical profiles for O_3, CO, NO, NO_2, CO_2 and CH_4 for all 20 flights across the four campaigns. Mean O_3 mixing ratios were lowest in the bottom two kilometres of the atmosphere with a mean mixing ratio of 44 ppbv $\pm$ 5.0 ppbv (0–1000 m) and 46 ppbv $\pm$ 6.6 ppbv (1000–2000 m), though there were more outliers in the lowest kilometre of the atmosphere with a minimum measured value of 14 ppbv. Between 2000–5000 m, O_3 mixing ratios were stable with a mean mixing ratio of 51 ppbv $\pm$ 10 ppbv. Between 5000–6000 m, the mean O_3 mixing ratio was slightly elevated at 55 ppbv $\pm$ 13 ppbv and between 6000–7000 m the mean mixing ratio was 49 ppbv $\pm$ 13 ppbv. A wider range of O_3 mixing ratios were observed in the free troposphere with a maximum value of 118 ppbv recorded between 5000–6000 m.

CO mixing ratios are highest in the lowest kilometre of the atmosphere, with a mean value of 117 ppbv $\pm$ 13 ppbv. CO mixing ratios decreased to a minimum between 3000 and 4000 m, with a mean value of 102 ppbv $\pm$ 19 ppbv though up to 202 ppbv was measured at this altitude, similar to the range recorded for the atmosphere below. Above 4000 m, the mean CO mixing ratio was enhanced, though a

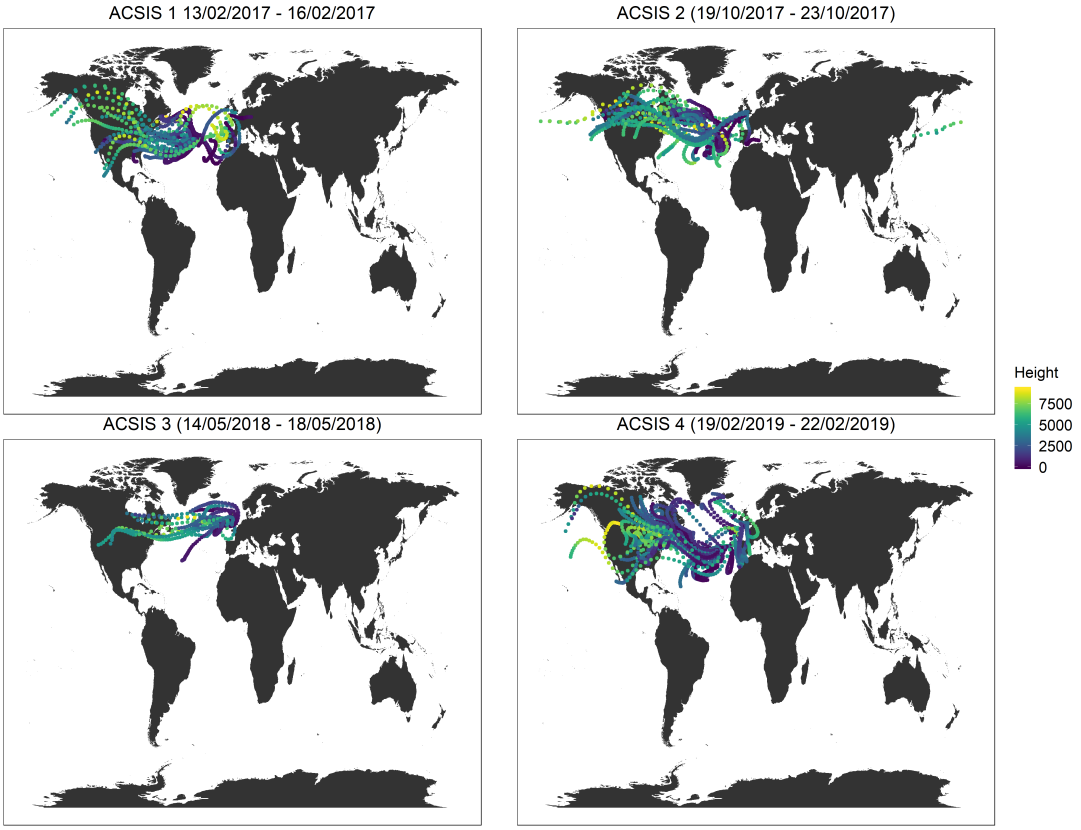

Figure 5.4: 96 hour HYSPLIT back trajectories for the four ACSIS campaigns. Trajectories were initiated at the midpoint of every straight-level run during the flights and are coloured by air mass altitude.

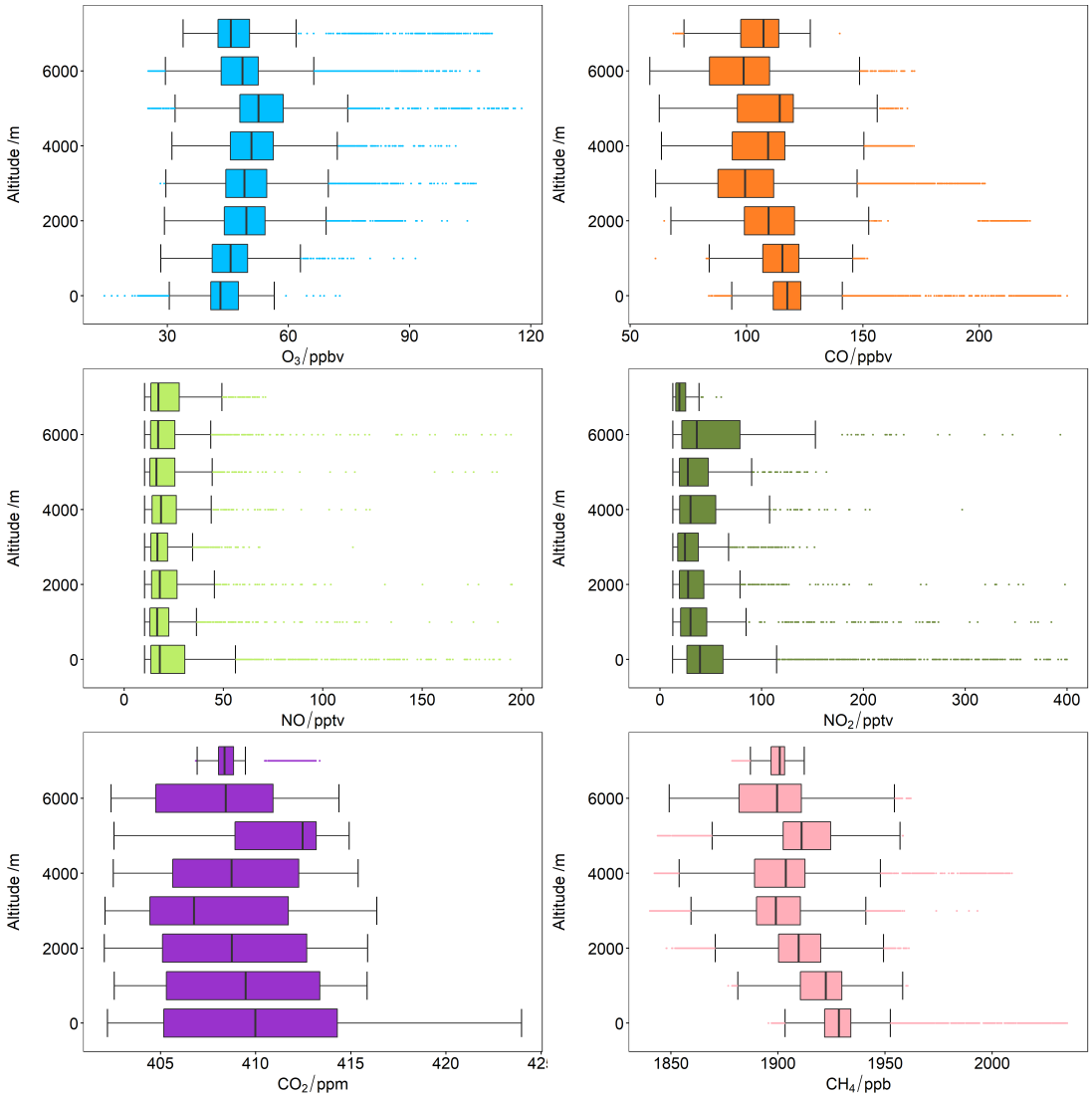

Figure 5.5: Box plots showing the vertical distribution of O_3, CO, NO, NO_2, CO_2 and CH_4 for all four ACSIS campaigns. Flight data is filtered to only include sections noted as "straight level runs" and "profiles" to avoid erroneous data from aircraft turns etc. Note that due to high mixing ratios of NO and NO_2 these data have been filtered to only show data below 200 pptv for NO and 400 pptv for NO_2.

smaller overall range of mixing ratios were observed at these levels with fewer "outliers" (instances higher than 1.5× the interquartile range (IQR)) than lower in the atmosphere. Mean CO mixing ratios in the top part of the atmosphere were 106 ppbv ± 19 ppbv (4000–5000 m), 108 ppbv ± 18 ppbv (5000–6000 m), 97 ppbv ± 16 ppbv (6000–7000 m) and 104 ppbv ± 11 ppbv (7000–8000 m).

NO and NO_2 mixing ratios follow a similar profile, as would be expected. The highest average mixing ratios are observed up to 1000 km in the atmosphere, with a wide range of mixing ratios measured due to influence from local sources. The median NO mixing ratio was 18 pptv ± 20 pptv (± IQR) and median NO_2 mixing ratio was 41 pptv ± 42 pptv (± IQR) for the lowest kilometre of the atmosphere. Average NO and NO_2 mixing ratios are uniformly distributed above 1000 m, aside from an enhancement between 6000–7000 m. In this region, maximum mixing ratios of 807 pptv and 467 pptv (note high NO_x values are not shown on Fig. 5.5) were recorded for NO and NO_2 respectively, suggesting the sample of a higher NO_x air mass at this altitude on one of the flights possibly caused by transport and mixing or from higher altitude formation due to lightning. Lightning NO_x is one of the most important sources of NO_x in the upper troposphere [Pickering et al., 1998]. Airborne observations made over Europe have shown that thunderstorms can lead to enhancements of several ppbv close to the storms and lead to enhancements of hundreds of pptv over wider regions as air is advected away from storms [Huntrieser et al., 2002]. At this altitude O_3, CO, CO_2, CH_4 mixing ratios appear to dip slightly.

CO_2 is uniformly distributed throughout the atmosphere up to 5000 m with a similar range of mixing ratios measured. The highest CO_2 mixing ratios were observed in the lowest kilometre of the atmosphere as for CO and NO_x. Between 5000 and 6000 m mean CO_2 mixing ratios are enhanced, with a mean value of 411 ppm ± 3.3 ppm. Above this the CO_2 mixing ratios decrease slightly. Between 7000–8000 m a narrower range of mixing ratios were observed compared to the rest of the atmosphere, though fewer observations were made at this level, possibly driving this.

CH_4 had a similar profile to that of CO, with the highest mixing ratios observed between 0–1000 m (mean CH_4 was 1930 ppb ± 14 ppb), decreased to the lowest observed mixing ratios between 3000 and 4000 m (mean CH_4 was 1900 ppb ± 19 ppb), above which CH_4 was elevated. Like CO_2, there was an enhanced layer in CH_4 be-

tween 5000 and 6000 m with a mean value of 1909 ppb ± 21 ppb.

5.3.1 Determining boundary layer height

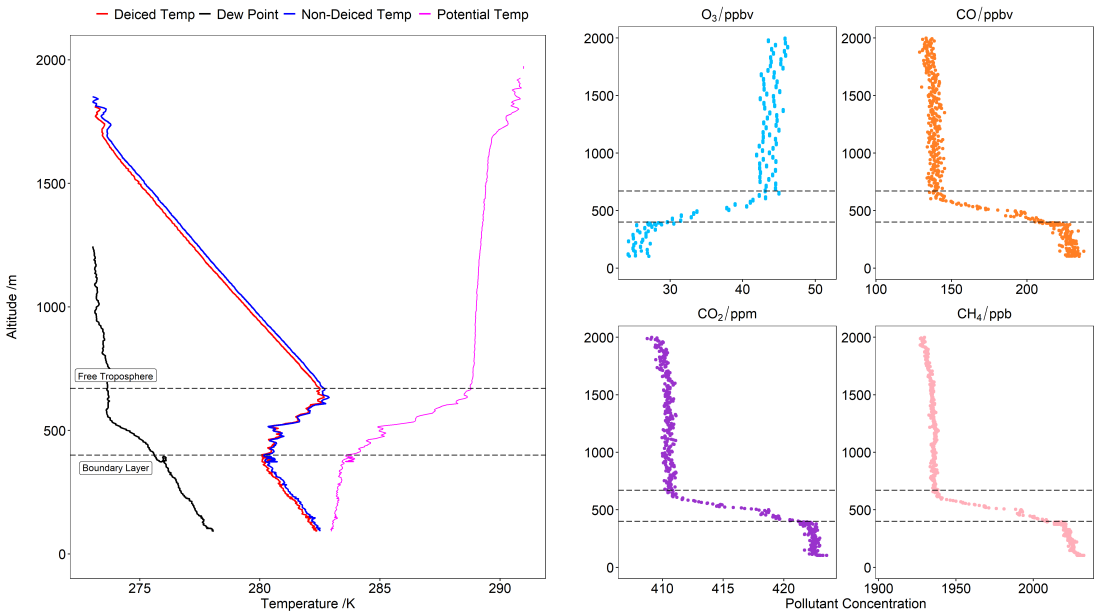

Figure 5.6: A profile from flight B996 showing the method used to determine boundary layer height and free troposphere. Within the boundary layer and the free troposphere (below and above dashed lines) potential temperature is relatively constant compared to the "transition layer" where the gradient changes. Changes in pollutant mixing ratios are generally seen between the boundary layer and the free troposphere as shown for O_3, CO, CO_2 and CH_4 in this profile.

It is overly simplistic to consider vertical distribution in 1000 m bins and it is important to determine the height of the boundary layer (or mixed layer height) to investigate its impact on pollutant mixing ratios. There are numerous methods to determine boundary layer from aircraft measurements [Dai et al., 2014]. Boundary layer height was determined for ACSIS 1–4 using the temperature gradient method as generally in the troposphere there is a temperature inversion at the boundary layer. This method has been widely used for identifying the boundary layer height for studies using aircraft

data [Lee et al., 2018]. For the ACSIS flight data, most flights had at least one long profile (from the surface to $>$ 6000 m) which was used to determine any temperature inversion layer. Potential temperature, "the temperature that an unsaturated parcel of dry air would have if brought adiabatically and reversibly from its initial state to a standard pressure, p_0, typically 100 kPa." [American Meteorological Society, 2012b], was calculated for each flight and plotted against altitude, alongside dew point temperature and air temperature. Figure 5.6 shows an example profile for flight B996 from which the boundary layer height was determined. Boundary layer top was defined as the starting point where the temperature gradient begins to change from the well mixed air below. Most flights showed a clear "transition layer" between the boundary layer top and free troposphere, as shown in Fig. 5.6 where there is a temperature inversion and change in gradient. The start of the free troposphere was defined as where the temperature gradient changed and the air became homogeneous once again. For some flights, the temperature profile did not show a clear temperature inversion layer so mixing ratios of CO, O_3, CO_2 and CH_4 were plotted against altitude and also used as a secondary check.

5.3.2 Comparison of pollutant mixing ratios within the boundary layer and in the free troposphere

Figure 5.7 compares pollutant mixing ratios measured within the boundary layer and the free troposphere. Mean O_3 within the boundary layer was 43 ppb $\pm$ 5 ppb, and ranged from 14–64 ppbv whereas O_3 mixing ratios were in the free troposphere were higher. Mean O_3 mixing ratios in the free troposphere were 50 ppb $\pm$ 11 ppbv and ranged from 25–118 ppbv. All other pollutants had higher mixing ratios within the boundary layer compared to above it. Mean CO mixing ratios in the boundary layer were 117 ppb $\pm$ 13 ppbv and 105 ppb $\pm$ 18 ppbv in the free troposphere. NO and NO_2 were varied within the boundary layer due to influence from local sources ranging between 10 and 13000 pptv and 13 and 4100 pptv respectively (note that high NO_x values have been omitted from Fig. 5.7). Median NO and NO_2 mixing ratios within the boundary layer were 20 pptv $\pm$ 20 pptv and 42 pptv $\pm$ 41 pptv respectively. In the free troposphere, median NO and NO_2 mixing ratios were 17 pptv $\pm$ 11 pptv and 30 pptv $\pm$ 30 pptv respectively. Mean CO_2 mixing ratios were similar in the

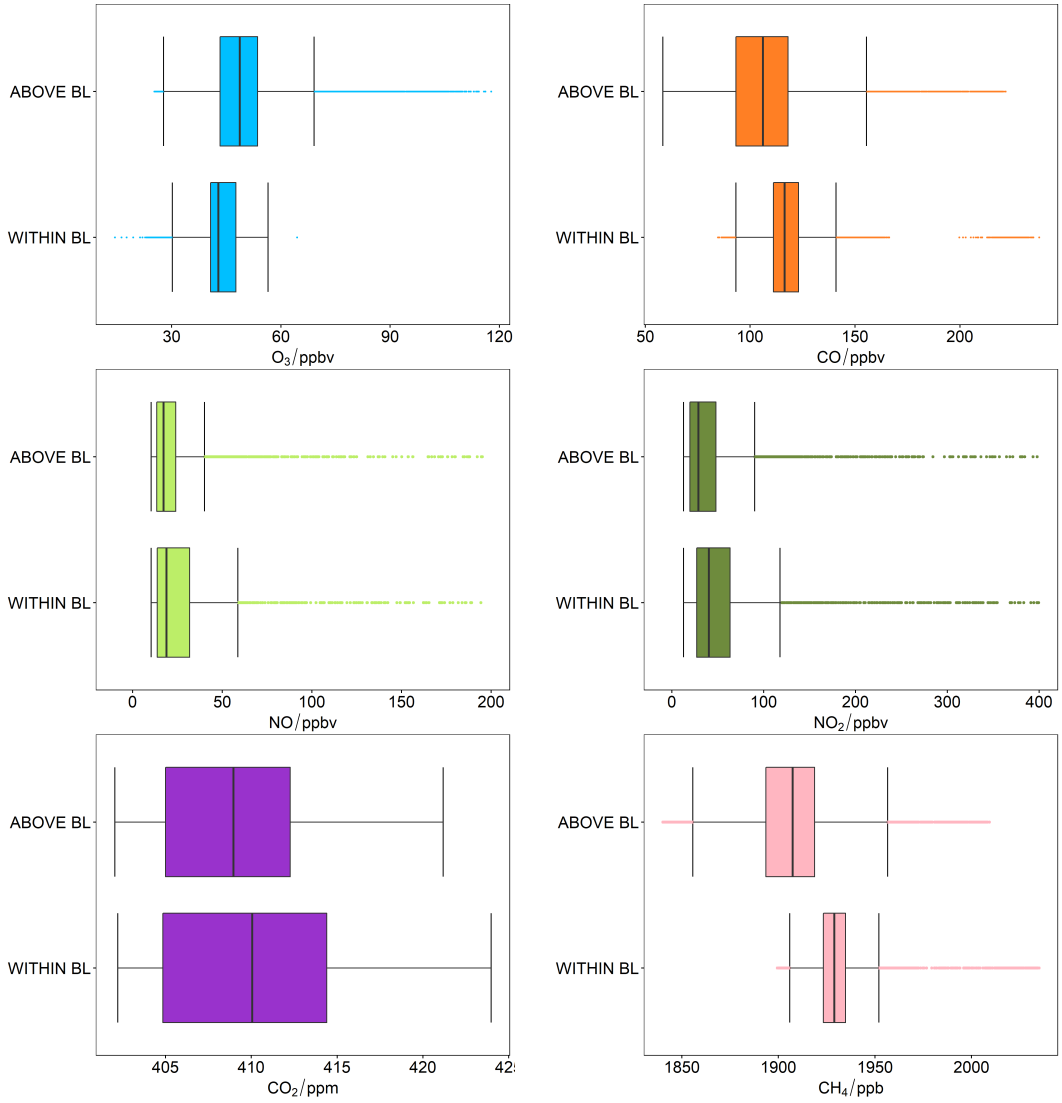

Figure 5.7: Mixing Ratios of O_3, CO, NO, NO_2, CO_2 and CH_4 above and below the boundary layer. All four ACSIS campaigns are included in this grouping. Note that due to high mixing ratios of NO and NO_2 these data have been filtered to only show data below 200 pptv for NO and 400 pptv for NO_2.

free troposphere (409 ppm ± 4 ppm) and boundary layer (410 ppm ± 5 ppm) but a wider range of values were observed within the boundary layer. CH_4 showed greater variability between the two with a mean mixing ratio of 1930 ppb ± 14 ppb within the boundary layer and 1900 ppb ± 21 ppb in the free troposphere.

5.4 Spatial distribution of pollutants

In order to gain some understanding of the spatial distribution of pollutants over the North Atlantic, the relationship between pollutant mixing ratio and longitude and latitude are shown in Figs. 5.8 and 5.9. Figure 5.8 shows that all species apart from O_3 are enhanced within the boundary layer between 0–10 °W. Within this longitude range, there is enhanced shipping activity with some of the main shipping lanes entering the English Channel here. The enhancements within the boundary layer are likely to be influenced by local sources such as ship or possibly emissions from Europe in some cases. The dip in O_3 mixing ratios in this region is likely due to its titration with the higher NO_x mixing ratios observed in this region. In the free troposphere, or above the boundary layer, there are some enhancements in pollutants within this longitude range. This enhancement is most notable in NO_x, CH_4 and CO and suggests some mixing from surface emissions to higher up into the atmosphere. Further west, NO_x mixing ratios within the boundary layer flatten out and remain low. There are few shipping lanes or land masses in this region and the lifetime of NO_x is short (on the order of < 1 day in the lower free troposphere [Val Martin et al., 2008] and so mixing ratios remain low. Above the boundary layer there is a some more variability in NO_x, with a small enhancement around 30 °W. CO mixing ratios within the boundary layer remain low and stable between 20–40 °W. In the free troposphere however, CO is enhanced between 20–40 °W, possibly due to long range transport of emissions. This enhancement within the free troposphere is also observed for CH_4 with low and stable CH_4 mixing ratios for the same region within the boundary layer. CO_2 mixing ratios are more variable compared to other species. For CO_2 in the free troposphere, mixing ratios decrease between 0–20 °W and there are some enhancements between 20–30 °W. It is difficult to see any trends in CO_2 mixing ratios within the boundary layer, though there appears to be some enhancements around 20 °W and 30 °W. O_3 mixing ratios are

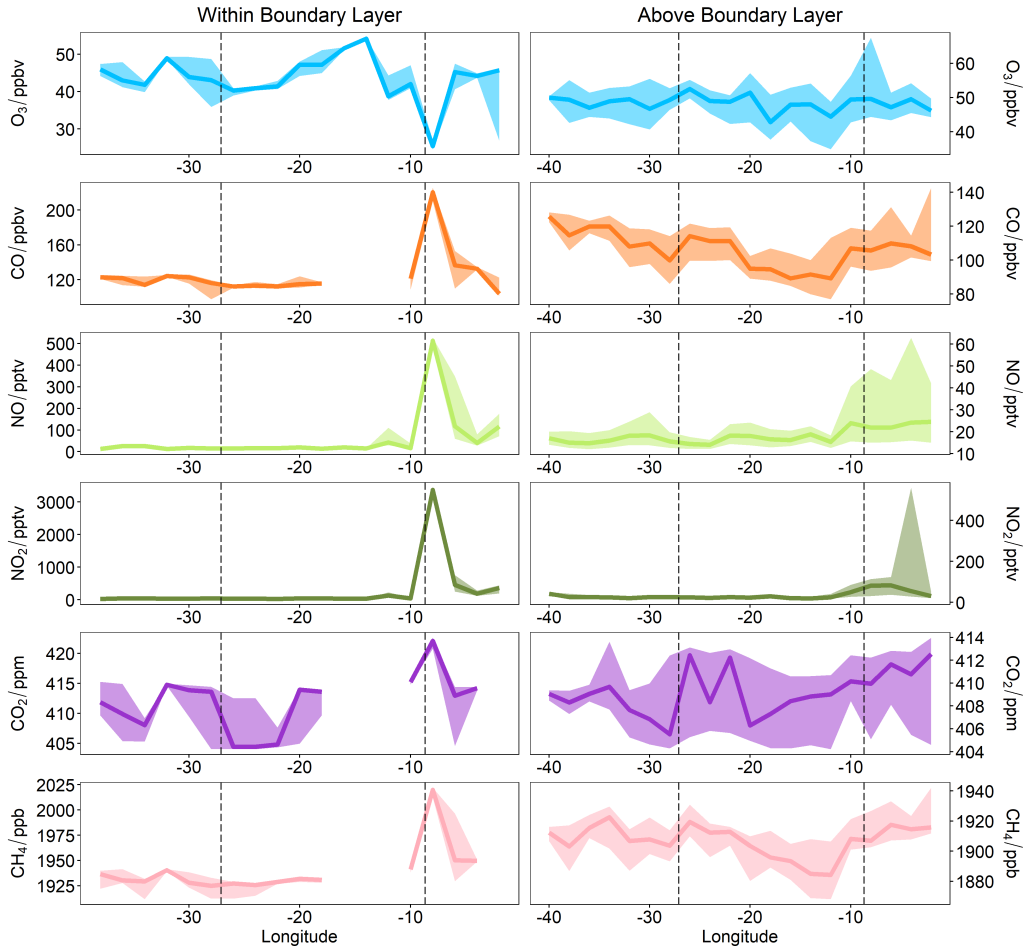

Figure 5.8: Mixing ratios of O_3, CO, NO, NO_2, CO_2 and CH_4 as a function of longitude. Data presented has been grouped into 2° longitude bins and the median value presented as a thick line and the shaded areas represent the lower and upper quartiles of the data. The dashed line at -27.1° and -8.68° are the longitudinal positions of Lajes Airport and Porto Airport respectively. All four ACSIS campaigns are included in this grouping.

enhanced within the boundary layer at 14 °W and 32 °W and are homogeneous within the free troposphere between 20–40 °W.

In terms of variability with latitude, shown in Fig. 5.9, NO_x within the boundary layer was enhanced at the most northerly point of the flight track (48–52 °N) where there is likely to be more shipping activity and influence from the European continent. CO within the boundary layer peaks at 50 °N (136 ppbv) with a dip at 48 °N (110 ppbv), as does CH_4 and CO_2, though there is no GHG information for areas further north. In general O_3 mixing ratios appear to follow CO mixing ratios closely with a maximum value of 46.9 ppbv recorded at 50 °N, falling to 37.1 ppbv at 48 °N. Further south, there is little variability of NO_x measured within the boundary layer between 30–46 °N. O_3 and CO mixing ratios remain largely constant within the boundary layer between 38–46 °N. CH_4 steadily decreases from its maximum at 50 °N (1951 ppb) to a minimum (1913 ppb) at 32 °N within the boundary layer. CO_2 mixing ratios within the boundary layer are lowest at 32 °N with a value of 404 ppm, though measurements showed a large degree of variability. Above the boundary layer, CO_2 mixing ratios do not show much variability. A median CO_2 mixing ratio of 410–411 ppm was measured between 36 and 50 °N with lower median mixing ratios north and south of these points. For CH_4, mixing ratios are generally lower in the free troposphere compared to within the boundary layer and peak at 32 °N, 38 °N and 46 °N. NO and NO_2, measured above the boundary layer, are enhanced between 40 and 50 °N with median mixing ratios between 17–32 pptv and 35–65 pptv respectively. CO ranged between 90 and 115 ppbv in the free troposphere, lower than within the boundary layer. The largest CO value was measured at 38 °N and average mixing ratios were consistent between 44 and 50 °N. O_3 was higher in the free troposphere than the boundary layer and ranged between 45 ppbv and 51 ppbv with averages uniformly distributed through the latitude range covered during the flights.

In order to investigate the spatial variation in atmospheric composition further, flights were grouped into five areas; north, east, south and west of the Azores archipelago and west of Cork, shown in Fig. 5.10. Any parts of the flights which occurred overland were removed. Table 5.2 shows the statistics for the flights within each area. The highest average (mean and median) mixing ratios of O_3 and NO_x were associated with flights in the west Ireland area. For CO and CO_2 the highest mixing

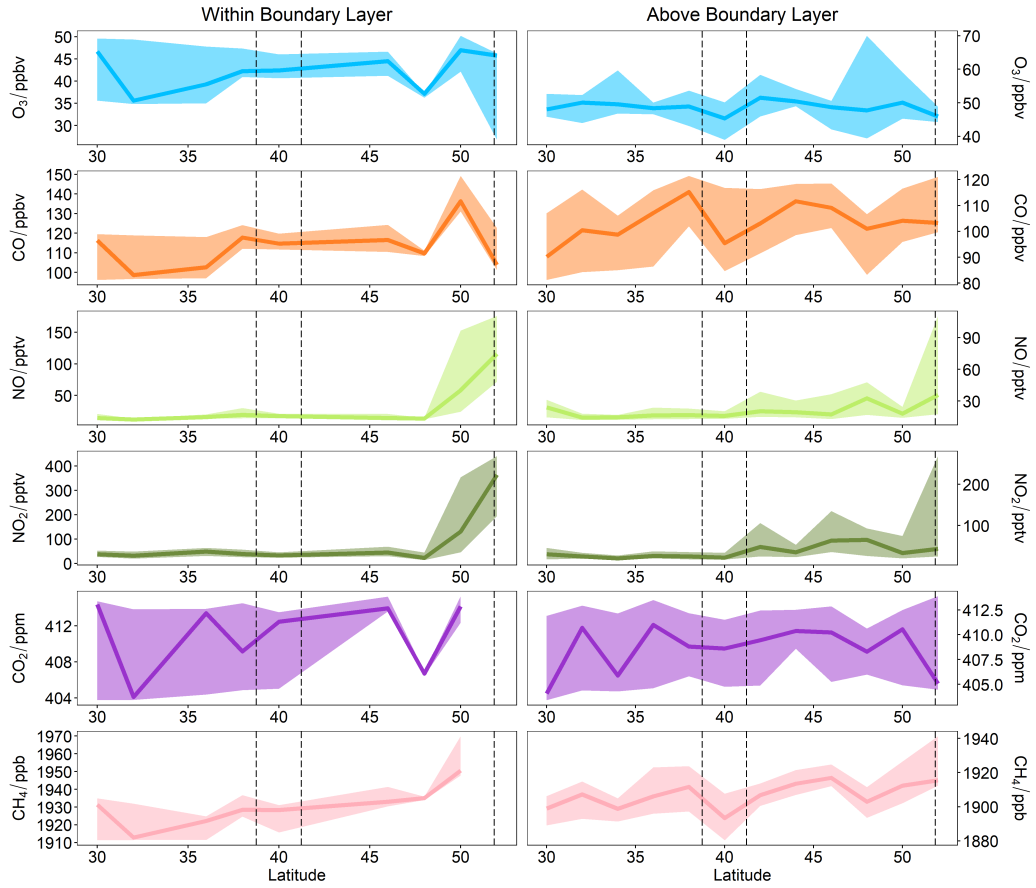

Figure 5.9: Mixing ratios of O_3, CO, NO, NO_2, CO_2 and CH_4 as a function of latitude. Data presented has been grouped into 2° latitude bins and the median value presented as a thick line with the shaded areas showing the lower and upper quartiles of the data. Dashed lines at 38.7°, 41.2° and 51.4° are the latitudinal positions of Lajes Airport, Porto Airport and Cranfield Airport respectively. All four ACSIS campaigns are included in this grouping.

Table 5.2: Key statistics for O_3 (ppbv), CO (ppbv), NO (pptv), NO_2 (pptv), CO_2 (ppm) and CH_4 (ppb) grouped by area. LQ, UQ and SD refer to the lower and upper quartiles and standard deviation of the data respectively. Note that NO and NO_2 mixing ratios are reported over a 10 s averaging period unlike all other data reported over a 1 s averaging period explaining their apparent low number of observations.

Area	Species	Mean	Median	SD	LQ	UQ	Minimum	Maximum	*n*
	O_3	48.42	47.52	10.22	42.16	51.92	14.39	117.7	217242
	CO	107.9	110.5	17.11	96.89	119.1	58.38	237.7	175936
All	NO	34.16	17.56	148.8	13.51	26.05	10.30	12790	9769
	NO_2	86.55	33.92	288.1	21.70	57.59	12.61	4109	7201
	CO_2	409.1	409.0	3.831	405.0	412.6	402.0	424.0	159775
	CH_4	1910	1911	21.42	1899	1926	1840	2035	159775
	O_3	50.70	50.18	4.01	48.81	52.34	38.10	65.42	9983
	CO	105.23	102.70	14.61	97.54	118.09	66.85	132.97	8283
North	NO	16.46	14.97	5.49	12.44	18.91	10.31	46.66	454
	NO_2	30.55	25.94	18.44	19.49	32.95	13.03	132.01	116
	CO_2	408.22	405.24	4.15	404.68	412.93	402.90	414.59	8111
	CH_4	1912.44	1915.30	13.88	1907.85	1919.67	1869.61	1936.65	8111
	O_3	49.59	41.32	14.27	40.61	55.43	38.70	117.70	5251
	CO	111.76	111.80	7.64	109.29	116.37	86.42	126.93	4598
East	NO	21.16	16.48	18.61	13.71	20.98	10.33	153.93	277
	NO_2	41.64	31.87	42.13	21.83	43.89	12.82	328.31	285
	CO_2	406.29	404.30	3.64	403.98	407.70	402.95	413.39	4420
	CH_4	1921.09	1926.46	11.98	1919.02	1928.24	1881.86	1932.95	4420
	O_3	47.28	47.53	8.42	41.67	51.46	31.82	68.84	12701
	CO	99.62	98.35	13.30	87.51	112.77	74.96	125.21	11050
South	NO	15.60	14.40	6.09	11.94	17.00	10.30	79.48	480
	NO_2	33.37	27.65	17.92	20.04	43.43	12.71	97.05	291
	CO_2	408.17	404.96	4.29	404.30	412.27	402.68	414.66	10794
	CH_4	1905.44	1904.25	13.43	1895.03	1911.92	1872.48	1935.79	10794
	O_3	46.10	45.52	5.62	41.64	49.65	32.51	70.32	19696
	CO	116.86	118.76	12.40	111.42	124.74	71.55	161.76	16936
West	NO	23.77	17.12	42.57	13.04	24.66	10.30	736.10	934
	NO_2	46.50	31.86	81.55	21.37	50.24	12.74	1307.72	876
	CO_2	409.09	408.76	3.30	406.32	410.40	403.42	415.92	16424
	CH_4	1917.57	1920.83	21.05	1908.19	1930.51	1854.08	2002.06	16424
	O_3	52.66	50.79	11.94	48.07	59.62	25.27	92.70	10022
	CO	91.79	95.84	11.64	83.13	99.26	64.09	119.30	2407
West Ireland	NO	25.53	17.43	39.21	14.14	22.15	10.32	663.19	586
	NO_2	70.31	36.34	92.48	22.21	91.45	12.71	1098.74	366
	CO_2	406.62	404.79	3.27	404.33	410.43	402.40	414.24	2710
	CH_4	1895.11	1908.10	21.93	1869.79	1913.03	1859.19	1929.33	2710

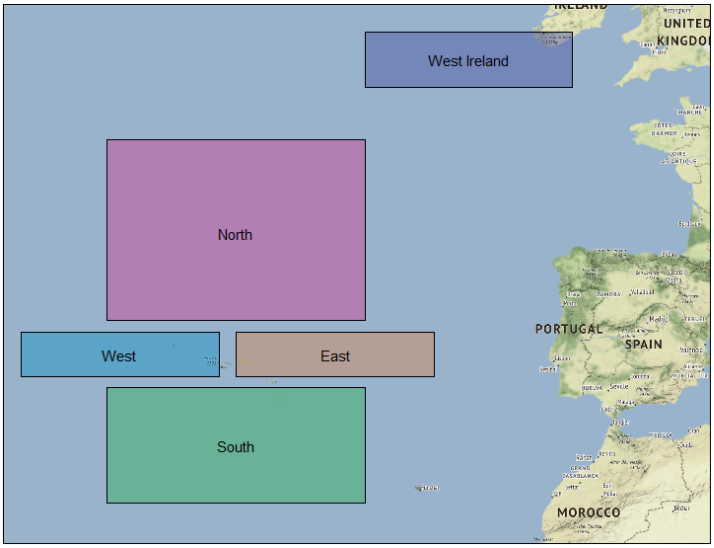

Figure 5.10: Map showing the grid boxes used for grouping flights for analysis.

ratios were measured during flights within the west (of the Azores) grouping with the highest average CH_4 measured east of the Azores. Figures 5.11a–5.11e show the mixing ratios of each pollutant separated for within boundary layer or above it for each area. For all areas, O_3 mixing ratio are higher in the free troposphere than within the boundary layer. In general, directly emitted pollutants (CO, NO_x, CH_4) show higher mixing ratios within the boundary layer compared to above it though there are some exceptions. For the "North" area, median mixing ratios of NO were higher in the free troposphere than within the boundary layer. During flights in the "North" and "South" areas high NO values ($>$ 40 pptv) were measured in the free troposphere, possibly due to recent lightning or a pollution transport event. These groupings show that for the most northerly parts of the North Atlantic NO_x pollution is more prevalent, due to shipping emissions and influence of European continental air, which could also be driving the slightly higher O_3 mixing ratios observed in this area. The open ocean west of the Azores is influenced by pollutant transport from North America leading to the higher CO mixing ratios measured in this region (9 ppbv higher than the average for all areas).

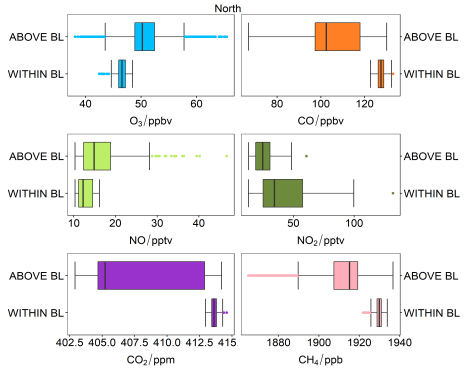

(a) North

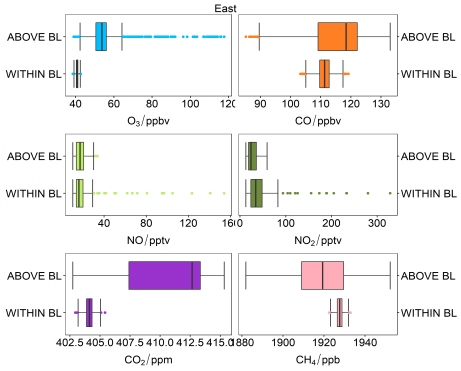

(b) East

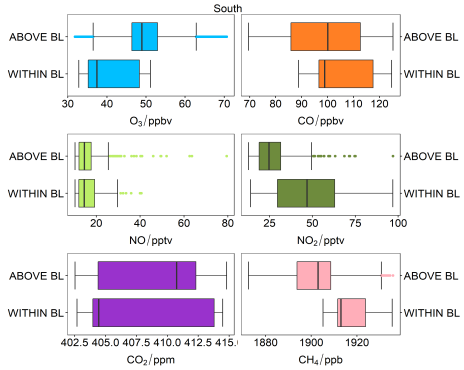

(c) South

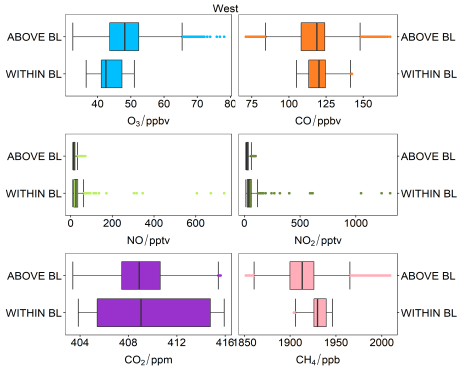

(d) West

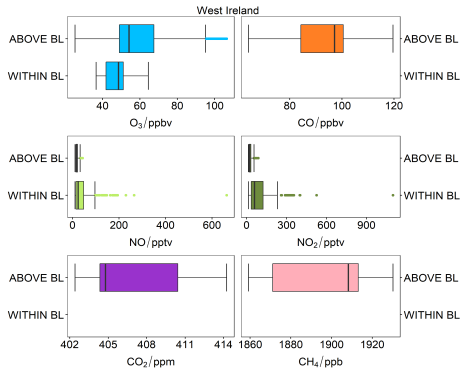

(e) West Ireland

Figure 5.11: Mixing ratios of O_3, CO, NO, NO_2, CO_2 and CH_4 above and below the boundary layer for each area grouping.

5.5 Investigating different air mass types

Over the four flight campaigns variability in pollutant mixing ratio is observed because a range of air masses with different chemical histories have been sampled. Figure 5.4 shows that during the four campaigns westerly winds dominated with many flights encountering air that had passed over North America. There was however, a high degree of variability in the history of the air masses. Previous studies, both airborne and ground-based, have attempted to classify air masses measured in the North Atlantic based on chemical composition and relationships between chemical species. A common method includes calculating the dO_3/dCO ratio, which provides information about changes in O_3 chemistry in the absence of fresh emissions and indicates the tendency for O_3 formation in a particular air mass. CO is longer lived in the troposphere, with a lifetime on the order of months rather than days or weeks as is the case for O_3. Whilst the relationship between O_3 and CO has been commonly investigated it is worth noting it is very difficult to link this relationship to sources due to a high degree of mixing of pollution plumes into a variable background [Parrish et al., 1998, Yokelson et al., 2013], however combined with back trajectory analysis and measurements of other species it can be a useful tool when classifying air mass type.

For the flights west and south of the Azores, the relationship between O_3 and CO mixing ratios was examined. Six flights (B998, B999, C068, C069, C142 and C143) were chosen as they cover an area free of major shipping lanes, unlike the area west of Ireland where enhancements in NO_x were observed. Figure 5.12 shows the relationship between O_3 and CO, coloured by run for each of the six flights, highlighting the number of different types of air masses encountered during a single flight.

5.5.1 Positive dO_3/dCO ratios

For some of the runs shown in Fig. 5.12 there is a positive correlation between O_3 and CO, suggesting O_3 formation [Parrish et al., 1993]. Figure 5.13 shows regression analysis for some of these runs that showed a positive relationship, during flights B998 and B999. dO_3/dCO for the air masses is taken as the reduced major axis (RMA) slope of the two species. RMA was used to determine the slope as it takes into account variability in both the x and y coordinates when determining fit, unlike standard linear

regression which is based on the assumption that variability only occurs in the y direction with the x values known precisely [Ayers, 2001, Parrish et al., 1998]. $d\mathrm{O_3}/d\mathrm{CO}$ values for the three runs vary between 0.15–0.68.

Biomass burning air mass

Numerous studies have demonstrated the influence of biomass burning and wildfires on the mid-North Atlantic region [e.g. Lapina et al., 2006, Lewis et al., 2007, Val Martin et al., 2008, Zhang et al., 2017]. Air masses influenced by biomass burning have enhanced CO mixing ratios and can affect $\mathrm{O_3}$ mixing ratios with $\mathrm{O_3}$ production in wildfire plumes widely reported, leading to enhancements in $\mathrm{O_3}$ [Jaffe and Wigder, 2012, and references therein]. Low $d\mathrm{O_3}/d\mathrm{CO}$ ratios have been associated with biomass burning influenced air masses, with ratios of 0.1–0.2 with plume ages between 2 and 5 days old reported in previous studies [Jaffe and Wigder, 2012]. Zhang et al. [2017] characterised different air masses sampled at Pico Mountain in the Azores by transport pattern and calculated $d\mathrm{O_3}/d\mathrm{CO}$ ratios for each type of air mass. In air masses associated with biomass burning the $d\mathrm{O_3}/d\mathrm{CO}$ was 0.12 for data recorded in the autumn. Data measured during summer has a higher $d\mathrm{O_3}/d\mathrm{CO}$ ratio of 0.31. $d\mathrm{O_3}/d\mathrm{CO}$ ratios tend to be lower for biomass burning plumes as there are high emissions of CO in wildfires.

Figure 5.13 shows that run 11 (mean altitude was 4400 m) during flight B998 has a $d\mathrm{O_3}/d\mathrm{CO}$ slope of 0.15, with CO ranging between 129 and 147 ppbv and $\mathrm{O_3}$ between 44 and 48 ppbv. Figure 5.14 shows the clear enhancement in CO compared to surrounding air masses which may be more representative of CO mixing ratios in the free troposphere. There is no continuous volatile organic compound data available for this flight but a sample taken during run 11 measured 3616 pptv of ethane and 87 pptv of ethene, considerably enhanced compared to the rest of the samples taken during flight B998. For other runs on the flight, the mean ethane mixing ratio was 2000 pptv and the mean ethene mixing ratio was 41 pptv. Lewis et al. [2007] commented that ethene was enhanced in biomass burning plumes encountered during flights over the North Atlantic when the air mass was sampled some days downwind of the fires. Enhancements of other VOC species in biomass burning plumes have been observed, namely acetylene, benzene, toluene, propane, *n*-butane and *iso*-butane [Lewis et al., 2007].

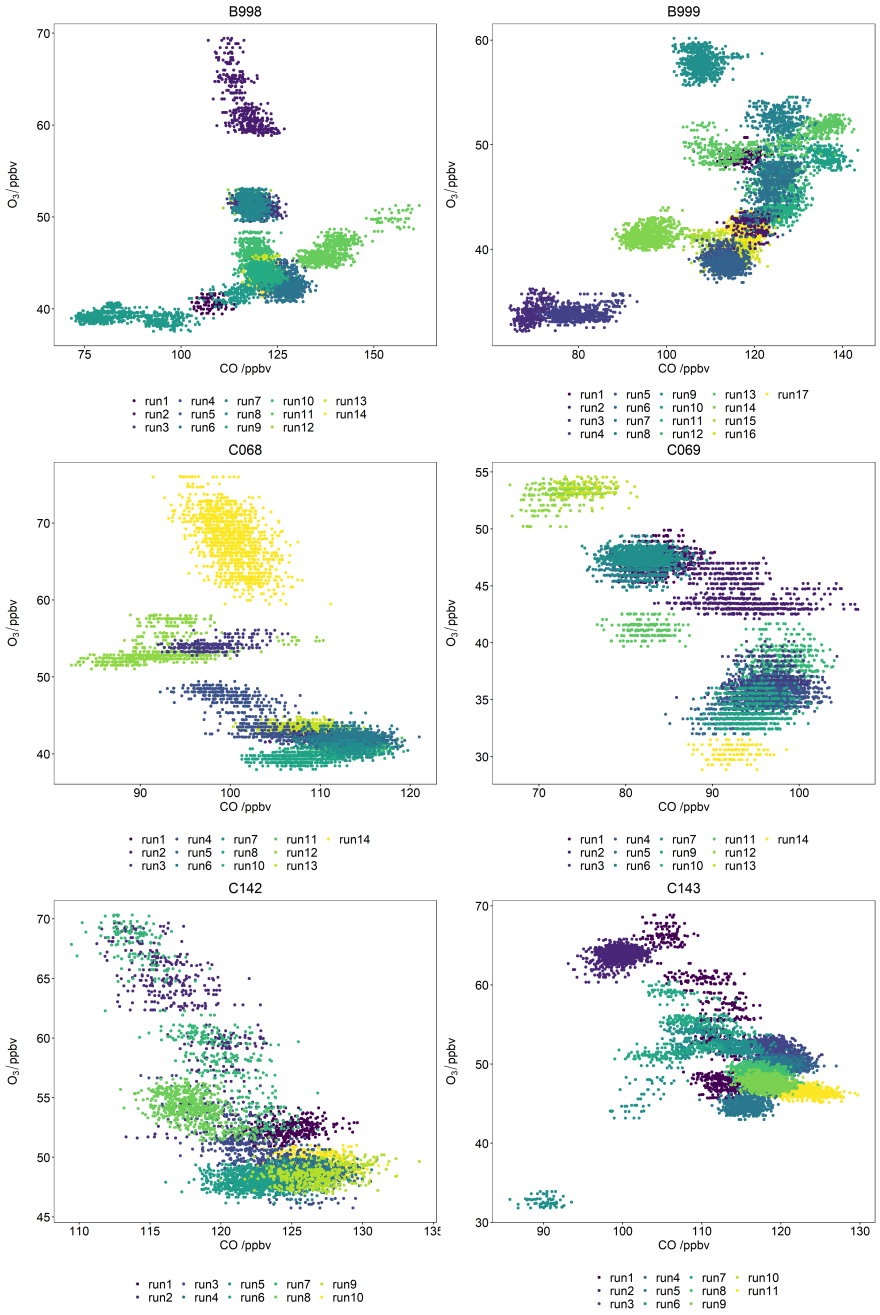

Figure 5.12: O_3 mixing ratio as a function of CO mixing ratio coloured by run number for flights south and west of the Azores. The different clusters highlight the variation in air mass sampled.

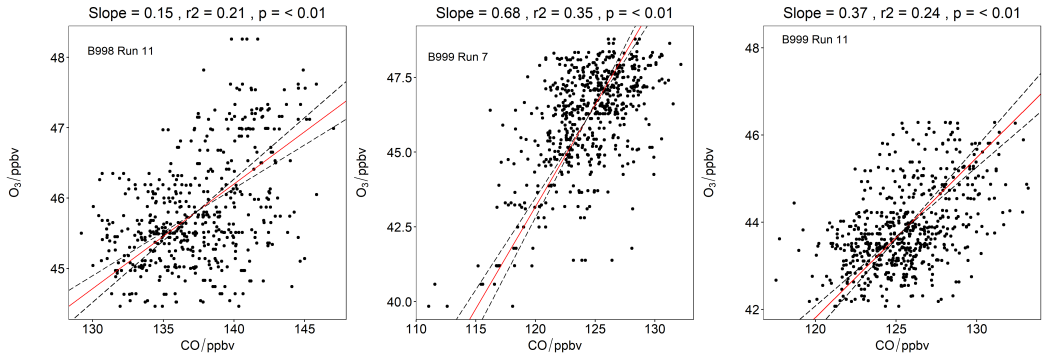

Figure 5.13: dO_3/dCO calculated for some flight runs that showed a positive correlation between O_3 and CO. Slope was calculated using a reduced major axis method which accounts for variability in both x and y coordinates. p is a measure of the statistical significance of the fit. The dashed black lines represent the error in the fit (95% confidence intervals).

Mixing ratios of all these species were enhanced compared to the median values measured during flight B998, summarised in Table 5.3. Enhancements in NO_x mixing ratios have been observed in biomass burning plumes measured in the North Atlantic. NO_x mixing ratios during run 11 on B998 were 40 pptv, but this value is not noticeably different from NO_x mixing ratios measured on other runs. Unfortunately no NO_y data is available. To assess whether a biomass burning influence was likely given the physical history of the air mass sampled during this run, a 96 hour back trajectory was computed using HYSPLIT, shown in Fig. 5.15. The map in Fig. 5.15 uses fire radiative power data from Global Fire Assimilation System (GFAS) for the 10th February 2017 to mark the location of active fires, shown by the orange dots. This suggests that the air mass is influenced by burning in the USA around the Gulf of Mexico and if this is the case the air mass sampled is on the order of 4 days since emission. Whilst ethene is enhanced relative to the average value for the rest of flight B998 by a factor of > 2, the mixing ratio measured is considerably lower than those measured by Lewis et al. [2007], where the mean value associated with biomass burning air was 410 pptv $\pm$ 380 pptv. Ethene has a lifetime on the order of 2 days [Dolan et al., 2016] which could explain the lower value observed compared to previous observations of biomass burning plumes. Toluene has a similar lifetime [Cabrera-Perez et al., 2016] and mixing

Table 5.3: Summary of VOC mixing ratios in a biomass burning plume observed during flight B998.

	B998 Run 11 Mixing Ratio	**Median Mixing Ratio B998**
Ethane /pptv	3616	2003
Ethene /pptv	87	35
Acetylene /pptv	264	253
Benzene /pptv	80	71
Toluene /pptv	19	1
Propane /pptv	1561	732
***n*-butane /pptv**	463	198
***iso*-butane /pptv**	200	98

ratios measured during run 11, B998 were lower than those reported by Lewis et al. [2007], where an average value of 43 pptv $\pm$ 41 pptv was reported for biomass burning plumes.

North American anthropogenic outflow

Pollution from North America has been reported to lead to enhanced O_3 and CO mixing ratios over the North Atlantic ocean. Zhang et al. [2017] reports $d\mathrm{O_3}/d\mathrm{CO}$ values of 0.45–0.71 for air masses associated with outflow from North America, with CO mixing ratios lower and O_3 mixing ratios slightly higher than those reported in biomass burning plumes. The air masses sampled during run 7 and run 11 on flight B999 (mean run altitudes were 970 and 360 m respectively, both within the boundary layer determined for the flight) had a $d\mathrm{O_3}/d\mathrm{CO}$ value of 0.68 and 0.37, close to or within the range of the values reported by Zhang et al. [2017]. The average O_3 and CO mixing ratios on these two runs were similar, with mean values of 46 ppbv and 124 ppbv (Run 7) and 44 ppbv and 126 ppbv (Run 11). Figure 5.16 shows a time series of the flight with run 7 and run 11 highlighted by pairs of dotted lines.

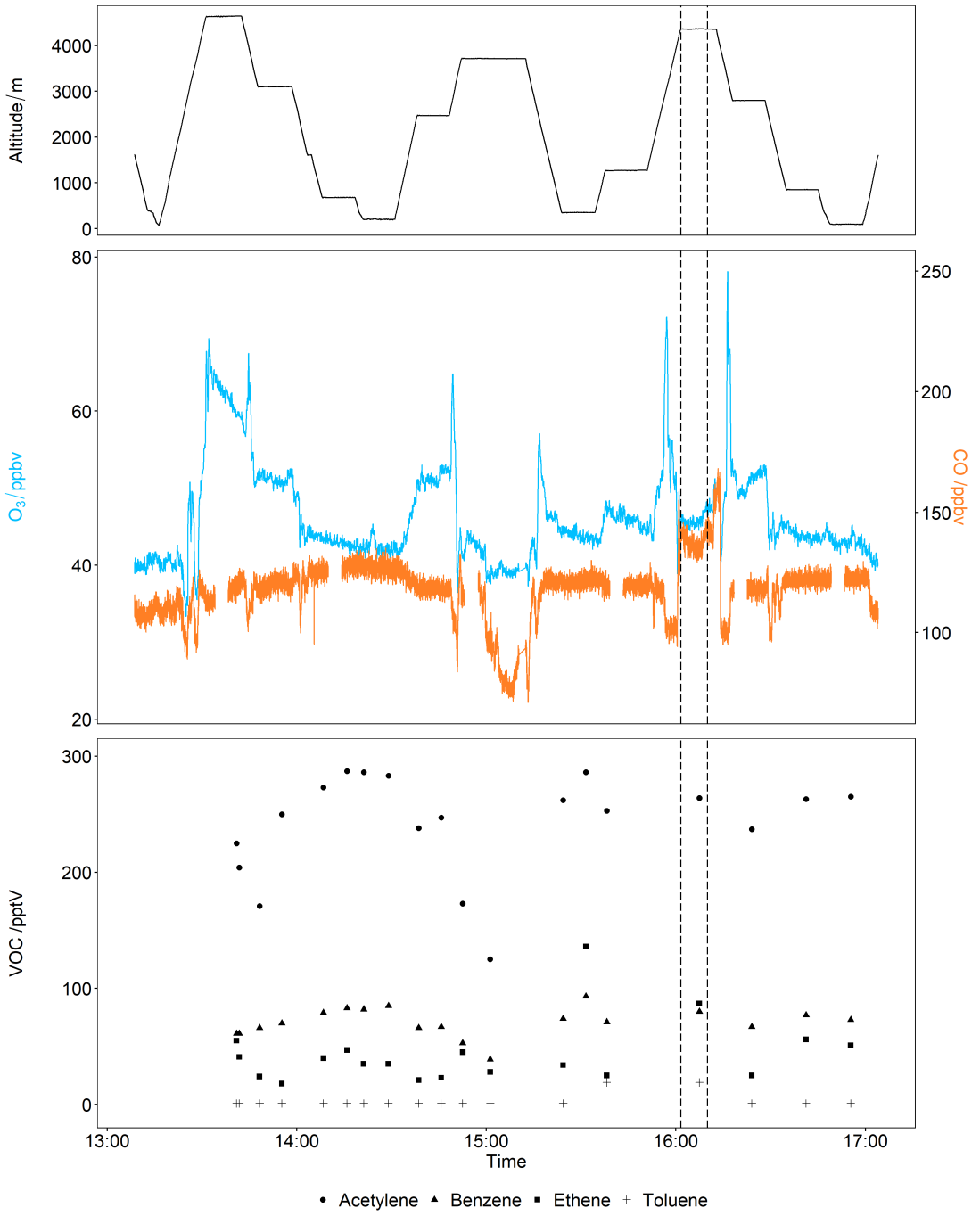

Figure 5.14: Time series of flight B998. The top panel shows altitude in metres, the middle panel shows O_3 (blue line) and CO (orange) mixing ratios and the lower panel shows acetylene, benzene, ethene and toluene mixing ratios measured in WAS. Run 11 is highlighted by dashed lines.

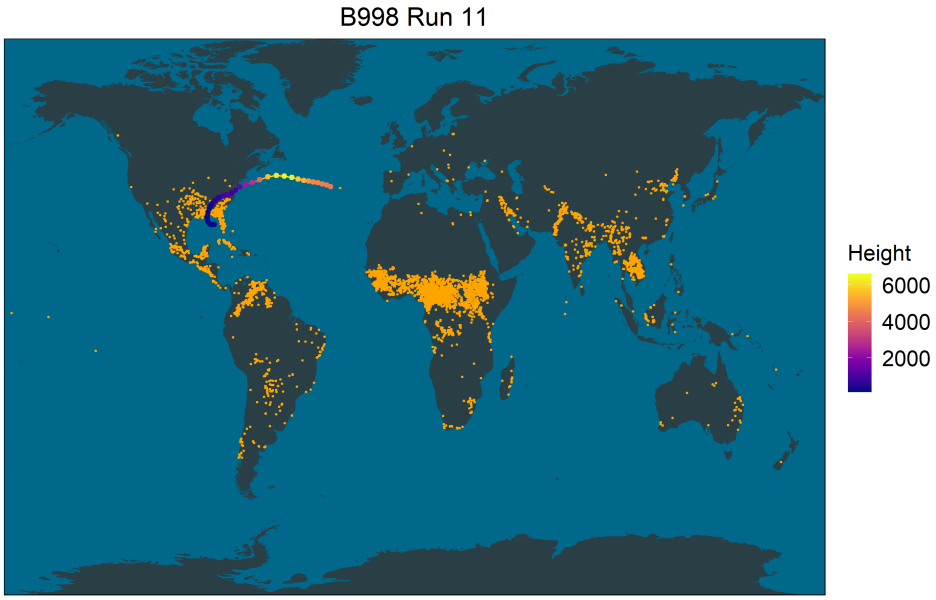

Figure 5.15: 96 hour HYSPLIT back trajectory initiated at the midpoint of run 11 on flight B998. Trajectory is coloured by height. Orange dots show the location of active fires on 10/02/2017, four days prior to flight B998. Fire location was determined using fire radiative power data from GFAS.

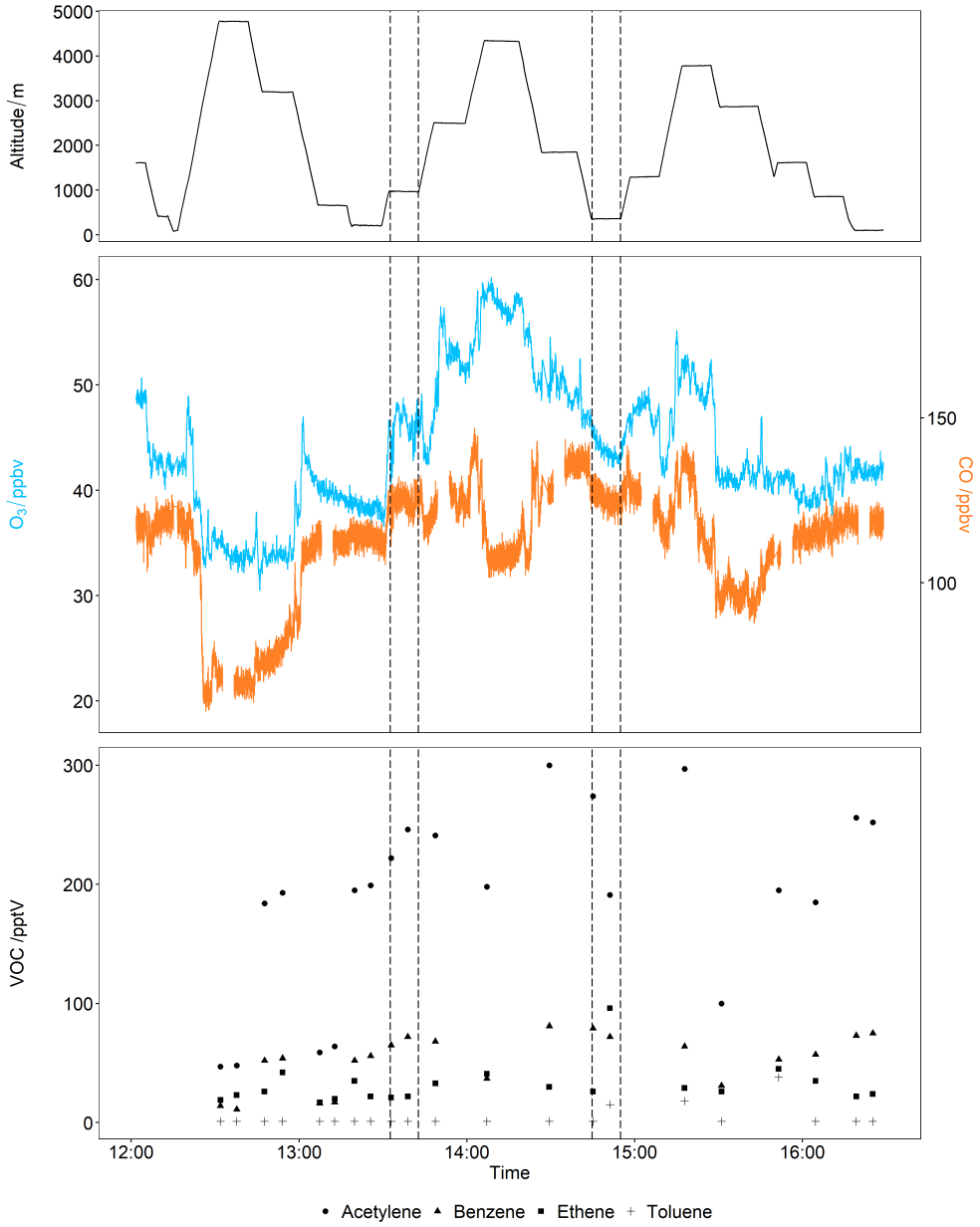

Figure 5.16: Time series of flight B999. The top panel shows altitude in metres, the middle panel shows O_3 (blue line) and CO (orange line) mixing ratios and the lower panel shows acetylene, benzene, ethene and toluene mixing ratios measured in WAS. Run 7 is highlighted by the first pair of dashed lines and run 11 by the second pair.

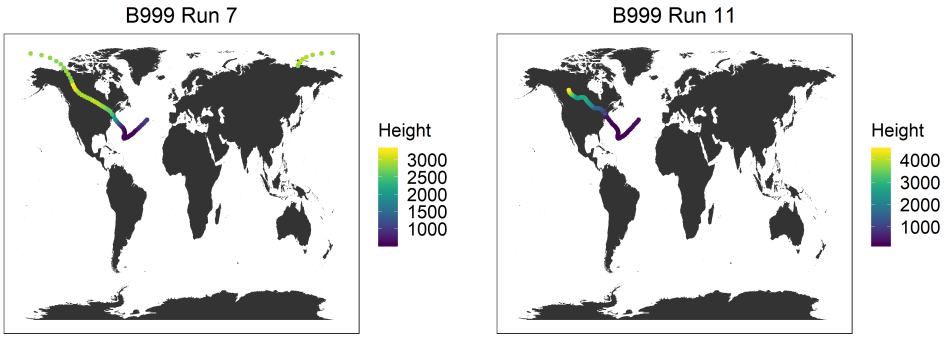

Figure 5.17: 10 day HYSPLIT back trajectory initiated at the midpoint of each run. Trajectory is coloured by height. These back trajectories indicate that the air masses sampled were slow having spent $>$ 4 days within the boundary layer.

For the VOC species shown in Fig. 5.16 there are no striking enhancements during runs 7 and 11, though the second sample taken during run 11 shows enhanced toluene and ethene. A 10-day back trajectory for these runs is presented in Fig. 5.17. It would be expected that O_3 and CO would be preserved over 10 days given their lifetimes in the troposphere. Runs 7 and 11 on flight B999 sampled air masses that have a similar history. The 10 day back trajectories showed that these air masses spent $>$ 4 days within the marine boundary layer and passed over east coast of the US at a low altitude (approximately 1500 m). The east coast of the US is a densely populated, industrialised region which would lead to enhancements in CO in these air masses as is observed. The discrepancies in the dO_3/dCO slope for the two runs are likely due to mixing with different types of air masses. Given the history of the air mass some enhancements in longer-lived hydrocarbons may be expected during the runs. Zhang et al. [2017] showed that propane and butane were enhanced in air masses associated North American anthropogenic outflow. Table 5.4 shows the average mixing ratios for some VOCs measured during runs 7 and 11 on flight B999 compared to the average for the flight. Ethane, acetylene, benzene, propane and *iso*-butane are enhanced in both runs compared to the average for the flight which further supports the idea that these air masses have been influenced by anthropogenic sources.

Table 5.4: Summary of VOC mixing ratios observed during runs 7 and 11 during flight B998.

	B999 Run 7 Mixing Ratio	**B999 Run 11 Mixing Ratio**	**Median Mixing Ratio B999**
Ethane	1911	1891	1790
Ethene	22	61	26
Acetylene	234	233	195
Benzene	69	76	56
Propane	583	613	540
***n*-butane**	128	140	120
***iso*-butane**	63	75	58

5.5.2 Negative dO_3/dCO Ratios: The influence of free tropospheric air

Section 5.5.1 discussed three examples where there was a positive correlation between O_3 and CO mixing ratios, but Fig. 5.12 shows that during many runs O_3 and CO were negatively correlated. The free troposphere is associated with high O_3 and low CO mixing ratios. For this reason, these air masses are typically associated with negative dO_3/dCO correlations [Fishman and Seiler, 1983]. Looking at Fig. 5.12 there are some runs that stand out with high O_3 mixing ratios. These are typically the highest level runs carried out during the flight, sampling the upper troposphere and generally have a negative dO_3/dCO value. Examples of the RMA analysis for runs which represent free tropospheric air masses are shown in Fig. 5.18. For almost all the runs, the value of dO_3/dCO became more negative as altitude increased (shown in Fig. 5.19) though run 14 on flight C068 stands out as having a strongly negative dO_3/dCO despite being sampled in the mid troposphere. A four day back trajectory calculated for this run indicates that whilst the run was sampled at 2500 m, the air mass had spent 43 hours out of the previous four days above 4000 m, mixing with O_3 rich air masses and is

representative of the free troposphere. Four day back trajectories were calculated for the other five runs presented in Fig. 5.18 indicate that all the air masses spent most of the previous four days above 4000 m ($>$ 59 hours). It is of note that even for the highest level runs sampled during the ACSIS campaigns, CO mixing ratios are frequently over 100 ppbv indicating that pollution from continental sources affects the remote North Atlantic atmosphere for all altitudes.

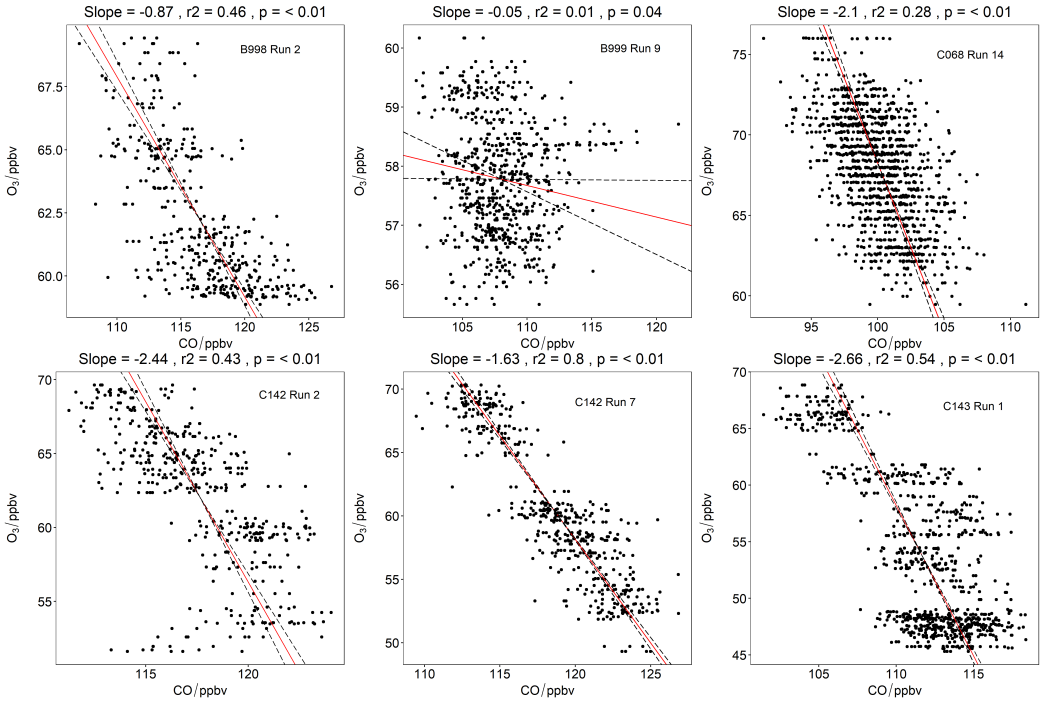

Figure 5.18: dO_3/dCO calculated for flight runs where free tropospheric air was sampled and where a negative correlation between O_3 and CO was observed. Slope was calculated using a reduced major axis method which accounts for variability in both x and y coordinates. p is a measure of the statistical significance of the fit. The dashed black lines represent the error in the fit (95% confidence intervals).

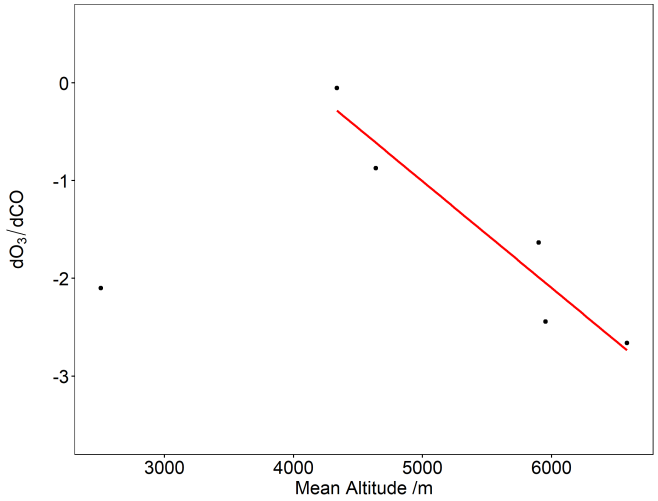

Figure 5.19: The relationship between mean run altitude and dO_3/dCO. In general, the higher the run the more negative dO_3/dCO.

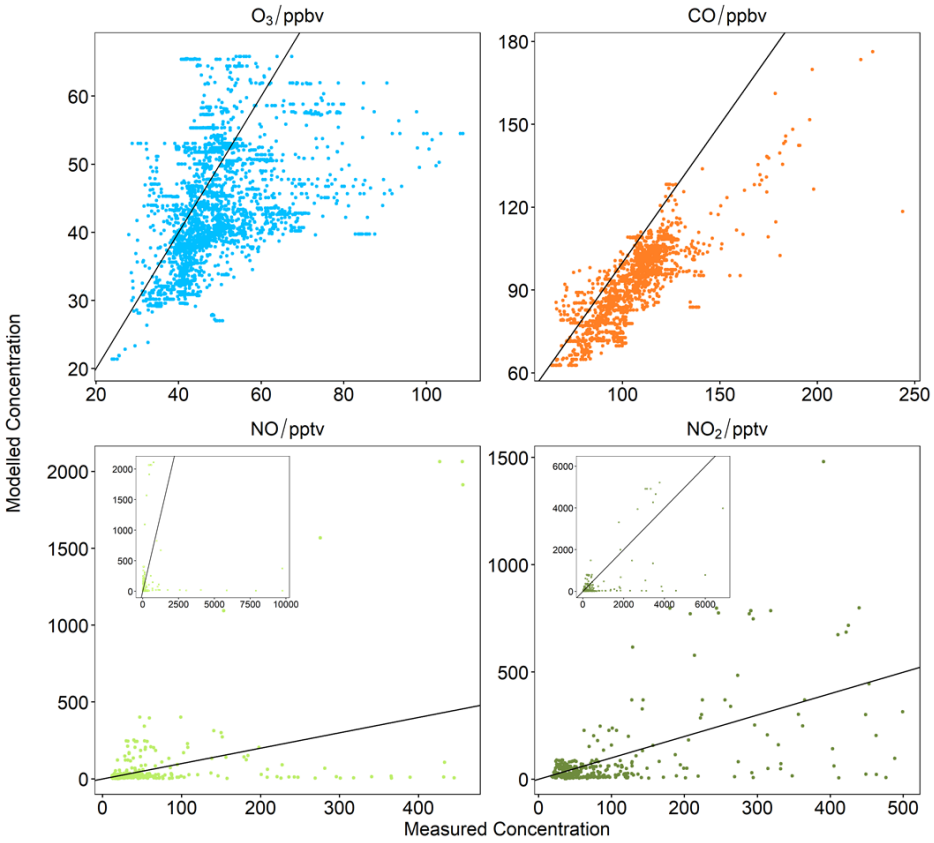

Figure 5.20: Relationship between measured and modelled mixing ratios for O_3 (top left panel), CO (top right panel), NO (bottom left panel) and NO_2 (bottom right panel). A black 1:1 line is included in each plot for reference.

5.6 Comparison with the GEOS-Chem model

One of the major motivations for making measurements in the North Atlantic, outlined in this chapter's introduction, is evaluating atmospheric models in order to reduce uncertainty about future climatic impacts of the North Atlantic. GEOS-Chem is a global 3D model of atmospheric chemistry (details of which can be found at `www.geos-chem.org`). Output presented here is from GEOS-Chem (v10-01) with an offline stratosphere, run along the flight tracks for ACSIS 1, 2 and 3. At the time of writing no model comparisons were available for ACSIS 4.

Figure 5.20 shows the agreement between the measured and modelled mixing ratios for O_3, CO, NO and NO_2 (CH_4 and CO_2 are not outputs of the model for this analysis). Modelled O_3 mixing ratios both overestimate and underestimate measured O_3 throughout the two campaigns. The highest measured O_3 mixing ratios (above $\sim$70 ppbv are all underestimated by the model). CO mixing ratios are systematically underestimated by the model during the two campaigns, with an offset of between 10 and 15 ppbv. A wide range of NO and NO_2 mixing ratios were measured with sporadic high values measured due to point sources which are not expected to be captured in the model and are shown in the inset plots of Fig. 5.20. For NO_x mixing ratios lower than 100 pptv, the modelled values agree relatively well but are largely underestimated by the model at higher mixing ratios.

Figure 5.20 includes all data from ACSIS 1, 2 and 3 at all altitudes and locations and as such does not show whether the model has particular biases at certain altitudes or in space (i.e. with longitude or latitude). Figure 5.21 shows the modelled and measured mixing ratios for ACSIS 1, 2 and 3 with altitude. Looking at O_3, median mixing ratios are underestimated throughout the atmosphere up until 5000 m, typically well into the free troposphere. The model predicts a strong increasing trend with altitude up until 6000 m above which mixing ratios decrease. This strong trend in O_3 is not observed in the measurement data with an increase in O_3 observed between 0 and 2000 m and then O_3 appears well mixed at higher altitudes. In the lowest 2 km of the atmosphere, the model underestimates O_3 mixing ratios by an average of 7 ppbv. Above 5 km, the model overestimates O_3 mixing ratios by an average of 2 ppbv. CO was consistently underestimated by the model throughout the atmosphere with modelled values being on average 10 ppbv lower than the measured values for the first 4 km of the atmosphere. Above 4 km modelled and measured quantities diverge further with modelled mixing ratios being on average 14 ppbv lower than those measured. Similarly, both NO and NO_2 mixing ratios are underestimated by the model. NO is underestimated in the model by an average of 13 pptv throughout the atmosphere. There is a larger discrepancy between measured and modelled NO_2 with an average discrepancy of 70 pptv with the largest differences between measured and modelled mixing ratios occurring between 4 and 7 km.

In order to assess if the model performs better in some regions the normalised mean

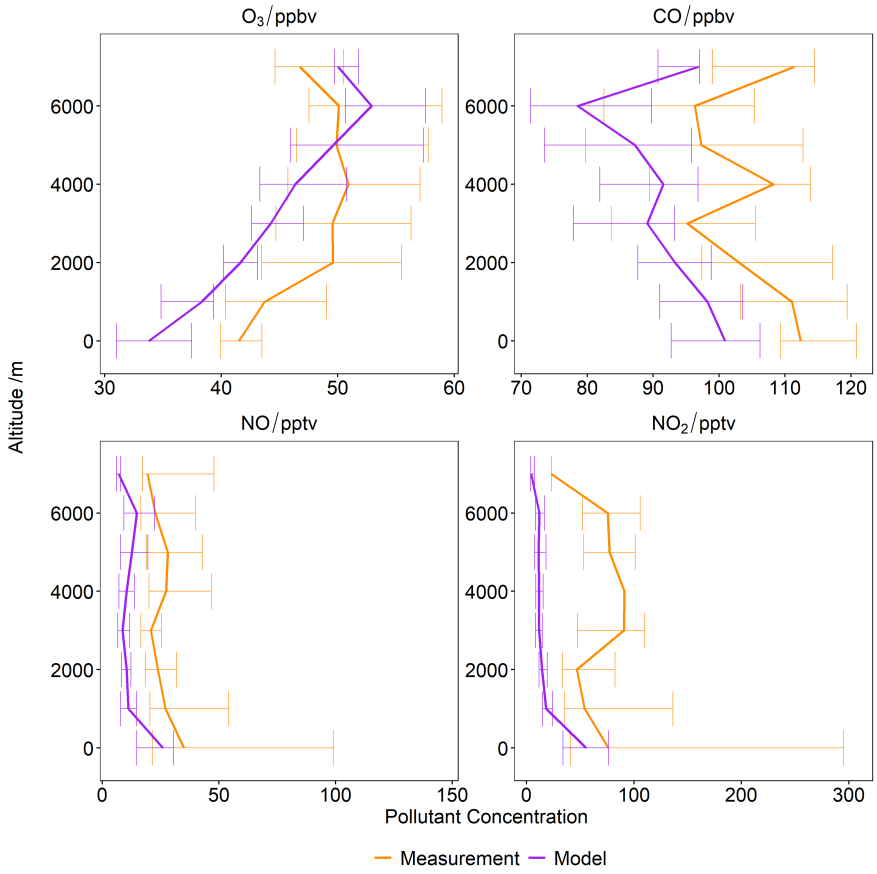

Figure 5.21: Plot showing the variation in pollutant mixing ratios with altitude. Median measured (gold) and modelled (purple) mixing ratios are shown with the error bar showing the 25th and 75th percentiles. Data has been grouped by altitude and presented every 1000 m. No error bar is shown for NO_2 at 4000 m due to the wide range of NO_2 mixing ratios sampled at this altitude which makes the relationship between the measured and modelled data unclear. For this level the lower quartile was 47.5 pptv and the upper quartile 817 pptv.

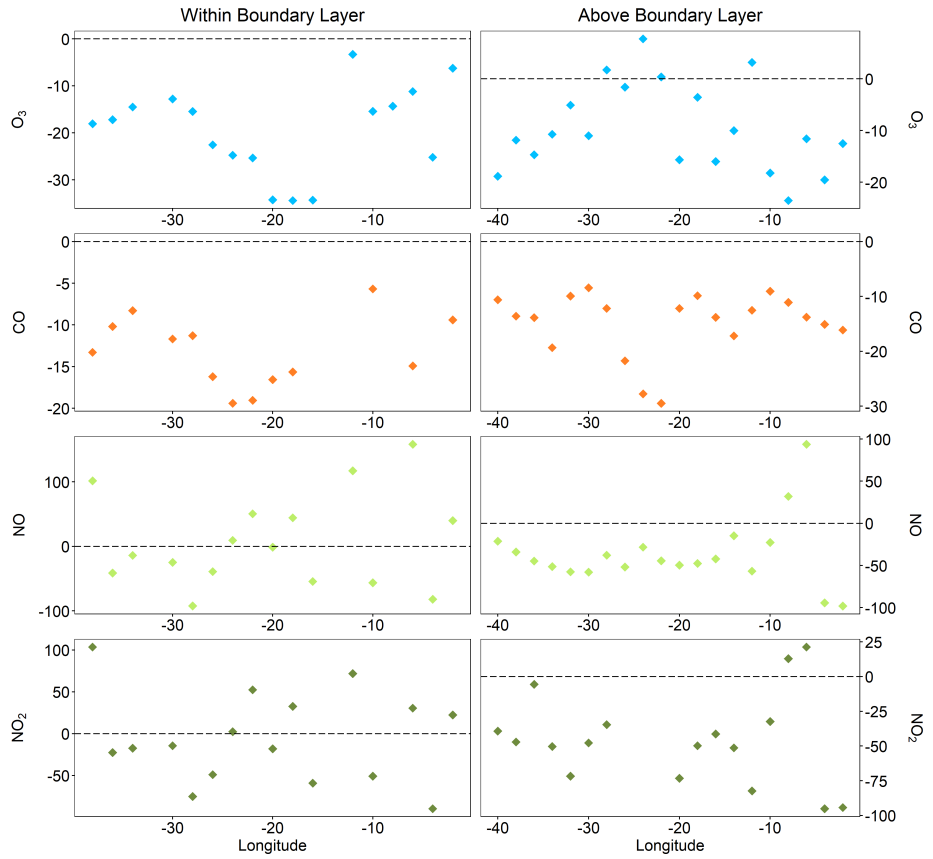

Figure 5.22: Plot showing the NMB for how well the model data agrees with the measurement across the longitude range covered during ACSIS 1, 2 and 3. Positive NMB indicate the model overestimates observed mixing ratios and negative NMB indicate an underestimation. Data presented has been grouped into 2° latitude bins.

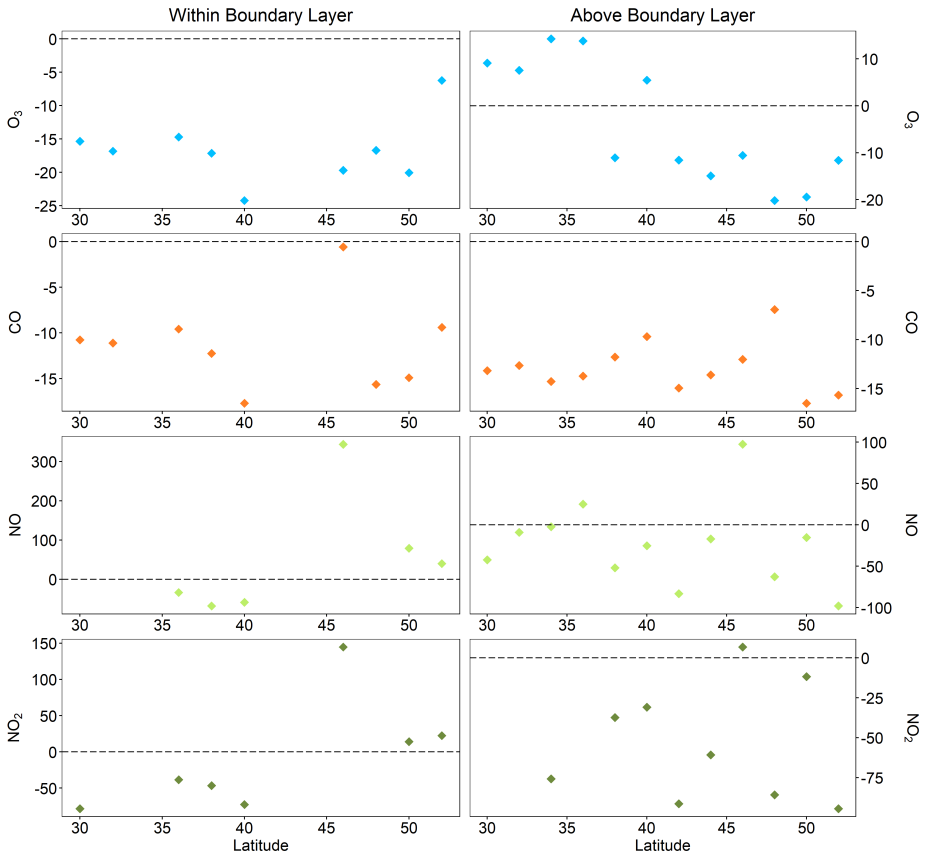

Figure 5.23: Plot showing the NMB for how well the model data agrees with the measurement across the latitude range covered during ACSIS 1, 2 and 3. Positive NMB indicate the model overestimates observed mixing ratios and negative NMB indicate an underestimation. Data presented has been grouped into 2° latitude bins.

bias (NMB) is presented as a function of longitude and latitude in Figs. 5.22 and 5.23. The NMB was calculated for 2 degree bins according to equation 5.1, where M is modelled mixing ratio and O is observed mixing ratio. A NMB over 0% indicates a positive bias in the model and a negative NMB indicates a negative bias in the model. NMB is a commonly used statistical method for evaluating atmospheric model performance [Emery et al., 2017].

$$NMB = \frac{\Sigma(M-O)}{\Sigma O} \times 100 \tag{5.1}$$

O_3 mixing ratios are underestimated within the boundary layer across all longitudes and latitudes covered along the flight tracks, with an overall NMB of -18%. CO is underestimated for all locations within the boundary layer with an overall NMB of -12%. There is a great deal of variation in NMB calculated for NO and NO_2 within the boundary layer across the whole longitude range with no clear trend. NO_x is slightly better represented in the model further west, between 18° and 38°W although large under and overestimations (tending towards $\pm$100%) were still calculated in this region. NO and NO_2 modelled and measured mixing ratios diverge for more northerly latitudes within the boundary layer with modelled data overestimating NO mixing ratios between 46° and 52°, with a NMB between 40 and 340%. NO_2 mixing ratios are overestimated in this region with a NMB between 14 and 140%. In general, O_3 is better represented in the free troposphere than the boundary layer for all longitudes and latitudes, with an overall NMB of -11%. In terms of variability with latitude O_3 in the free troposphere tends to be overestimated (average NMB of 11%) between 30 and 36°N and underestimated further north between 42 and 52°N (average NMB of -14%). As for within the boundary layer CO is consistently underestimated by the model in the free troposphere for all locations (overall NMB is -13%). NO is consistently underestimated between 20° and 40°W in the model above the boundary layer (mean NMB of -43%), with model-measurement agreement worsening further east. In terms of variability with latitude NO appears to be best represented furthest south (between 30 and 36°N) but is generally underestimated across the latitude range covered. NO_2 mixing ratios above the boundary layer are also almost consistently underestimated for all locations.

As outlined in section 5.5, several different air masses were encountered during the flights. The NMBs of O_3, CO, NO and NO_2 are presented in Table 5.5 alongside

Table 5.5: Modelled/Measured Ratios for different air mass classifications.

Flight and Run Number	Air Mass Classification	NMB /%			
		O_3	CO	NO	NO_2
B998, Run 11	Biomass Burning	-3.7	-37	-44	-
B999, Run 7	N. Am. Anthropogenic	-18	-15	-	-
B999, Run 11	N. Am. Anthropogenic	-19	-14	-	+74
B998, Run 2	Free Troposphere	-30	-19	-76	-
B999, Run 9	Free Troposphere	-20	-12	-15	-
C068, Run 14	Free Troposphere	-36	-7.1	-65	-56

run details and air mass classification. O_3 mixing ratios are underestimated for all examples given in Table 5.5, though are best represented in the biomass burning air mass, followed by the air masses associated with anthropogenic pollution. O_3 mixing ratios in the free troposphere tend to be underestimated to a greater degree though run 9 on B999 has a similar model-measurement discrepancy to the runs representing North American anthropogenic outflow. The worst agreement is between model and measurement is on run 14, flight C068 with a NMB of -36%. This run was performed at an altitude of 2500 m which may explain the larger discrepancy suggesting that the model does not appear to capture the vertical mixing of air masses well (shown in Fig. 5.21). As for O_3, CO is underestimated for all air masses. The largest underestimation for CO is associated with the biomass burning air mass sampled during flight B998. Air masses associated with anthropogenic pollution outflow and free tropospheric air are better represented for CO. The best represented air mass for CO is the free tropospheric air mass sampled during flight C068, likely driven by the fact that this was sampled at a lower altitude where the model anticipated higher CO mixing ratios. NO_x data is more limited and as such it is difficult to comment on the performance of the model at representing NO_x in different air masses. NO mixing ratios are underestimated for all air masses, though to varying degrees. NO_2 was overestimated by the model for the air mass sampled during run 11, flight B999 representative of North American anthropogenic outflow.

The comparisons modelled and measured mixing ratios highlight a systematic underestimation of CO by GEOS-Chem. GEOS-Chem has been reported to systemati-

cally underestimate CO mixing ratios in several studies [Bey et al., 2001, Val Martin et al., 2008, Kopacz et al., 2010, Kumar et al., 2013] which may be due to a missing source of emissions in the model. Yamasoe et al. [2015] showed that GEOS-Chem captured anthropogenic emissions reasonably well but underestimated those from biomass burning to a larger extent. This is supported by the NMB determined for the different air mass classifications in this work, with the air masses associated with anthropogenic outflow appearing to be better represented for CO than those influenced by biomass burning. However, the two air masses associated with North American anthropogenic outflow are from the same flight and so another factor specific to this flight could lead to the improved model-measurement agreement observed. A more extensive air mass classification, with categories spanning a range of flights and campaigns is required to more confidently determine if biomass burning emissions are low in the model. Aside from a missing source of emissions in the model, an excess of OH which acts as a sink of CO, could lead to CO mixing ratios that are lower than those measured.

As well as underestimations in CO mixing ratios, NO_x is largely underestimated by the model. This is possibly due to a missing source of NO_x emissions, a missing method of transport of NO_x to the North Atlantic region or partitioning from NO_y not being well represented in the model. Previous studies have estimated that $< 20\%$ of NO_x emitted over the eastern US is exported to the North Atlantic and of this fraction, less than 10% is transported as NO_x [Parrish et al., 2004]. PAN and HNO_3 have been reported to be the dominant nitrogen species for the region in previous studies [Val Martin et al., 2008]. Without an NO_y measurement from the aircraft it is difficult to evaluate potential drivers of the low NO_x mixing ratios in the model however.

O_3 mixing ratios are also largely underestimated by the model. The situation with O_3 underestimations are more complicated given that O_3 is not directly emitted but formed from precursor emissions. Figures 5.22 and 5.23 show that the NMB for O_3 and CO appear to follow one another between -40° and -20° longitude and 30° and 40° latitude, within the boundary layer. This may suggest that, in this region at least, the drivers of the model's underestimation of O_3 mixing ratios could be linked to the underestimation of CO mixing ratios. As well as this the relationship between NO_x and O_3 is highly non-linear, with small changes in the amount of NO_x having significant impacts on the amount of O_3. For example, O_3 production efficiency is greater at low

levels of NO_x [Liu et al., 1987]. Discrepancies between precursor emissions likely lead to the misrepresentation of O_3 mixing ratios in the model.

5.7 Conclusions and further work

This chapter presents a series of airborne measurements of trace gases made over the North Atlantic Ocean between 2017 and 2019. Measurements were made as part of the ongoing ACSIS programme, which aims to improve understanding of the North Atlantic region, in part through provision of a comprehensive set of atmospheric composition measurements. The values measured compare well with previous measurements over the North Atlantic Ocean indicating that this data is representative of the region. The spatial variation in atmospheric composition has been explored which showed different pollutants were more prevalent in some areas compared to others. For example, during flights west of Ireland the highest NO_x and O_3 mixing ratios were observed, but CO and CH_4 were highest during flights west of the Azores, presumably due to long range transport of pollution from North America. The variability in pollutant amounts and relationships between pollutants demonstrate that the atmosphere above the North Atlantic is composed of a range of air masses of different origins. Despite being a remote region the North Atlantic is polluted.

The comparison with the GEOS-Chem model shows that this data set is suitable for use evaluating the performance of models over the North Atlantic region. The data set collected is valuable in that it allows an understanding of the spatial variation in atmospheric composition over the North Atlantic and can be used to highlight biases in models for particular areas. The GEOS-Chem model data presented consistently show underestimations for O_3, CO and NO_x suggesting that the extent to which the North Atlantic is polluted is not captured. Significant underestimations of CO mixing ratios in a biomass burning air mass suggest that there is a missing source of biomass burning emissions in the model. There were no clear spatial biases in the model in terms of longitude and latitude, though better data coverage, by including more flights from future ACSIS campaigns could add weight to this. The vertical profile in modelled O_3 does not capture the mixing observed between 2 km and 6 km, instead predicting a steady decline in O_3 mixing ratios throughout the atmosphere up to 6 km.

Going forward, it would be beneficial to improve the methods used to identify air mass types, for example performing a cluster analysis using more parameters which would enable air masses to be classified more reliably. Additionally, ACSIS is an ongoing project (2017–2021) and more data sets can be incorporated into this analysis to create a more complete set of atmospheric composition data. In this chapter a few examples were selected to show the types of air mass typically encountered on the flights but more data, particularly more VOC data, would allow a more thorough analysis to be performed. No work has currently been carried out to assess whether the composition of the atmosphere is changing over time from this data set. Given that the ACSIS flying campaigns are an ongoing series of measurements which have occurred in different months they provide a unique opportunity to evaluate any seasonal change over a wide area, something which cannot be achieved with a ground-based measurement station. In addition to seasonal variation it may be possible to evaluate any longer term trends once the five year period is over.

6 Conclusions

Air pollution has serious public health and climate implications. In order to control air pollution and minimise harm to the planet and public health it is necessary to understand the drivers of pollution. This thesis has explored gas-phase pollution in two contrasting atmospheres, examining the role of meteorology, chemistry and emissions in these environments.

Chapters 3 and 4 presented pollutant concentration and emission measurements in Beijing during the winter and summer seasons. During the summertime in Beijing there are significant O_3 problems with half of the days during the summer measurement campaign breaching the 8 hourly limit for O_3 concentrations set by the World Health Organisation. O_3 is a dangerous air pollutant with a positive radiative forcing and as such it is imperative that O_3 pollution is brought under control. The chemistry of O_3 formation is complex, with a non-linear relationship to its precursor species so the design of O_3 pollution control measures can be difficult. Ozone production efficiencies calculated for both the winter and summer field campaigns indicate that targeting VOC pollution would be beneficial for the reduction of O_3 pollution.

The Air Pollution and Human Health Beijing program has demonstrated the value of an intensive measurement campaign which allow exploration of the complex chemistry occurring in urban atmospheres due to the mixture of pollutants present. Air quality monitoring stations are a useful tool for evaluating long-term trends in atmospheric composition or the impacts of legislation, but many stations only measure pollutants which are regulated because of their direct health impacts. Gas-phase pollutant data from the air quality network in Beijing (presented in section 3.1.1) is only available for NO_2, SO_2, O_3 and CO but no information is readily available for NO or VOCs.

This lack of information limits the degree to which the atmospheric chemistry of a region can be explored and consequently hinders the ability to design pollution control measures. Recognising the importance of a complete set of measurement data when studying atmospheric processes, the UK has recently granted funding for the installation of so-called air quality 'supersites' which will provide more in-depth information over a longer period of time. This level of air quality monitoring could be useful for cities like Beijing. Analysis presented in this thesis shows that deviations from the O_3-NO-NO_2 photostationary state cannot be explained by peroxy radicals alone and suggest the presence of an unknown oxidant at work in Beijing. Further monitoring could help uncover what oxidants are at work in Beijing's atmosphere.

During the winter campaign the impacts of meteorology were clear on the ambient pollution concentrations experienced in Beijing. Through the direct measurement of local emissions the relationship between meteorology, local emissions and pollutant concentration was shown. Due to reduced vertical mixing driven by a low boundary layer height, concentrations measured during the winter campaign were higher than those measured during the summer campaign for all pollutants apart from O_3. The highest pollutant concentrations were observed during periods associated with low wind speeds which allow the build-up of pollution due to lack of advection out of the city. Direct emission measurements allowed an investigation contrasting a low-pollution and high-pollution period and determined that the high pollution concentrations were not driven by an increase in local emissions, but rather a change in wind speed reducing ventilation and allowing pollution to build up over the city under stagnant conditions.

As well as using measurements to aid greater understanding of a polluted atmosphere, it is vital to understand pollutant emissions in order to control air pollution. Air quality models which can be used to design and test management strategies are limited by the quality of their inputs and it is therefore important to have access to accurate and reliable emissions inventories. The work presented in Chapter 4 of this thesis presents the first direct measurements of NO_x, CO and aromatic VOC emissions made in Beijing. Comparison of measured emissions and those estimated by the MEIC inventory reveal that the inventory does not accurately represent important O_3 precursor species; NO_x and CO, for a central region of Beijing. NO_x and CO were consistently over-

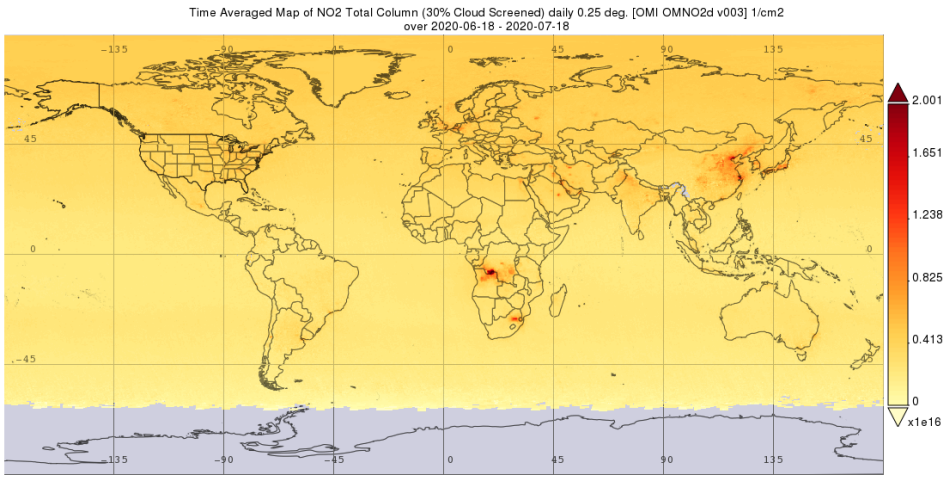

Figure 6.1: Average global NO_2 column density for 18 June 2020 – 18 July 2020. Data obtained from Krotkov et al. [2019].

estimated by the inventory, providing strong evidence that when using spatial proxies to scale-down inventories to urban scales, emissions in urban regions can be overestimated. VOC emissions were compared to the MEIC inventory in another publication associated with the campaign and it was found that the MEIC inventory also did not accurately represent a wide range of VOC emissions with certain species overestimated and some underestimated [Acton et al., 2020]. The emissions measurements presented in this work provide useful information for future inventory development and highlight the need to update the spatial proxies used to rescale inventories or to derive emissions using bottom-up approaches in order to correctly represent emissions in the city.

Figure 6.1 shows the global NO_2 column density for 18 June 2020 – 18 July 2020. It is clear from this image that pollution is generated from anthropogenic activities in urban or populated regions, but it is not just urban atmospheres that need to be studied. The atmosphere is interconnected and pollutant emissions generated in one region can be transported and transformed, impacting regions far away from the emission source. It is necessary to investigate atmospheric composition across all scales to fully appreciate the impacts that humans have on the planet. The North Atlantic ocean is a globally important climate system and a cause of major uncertainty in climate models due to difficulty predicting Atlantic Multidecadal Variability. Chapter 5 of this thesis

explored atmospheric composition over the North Atlantic ocean using measurements made from a research aircraft. By examining pollutant ratios and performing backwards trajectory analysis it was shown that transport of air pollutants away from their emission source impact the atmospheric composition of this region. In particular, anthropogenic pollution and biomass burning from North America leads to enhanced CO, O_3 and VOC mixing ratios over the North Atlantic. Measurements made are part of an ongoing project which when completed will form the most complete record of the region's atmospheric composition to date. Future work will provide insight into pollutant trends in the region.

The atmospheric composition data collected over the North Atlantic was compared to a global atmospheric chemistry model. Given the region's global importance and it being a large source of uncertainty in climate models, ensuring models can represent its atmospheric composition accurately is vital. The model comparison indicated a systematic underestimation of CO mixing ratios by the model. This could be due to an excess of a chemical sink (OH) or a missing source of CO emissions in the model and could highlight a problem with the emissions inventories used as an input to the model. The work in this thesis has outlined that emissions inventories can be limited on local scales, for Beijing, and has shown that measurement data is critical to identify discrepancies in emission estimates and reality. These measurements over the North Atlantic may also hint at errors in the emissions inventory used. Bias in the model for O_3 and CO appear to be correlated in some regions at least, which could suggest common drivers of the underestimations in these two species. Future work will continue to evaluate and inform atmospheric chemistry models of the region using the extended data set collected as part of the full ACSIS program.

This is a critical time for air quality. With the COVID-19 pandemic public concern about air pollution is growing and time is rapidly running out in order to tackle dangerous climate warming. By making measurements in urban and remote atmospheres it is possible to identify drivers of atmospheric composition change and deliver solutions for clean, healthy air.

Flight 'quicklook' files for data presented in Chapter 5

A

The following pages present the 'quicklook' files generated for each flight used in the analysis presented in Chapter 5. For each flight a time series of CO, O_3, NO and NO_2 alongside quality flags are presented. Profile data for temperature data and gas-phase pollutants (CO, O_3, CH_4 and CO_2) are shown which were used to determine the boundary layer height. A map of each flight track is also presented.

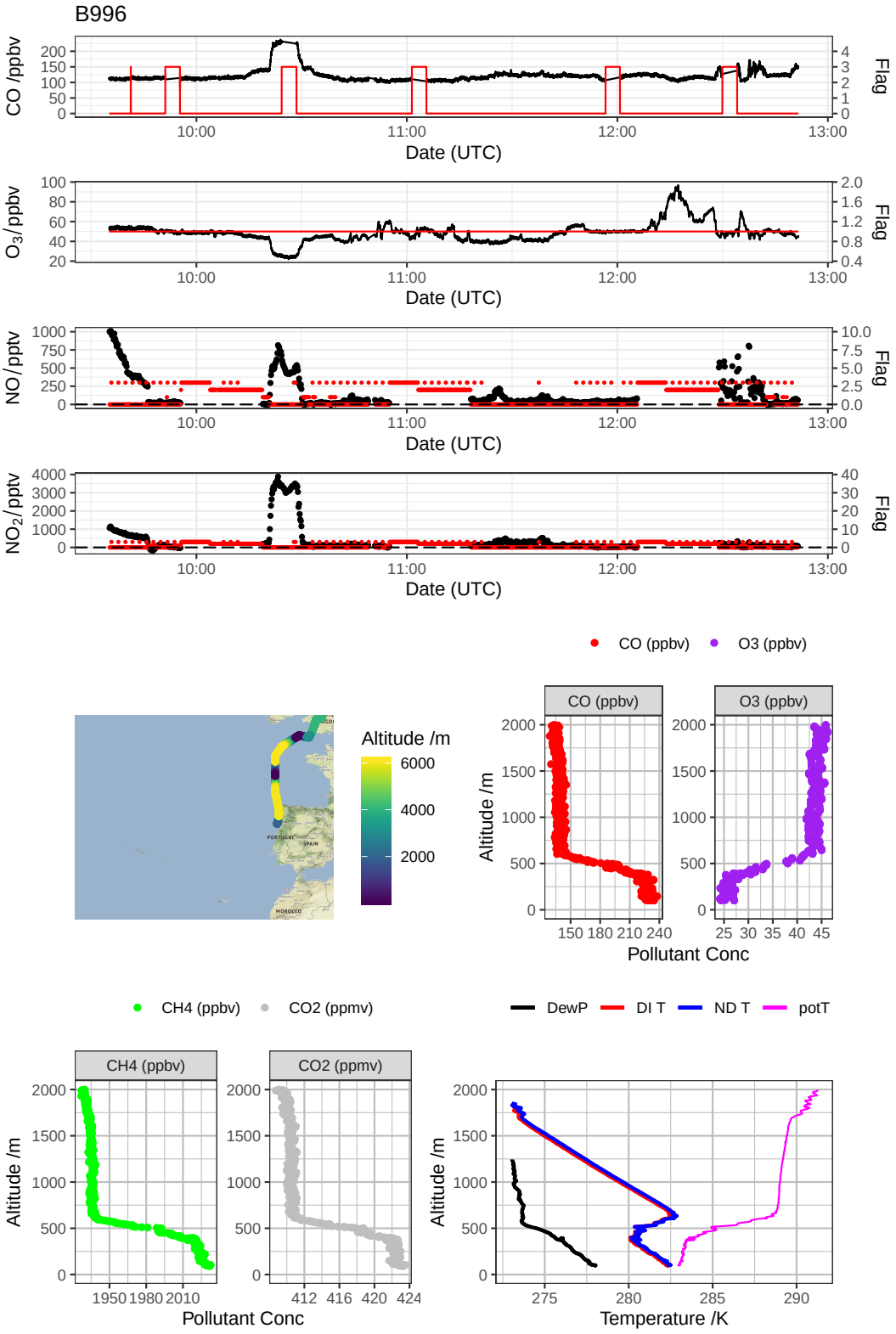
B996
CO /ppbv
Flag
Date (UTC)
O_3/ppbv
NO/pptv
NO_2/pptv
10:00
11:00
12:00
13:00
CO (ppbv)
O3 (ppbv)
Altitude /m
Pollutant Conc
CH4 (ppbv)
CO2 (ppmv)
DewP
DI T
ND T
potT
Temperature /K

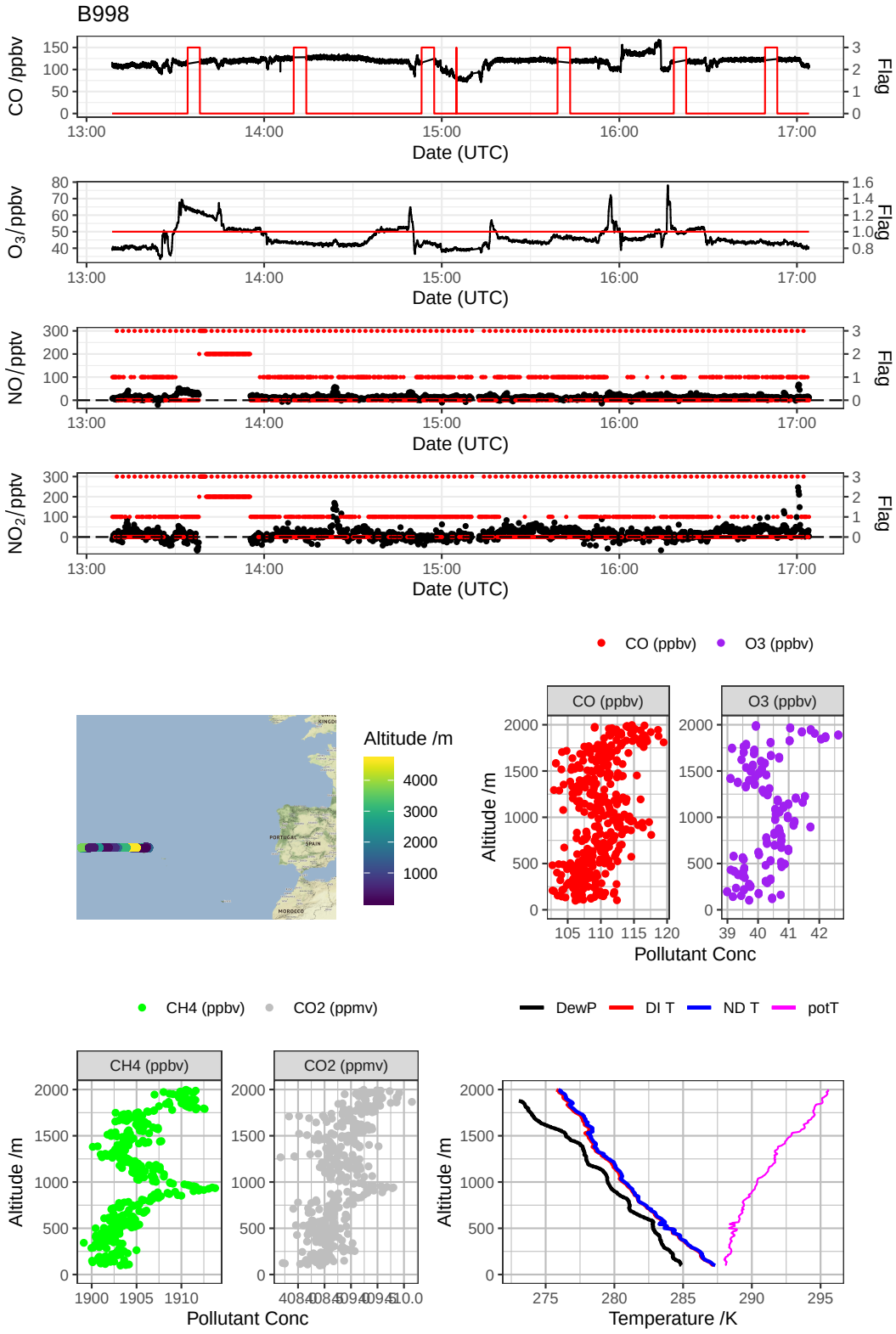
B998
CO /ppbv
Flag
Date (UTC)
O_3/ppbv
NO/pptv
NO_2/pptv
CO (ppbv)
O3 (ppbv)
Altitude /m
Pollutant Conc
CH4 (ppbv)
CO2 (ppmv)
DewP
DI T
ND T
potT
Temperature /K

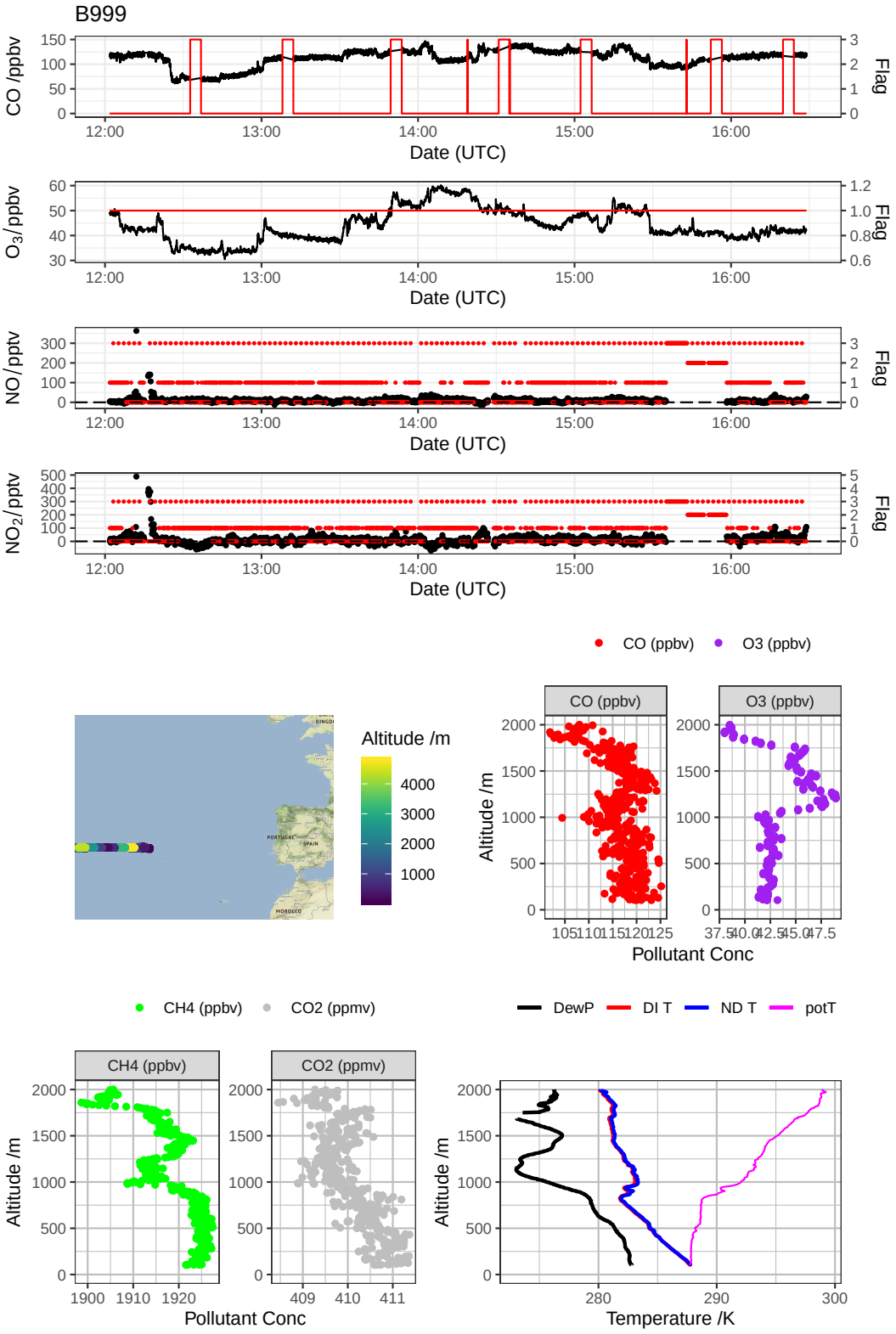
B999
CO /ppbv
Flag
Date (UTC)
O_3/ppbv
NO/pptv
NO_2/pptv
CO (ppbv)
O3 (ppbv)
Altitude /m
Pollutant Conc
CH4 (ppbv)
CO2 (ppmv)
DewP
DI T
ND T
potT
Temperature /K

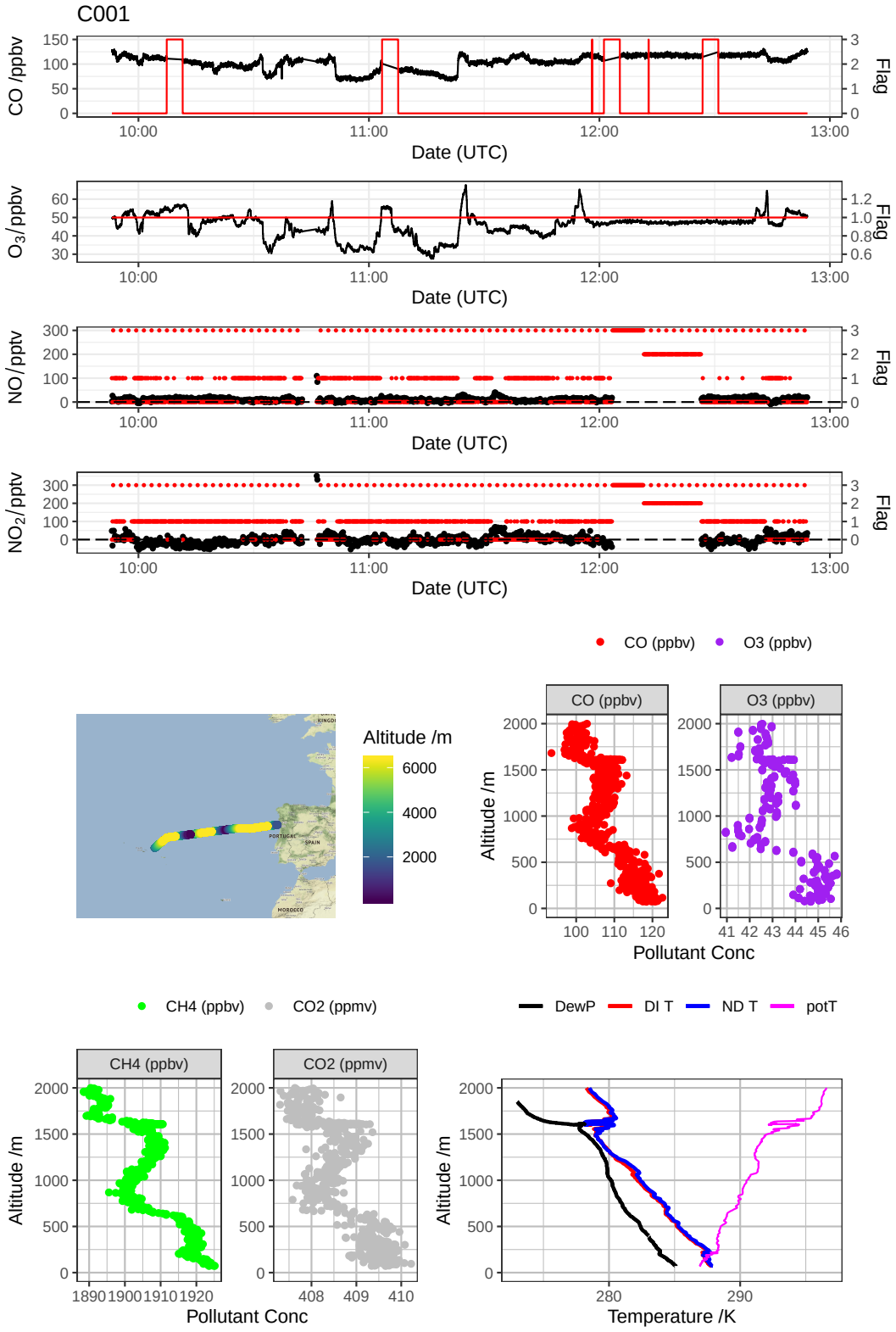
C001
CO /ppbv
Flag
Date (UTC)
O_3/ppbv
NO/pptv
NO_2/pptv
CO (ppbv)
O3 (ppbv)
Altitude /m
Pollutant Conc
CH4 (ppbv)
CO2 (ppmv)
DewP
DI T
ND T
potT
Temperature /K

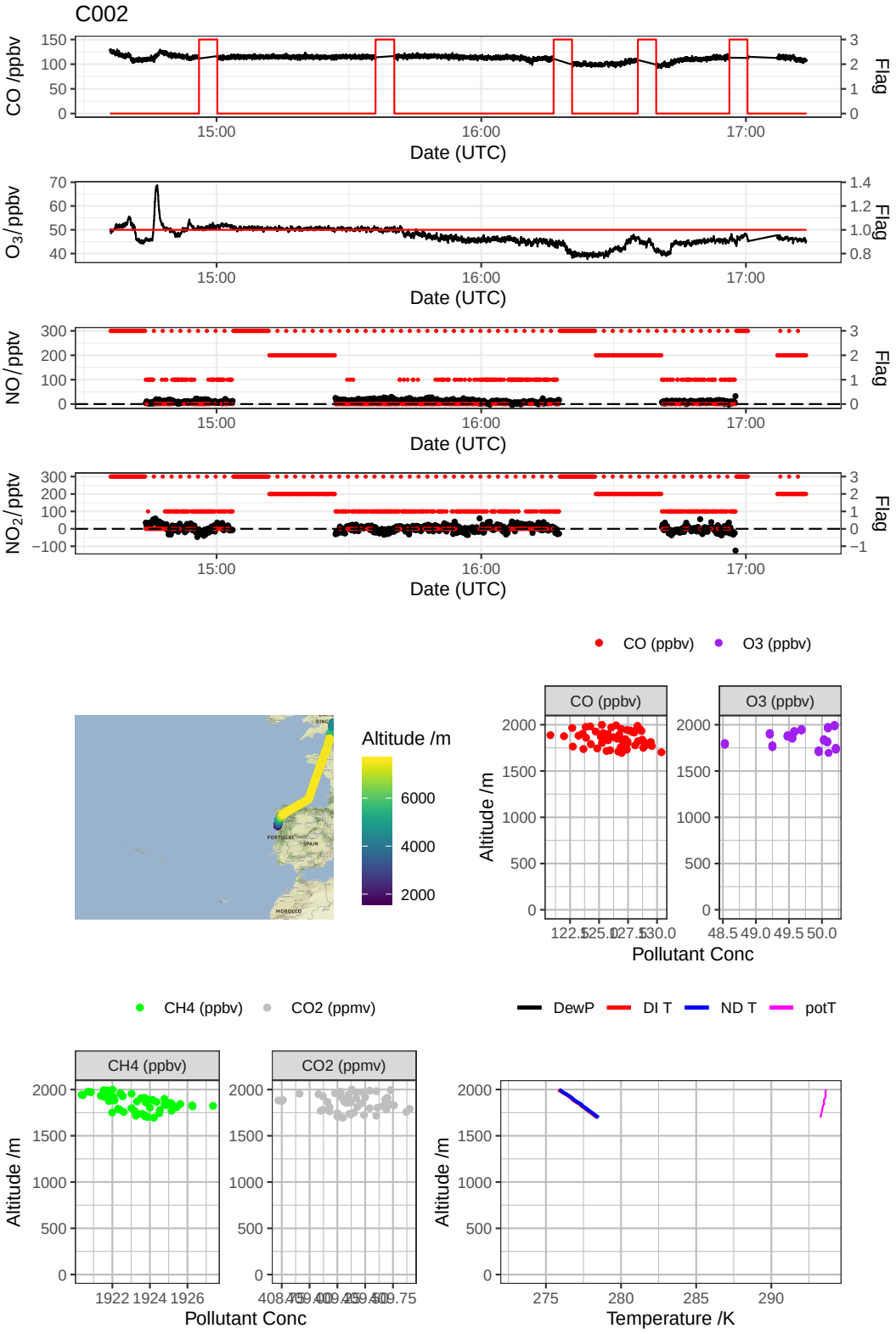
C002
CO /ppbv
Flag
Date (UTC)
15:00
16:00
17:00
O3/ppbv
NO/pptv
NO2/pptv
CO (ppbv)
O3 (ppbv)
Altitude /m
6000
4000
2000
Pollutant Conc
CH4 (ppbv)
CO2 (ppmv)
DewP
DI T
ND T
potT
Temperature /K

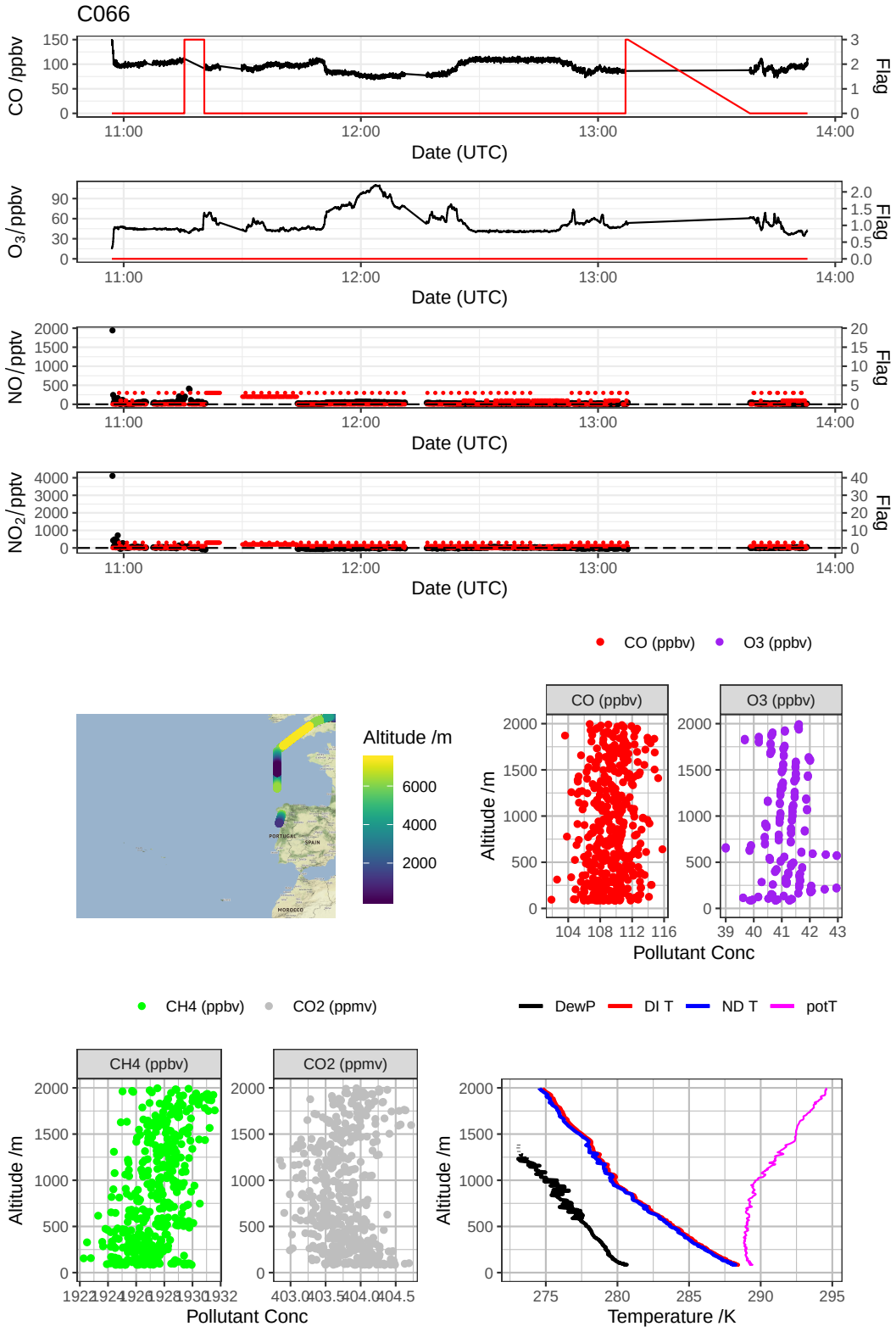
C066
CO /ppbv
Flag
Date (UTC)
O_3/ppbv
NO/pptv
NO_2/pptv
CO (ppbv)
O3 (ppbv)
Altitude /m
Pollutant Conc
CH4 (ppbv)
CO2 (ppmv)
DewP
DI T
ND T
potT
Temperature /K

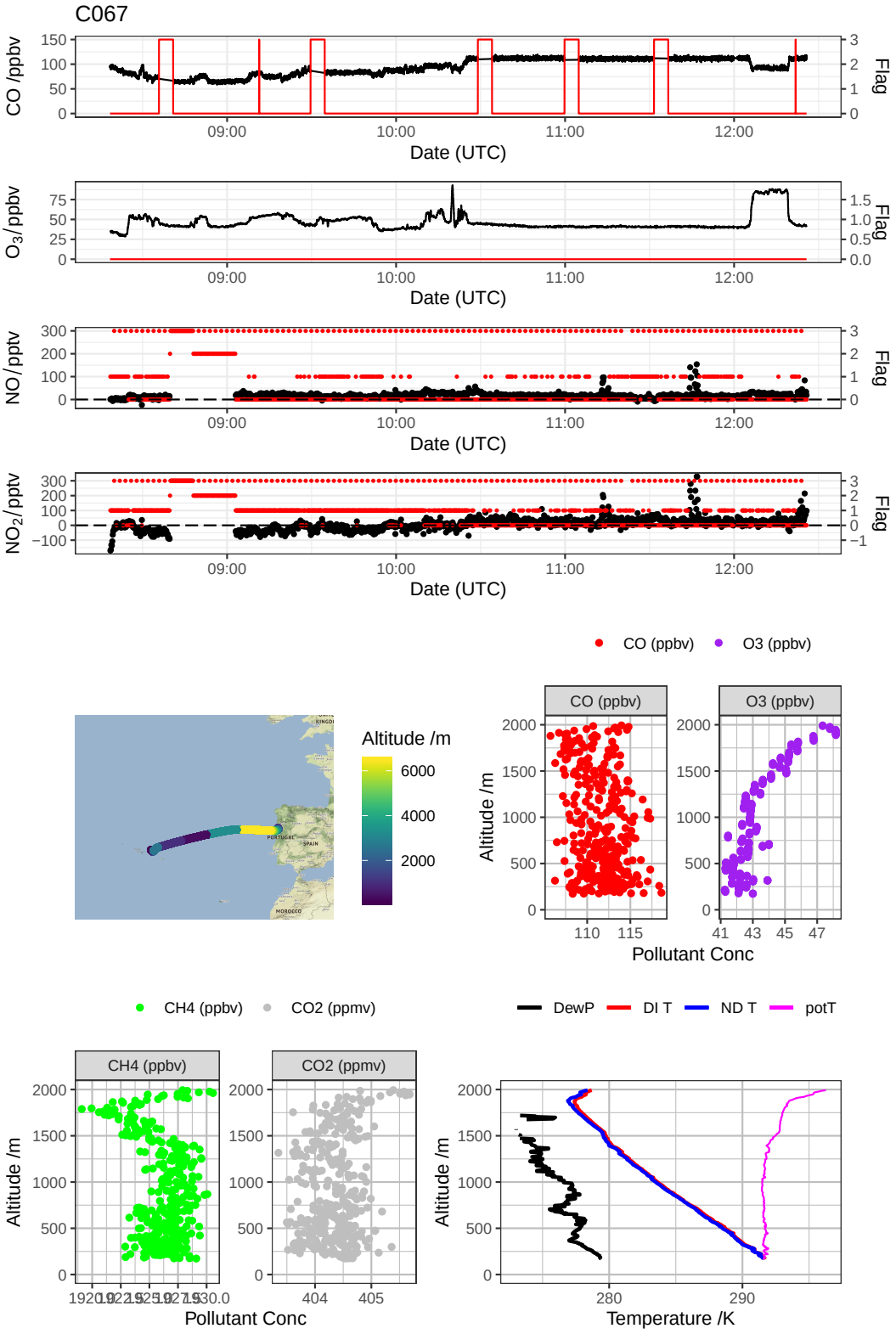
C067
CO /ppbv
Flag
Date (UTC)
09:00
10:00
11:00
12:00
O3/ppbv
NO/pptv
NO2/pptv
CO (ppbv)
O3 (ppbv)
Altitude /m
6000
4000
2000
Pollutant Conc
CH4 (ppbv)
CO2 (ppmv)
DewP
DI T
ND T
potT
Temperature /K

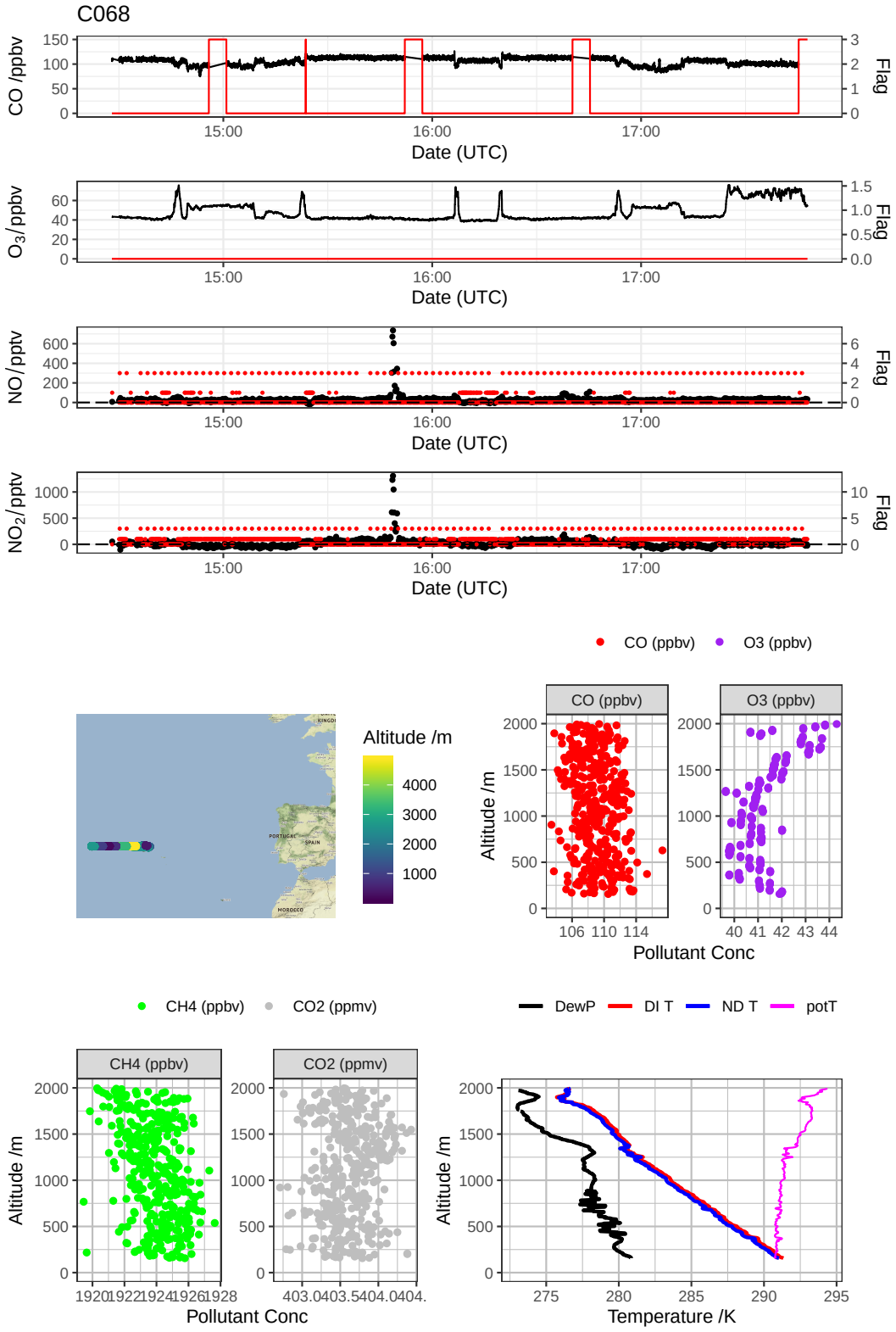
C068
CO /ppbv
Flag
Date (UTC)
O_3/ppbv
NO/pptv
NO_2/pptv
CO (ppbv)
O3 (ppbv)
Altitude /m
Pollutant Conc
CH4 (ppbv)
CO2 (ppmv)
DewP
DI T
ND T
potT
Temperature /K

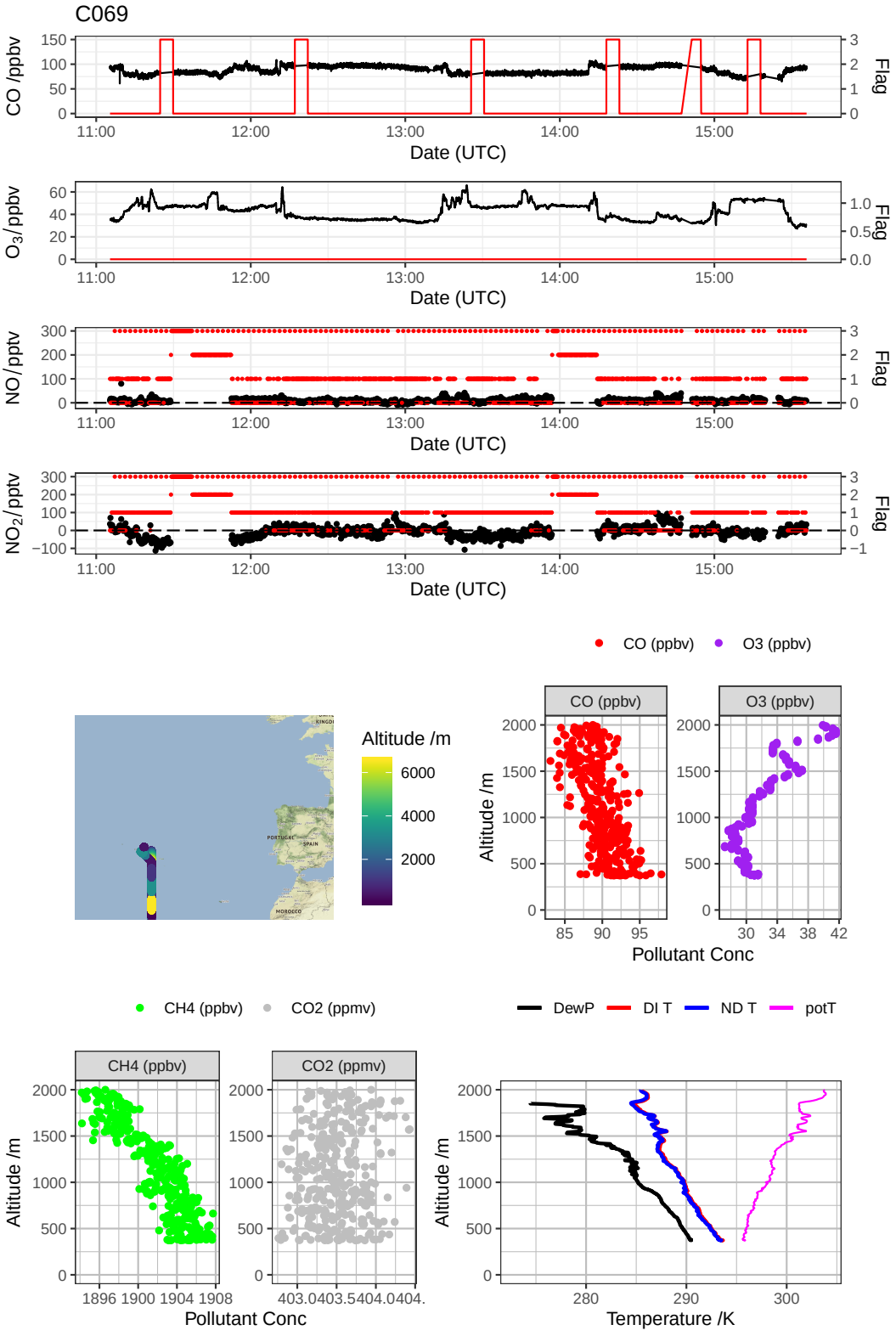
C069
CO /ppbv
Flag
Date (UTC)
O_3/ppbv
NO/pptv
NO_2/pptv
11:00
12:00
13:00
14:00
15:00
CO (ppbv)
O3 (ppbv)
Altitude /m
6000
4000
2000
Pollutant Conc
CH4 (ppbv)
CO2 (ppmv)
DewP
DI T
ND T
potT
Temperature /K

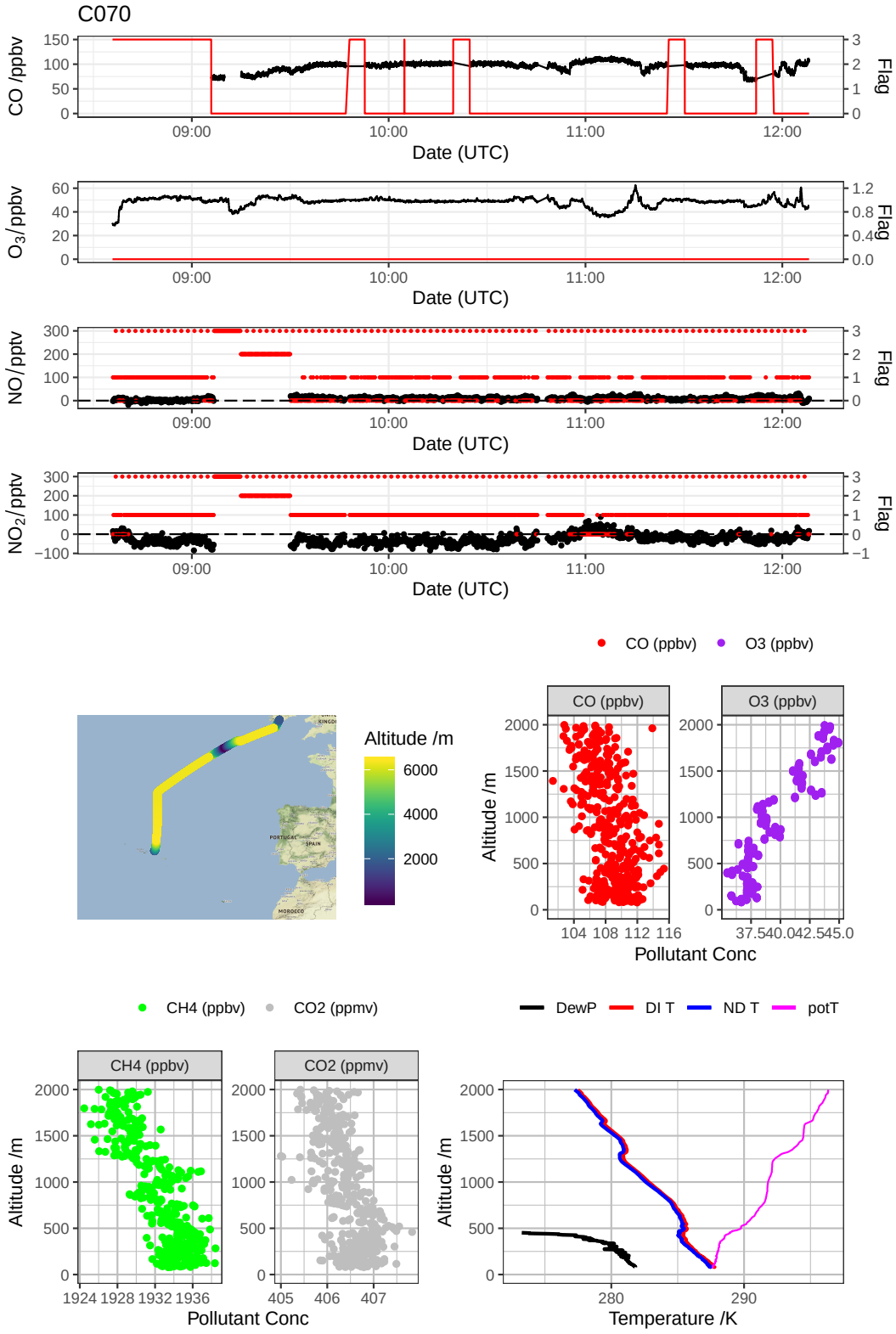
C070
CO /ppbv
Flag
Date (UTC)
O_3/ppbv
NO/pptv
NO_2/pptv
09:00
10:00
11:00
12:00
CO (ppbv)
O3 (ppbv)
Altitude /m
6000
4000
2000
Pollutant Conc
CH4 (ppbv)
CO2 (ppmv)
DewP
DI T
ND T
potT
Temperature /K

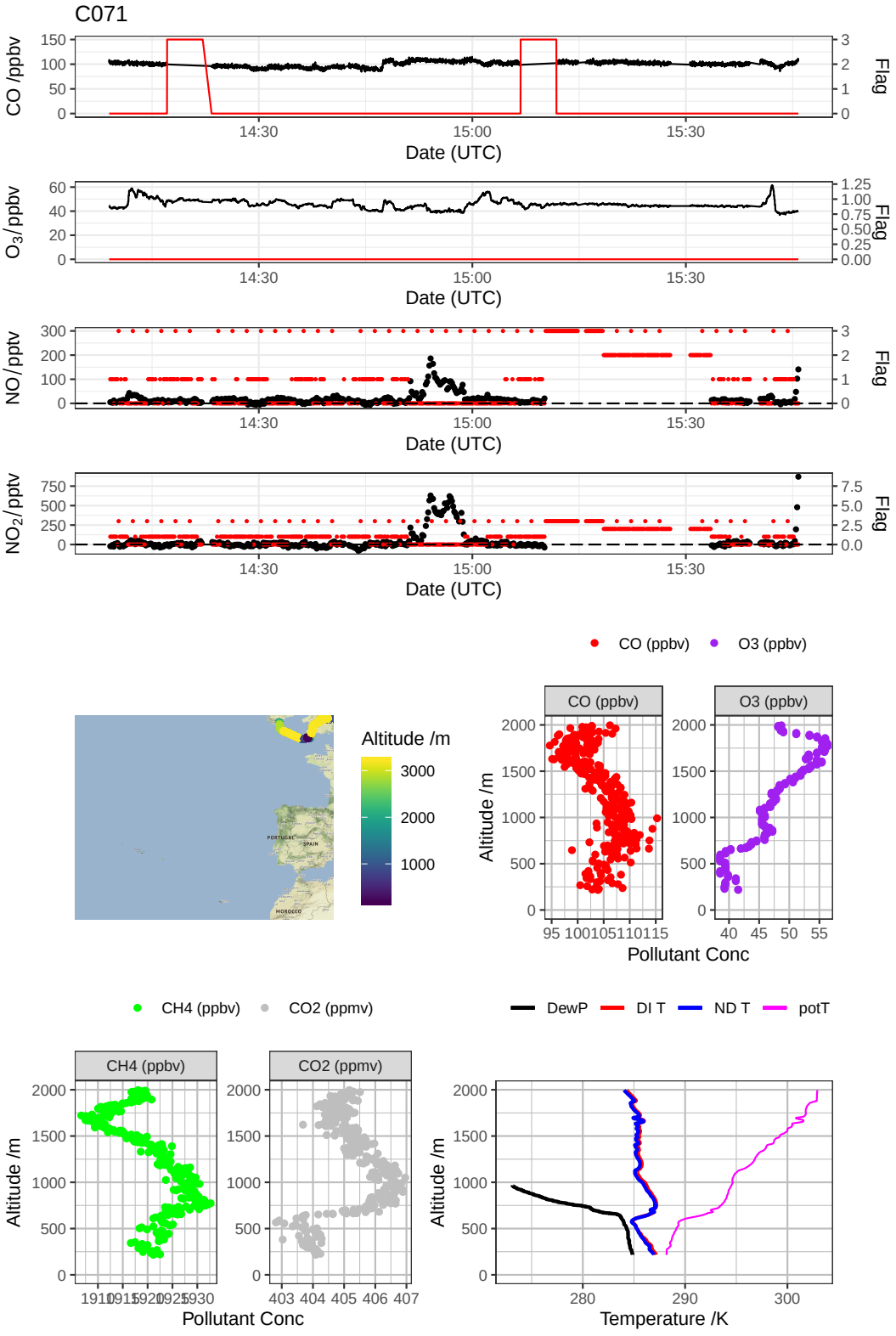
C071
CO /ppbv
Flag
Date (UTC)
14:30
15:00
15:30
O3/ppbv
NO/pptv
NO2/pptv
CO (ppbv)
O3 (ppbv)
Altitude /m
Pollutant Conc
CH4 (ppbv)
CO2 (ppmv)
DewP
DI T
ND T
potT
Temperature /K

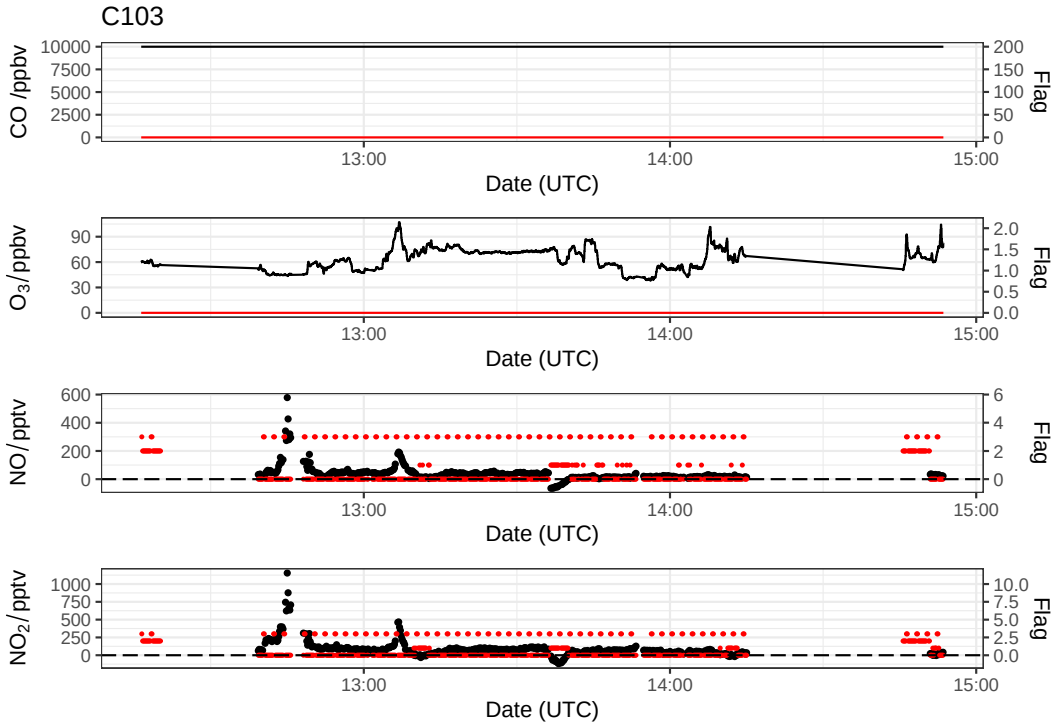

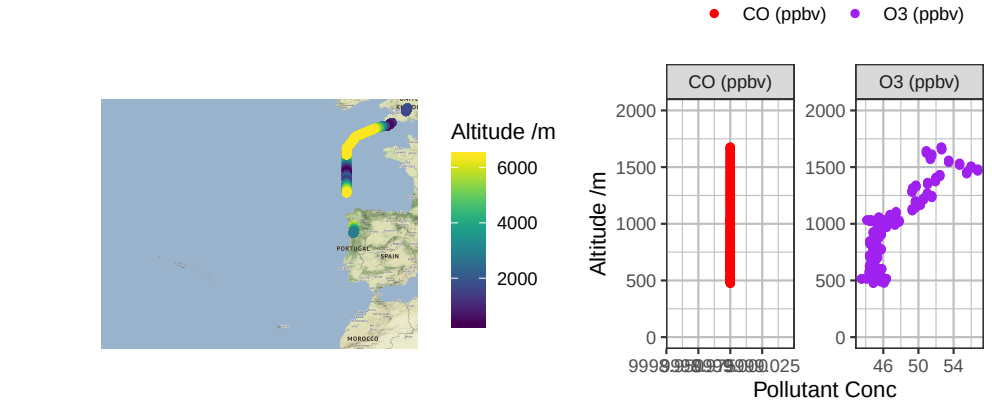

NO DATA FOR THIS PROFILE

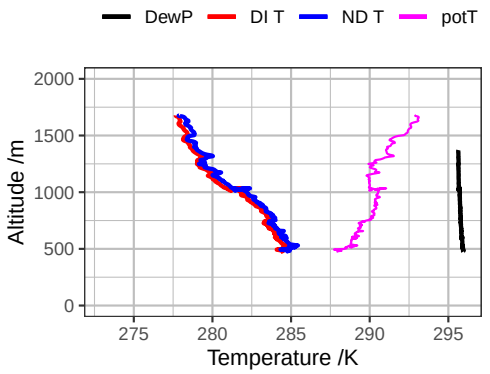

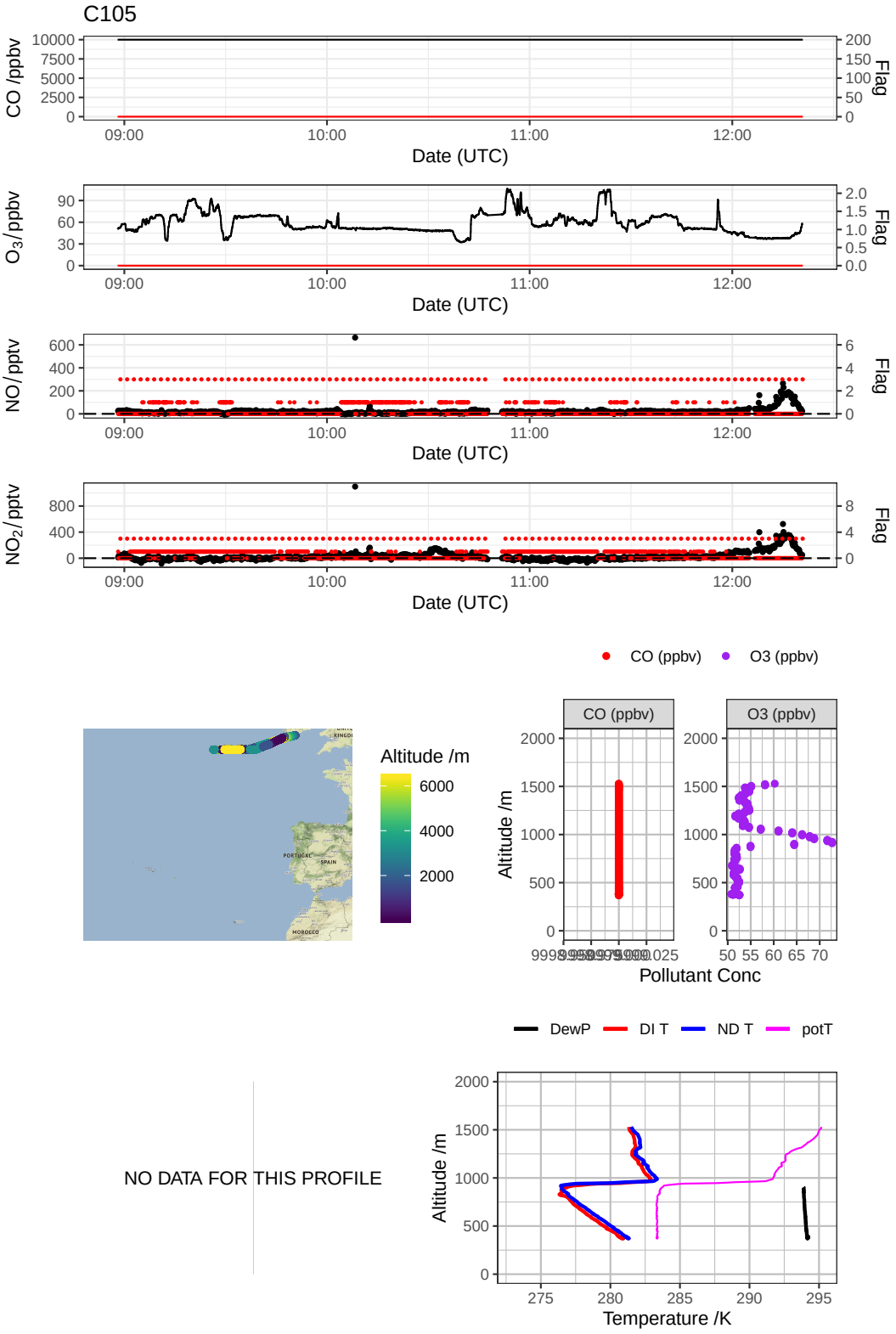
C105
CO /ppbv
Flag
Date (UTC)
O3/ppbv
NO/pptv
NO2/pptv
09:00
10:00
11:00
12:00
CO (ppbv)
O3 (ppbv)
Altitude /m
6000
4000
2000
Pollutant Conc
DewP
DI T
ND T
potT
NO DATA FOR THIS PROFILE
Temperature /K

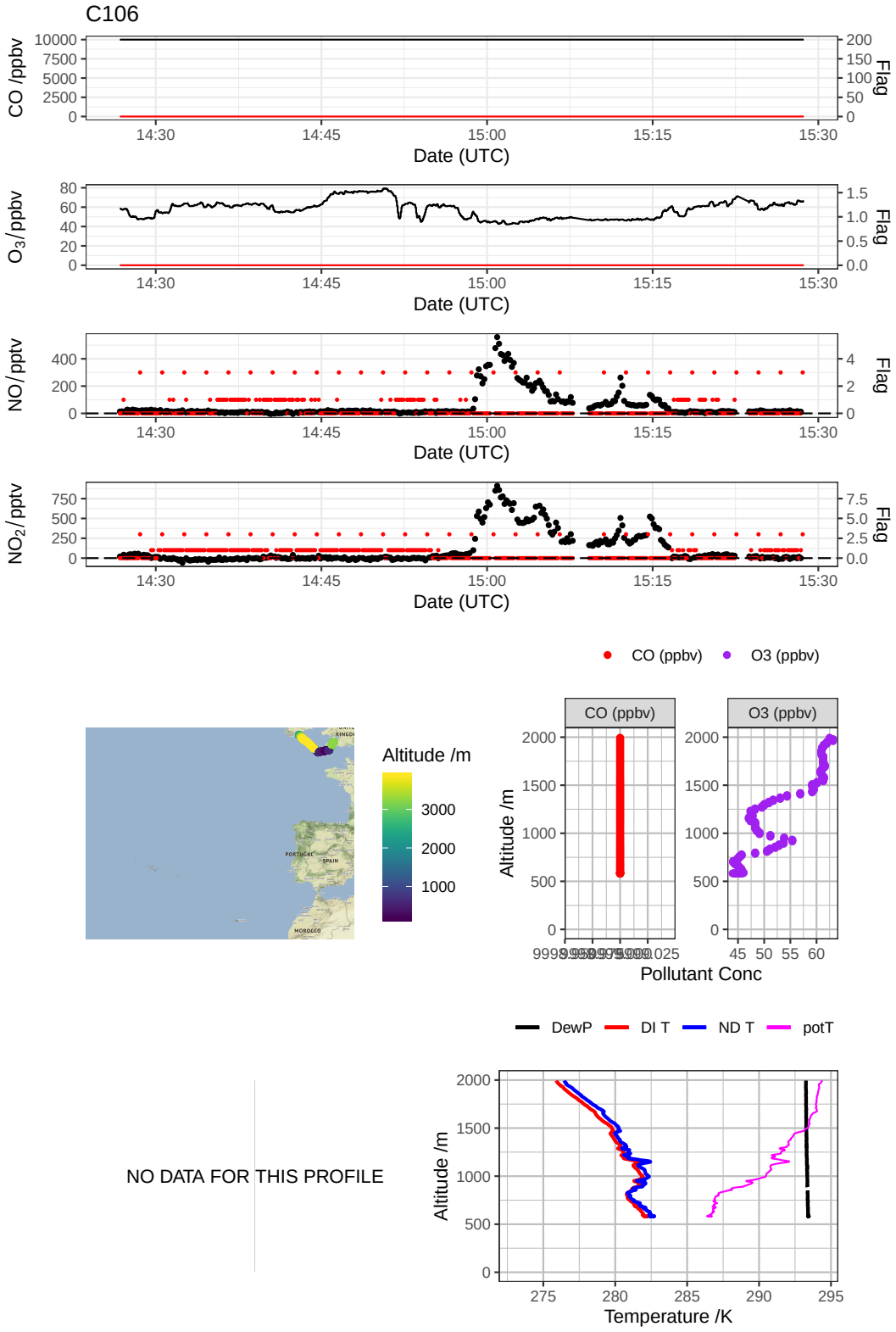
C106
CO /ppbv
Flag
Date (UTC)
O3/ppbv
NO/pptv
NO2/pptv
14:30
14:45
15:00
15:15
15:30
CO (ppbv)
O3 (ppbv)
Altitude /m
Pollutant Conc
DewP
DI T
ND T
potT
NO DATA FOR THIS PROFILE
Temperature /K

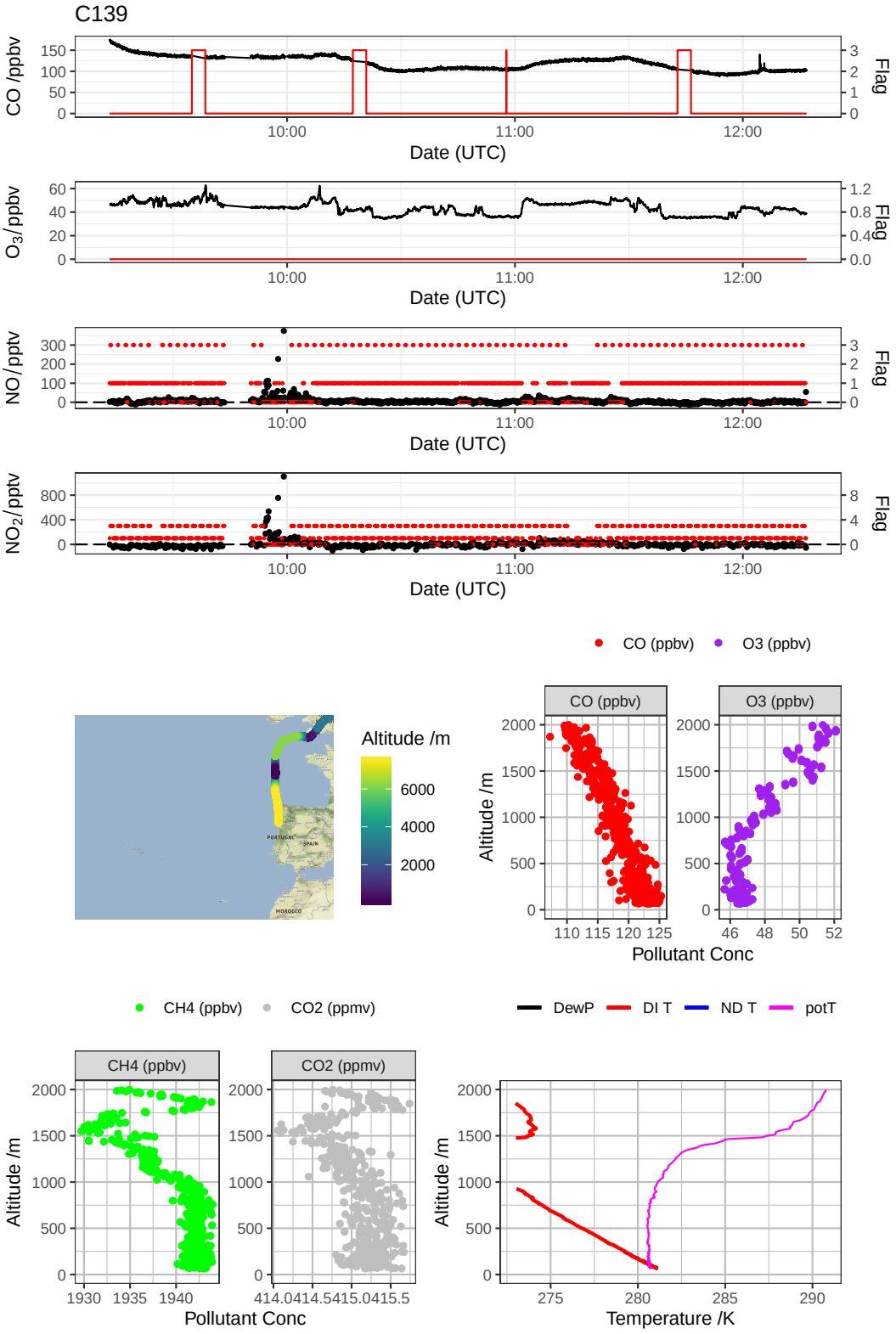
C139
CO /ppbv
Flag
Date (UTC)
10:00
11:00
12:00
O3/ppbv
NO/pptv
NO2/pptv
CO (ppbv)
O3 (ppbv)
Altitude /m
6000
4000
2000
Pollutant Conc
CH4 (ppbv)
CO2 (ppmv)
DewP
DI T
ND T
potT
Temperature /K

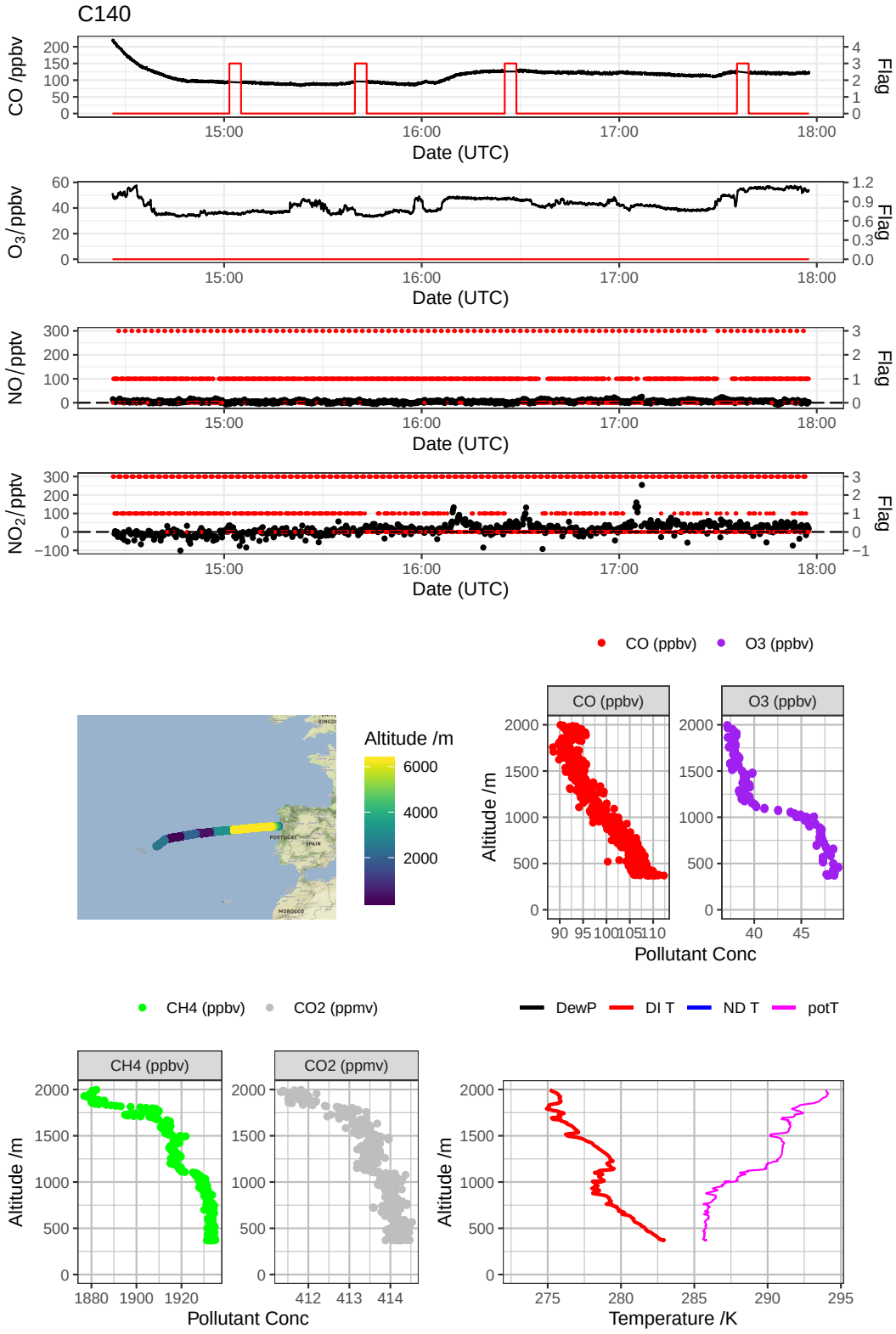
C140
CO /ppbv
Flag
Date (UTC)
O_3/ppbv
NO/pptv
NO_2/pptv
CO (ppbv)
O3 (ppbv)
Altitude /m
Pollutant Conc
CH4 (ppbv)
CO2 (ppmv)
DewP
DI T
ND T
potT
Temperature /K

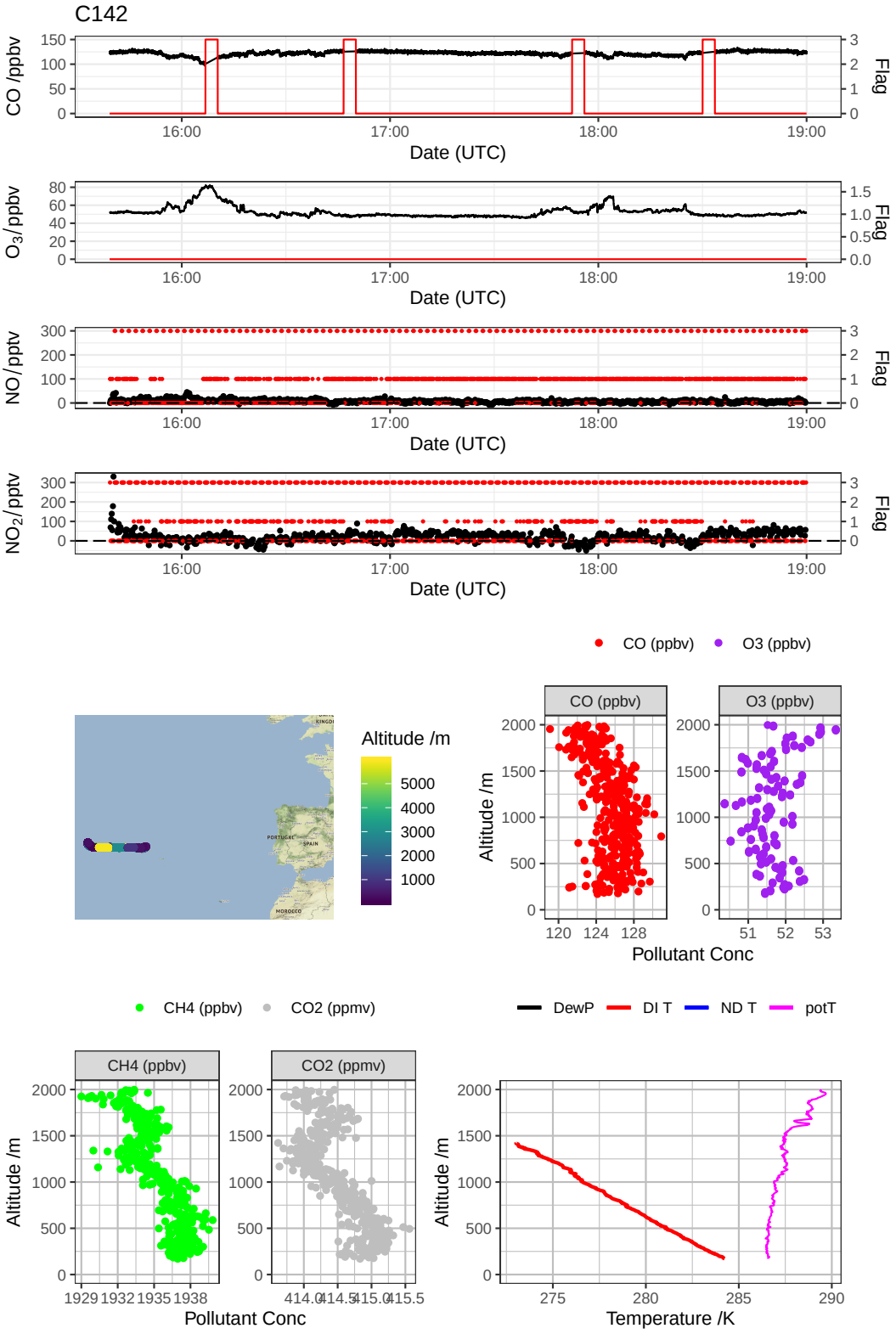
C142
CO /ppbv
Flag
Date (UTC)
16:00
17:00
18:00
19:00
O3/ppbv
NO/pptv
NO2/pptv
CO (ppbv)
O3 (ppbv)
Altitude /m
Pollutant Conc
CH4 (ppbv)
CO2 (ppmv)
DewP
DI T
ND T
potT
Temperature /K

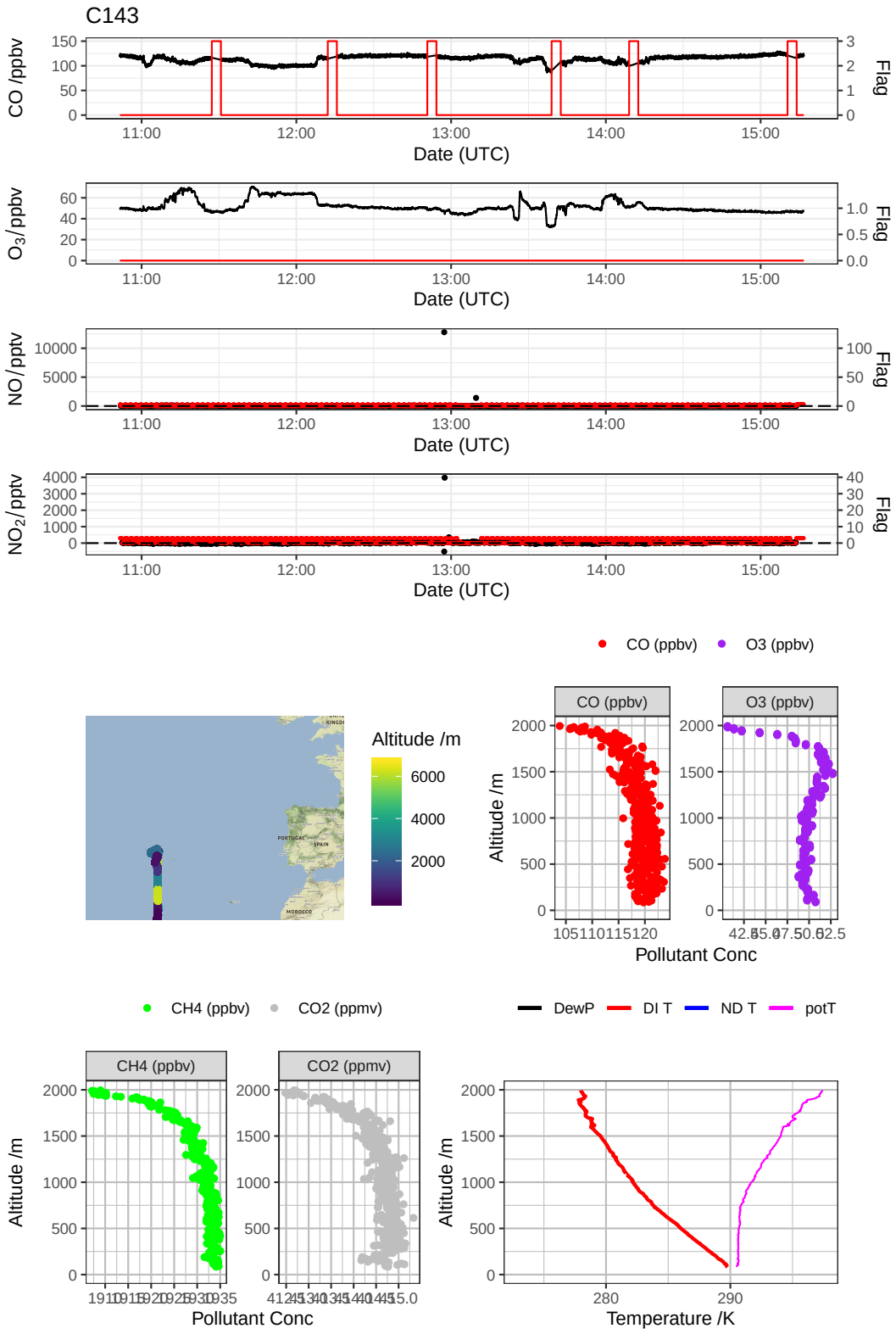
C143
CO /ppbv
Flag
Date (UTC)
O_3/ppbv
NO/pptv
NO_2/pptv
CO (ppbv)
O3 (ppbv)
Altitude /m
Pollutant Conc
CH4 (ppbv)
CO2 (ppmv)
DewP
DI T
ND T
potT
Temperature /K

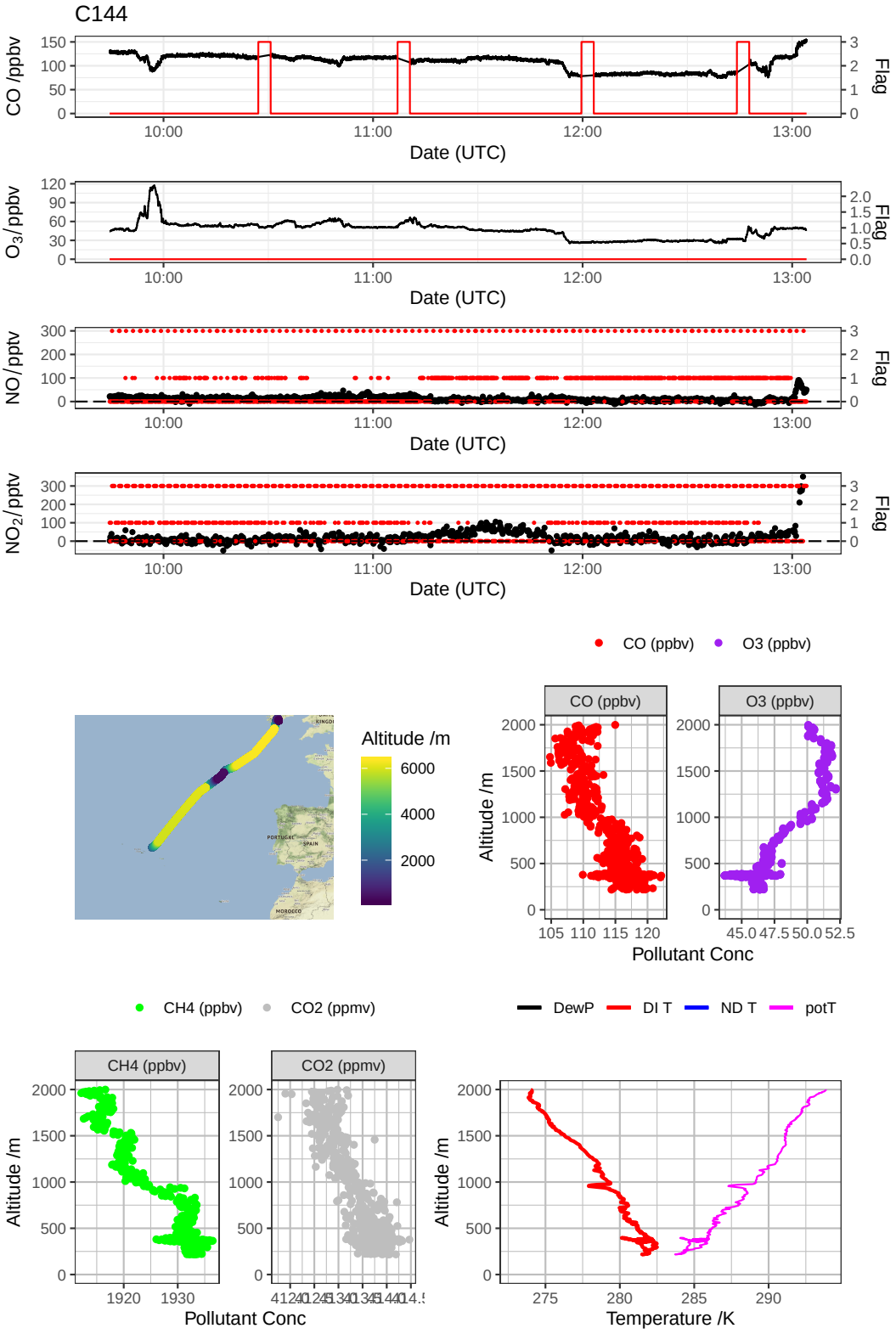
C144
CO /ppbv
Flag
Date (UTC)
O_3/ppbv
NO/pptv
NO_2/pptv
10:00
11:00
12:00
13:00
CO (ppbv)
O3 (ppbv)
Altitude /m
Pollutant Conc
CH4 (ppbv)
CO2 (ppmv)
DewP
DI T
ND T
potT
Temperature /K

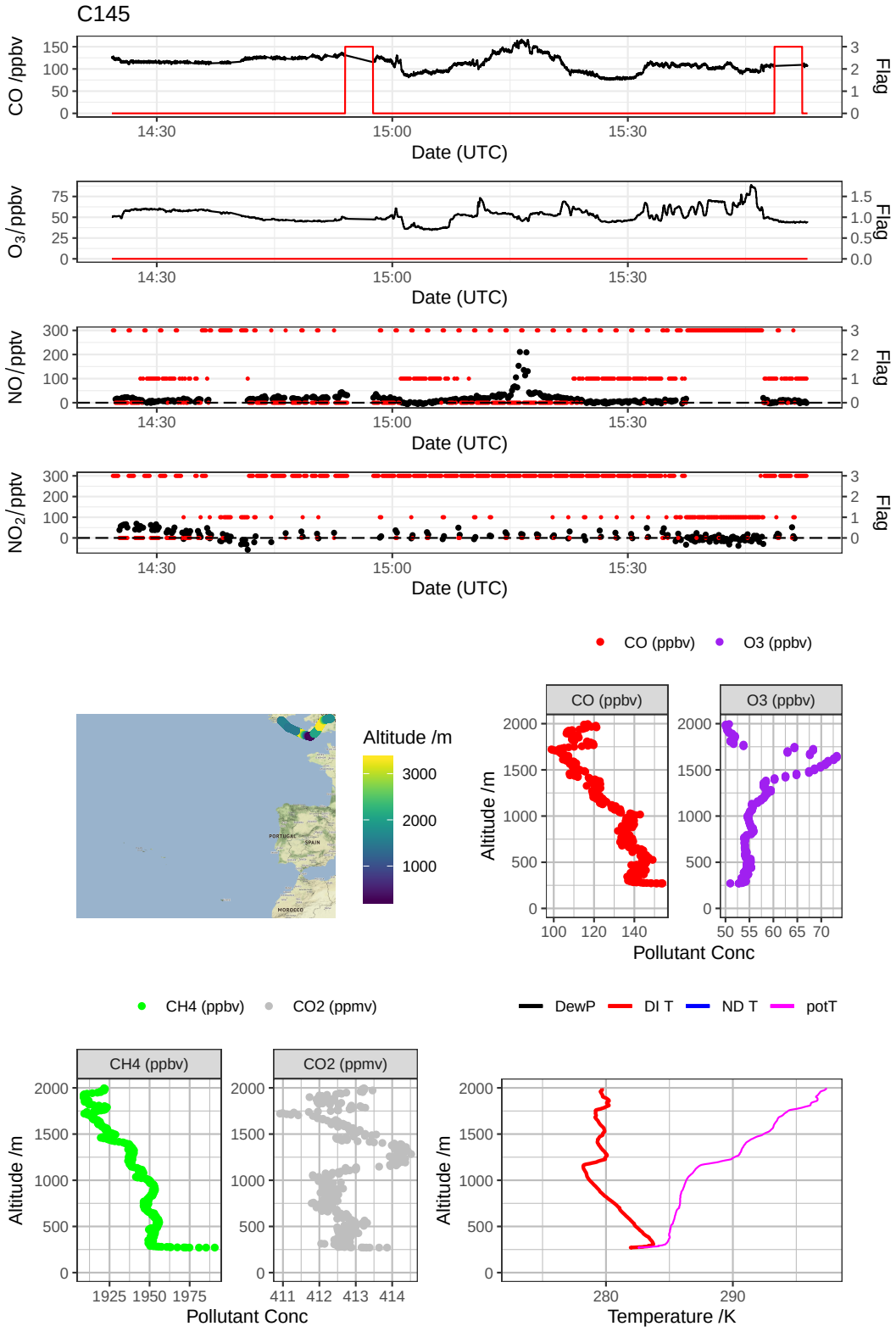
C145
CO /ppbv
Flag
Date (UTC)
O_3/ppbv
NO/pptv
NO_2/pptv
CO (ppbv)
O3 (ppbv)
Altitude /m
Pollutant Conc
CH4 (ppbv)
CO2 (ppmv)
DewP
DI T
ND T
potT
Temperature /K

Acronyms

ACSIS North Atlantic Climate System Integrated Study. 158–160, 162, 163, 166, 167, 169, 171, 186, 197, 198

AMOC Atlantic meridional overturning circulation. 154

AMV Atlantic multidecadal variability. 153, 154

APEC Asia-Pacific Economic Cooperation. 26

APHH Air Pollution and Human Health-Beijing. 40, 43, 56, 59, 74, 85, 115, 140

AQD Air Quality Design Inc.. 9, 11, 51, 52, 55, 56, 60–65, 67

ARA Atmospheric Research Aircraft. 156–158

BLC blue light converter. 51, 53, 55, 56

CAPS Cavity Attenuated Phase Shift. 46, 66

CAS Chinese Academy of Sciences. 43, 115

COVID-19 Coronavirus disease 2019. 19, 25, 26

CVAO Cape Verde Atmospheric Observatory. 38

DALY disability-adjusted life-year. 69

EC eddy-covariance. 33, 41, 115, 120, 121

EDGAR Emissions Database for Global Atmospheric Research. 32, 90, 92, 93

ESA European Space Agency. 20

FAAM Facility for Airborne Atmospheric Measurements. 156–158

GDAS NCEP Global Data Assimilation System. 90

GDP gross domestic product. 69, 70, 149

GFAS Global Fire Assimilation System. 179, 182

GHG greenhouse gas. 23, 25, 34, 154, 157, 170

GPT gas phase titration. 55, 56

HDV heavy duty vehicles. 133

IAP Institute of Atmospheric Physics. 43, 45, 50, 115, 121

IPCC Intergovernmental Panel on Climate Change. 23

IQR interquartile range. 164

ITOP Intercontinental Transport of Ozone and Precursors. 158

LDGV light-duty gasoline vehicle. 130

LDV light duty vehicles. 133

LED light emitting diode. 47, 51, 52

MEIC Multi-resolution Emissions Inventory for China. 32, 126, 127, 146, 148–150

MLH mixed layer height. 28, 78, 79, 82–84, 98, 130–132, 134, 135, 165

NAEI National Atmospheric Emissions Inventory. 32, 33

NAO North Atlantic Oscillation. 28, 154, 155, 159, 161

NAOI North Atlantic Oscillation Index. 28

NBL nocturnal boundary layer. 109

NMB normalised mean bias. 190, 192–195

NMVOC non-methane VOC. 38, 114

NPL National Physical Laboratory. 49, 61, 67, 116, 117

OMI Ozone Monitoring Instrument. 155

OPE ozone production efficiency. 98, 99, 111

PM particulate matter. 22, 31, 70, 113, 133

PMT photomultiplier tube. 46, 48, 53, 54, 57, 58

PSS photostationary state. 35, 100–103, 105, 106, 108–110, 112

PTR-MS Proton Transfer Reaction Mass Spectrometer. 144

PTR-ToF-MS Proton Transfer Reaction Time-of-Flight Mass Spectrometer. 9, 117, 118, 120, 141, 142

RF radiative forcing. 23, 39

RH relative humidity. 27

RMA reduced major axis. 176, 185

SOA secondary organic aerosol. 39, 100

SST sea surface temperature. 153, 154

TROPOMI Tropospheric Monitoring Instrument. 20

UN United Nations. 22, 69, 113

VOC volatile organic compound. 9, 10, 25, 28, 31, 33, 35–37, 39, 41, 73, 95, 98–101, 109, 111, 113–115, 117, 120, 140, 141, 143–147, 151, 152, 177, 180, 184, 185, 198

VUV Vacuum ultra-violet. 57

WAS Whole Air Sampling. 181, 183

WHO World Health Organisation. 9, 21–23, 26, 70, 71, 83, 111, 113

References

W. Aas, A. Mortier, V. Bowersox, R. Cherian, G. Faluvegi, H. Fagerli, J. Hand, Z. Klimont, C. Galy-Lacaux, C. M. B. Lehmann, C. L. Myhre, G. Myhre, D. Olivié, K. Sato, J. Quaas, P. S. P. Rao, M. Schulz, D. Shindell, R. B. Skeie, A. Stein, T. Takemura, S. Tsyro, R. Vet, and X. Xu. Global and regional trends of atmospheric sulfur. *Scientific Reports*, 9(1):953, 2019. doi: 10.1038/s41598-018-37304-0. [Page 31.]

W. J. F. Acton, Z. Huang, B. Davison, W. S. Drysdale, P. Fu, M. Hollaway, B. Langford, J. Lee, Y. Liu, S. Metzger, N. Mullinger, E. Nemitz, C. E. Reeves, F. A. Squires, A. R. Vaughan, X. Wang, Z. Wang, O. Wild, Q. Zhang, Y. Zhang, and C. N. Hewitt. Surface–atmosphere fluxes of volatile organic compounds in Beijing. *Atmospheric Chemistry and Physics Discussions*, 2020:1–36, 2020. doi: 10.5194/acp-2020-343. [Pages 99, 117, and 199.]

Air Quality Expert Group. Fine Particulate Matter ($PM_{2.5}$) in the United Kingdom. Technical report, Department for Environment, Food and Rural Affairs, UK, 2012. [Page 39.]

Air Quality Expert Group. Estimation of changes in air pollution emissions, concentrations and exposure during the COVID-19 outbreak in the UK Rapid Evidence Review – June 2020. Technical report, Department for Environment, Food and Rural Affairs, UK, 2020. [Page 19.]

M. Allen, D. O.P., W. Solecki, F. Aragón-Durand, W. Cramer, S. Humphreys, J. Kainuma, M. Kala, N. Mahowald, Y. Mulugetta, R. Perez, M. Wairiu, and K. Zickfeld. Framing and context. In V. Masson-Delmotte, P. Zhai, H.-O. Pörtner, D. Roberts, J. Skea, P. Shukla, A. Pirani, W. Moufouma-Okia, C. Péan, R. Pidcock,

S. Connors, J. Matthews, Y. Chen, M. Zhou, X. ans Gomis, T. Lonnoy, E. ansd Maycock, M. Tignor, and T. Waterfield, editors, *Global Warming of 1.5°C. An IPCC Special Report on the impacts of global warming of 1.5°C above pre-industrial levels and related global greenhouse gas emission pathways, in the context of strengthening the global response to the threat of climate change, sustainable development, and efforts to eradicate poverty*, chapter 1. IPCC, 2018. [Page 23.]

American Meteorological Society. AMS Glossary: Air Pollution, 2012a. URL `http://glossary.ametsoc.org/wiki/Air_pollution`. [Page 21.]

American Meteorological Society. AMS Glossary: Potential temperature, 2012b. URL `http://glossary.ametsoc.org/wiki/Potential_temperature`. [Page 166.]

S. T. Andersen, L. J. Carpenter, B. Nelson, L. Neves, K. A. Read, C. Reed, M. Ward, and J. D. Lee. Long-term NO_x measurements in marine air, *in prep.* 2020. [Page 63.]

M. O. Andreae and D. S. Schimel. *Exchange of trace gases between terrestrial ecosystems and the atmosphere*. John Wiley and Sons Inc., New York, USA, 1990. ISBN 0471925519. [Page 124.]

R. Atkinson. Atmospheric chemistry of VOCs and NO_x. *Atmospheric Environment*, 34(12–14):2063–2101, 2000. doi: 10.1016/S1352-2310(99)00460-4. [Pages 36 and 40.]

R. Atkinson and J. Arey. Atmospheric degradation of volatile organic compounds. *Chemical Reviews*, 103(12):4605–4638, 2003. doi: 10.1021/cr0206420. [Page 40.]

R. Atkinson, D. L. Baulch, R. A. Cox, J. N. Crowley, R. F. Hampson, R. G. Hynes, M. E. Jenkin, M. J. Rossi, and J. Troe. Evaluated kinetic and photochemical data for atmospheric chemistry: Volume I - gas phase reactions of O_x, HO_x, NO_x and SO_x species. *Atmospheric Chemistry and Physics*, 4(6):1461–1738, 2004. doi: 10.5194/acp-4-1461-2004. [Pages 67 and 100.]

M. Aubinet. Eddy covariance CO_2 flux measurements in nocturnal conditions: An analysis of the problem. *Ecological Applications*, 18(6):1368–1378, 2008. doi: 10.1890/06-1336.1. [Page 121.]

G. Ayers. Comment on regression analysis of air quality data. *Atmospheric Environment*, 35(13):2423–2425, 2001. doi: 10.1016/S1352-2310(00)00527-6. [Page 176.]

J. Ba, N. S. Keenlyside, M. Latif, W. Park, H. Ding, K. Lohmann, J. Mignot, M. Menary, O. H. Otterå, B. Wouters, et al. A multi-model comparison of Atlantic multidecadal variability. *Climate Dynamics*, 43(9–10):2333–2348, 2014. doi: 10.1007/s00382-014-2056-1. [Page 154.]

A. M. Baergen and D. J. Donaldson. Photochemical Renoxification of Nitric Acid on Real Urban Grime. *Environmental Science & Technology*, 47(2):815–820, 2013. doi: 10.1021/es3037862. [Page 38.]

T. J. Bannan, A. M. Booth, A. Bacak, J. B. A. Muller, K. E. Leather, M. Le Breton, B. Jones, D. Young, H. Coe, J. Allan, S. Visser, J. G. Slowik, M. Furger, A. S. H. Prevot, J. Lee, R. E. Dunmore, J. R. Hopkins, J. F. Hamilton, A. C. Lewis, L. K. Whalley, T. Sharp, D. Stone, D. E. Heard, Z. L. Fleming, R. Leigh, D. E. Shallcross, and C. J. Percival. The first UK measurements of nitryl chloride using a chemical ionization mass spectrometer in central london in the summer of 2012, and an investigation of the role of Cl atom oxidation. *Journal of Geophysical Research: Atmospheres*, 120(11):5638–5657, 2015. doi: 10.1002/2014JD022629. [Page 108.]

R. Bao and A. Zhang. Does lockdown reduce air pollution? Evidence from 44 cities in northern China. *Science of The Total Environment*, 731:139052, 2020. doi: 10.1016/j.scitotenv.2020.139052. [Page 19.]

B. Barletta, S. Meinardi, F. S. Rowland, C.-Y. Chan, X. Wang, S. Zou, L. Y. Chan, and D. R. Blake. Volatile organic compounds in 43 Chinese cities. *Atmospheric Environment*, 39(32):5979–5990, 2005. doi: 10.1016/j.atmosenv.2005.06.029. [Page 145.]

B. Beach and W. W. Hanlon. Coal Smoke and Mortality in an Early Industrial Economy. *The Economic Journal*, 128(615):2652–2675, 2017. doi: 10.1111/ecoj.12522. [Page 21.]

Beijing Municipal Bureau of Statistics. 2016 Beijing Statistical Yearbook, 2016. URL `http://nj.tjj.beijing.gov.cn/nj/main/2016-tjnj/zk/indexeh.htm`. Last access: 25 July 2020. [Page 69.]

S. Beirle, U. Platt, R. von Glasow, M. Wenig, and T. Wagner. Estimate of nitrogen oxide emissions from shipping by satellite remote sensing. *Geophysical Research Letters*, 31(18), 2004. doi: 10.1029/2004gl020312. [Page 156.]

S. Bell. A Beginner's Guide to Uncertainty of Measurement. In *Measurement Good Practice Guide No. 11*. National Physical Laboratory, Teddington, 2nd edition, 2001. [Page 65.]

P. Bergamaschi, M. Corazza, U. Karstens, M. Athanassiadou, R. L. Thompson, I. Pison, A. J. Manning, P. Bousquet, A. Segers, A. T. Vermeulen, G. Janssens-Maenhout, M. Schmidt, M. Ramonet, F. Meinhardt, T. Aalto, L. Haszpra, J. Moncrieff, M. E. Popa, D. Lowry, M. Steinbacher, A. Jordan, S. O'Doherty, S. Piacentino, and E. Dlugokencky. Top-down estimates of European CH_4 and N_2O emissions based on four different inverse models. *Atmospheric Chemistry and Physics*, 15(2):715–736, 2015. doi: 10.5194/acp-15-715-2015. [Page 34.]

I. Bey, D. J. Jacob, R. M. Yantosca, J. A. Logan, B. D. Field, A. M. Fiore, Q. Li, H. Y. Liu, L. J. Mickley, and M. G. Schultz. Global modeling of tropospheric chemistry with assimilated meteorology: Model description and evaluation. *Journal of Geophysical Research: Atmospheres*, 106(D19):23073–23095, 2001. doi: 10.1029/2001JD000807. [Page 194.]

M. Biggart, J. Stocker, R. M. Doherty, O. Wild, M. Hollaway, D. Carruthers, J. Li, Q. Zhang, R. Wu, S. Kotthaus, S. Grimmond, F. A. Squires, J. Lee, and Z. Shi. Street-scale air quality modelling for Beijing during a winter 2016 measurement campaign. *Atmospheric Chemistry and Physics*, 20(5), 2020. doi: 10.5194/acp-20-2755-2020. [Page 147.]

B. B. Booth, N. J. Dunstone, P. R. Halloran, T. Andrews, and N. Bellouin. Aerosols implicated as a prime driver of twentieth-century North Atlantic climate variability. *Nature*, 484(7393):228–232, 2012. doi: 10.1038/nature10946. [Page 154.]

A. Borbon, J. B. Gilman, W. C. Kuster, N. Grand, S. Chevaillier, A. Colomb, C. Dolgorouky, V. Gros, M. Lopez, R. Sarda-Esteve, J. Holloway, J. Stutz, H. Petetin, S. McKeen, M. Beekmann, C. Warneke, D. D. Parrish, and J. A. de Gouw. Emission ratios of anthropogenic volatile organic compounds in northern mid-latitude

megacities: Observations versus emission inventories in Los Angeles and Paris. *Journal of Geophysical Research: Atmospheres*, 118(4):2041–2057, 2013. doi: 10.1002/jgrd.50059. [Page 133.]

P. Brimblecombe. The Clean Air Act after 50 years. *Weather*, 61(11):311–314, 2006. doi: 10.1256/wea.127.06. [Page 21.]

F. V. Brock. A nonlinear filter to remove impulse noise from meteorological data. *Journal of Atmospheric and Oceanic Technology*, 3(1):51–58, 1986. doi: 10.1175/1520-0426(1986)003<0051:anftri>2.0.co;2. [Page 118.]

D. J. Bryant, W. J. Dixon, J. R. Hopkins, R. E. Dunmore, K. L. Pereira, M. Shaw, F. A. Squires, T. J. Bannan, A. Mehra, S. D. Worrall, A. Bacak, H. Coe, C. J. Percival, L. K. Whalley, D. E. Heard, E. J. Slater, B. Ouyang, T. Cui, J. D. Surratt, D. Liu, Z. Shi, R. Harrison, Y. Sun, W. Xu, A. C. Lewis, J. D. Lee, A. R. Rickard, and J. F. Hamilton. Strong anthropogenic control of secondary organic aerosol formation from isoprene in Beijing. *Atmospheric Chemistry and Physics*, 20(12):7531–7552, 2020. doi: 10.5194/acp-20-7531-2020. [Page 105.]

M. W. Buckley and J. Marshall. Observations, inferences, and mechanisms of the Atlantic Meridional Overturning Circulation: A review. *Reviews of Geophysics*, 54 (1):5–63, 2016. doi: 10.1002/2015RG000493. [Page 153.]

M. P. Buhr. Solid-state light source photolytic nitrogen dioxide converter, 2007. US Patent 7238328BT. [Pages 51 and 52.]

Bureau International des Poids et Mesures. Evaluation of measurement data – Guide to the expression of uncertainty in measurement, 2008. URL `https://www.bipm.org/en/publications/guides/gum.html`. Last accessed: 23 July 2020. [Page 60.]

D. Cabrera-Perez, D. Taraborrelli, R. Sander, and A. Pozzer. Global atmospheric budget of simple monocyclic aromatic compounds. *Atmospheric Chemistry and Physics*, 16(11):6931–6947, 2016. doi: 10.5194/acp-16-6931-2016. [Page 178.]

W. Cai, K. Li, H. Liao, H. Wang, and L. Wu. Weather conditions conducive to Beijing severe haze more frequent under climate change. *Nature Climate Change*, 7(4): 257–262, 2017. doi: 10.1038/nclimate3249. [Pages 72 and 73.]

M. O. L. Cambaliza, P. B. Shepson, D. R. Caulton, B. Stirm, D. Samarov, K. R. Gurney, J. Turnbull, K. J. Davis, A. Possolo, A. Karion, C. Sweeney, B. Moser, A. Hendricks, T. Lauvaux, K. Mays, J. Whetstone, J. Huang, I. Razlivanov, N. L. Miles, and S. J. Richardson. Assessment of uncertainties of an aircraft-based mass balance approach for quantifying urban greenhouse gas emissions. *Atmospheric Chemistry and Physics*, 14(17):9029–9050, 2014. doi: 10.5194/acp-14-9029-2014. [Page 33.]

I. Caplain, F. Cazier, H. Nouali, A. Mercier, J.-C. Déchaux, V. Nollet, R. Joumard, J.-M. André, and R. Vidon. Emissions of unregulated pollutants from European gasoline and diesel passenger cars. *Atmospheric Environment*, 40(31):5954–5966, 2006. doi: 10.1016/j.atmosenv.2005.12.049. [Page 140.]

I. M. Carey, H. R. Anderson, R. W. Atkinson, S. D. Beevers, D. G. Cook, D. P. Strachan, D. Dajnak, J. Gulliver, and F. J. Kelly. Are noise and air pollution related to the incidence of dementia? A cohort study in London, England. *BMJ Open*, 8(9): e022404, 2018. doi: 10.1136/bmjopen-2018-022404. [Page 70.]

F. Carozzi and S. Roth. Dirty density: Air quality and the density of American cities. CEP Discussion Papers dp1635, Centre for Economic Performance, LSE, 2019. URL `https://ideas.repec.org/p/cep/cepdps/dp1635.html`. [Page 72.]

L. J. Carpenter, K. C. Clemitshaw, R. A. Burgess, S. A. Penkett, J. N. Cape, and G. G. McFadyen. Investigation and evaluation of the NO_x/O_3 photochemical steady state. *Atmospheric Environment*, 32(19):3353–3365, 1998. doi: 10.1016/S1352-2310(97)00416-0. [Pages 100 and 104.]

D. C. Carslaw and G. Rhys-Tyler. New insights from comprehensive on-road measurements of NO_x, NO_2 and NH_3 from vehicle emission remote sensing in London, UK. *Atmospheric Environment*, 81:339–347, 2013. doi: 10.1016/j.atmosenv.2013.09.026. [Page 33.]

D. C. Carslaw and K. Ropkins. openair — an R package for air quality data analysis. *Environmental Modelling & Software*, 27–28(0):52–61, 2012. doi: 10.1016/j.envsoft.2011.09.008. [Page 89.]

D. M. Chate, S. D. Ghude, G. Beig, A. S. Mahajan, C. Jena, R. Srinivas, A. Dahiya, and N. Kumar. Deviations from the O_3–no–NO_2 photo-stationary state in Delhi, India. *Atmospheric Environment*, 96:353–358, 2014. doi: 10.1016/j.atmosenv.2014.07.054. [Page 100.]

P. Cheewaphongphan, S. Chatani, and N. Saigusa. Exploring Gaps between Bottom-Up and Top-Down Emission Estimates Based on Uncertainties in Multiple Emission Inventories: A Case Study on CH_4 Emissions in China. *Sustainability*, 11(7), 2019. doi: 10.3390/su11072054. [Page 32.]

L. X. Chen, M. Dong, and Y. N. Shao. The characteristics of interannual variations on the East Asian monsoon. *Journal of the Meteorological Society of Japan*, 70(1B): 397–421, 1992. doi: 10.2151/jmsj1965.70.1B_397. [Pages 73 and 135.]

J. Cheng, J. Su, T. Cui, X. Li, X. Dong, F. Sun, Y. Yang, D. Tong, Y. Zheng, Y. Li, J. Li, Q. Zhang, and K. He. Dominant role of emission reduction in $PM_{2.5}$ air quality improvement in Beijing during 2013–2017: a model-based decomposition analysis. *Atmospheric Chemistry and Physics*, 19(9):6125–6146, 2019. doi: 10.5194/acp-19-6125-2019. [Pages 73, 147, and 149.]

M. Chin, D. J. Jacob, J. W. Munger, D. D. Parrish, and B. G. Doddridge. Relationship of ozone and carbon monoxide over North America. *Journal of Geophysical Research: Atmospheres*, 99(D7):14565–14573, 1994. doi: 10.1029/94JD00907. [Page 94.]

Client Earth. Air pollution beyond lockdown: could the UK breathe cleaner air?, 2020. URL `https://www.clientearth.org/air-pollution-beyond-lockdown-could-the-uk-breathe-cleaner-air/`. Last access: 03 August 2020. [Page 21.]

A. J. Cohen, M. Brauer, R. Burnett, H. R. Anderson, J. Frostad, K. Estep, K. Balakrishnan, B. Brunekreef, L. Dandona, R. Dandona, V. Feigin, G. Freedman, B. Hubbell,

A. Jobling, H. Kan, L. Knibbs, Y. Liu, R. Martin, L. Morawska, C. A. Pope, III, H. Shin, K. Straif, G. Shaddick, M. Thomas, R. van Dingenen, A. van Donkelaar, T. Vos, C. J. L. Murray, and M. H. Forouzanfar. Estimates and 25-year trends of the global burden of disease attributable to ambient air pollution: an analysis of data from the Global Burden of Diseases Study 2015. *The Lancet*, 389(10082):1907–1918, 2017. doi: 10.1016/S0140-6736(17)30505-6. [Pages 21 and 69.]

O. Cooper, D. Derwent, B. Collins, R. Doherty, D. Stevenson, A. Stohl, and P. Hess. Conceptual overview of hemispheric or intercontinental transport of ozone and particulate matter. In F. Dentener, T. Keating, and H. Akimoto, editors, *Hemispheric Transport of Air Pollution 2010. Part A: Ozone and Particulate Matter*, Air Pollution Studies No. 17, pages 1–24. United Nations, New York and Geneva, 2010. [Page 155.]

O. R. Cooper, D. Parrish, J. Ziemke, M. Cupeiro, I. Galbally, S. Gilge, L. Horowitz, N. Jensen, J.-F. Lamarque, V. Naik, S. Oltmans, J. Schwab, D. Shindell, A. Thompson, V. Thouret, Y. Wang, and R. Zbinden. Global distribution and trends of tropospheric ozone: An observation-based review. *Elementa Science of the Anthropocene*, 2:000029, 2014. doi: 10.12952/journal.elementa.000029. [Page 155.]

M. Crippa, E. Solazzo, G. Huang, D. Guizzardi, E. Koffi, M. Muntean, C. Schieberle, R. Friedrich, and G. Janssens-Maenhout. High resolution temporal profiles in the Emissions Database for Global Atmospheric Research. *Scientific Data*, 7(1):1–17, 2020. doi: 10.1038/s41597-020-0462-2. [Page 32.]

C. Dai, Q. Wang, J. Kalogiros, D. Lenschow, Z. Gao, and M. Zhou. Determining boundary-layer height from aircraft measurements. *Boundary-Layer Meteorology*, 152(3):277–302, 2014. doi: 10.1007/s10546-014-9929-z. [Page 165.]

J. W. Deardorff. Convective velocity and temperature scales for the unstable planetary boundary layer and for Rayleigh convection. *Journal of the Atmospheric Sciences*, 27(8):1211–1213, 1970. doi: 10.1175/1520-0469(1970)027<1211:CVATSF>2.0.CO;2. [Page 125.]

DEFRA. National Atmospheric Emissions Inventory, 2014. URL `https://naei.beis.gov.uk/`. Last access: 26 July 2020. [Page 32.]

F. Dentener, T. Keating, and H. Akimoto, editors. *Hemispheric transport of air pollution: Part A Ozone and particulate matter*. Number 17 in Air Pollution Studies. United Nations, Geneva, Switzerland, 2010. ISBN 978-92-1-117043-6. [Page 28.]

R. Derwent, D. Stevenson, R. Doherty, W. Collins, M. Sanderson, and C. Johnson. Radiative forcing from surface NO_x emissions: spatial and seasonal variations. *Climatic Change*, 88(3-4):385–401, 2008. doi: 10.1007/s10584-007-9383-8. [Page 25.]

R. G. Derwent, A. J. Manning, P. G. Simmonds, T. G. Spain, and S. O'Doherty. Long-term trends in ozone in baseline and European regionally-polluted air at Mace Head, Ireland over a 30-year period. *Atmospheric Environment*, 179:279–287, 2018. doi: 10.1016/j.atmosenv.2018.02.024. [Page 156.]

A. J. Ding, T. Wang, V. Thouret, J.-P. Cammas, and P. Nédélec. Tropospheric ozone climatology over Beijing: analysis of aircraft data from the MOZAIC program. *Atmospheric Chemistry and Physics*, 8(1):1–13, 2008. doi: 10.5194/acp-8-1-2008. [Page 73.]

W. Dolan, V. H. Payne, S. S. Kualwik, and K. W. Bowman. Satellite observations of ethylene (C2H4) from the Aura Tropospheric Emission Spectrometer: A scoping study. *Atmospheric Environment*, 141:388–393, 2016. doi: 10.1016/j.atmosenv.2016.07.009. [Page 178.]

J. W. Drummond, A. Volz, and D. H. Ehhalt. An optimized chemiluminescence detector for tropospheric NO measurements. *Journal of Atmospheric Chemistry*, 2(3):287–306, 1985. doi: 10.1007/BF00051078. [Pages 46, 53, and 63.]

J. Duan, J. Tan, L. Yang, S. Wu, and J. Hao. Concentration, sources and ozone formation potential of volatile organic compounds (VOCs) during ozone episode in Beijing. *Atmospheric Research*, 88(1):25–35, 2008. doi: 10.1016/j.atmosres.2007.09.004. [Page 39.]

J. Duan, R.-J. Huang, Y. Li, Q. Chen, Y. Zheng, Y. Chen, C. Lin, H. Ni, M. Wang, J. Ovadnevaite, D. Ceburnis, C. Chen, D. R. Worsnop, T. Hoffmann, C. O'Dowd, and J. Cao. Summertime and wintertime atmospheric processes of secondary aerosol

in Beijing. *Atmospheric Chemistry and Physics*, 20(6), 2020. doi: 10.5194/acp-20-3793-2020. [Pages 39 and 114.]

B. N. Duncan, L. N. Lamsal, A. M. Thompson, Y. Yoshida, Z. Lu, D. G. Streets, M. M. Hurwitz, and K. E. Pickering. A space-based, high-resolution view of notable changes in urban NO_x pollution around the world (2005–2014). *Journal of Geophysical Research: Atmospheres*, 121(2):976–996, 2016. doi: 10.1002/2015JD024121. [Page 71.]

E. J. Dunlea, S. C. Herndon, D. D. Nelson, R. M. Volkamer, F. San Martini, P. M. Sheehy, M. S. Zahniser, J. H. Shorter, J. C. Wormhoudt, B. K. Lamb, E. J. Allwine, J. S. Gaffney, N. A. Marley, M. Grutter, C. Marquez, S. Blanco, B. Cardenas, A. Retama, C. R. Ramos Villegas, C. E. Kolb, L. T. Molina, and M. J. Molina. Evaluation of nitrogen dioxide chemiluminescence monitors in a polluted urban environment. *Atmospheric Chemistry and Physics*, 7(10):2691–2704, 2007. doi: 10.5194/acp-7-2691-2007. [Pages 47 and 50.]

C. Eden and J. Willebrand. Mechanism of interannual to decadal variability of the North Atlantic Circulation. *Journal of Climate*, 14(10):2266–2280, 2001. doi: 10.1175/1520-0442(2001)014<2266:MOITDV>2.0.CO;2. [Page 154.]

M. Ehn, J. A. Thornton, E. Kleist, M. Sipila, H. Junninen, I. Pullinen, M. Springer, F. Rubach, R. Tillmann, B. Lee, F. Lopez-Hilfiker, S. Andres, I.-H. Acir, M. Rissanen, T. Jokinen, S. Schobesberger, J. Kangasluoma, J. Kontkanen, T. Nieminen, T. Kurten, L. B. Nielsen, S. Jorgensen, H. G. Kjaergaard, M. Canagaratna, M. Dal Maso, T. Berndt, T. Petaja, A. Wahner, V.-M. Kerminen, M. Kulmala, D. R. Worsnop, J. Wildt, and T. F. Mentel. A large source of low-volatility secondary organic aerosol. *Nature*, 506(7489):476–479, 2014. doi: 10.1038/nature13032. [Page 99.]

S. Emeis and K. Schäfer. Remote sensing methods to investigate boundary-layer structures relevant to air pollution in cities. *Boundary-Layer Meteorology*, 121(2):377–385, 2006. doi: 10.1007/s10546-006-9068-2. [Page 28.]

C. Emery, Z. Liu, A. G. Russell, M. T. Odman, G. Yarwood, and N. Kumar. Recommendations on statistics and benchmarks to assess photochemical model perfor-

mance. *Journal of the Air & Waste Management Association*, 67(5):582–598, 2017. doi: 10.1080/10962247.2016.1265027. [Page 192.]

M. Etminan, G. Myhre, E. Highwood, and K. Shine. Radiative forcing of carbon dioxide, methane, and nitrous oxide: A significant revision of the methane radiative forcing. *Geophysical Research Letters*, 43(24):12,614–12,623, 2016. doi: 10.1002/2016GL071930. [Page 23.]

European Database For Global Atmospheric Research. Global emissions EDGAR v4.2, 2000–2012. URL `https://edgar.jrc.ec.europa.eu/overview.php?v=42`. [Page 114.]

European Environment Agency. Temperature inversion traps pollution at ground level, 2016. URL `https://www.eea.europa.eu/media/infographics/temperature-inversion-traps-pollution-at/view`. Last access: 03 August 2020. [Page 29.]

D. Famulari, E. Nemitz, C. Di Marco, G. J. Phillips, R. Thomas, E. House, and D. Fowler. Eddy-covariance measurements of nitrous oxide fluxes above a city. *Agricultural and Forest Meteorology*, 150(6):786–793, 2010. doi: 10.1016/j.agrformet.2009.08.003. [Page 117.]

F. C. Fehsenfeld, R. R. Dickerson, G. Hübler, W. T. Luke, L. J. Nunnermacker, E. J. Williams, J. M. Roberts, J. G. Calvert, C. M. Curran, A. C. Delany, C. S. Eubank, D. W. Fahey, A. Fried, B. W. Gandrud, A. O. Langford, P. C. Murphy, R. B. Norton, K. E. Pickering, and B. A. Ridley. A ground-based intercomparison of NO, NO_x, and NO_y measurement techniques. *Journal of Geophysical Research: Atmospheres*, 92(D12):14710–14722, 1987. doi: 10.1029/JD092iD12p14710. [Page 47.]

L. Feng and W. Liao. Legislation, plans, and policies for prevention and control of air pollution in China: achievements, challenges, and improvements. *Journal of Cleaner Production*, 112:1549–1558, 2016. doi: 10.1016/j.jclepro.2015.08.013. [Page 70.]

B. Finlayson-Pitts, M. Ezell, and J. Pitts. Formation of chemically active chlorine com-

pounds by reactions of atmospheric NaCl particles with gaseous N_2O_5 and $ClONO_2$. *Nature*, 337(6204):241–244, 1989. doi: 10.1038/337241a0. [Page 109.]

B. J. Finlayson-Pitts and J. N. Pitts. CHAPTER 1 - Overview of the Chemistry of Polluted and Remote Atmospheres. In *Chemistry of the Upper and Lower Atmosphere*, pages 1–14. Academic Press, San Diego, 2000a. ISBN 978-0-12-257060-5. doi: 10.1016/B978-012257060-5/50003-4. [Page 21.]

B. J. Finlayson-Pitts and J. N. Pitts. Applications of Atmospheric Chemistry: Air Pollution Control Strategies and Risk Assessments for Tropospheric Ozone and Associated Photochemical Oxidants, Acids, Particles, and Hazardous Air Pollutants. In B. J. Finlayson-Pitts and J. N. Pitts, editors, *Chemistry of the Upper and Lower Atmosphere*, pages 871–942. Academic Press, San Diego, 2000b. ISBN 9780122570605. [Page 37.]

J. J. Finnigan. The storage term in eddy flux calculations. *Agricultural and Forest Meteorology*, 136(3–4):108–113, 2006. doi: 10.1016/j.agrformet.2004.12.010. [Page 124.]

V. E. Fioletov, C. A. McLinden, N. Krotkov, C. Li, J. Joiner, N. Theys, S. Carn, and M. D. Moran. A global catalogue of large SO_2 sources and emissions derived from the Ozone Monitoring Instrument. *Atmospheric Chemistry and Physics*, 16(18): 11497–11519, 2016. doi: 10.5194/acp-16-11497-2016. [Page 31.]

A. M. Fiore, V. Naik, D. V. Spracklen, A. Steiner, N. Unger, M. Prather, D. Bergmann, P. J. Cameron-Smith, I. Cionni, W. J. Collins, S. Dalsoren, V. Eyring, G. A. Folberth, P. Ginoux, L. W. Horowitz, B. Josse, J.-F. Lamarque, I. A. MacKenzie, T. Nagashima, F. M. O'Connor, M. Righi, S. T. Rumbold, D. T. Shindell, R. B. Skeie, K. Sudo, S. Szopa, T. Takemura, and G. Zeng. Global air quality and climate. *Chemical Reviews*, 41(19):6663–6683, 2012. doi: 10.1039/c2cs35095e. [Page 39.]

A. M. Fiore, V. Naik, and E. M. Leibensperger. Air quality and climate connections. *Journal of the Air & Waste Management Association*, 65(6):645–685, 2015. doi: 10.1080/10962247.2015.1040526. [Pages 23 and 39.]

E. V. Fischer, D. J. Jacob, R. M. Yantosca, M. P. Sulprizio, D. B. Millet, J. Mao, F. Paulot, H. B. Singh, A. Roiger, L. Ries, R. W. Talbot, K. Dzepina, and S. Pandey Deolal. Atmospheric peroxyacetyl nitrate (PAN): a global budget and source attribution. *Atmospheric Chemistry and Physics*, 14(5):2679–2698, 2014. doi: 10.5194/acp-14-2679-2014. [Page 38.]

J. Fishman and W. Seiler. Correlative nature of ozone and carbon monoxide in the troposphere: Implications for the tropospheric ozone budget. *Journal of Geophysical Research: Oceans*, 88(C6):3662–3670, 1983. doi: 10.1029/JC088iC06p03662. [Page 184.]

T. Foken. *Micrometeorology*. Springer, Berlin, Heidelberg, Germany, 2 edition, 2017. ISBN 354074665X. doi: 10.1007/978-3-642-25440-6. [Page 121.]

T. Foken and B. Wichura. Tools for quality assessment of surface-based flux measurements. *Agricultural and Forest Meteorology*, 78(1–2):83–105, 1996. doi: 10.1016/0168-1923(95)02248-1. [Page 123.]

T. Foken, M. Göockede, M. Mauder, L. Mahrt, B. Amiro, and W. Munger. Post-field data quality control. In X. Lee, W. Massman, and B. Law, editors, *Handbook of Micrometeorology*, volume 29 of *Atmospheric and Oceanographic Sciences Library*, pages 181–208. Springer Academic Publisher, Dordrecht, 2004. doi: 10.1007/1-4020-2265-4_9. [Page 124.]

D. Fowler, K. Pilegaard, M. A. Sutton, P. Ambus, M. Raivonen, J. Duyzer, D. Simpson, H. Fagerli, S. Fuzzi, J. K. Schjoerring, C. Granier, A. Neftel, I. S. A. Isaksen, P. Laj, M. Maione, P. S. Monks, J. Burkhardt, U. Daemmgen, J. Neirynck, E. Personne, R. Wichink-Kruit, K. Butterbach-Bahl, C. Flechard, J. P. Tuovinen, M. Coyle, G. Gerosa, B. Loubet, N. Altimir, L. Gruenhage, C. Ammann, S. Cieslik, E. Paoletti, T. N. Mikkelsen, H. Ro-Poulsen, P. Cellier, J. N. Cape, L. Horvath, F. Loreto, U. Niinemets, P. I. Palmer, J. Rinne, P. Misztal, E. Nemitz, D. Nilsson, S. Pryor, M. W. Gallagher, T. Vesala, U. Skiba, N. Brueggemann, S. Zechmeister-Boltenstern, J. Williams, C. O'Dowd, M. C. Facchini, G. de Leeuw, A. Flossman, N. Chaumerliac, and J. W. Erisman. Atmospheric composition change: ecosystems–

atmosphere interactions. *Atmospheric Environment*, 43(33):5193–5267, 2009. doi: 10.1016/j.atmosenv.2009.07.068. [Page 34.]

H. Fuchs, B. Bohn, A. Hofzumahaus, F. Holland, K. D. Lu, S. Nehr, F. Rohrer, and A. Wahner. Detection of HO_2 by laser-induced fluorescence: calibration and interferences from RO_2 radicals. *Atmospheric Measurement Techniques*, 4(6):1209–1225, 2011. doi: 10.5194/amt-4-1209-2011. [Page 105.]

J. S. Gaffney and N. A. Marley. The impacts of combustion emissions on air quality and climate–From coal to biofuels and beyond. *Atmospheric Environment*, 43(1): 23–36, 2009. doi: 10.1016/j.atmosenv.2008.09.016. [Page 21.]

B. Ge, Y. Sun, Y. Liu, H. Dong, D. Ji, Q. Jiang, J. Li, and Z. Wang. Nitrogen dioxide measurement by cavity attenuated phase shift spectroscopy (CAPS) and implications in ozone production efficiency and nitrate formation in Beijing, China. *Journal of Geophysical Research: Atmospheres*, 118(16):9499–9509, 2013. doi: 10.1002/jgrd.50757. [Pages 47 and 97.]

C. Gerbig, D. Kley, A. Volz-Thomas, J. Kent, K. Dewey, and D. S. McKenna. Fast response resonance fluorescence CO measurements aboard the C-130: Instrument characterization and measurements made during North Atlantic Regional Experiment 1993. *Journal of Geophysical Research: Atmospheres*, 101(D22):29229–29238, 1996. doi: 10.1029/95JD03272. [Pages 57 and 117.]

C. Gerbig, S. Schmitgen, D. Kley, A. Volz-Thomas, K. Dewey, and D. Haaks. An improved fast-response vacuum-UV resonance fluorescence CO instrument. *Journal of Geophysical Research: Atmospheres*, 104(D1):1699–1704, 1999. doi: 10.1029/1998JD100031. [Pages 57, 58, 59, and 117.]

B. Gioli, G. Gualtieri, C. Busillo, F. Calastrini, A. Zaldei, and P. Toscano. Improving high resolution emission inventories with local proxies and urban eddy covariance flux measurements. *Atmospheric Environment*, 115:246–256, 2015. doi: 10.1016/j.atmosenv.2015.05.068. [Page 33.]

S. K. Grange and D. C. Carslaw. Using meteorological normalisation to detect inter-

ventions in air quality time series. *Science of The Total Environment*, 653:578–588, 2019. doi: 10.1016/j.scitotenv.2018.10.344. [Page 26.]

C. Granier, U. Niemeier, J. H. Jungclaus, L. Emmons, P. Hess, J.-F. Lamarque, S. Walters, and G. P. Brasseur. Ozone pollution from future ship traffic in the Arctic northern passages. *Geophysical Research Letters*, 33(13), 2006. doi: 10.1029/2006GL026180. [Page 30.]

M. Grundstrom, L. Tang, M. Hallquist, H. Nguyen, D. Chen, and H. Pleijel. Influence of atmospheric circulation patterns on urban air quality during the winter. *Atmospheric Pollution Research*, 6(2):278–285, 2015. doi: 10.5094/APR.2015.032. [Page 28.]

D. S. Gu, Y. H. Wang, C. Smeltzer, and Z. Liu. Reduction in NO_x emission trends over China: Regional and seasonal variations. *Environmental Science & Technology*, 47 (22):12912–12919, 2013. doi: 10.1021/es401727e. [Page 71.]

H. Guo, X. Gu, G. Ma, S. Shi, W. Wang, X. Zuo, and X. Zhang. Spatial and temporal variations of air quality and six air pollutants in China during 2015–2017. *Scientific Reports*, 9(1):1–11, 2019. doi: 10.1038/s41598-019-50655-6. [Page 30.]

J. Guo, J. He, H. Liu, Y. Miao, H. Liu, and P. Zhai. Impact of various emission control schemes on air quality using WRF-Chem during APEC China 2014. *Atmospheric Environment*, 140:311–319, 2016. doi: 10.1016/j.atmosenv.2016.05.046. [Page 26.]

S. Guo, M. Hu, M. L. Zamora, J. Peng, D. Shang, J. Zheng, Z. Du, Z. Wu, M. Shao, L. Zeng, M. J. Molina, and R. Zhang. Elucidating severe urban haze formation in China. *Proceedings of the National Academy of Sciences*, 111(49):17373–17378, 2014. doi: 10.1073/pnas.1419604111. [Pages 39 and 114.]

R. M. Harrison. Urban Atmospheric Chemistry. *npj Climate and Atmospheric Science*, 1(5):20175, 2018. doi: 10.1038/s41612-017-0010-8. [Page 35.]

R. M. Harrison, M. Dall'Osto, D. C. S. Beddows, A. J. Thorpe, W. J. Bloss, J. D. Allan, H. Coe, J. R. Dorsey, M. Gallagher, C. Martin, J. Whitehead, P. I. Williams, R. L. Jones, J. M. Langridge, A. K. Benton, S. M. Ball, B. Langford, C. N. Hewitt,

B. Davison, D. Martin, K. F. Petersson, S. J. Henshaw, I. R. White, D. E. Shallcross, J. F. Barlow, T. Dunbar, F. Davies, E. Nemitz, G. J. Phillips, C. Helfter, C. F. Di Marco, and S. Smith. Atmospheric chemistry and physics in the atmosphere of a developed megacity (London): an overview of the REPARTEE experiment and its conclusions. *Atmospheric Chemistry and Physics*, 12(6):3065–3114, 2012. doi: 10.5194/acp-12-3065-2012. [Page 117.]

J. Hartmann, M. Gehrmann, K. Kohnert, S. Metzger, and T. Sachs. New calibration procedures for airborne turbulence measurements and accuracy of the methane fluxes during the AirMeth campaigns. *Atmospheric Measurement Techniques*, 11 (11):4567–4581, 2018. doi: 10.5194/amt-11-4567-2018. [Page 119.]

N. V. Heeb, A.-M. Forss, C. Bach, S. Reimann, A. Herzog, and H. W. Jäckle. A comparison of benzene, toluene and C_2-benzenes mixing ratios in automotive exhaust and in the suburban atmosphere during the introduction of catalytic converter technology to the Swiss car fleet. *Atmospheric Environment*, 34(19):3103–3116, 2000. doi: 10.1016/S1352-2310(99)00446-X. [Pages 145 and 146.]

K. Heidorn. Chronology of important events in the history of air-pollution meteorology to 1970. *Bulletin of the American Meteorological Society*, 59(12):1589–1597, 1978. doi: 10.1175/1520-0477(1978)059<1589:ACOIEI>2.0.CO;2. [Page 21.]

C. Helfter, A. H. Tremper, C. H. Halios, S. Kotthaus, A. Bjorkegren, C. S. B. Grimmond, J. F. Barlow, and E. Nemitz. Spatial and temporal variability of urban fluxes of methane, carbon monoxide and carbon dioxide above London, UK. *Atmospheric Chemistry and Physics*, 16(16):10543–10557, 2016. doi: 10.5194/acp-16-10543-2016. [Pages 117, 130, and 134.]

R. M. Hoesly, S. J. Smith, L. Feng, Z. Klimont, G. Janssens-Maenhout, T. Pitkanen, J. J. Seibert, L. Vu, R. J. Andres, R. M. Bolt, T. C. Bond, L. Dawidowski, N. Kholod, J.-i. Kurokawa, M. Li, L. Liu, Z. Lu, M. C. P. Moura, P. R. O'Rourke, and Q. Zhang. Historical (1750–2014) anthropogenic emissions of reactive gases and aerosols from the Community Emission Data System (CEDS). *Geoscientific Model Development*, 11:369–408, 2018. doi: 10.5194/gmd-11-369-2018. [Page 25.]

M. Hollaway, O. Wild, T. Yang, Y. Sun, W. Xu, C. Xie, L. Whalley, E. Slater, D. Heard, and D. Liu. Photochemical impacts of haze pollution in an urban environment. *Atmospheric Chemistry and Physics*, 19(15):9699–9714, 2019. doi: 10.5194/acp-19-9699-2019. [Page 108.]

R. E. Honrath, R. C. Owen, M. Val Martín, J. S. Reid, K. Lapina, P. Fialho, M. P. Dziobak, J. Kleissl, and D. L. Westphal. Regional and hemispheric impacts of anthropogenic and biomass burning emissions on summertime CO and O_3 in the North Atlantic lower free troposphere. *Journal of Geophysical Research: Atmospheres*, 109(D24):D24310, 2004. doi: 10.1029/2004JD005147. [Page 155.]

L. W. Horowitz, S. Walters, D. L. Mauzerall, L. K. Emmons, P. J. Rasch, C. Granier, X. Tie, J.-F. Lamarque, M. G. Schultz, G. S. Tyndall, J. J. Orlando, and G. P. Brasseur. A global simulation of tropospheric ozone and related tracers: Description and evaluation of MOZART, version 2. *Journal of Geophysical Research: Atmospheres*, 108(D24):4784, 2003. doi: 10.1029/2002JD002853. [Page 155.]

T. Huang, X. Zhu, Q. Zhong, X. Yun, W. Meng, B. Li, J. Ma, E. Y. Zeng, and S. Tao. Spatial and temporal trends in global emissions of nitrogen oxides from 1960 to 2014. *Environmental Science & Technology*, 51(14):7992–8000, 2017. doi: 10.1021/acs.est.7b02235. [Pages 30 and 31.]

H. Huntrieser, C. Feigl, H. Schlager, F. Schröder, C. Gerbig, P. Van Velthoven, F. Flatøy, C. Théry, A. Petzold, H. Höller, et al. Airborne measurements of NO_x, tracer species, and small particles during the European Lightning Nitrogen Oxides Experiment. *Journal of Geophysical Research: Atmospheres*, 107(D11):4113,, 2002. doi: 10.1029/2000JD000209. [Page 164.]

IATA. International Air Transport Association: Air Passenger Market Analysis, May 2020, 2020. URL `https://www.iata.org/en/iata-repository/publications/economic-reports/air-passenger-monthly-analysis---may-2020/`. Last access: 18 July 2020. [Page 19.]

F. Iglesias-Suarez, D. E. Kinnison, A. Rap, A. C. Maycock, O. Wild, and P. J. Young. Key drivers of ozone change and its radiative forcing over the 21st century. *At-*

mospheric Chemistry and Physics, 18(9):6121–6139, 2018. doi: 10.5194/acp-18-6121-2018. [Page 23.]

International Energy Agency. International Energy Agency, Energy and Air Pollution: World Energy Outlook Special Report 2016, 2016. URL `https://www.iea.org/reports/energy-and-air-pollution`. Last access: 10 July 2020. [Pages 71 and 146.]

IUPAC. IUPAC Task Group on Atmospheric Chemical Kinetic Data Evaluation – data sheet ClOx, 2013. URL `http://iupac.pole-ether.fr`. Last access: 2 August 2020. [Page 109.]

D. J. Jacob and D. A. Winner. Effect of climate change on air quality. *Atmospheric Environment*, 43(1):51–63, 2009. doi: 10.1016/j.atmosenv.2008.09.051. [Page 23.]

D. A. Jaffe and N. L. Wigder. Ozone production from wildfires: A critical review. *Atmospheric Environment*, 51:1–10, 2012. doi: 10.1016/j.atmosenv.2011.11.063. [Page 176.]

M. E. Jenkin, R. Valorso, B. Aumont, and A. R. Rickard. Estimation of rate coefficients and branching ratios for reactions of organic peroxy radicals for use in automated mechanism construction. *Atmospheric Chemistry and Physics*, 19(11):7691–7717, 2019. doi: 10.5194/acp-19-7691-2019. [Pages 104 and 105.]

Y. T. Jia, K. A. Rahn, K. B. He, T. X. Wen, and Y. S. Wang. A novel technique for quantifying the regional component of urban aerosol solely from its sawtooth cycles. *Journal of Geophysical Research: Atmospheres*, 113(D21), 2008. doi: 10.1029/2008jd010389. [Pages 72 and 135.]

Z. Jiang, J. R. Worden, H. Worden, M. Deeter, D. Jones, A. F. Arellano, and D. K. Henze. A 15-year record of CO emissions constrained by MOPITT CO observations. *Atmospheric Chemistry and Physics*, 17(7):4565–4583, 2017. doi: 10.5194/acp-17-4565-2017. [Page 31.]

X. M. Jin and T. Holloway. Spatial and temporal variability of ozone sensitivity over China observed from the Ozone Monitoring Instrument. *Journal of Geophysical*

Research: Atmospheres, 120(14):7229–7246, 2015. doi: 10.1002/2015jd023250. [Page 71.]

Y. Jin, H. Andersson, and S. Zhang. Air pollution control policies in China: a retrospective and prospects. *International Journal of Environmental Research and Public Health*, 13(12):1219, 2016. doi: 10.3390/ijerph13121219. [Page 70.]

B. Y. Jing, L. Wu, H. J. Mao, S. N. Gong, J. J. He, C. Zou, G. H. Song, X. Y. Li, and Z. Wu. Development of a vehicle emission inventory with high temporal-spatial resolution based on NRT traffic data and its impact on air pollution in Beijing - Part 1: Development and evaluation of vehicle emission inventory. *Atmospheric Chemistry and Physics*, 16(5):3161–3170, 2016. doi: 10.5194/acp-16-3161-2016. [Pages 81 and 133.]

M. Kampa and E. Castanas. Human health effects of air pollution. *Environmental Pollution*, 151(2):362–367, 2008. doi: 10.1016/j.envpol.2007.06.012. [Page 22.]

T. Karl, E. Apel, A. Hodzic, D. Riemer, D. Blake, and C. Wiedinmyer. Emissions of volatile organic compounds inferred from airborne flux measurements over a megacity. *Atmospheric Chemistry and Physics*, 9(1):271–285, 2009. doi: 10.5194/acp-9-271-2009. [Pages 142, 144, 145, and 146.]

T. Karl, M. Graus, M. Striednig, C. Lamprecht, A. Hammerle, G. Wohlfahrt, A. Held, L. von der Heyden, M. J. Deventer, A. Krismer, C. Haun, R. Feichter, and J. Lee. Urban eddy covariance measurements reveal significant missing NO_x emissions in Central Europe. *Scientific Reports*, 7:2536, 2017. doi: 10.1038/s41598-017-02699-9. [Pages 33, 50, and 130.]

T. Karl, M. Striednig, M. Graus, A. Hammerle, and G. Wohlfahrt. Urban flux measurements reveal a large pool of oxygenated volatile organic compound emissions. *Proceedings of the National Academy of Sciences*, 115(6):1186–1191, 2018. doi: 10.1073/pnas.1714715115. [Pages 114 and 144.]

P. Kasibhatla, H. Levy, W. J. Moxim, S. N. Pandis, J. J. Corbett, M. C. Peterson, R. E. Honrath, G. J. Frost, K. Knapp, D. D. Parrish, and T. B. Ryerson. Do emissions from ships have a significant impact on concentrations of nitrogen oxides in the

marine boundary layer? *Geophysical Research Letters*, 27(15):2229–2232, 2000. doi: 10.1029/2000gl011387. [Page 156.]

P. L. Kebabian, S. C. Herndon, and A. Freedman. Detection of nitrogen dioxide by cavity attenuated phase shift spectroscopy. *Analytical Chemistry*, 77(2):724–728, 2005. doi: 10.1021/ac048715y. [Page 47.]

L. I. Kleinman, P. H. Daum, Y.-N. Lee, L. J. Nunnermacker, S. R. Springston, J. Weinstein-Lloyd, and J. Rudolph. Ozone production efficiency in an urban area. *Journal of Geophysical Research: Atmospheres*, 107(D23):ACH 23–1–ACH 23–12, 2002. doi: 10.1029/2002JD002529. [Page 97.]

D. Kley and M. McFarland. Chemiluminescence detector for NO and NO_2. *Atmospheric Technology*, 12:63–69, 1980. [Page 50.]

Z. Klimont, S. J. Smith, and J. Cofala. The last decade of global anthropogenic sulfur dioxide: 2000–2011 emissions. *Environmental Research Letters*, 8(1):014003, 2013. doi: 10.1088/1748-9326/8/1/014003. [Page 31.]

N. Kljun, P. Calanca, M. W. Rotach, and H. P. Schmid. A simple parameterisation for flux footprint predictions. *Boundary-Layer Meteorology*, 112(3):503–523, 2004. doi: 10.1023/b:boun.0000030653.71031.96. [Page 125.]

J. R. Knight, C. K. Folland, and A. A. Scaife. Climate impacts of the Atlantic Multidecadal Oscillation. *Geophysical Research Letters*, 33(17):L17706, 2006. doi: 10.1029/2006GL026242. [Page 153.]

M. Kopacz, D. J. Jacob, J. A. Fisher, J. A. Logan, L. Zhang, I. A. Megretskaia, R. M. Yantosca, K. Singh, D. K. Henze, J. P. Burrows, M. Buchwitz, I. Khlystova, W. W. McMillan, J. C. Gille, D. P. Edwards, A. Eldering, V. Thouret, and P. Nedelec. Global estimates of CO sources with high resolution by adjoint inversion of multiple satellite datasets (MOPITT, AIRS, SCIAMACHY, TES). *Atmospheric Chemistry and Physics*, 10(3):855–876, 2010. doi: 10.5194/acp-10-855-2010. [Page 194.]

S. Kotthaus and C. S. B. Grimmond. Atmospheric boundary-layer characteristics from ceilometer measurements. Part 1: A new method to track mixed layer height and

classify clouds. *Quarterly Journal of the Royal Meteorological Society*, 144(714): 1525–1538, 2018. doi: 10.1002/qj.3299. [Pages 76 and 124.]

N. A. Krotkov, C. A. McLinden, C. Li, L. N. Lamsal, E. A. Celarier, S. V. Marchenko, W. H. Swartz, E. J. Bucsela, J. Joiner, B. N. Duncan, K. F. Boersma, J. P. Veefkind, P. F. Levelt, V. E. Fioletov, R. R. Dickerson, H. He, Z. F. Lu, and D. G. Streets. Aura OMI observations of regional SO_2 and NO_2 pollution changes from 2005 to 2015. *Atmospheric Chemistry and Physics*, 16(7):4605–4629, 2016. doi: 10.5194/acp-16-4605-2016. [Pages 71 and 146.]

N. A. Krotkov, L. N. Lamsal, S. V. Marchenko, E. A. Celarier, E. J. Bucsela, W. H. Swartz, and J. Joiner. OMI/Aura NO2 Cloud-Screened Total and Tropospheric Column L3 Global Gridded 0.25 degree x 0.25 degree V3, NASA Goddard Space Flight Center, Goddard Earth Sciences Data and Information Services Center (GES DISC), 2019. [Page 199.]

A. Kumar, S. Wu, M. F. Weise, R. Honrath, R. C. Owen, D. Helmig, L. Kramer, M. Val Martin, and Q. Li. Free-troposphere ozone and carbon monoxide over the North Atlantic for 2001–2011. *Atmospheric Chemistry and Physics*, 13(24):12537–12547, 2013. doi: 10.5194/acp-13-12537-2013. [Pages 155, 156, and 194.]

J. F. Lamarque, T. C. Bond, V. Eyring, C. Granier, A. Heil, Z. Klimont, D. Lee, C. Liousse, A. Mieville, B. Owen, M. G. Schultz, D. Shindell, S. J. Smith, E. Stehfest, J. Van Aardenne, O. R. Cooper, M. Kainuma, N. Mahowald, J. R. McConnell, V. Naik, K. Riahi, and D. P. van Vuuren. Historical (1850–2000) gridded anthropogenic and biomass burning emissions of reactive gases and aerosols: methodology and application. *Atmospheric Chemistry and Physics*, 10(15):7017–7039, 2010. doi: 10.5194/acp-10-7017-2010. [Page 25.]

B. Langford. Submicron aerosol fluxes above three contrasting megacities, in preparation. 2020. [Pages 84, 133, and 134.]

B. Langford, B. Davison, E. Nemitz, and C. N. Hewitt. Mixing ratios and eddy covariance flux measurements of volatile organic compounds from an urban canopy (Manchester, UK). *Atmospheric Chemistry and Physics*, 9(6):1971–1987, 2009. doi: 10.5194/acp-9-1971-2009. [Pages 140, 144, and 145.]

B. Langford, E. Nemitz, E. House, G. J. Phillips, D. Famulari, B. Davison, J. R. Hopkins, A. C. Lewis, and C. N. Hewitt. Fluxes and concentrations of volatile organic compounds above central London, UK. *Atmospheric Chemistry and Physics*, 10(2): 627–645, 2010. doi: 10.5194/acp-10-627-2010. [Pages 114 and 144.]

B. Langford, J. Acton, C. Ammann, A. Valach, and E. Nemitz. Eddy-covariance data with low signal-to-noise ratio: time-lag determination, uncertainties and limit of detection. *Atmospheric Measurement Techniques*, 8:4197–4213, 2015. doi: 10.5194/amt-8-4197-2015. [Page 119.]

K. Lapina, R. Honrath, R. Owen, M. Val Martin, and G. Pfister. Evidence of significant large-scale impacts of boreal fires on ozone levels in the midlatitude Northern Hemisphere free troposphere. *Geophysical Research Letters*, 33(10):L10815, 2006. doi: 10.1029/2006GL025878. [Pages 155 and 176.]

J. L. Laughner and R. C. Cohen. Direct observation of changing NO_x lifetime in North American cities. *Science*, 366(6466):723–727, 2019. doi: 10.1126/science.aax6832. [Page 38.]

M. G. Lawrence and P. J. Crutzen. Influence of NO_x emissions from ships on tropospheric photochemistry and climate. *Nature*, 402(6758):167–170, 1999. doi: 10.1038/46013. [Page 156.]

T. Le, Y. Wang, L. Liu, J. Yang, Y. L. Yung, G. Li, and J. H. Seinfeld. Unexpected air pollution with marked emission reductions during the COVID-19 outbreak in China. *Science*, page eabb7431, 2020. doi: 10.1126/science.abb7431. [Page 26.]

M. Le Breton, Å. M. Hallquist, R. K. Pathak, D. Simpson, Y. Wang, J. Johansson, J. Zheng, Y. Yang, D. Shang, H. Wang, Q. Liu, C. Chan, T. Wang, T. J. Bannan, M. Priestley, C. J. Percival, D. E. Shallcross, K. Lu, S. Guo, M. Hu, and M. Hallquist. Chlorine oxidation of VOCs at a semi-rural site in Beijing: significant chlorine liberation from $ClNO_2$ and subsequent gas- and particle-phase Cl–VOC production. *Atmospheric Chemistry and Physics*, 18(17):13013–13030, 2018. doi: 10.5194/acp-18-13013-2018. [Page 108.]

J. D. Lee, S. J. Møller, K. A. Read, A. C. Lewis, L. Mendes, and L. J. Carpenter. Year-round measurements of nitrogen oxides and ozone in the tropical North Atlantic marine boundary layer. *Journal of Geophysical Research: Atmospheres*, 114, 2009. doi: 10.1029/2009jd011878. [Pages 50, 60, 63, and 116.]

J. D. Lee, C. Helfter, R. M. Purvis, S. D. Beevers, D. C. Carslaw, A. C. Lewis, S. J. Moller, A. Tremper, A. Vaughan, and E. G. Nemitz. Measurement of NO_x fluxes from a tall tower in central London, UK and comparison with emissions inventories. *Environmental Science & Technology*, 49(2):1025–1034, 2015. doi: 10.1021/es5049072. [Pages 33, 114, 130, and 133.]

J. D. Lee, S. D. Mobbs, A. Wellpott, G. Allen, S. J.-B. Bauguitte, R. R. Burton, R. Camilli, H. Coe, R. E. Fisher, J. L. France, M. Gallagher, J. R. Hopkins, M. Lanoiselle, A. C. Lewis, D. Lowry, E. G. Nisbet, R. M. Purvis, S. O'Shea, J. A. Pyle, and T. B. Ryerson. Flow rate and source reservoir identification from airborne chemical sampling of the uncontrolled Elgin platform gas release. *Atmospheric Measurement Techniques*, 11(3):1725–1739, 2018. doi: 10.5194/amt-11-1725-2018. [Pages 158 and 166.]

X. Lee, W. Massman, and B. Law. *Handbook of Micrometeorology: A Guide for Surface Flux Measurement and Analysis*. Atmospheric and Oceanographic Sciences Library. Springer Netherlands, Dordrecht, The Netherlands, 2004. doi: 10.1007/1-4020-2265-4. [Page 120.]

J. Lelieveld, F. J. Dentener, W. Peters, and M. C. Krol. On the role of hydroxyl radicals in the self-cleansing capacity of the troposphere. *Atmospheric Chemistry and Physics*, 4(9/10):2337–2344, 2004. doi: 10.5194/acp-4-2337-2004. [Page 34.]

J. Lelieveld, S. Gromov, A. Pozzer, and D. Taraborrelli. Global tropospheric hydroxyl distribution, budget and reactivity. *Atmospheric Chemistry and Physics*, 16(19): 12477–12493, 2016. doi: 10.5194/acp-16-12477-2016. [Page 39.]

J. Lelieveld, K. Klingmüller, A. Pozzer, R. Burnett, A. Haines, and V. Ramanathan. Effects of fossil fuel and total anthropogenic emission removal on public health and climate. *Proceedings of the National Academy of Sciences*, 116(15):7192–7197, 2019. doi: 10.1073/pnas.1819989116. [Page 25.]

A. C. Lewis, M. J. Evans, J. Methven, N. Watson, J. D. Lee, J. R. Hopkins, R. M. Purvis, S. R. Arnold, J. B. McQuaid, L. K. Whalley, M. J. Pilling, D. E. Heard, P. S. Monks, A. E. Parker, C. E. Reeves, D. E. Oram, G. Mills, B. J. Bandy, D. Stewart, H. Coe, P. Williams, and J. Crosier. Chemical composition observed over the mid-Atlantic and the detection of pollution signatures far from source regions. *Journal of Geophysical Research: Atmospheres*, 112(D10):D10S39, 2007. doi: 10.1029/2006JD007584. [Pages 155, 176, 178, and 179.]

H. Y. Li, Q. Zhang, C. R. Chen, L. T. Wang, Z. Wei, S. Zhou, C. Parworth, B. Zheng, F. Canonaco, A. S. H. Prevot, P. Chen, H. L. Zhang, T. J. Wallington, and K. B. He. Wintertime aerosol chemistry and haze evolution in an extremely polluted city of the North China Plain: significant contribution from coal and biomass combustion. *Atmospheric Chemistry and Physics*, 17(7):4751–4768, 2017a. doi: 10.5194/acp-17-4751-2017. [Pages 72 and 135.]

K. Li, D. J. Jacob, H. Liao, L. Shen, Q. Zhang, and K. H. Bates. Anthropogenic drivers of 2013–2017 trends in summer surface ozone in China. *Proceedings of the National Academy of Sciences*, 116(2):422–427, 2019a. [Page 72.]

L. Li, Q. Li, L. Huang, Q. Wang, A. Zhu, J. Xu, Z. Liu, H. Li, L. Shi, R. Li, M. Azari, Y. Wang, X. Zhang, Z. Liu, Y. Zhu, K. Zhang, S. Xue, M. C. G. Ooi, D. Zhang, and A. Chan. Air quality changes during the COVID-19 lockdown over the Yangtze River Delta Region: An insight into the impact of human activity pattern changes on air pollution variation. *Science of The Total Environment*, 732:139282, 2020a. doi: 10.1016/j.scitotenv.2020.139282. [Page 19.]

M. Li, H. Liu, G. Geng, C. Hong, F. Liu, Y. Song, D. Tong, B. Zheng, H. Cui, H. Man, Q. Zhang, and K. He. Anthropogenic emission inventories in China: a review. *National Science Review*, 4(6):834–866, 2017b. doi: 10.1093/nsr/nwx150. [Page 32.]

Q. Li, G. Su, C. Li, P. Liu, X. Zhao, C. Zhang, X. Sun, Y. Mu, M. Wu, Q. Wang, and B. Sun. An investigation into the role of VOCs in SOA and ozone production in Beijing, China. *Science of The Total Environment*, 720:137536, 2020b. doi: 10.1016/j.scitotenv.2020.137536. [Page 98.]

Y. Li, Y.-h. Chiu, and T.-Y. Lin. The impact of economic growth and air pollution on public health in 31 Chinese cities. *International Journal of Environmental Research and Public Health*, 16(3):393, 2019b. doi: 10.3390/ijerph16030393. [Page 30.]

D. Liang, L. Shi, J. Zhao, P. Liu, J. Schwartz, S. Gao, J. Sarnat, Y. Liu, S. Ebelt, N. Scovronick, and H. Chang. Urban air pollution may enhance COVID-19 case-fatality and mortality rates in the United States. *medRxiv*, 2020. doi: 10.1101/2020.05.04.20090746. [Page 19.]

W. Lin, X. Xu, B. Ge, and X. Liu. Gaseous pollutants in Beijing urban area during the heating period 2007–2008: variability, sources, meteorological, and chemical impacts. *Atmospheric Chemistry and Physics*, 11(15):8157–8170, 2011. doi: 10.5194/acp-11-8157-2011. [Page 97.]

C. Liu, P. Yin, R. Chen, X. Meng, L. Wang, Y. Niu, Z. Lin, Y. Liu, J. Liu, and J. Qi. Ambient carbon monoxide and cardiovascular mortality: a nationwide time-series analysis in 272 cities in China. *The Lancet Planetary Health*, 2(1):e12–e18, 2018. doi: 10.1016/S2542-5196(17)30181-X. [Page 114.]

F. Liu, Q. Zhang, J. v. d. A. Ronald, B. Zheng, D. Tong, L. Yan, Y. Zheng, and K. He. Recent reduction in NO_x emissions over China: synthesis of satellite observations and emission inventories. *Environmental Research Letters*, 11(11):114002, 2016. doi: 10.1088/1748-9326/11/11/114002. [Pages 30, 71, and 146.]

H. Liu, J. He, J. Guo, Y. Miao, J. Yin, Y. Wang, H. Xu, H. Liu, Y. Yan, Y. Li, and P. Zhai. The blue skies in Beijing during APEC 2014: A quantitative assessment of emission control efficiency and meteorological influence. *Atmospheric Environment*, 167:235–244, 2017a. doi: 10.1016/j.atmosenv.2017.08.032. [Page 26.]

H. Z. Liu, J. W. Feng, L. Jarvi, and T. Vesala. Four-year (2006–2009) eddy covariance measurements of CO_2 flux over an urban area in Beijing. *Atmospheric Chemistry and Physics*, 12(17):7881–7892, 2012. doi: 10.5194/acp-12-7881-2012. [Pages 121 and 125.]

S. C. Liu, M. Trainer, F. C. Fehsenfeld, D. D. Parrish, E. J. Williams, D. W. Fahey, G. Hübler, and P. C. Murphy. Ozone production in the rural troposphere and the

implications for regional and global ozone distributions. *Journal of Geophysical Research: Atmospheres*, 92(D4):4191–4207, 1987. doi: 10.1029/JD092iD04p04191. [Page 195.]

X. Liu, H. Qu, L. G. Huey, Y. Wang, S. Sjostedt, L. Zeng, K. Lu, Y. Wu, M. Ho, M. Shao, T. Zhu, and Y. Zhang. High levels of daytime molecular chlorine and nitryl chloride at a rural site on the North China Plain. *Environmental Science & Technology*, 51(17):9588–9595, 2017b. doi: 10.1021/acs.est.7b03039. [Page 108.]

Y. Ma, K. Lu, C. C.-K. Chou, X. Li, and Y. Zhang. Strong deviations from the NO-NO_2-O_3 photostationary state in the Pearl River Delta: Indications of active peroxy radical and chlorine radical chemistry. *Atmospheric Environment*, 163:22–34, 2017. doi: 10.1016/j.atmosenv.2017.05.012. [Page 109.]

Z. Ma, X. Hu, A. M. Sayer, R. Levy, Q. Zhang, Y. Xue, S. Tong, J. Bi, L. Huang, and Y. Liu. Satellite-based spatiotemporal trends in $PM_{2.5}$ concentrations: China, 2004–2013. *Environmental Health Perspectives*, 124(2):184–192, 2016. doi: 10.1289/ehp.1409481. [Page 71.]

S. Mahato, S. Pal, and K. G. Ghosh. Effect of lockdown amid COVID-19 pandemic on air quality of the megacity Delhi, India. *Science of The Total Environment*, 730:139086, 2020. doi: 10.1016/j.scitotenv.2020.139086. [Page 19.]

L. Mandel. Fluctuations of photon beams and their correlations. *Proceedings of the Physical Society*, 72(6):1037–1048, 1958. doi: 10.1088/0370-1328/72/6/312. [Page 60.]

J. Mann and D. H. Lenschow. Errors in airborne flux measurements. *Journal of Geophysical Research: Atmospheres*, 99(D7):14519–14526, 1994. doi: 10.1029/94jd00737. [Page 120.]

K. Mannschreck, S. Gilge, C. Plass-Duelmer, W. Fricke, and H. Berresheim. Assessment of the applicability of NO-NO_2-O_3 photostationary state to long-term measurements at the Hohenpeissenberg GAW Station, Germany. *Atmospheric Chemistry and Physics*, 4(5):1265–1277, 2004. doi: 10.5194/acp-4-1265-2004. [Page 107.]

L. C. Marr, T. O. Moore, M. E. Klapmeyer, and M. B. Killar. Comparison of NO_x fluxes measured by eddy covariance to emission inventories and land use. *Environmental Science & Technology*, 47(4):1800–1808, 2013. doi: 10.1021/es303150y. [Page 130.]

K. L. Mays, P. B. Shepson, B. H. Stirm, A. Karion, C. Sweeney, and K. R. Gurney. Aircraft-based measurements of the carbon footprint of Indianapolis. *Environmental Science & Technology*, 43(20):7816–7823, 2009. doi: 10.1021/es901326b. [Page 33.]

K. McBeath. The use of aircraft for meteorological research in the United Kingdom. *Meteorological Applications*, 21(1):105–116, 2014. doi: 10.1002/met.1448. [Page 156.]

B. C. McDonald, J. A. de Gouw, J. B. Gilman, S. H. Jathar, A. Akherati, C. D. Cappa, J. L. Jimenez, J. Lee-Taylor, P. L. Hayes, S. A. McKeen, Y. Y. Cui, S.-W. Kim, D. R. Gentner, G. Isaacman-VanWertz, A. H. Goldstein, R. A. Harley, G. J. Frost, J. M. Roberts, T. B. Ryerson, and M. Trainer. Volatile chemical products emerging as largest petrochemical source of urban organic emissions. *Science*, 359(6377): 760–764, 2018. doi: 10.1126/science.aaq0524. [Pages 32 and 114.]

M. Mead, O. Popoola, G. Stewart, P. Landshoff, M. Calleja, M. Hayes, J. Baldovi, M. McLeod, T. Hodgson, J. Dicks, A. Lewis, J. Cohen, R. Baron, J. Safell, and R. Jones. The use of electrochemical sensors for monitoring urban air quality in low-cost, high-density networks. *Atmospheric Environment*, 70:186–203, 2013. doi: 10.1016/j.atmosenv.2012.11.060. [Page 49.]

A. Mellouki, T. Wallington, and J. Chen. Atmospheric chemistry of oxygenated volatile organic compounds: impacts on air quality and climate. *Chemical Reviews*, 115(10):3984–4014, 2015. doi: 10.1021/cr500549n. [Page 39.]

S. Metzger, W. Junkermann, M. Mauder, F. Beyrich, K. Butterbach-Bahl, H. P. Schmid, and T. Foken. Eddy-covariance flux measurements with a weight-shift microlight aircraft. *Atmospheric Measurement Techniques*, 5(7):1699–1717, 2012. doi: 10.5194/amt-5-1699-2012. [Page 125.]

S. Metzger, D. Durden, C. Sturtevant, H. Luo, N. Pingintha-Durden, T. Sachs, A. Serafimovich, J. Hartmann, J. H. Li, K. Xu, and A. R. Desai. eddy4R 0.2.0: a DevOps model for community-extensible processing and analysis of eddy-covariance data based on R, Git, Docker, and HDF5. *Geoscientific Model Development*, 10(9): 3189–3206, 2017. doi: 10.5194/gmd-10-3189-2017. [Page 120.]

L. H. Mielke, A. Furgeson, and H. D. Osthoff. Observation of $ClNO_2$ in a mid-continental urban environment. *Environmental Science & Technology*, 45(20):8889–8896, 2011. doi: 10.1021/es201955u. [Page 108.]

Ministry of Ecology and Environment, the People's Republic of China. 2017 report on the state of the ecology and environment in China, 2018. [Pages 113 and 114.]

K. Miyazaki, H. Eskes, K. Sudo, K. F. Boersma, K. Bowman, and Y. Kanaya. Decadal changes in global surface NO_x emissions from multi-constituent satellite data assimilation. *Atmospheric Chemistry and Physics*, 17(2):807–837, 2017. doi: 10.5194/acp-17-807-2017. [Pages 71 and 146.]

P. S. Monks. A review of the observations and origins of the spring ozone maximum. *Atmospheric Environment*, 34(21):3545–3561, 2000. doi: 10.1016/S1352-2310(00)00129-1. [Page 155.]

P. S. Monks, C. Granier, S. Fuzzi, A. Stohl, M. L. Williams, H. Akimoto, M. Amann, A. Baklanov, U. Baltensperger, I. Bey, N. Blake, R. S. Blake, K. Carslaw, O. R. Cooper, F. Dentener, D. Fowler, E. Fragkou, G. J. Frost, S. Generoso, P. Ginoux, V. Grewe, A. Guenther, H. C. Hansson, S. Henne, J. Hjorth, A. Hofzumahaus, H. Huntrieser, I. S. A. Isaksen, M. E. Jenkin, J. Kaiser, M. Kanakidou, Z. Klimont, M. Kulmala, P. Laj, M. G. Lawrence, J. D. Lee, C. Liousse, M. Maione, G. McFiggans, A. Metzger, A. Mieville, N. Moussiopoulos, J. J. Orlando, C. D. O'Dowd, P. I. Palmer, D. D. Parrish, A. Petzold, U. Platt, U. Poeschl, A. S. H. Prevot, C. E. Reeves, S. Reimann, Y. Rudich, K. Sellegri, R. Steinbrecher, D. Simpson, H. ten Brink, J. Theloke, G. R. van der Werf, R. Vautard, V. Vestreng, C. Vlachokostas, and R. von Glasow. Atmospheric composition change–global and regional air quality. *Atmospheric Environment*, 43(33):5268–5350, 2009. doi: 10.1016/j.atmosenv.2009.08.021. [Pages 26 and 81.]

P. S. Monks, A. T. Archibald, A. Colette, O. Cooper, M. Coyle, R. Derwent, D. Fowler, C. Granier, K. S. Law, G. E. Mills, D. S. Stevenson, O. Tarasova, V. Thouret, E. von Schneidemesser, R. Sommariva, O. Wild, and M. L. Williams. Tropospheric ozone and its precursors from the urban to the global scale from air quality to short-lived climate forcer. *Atmospheric Chemistry and Physics*, 15(15):8889–8973, 2015. doi: 10.5194/acp-15-8889-2015. [Pages 35, 36, and 38.]

A. Moravek, S. Singh, E. Pattey, L. Pelletier, and J. G. Murphy. Measurements and quality control of ammonia eddy covariance fluxes: a new strategy for high-frequency attenuation correction. *Atmospheric Measurement Techniques*, 12(11): 6059–6078, 2019. doi: 10.5194/amt-12-6059-2019. [Page 121.]

G. Myhre, D. Shindell, F. Bréon, W. Collins, J. Fuglestvedt, J. Huang, D. Koch, J. Lamarque, D. Lee, B. Mendoza, T. Nakajima, A. Robock, G. Stephens, T. Takemura, and H. Zhang. Anthropogenic and natural radiative forcing. In T. F. Stocker, D. Qin, G.-K. Plattner, M. Tignor, S. K. Allen, J. Boschung, A. Nauels, Y. Xia, V. Bex, and P. M. Midgley, editors, *Climate Change 2013. The Physical Science Basis. Contribution of Working Group I to the Fifth Assessment Report of the Intergovernmental Panel on Climate Change*, chapter 8, pages 659–740. Cambridge University Press, Cambridge, United Kingdom and New York, NY, USA, 2013. [Pages 23 and 24.]

NASA Earth Observatory. Airborne Nitrogen Dioxide Plummets Over China, 2020. URL `https://earthobservatory.nasa.gov/images/146362/airborne-nitrogen-dioxide-plummets-over-china`. Last access: 03 August 2020. [Page 20.]

National Oceanic and Atmospheric Administration. NOAA National Centers for Environmental Information: North Atlantic Oscillation (NAO), 2020. URL `https://www.ncdc.noaa.gov/teleconnections/nao/`. Last access: 03 August 2020. [Page 161.]

E. Nemitz, I. Mammarella, A. Ibrom, M. Aurela, G. G. Burba, S. Dengel, B. Gielen, A. Grelle, B. Heinesch, M. Herbst, L. Hortnagl, L. Klemedtsson, A. Lindroth, A. Lohila, D. K. McDermitt, P. Meier, L. Merbold, D. Nelson, G. Nicolini, M. B.

Nilsson, O. Peltola, J. Rinne, and M. Zahniser. Standardisation of eddy-covariance flux measurements of methane and nitrous oxide. *International Agrophysics*, 32: 517–549, 2018. doi: 10.1515/intag-2017-0042. [Page 123.]

M. J. Newland, D. J. Bryant, R. E. Dunmore, T. J. Bannan, W. J. F. Acton, B. Langford, J. R. Hopkins, F. A. Squires, W. Dixon, W. S. Drysdale, P. D. Ivatt, M. J. Evans, P. M. Edwards, L. K. Whalley, D. E. Heard, E. J. Slater, R. Woodward-Massey, C. Ye, A. Mehra, S. D. Worrall, A. Bacak, H. Coe, C. J. Percival, C. N. Hewitt, J. D. Lee, T. Cui, J. D. Surratt, X. Wang, A. C. Lewis, A. R. Rickard, and J. F. Hamilton. Rainforest-like atmospheric chemistry in a polluted megacity. *Atmospheric Chemistry and Physics Discussions*, 2020:1–18, 2020. doi: 10.5194/acp-2020-35. [Page 99.]

E. G. Nisbet, E. J. Dlugokencky, M. R. Manning, D. Lowry, R. E. Fisher, J. L. France, S. E. Michel, J. B. Miller, J. W. C. White, B. Vaughn, P. Bousquet, J. A. Pyle, N. J. Warwick, M. Cain, R. Brownlow, G. Zazzeri, M. Lanoisellé, A. C. Manning, E. Gloor, D. E. J. Worthy, E.-G. Brunke, C. Labuschagne, E. W. Wolff, and A. L. Ganesan. Rising atmospheric methane: 2007–2014 growth and isotopic shift. *Global Biogeochemical Cycles*, 30(9):1356–1370, 2016. doi: 10.1002/2016GB005406. [Page 156.]

A. Nordbo and G. Katul. A wavelet-based correction method for eddy-covariance high-frequency losses in scalar concentration measurements. *Boundary-Layer Meteorology*, 146(1):81–102, 2013. doi: 10.1007/s10546-012-9759-9. [Page 121.]

P. Novelli, K. Masarie, and P. Lang. Distributions and recent changes of carbon monoxide in the lower troposphere. *Journal of Geophysical Research: Atmospheres*, 103 (D15):19015–19033, 1998. doi: 10.1029/98JD01366. [Page 39.]

T. Oda, R. Bun, V. Kinakh, P. Topylko, M. Halushchak, G. Marland, T. Lauvaux, M. Jonas, S. Maksyutov, Z. Nahorski, M. Lesiv, O. Danylo, and J. Horabik-Pyzel. Errors and uncertainties in a gridded carbon dioxide emissions inventory. *Mitigation and Adaptation Strategies for Global Change*, 24(6):1007–1050, 2019. doi: 10.1007/s11027-019-09877-2. [Page 32.]

H. Okabe, P. L. Splitstone, and J. J. Ball. Ambient and source SO_2 detector based on a fluorescence method. *Journal of the Air Pollution Control Association*, 23(6): 514–516, 1973. doi: 10.1080/00022470.1973.10469797. [Page 48.]

S. J. O'Shea, S. J.-B. Bauguitte, M. W. Gallagher, D. Lowry, and C. J. Percival. Development of a cavity-enhanced absorption spectrometer for airborne measurements of CH_4 and CO_2. *Atmospheric Measurement Techniques*, 6(5):1095–1109, 2013. doi: 10.5194/amt-6-1095-2013. [Page 157.]

S. J. O'Shea, G. Allen, Z. L. Fleming, S. J.-B. Bauguitte, C. J. Percival, M. W. Gallagher, J. Lee, C. Helfter, and E. Nemitz. Area fluxes of carbon dioxide, methane, and carbon monoxide derived from airborne measurements around Greater London: A case study during summer 2012. *Journal of Geophysical Research: Atmospheres*, 119(8):4940–4952, 2014. doi: 10.1002/2013JD021269. [Page 33.]

Y. Ouyang. China wakes up to the crisis of air pollution. *The Lancet Respiratory Medicine*, 1(1):12, 2013. doi: 10.1016/S2213-2600(12)70065-6. [Page 26.]

M. Panagi, Z. L. Fleming, P. S. Monks, M. J. Ashfold, O. Wild, M. Hollaway, Q. Zhang, F. A. Squires, and J. D. Vande Hey. Investigating the regional contributions to air pollution in Beijing: a dispersion modelling study using CO as a tracer. *Atmospheric Chemistry and Physics*, 20(5):2825–2838, 2020. doi: 10.5194/acp-20-2825-2020. [Page 39.]

C. Park, G. W. Schade, and I. Boedeker. Flux measurements of volatile organic compounds by the relaxed eddy accumulation method combined with a GC-FID system in urban Houston, Texas. *Atmospheric Environment*, 44(21–22):2605–2614, 2010. doi: 10.1016/j.atmosenv.2010.04.016. [Page 144.]

D. D. Parrish and F. C. Fehsenfeld. Methods for gas-phase measurements of ozone, ozone precursors and aerosol precursors. *Atmospheric Environment*, 34(12–14): 1921–1957, 2000. doi: 10.1016/S1352-2310(99)00454-9. [Page 46.]

D. D. Parrish, J. S. Holloway, M. Trainer, P. C. Murphy, F. C. Fehsenfeld, and G. L. Forbes. Export of North American ozone pollution to the north Atlantic

Ocean. *Science*, 259(5100):1436–1439, 1993. doi: 10.1126/science.259.5100.1436. [Page 175.]

D. D. Parrish, M. Trainer, J. S. Holloway, J. E. Yee, M. S. Warshawsky, F. C. Fehsenfeld, G. L. Forbes, and J. L. Moody. Relationships between ozone and carbon monoxide at surface sites in the North Atlantic region. *Journal of Geophysical Research: Atmospheres*, 103(D11):13357–13376, 1998. doi: 10.1029/98JD00376. [Pages 155, 175, and 176.]

D. D. Parrish, E. J. Dunlea, E. L. Atlas, S. Schauffler, S. Donnelly, V. Stroud, A. H. Goldstein, D. B. Millet, M. McKay, D. A. Jaffe, H. U. Price, P. G. Hess, F. Flocke, and J. M. Roberts. Changes in the photochemical environment of the temperate North Pacific troposphere in response to increased Asian emissions. *Journal of Geophysical Research: Atmospheres*, 109(D23):D23S18, 2004. doi: 10.1029/2004JD004978. [Page 194.]

D. D. Parrish, W. C. Kuster, M. Shao, Y. Yokouchi, Y. Kondo, P. D. Goldan, J. A. de Gouw, M. Koike, and T. Shirai. Comparison of air pollutant emissions among mega-cities. *Atmospheric Environment*, 43(40):6435–6441, 2009. doi: 10.1016/j.atmosenv.2009.06.024. [Page 133.]

D. D. Parrish, J. Xu, B. Croes, and M. Shao. Air quality improvement in Los Angeles - Perspectives for developing cities. *Frontiers of Environmental Science & Engineering*, 10(5):11, 2016. doi: 10.1007/s11783-016-0859-5. [Page 31.]

E. Pattey, R. L. Desjardins, F. Boudreau, and P. Rochette. Impact of density fluctuations on flux measurements of trace gases: Implications for the relaxed eddy accumulation technique. *Boundary-Layer Meteorology*, 59(1):195–203, 1992. doi: 10.1007/BF00120695. [Page 121.]

K. E. Pickering, Y. Wang, W.-K. Tao, C. Price, and J.-F. Müller. Vertical distributions of lightning NO_x for use in regional and global chemical transport models. *Journal of Geophysical Research: Atmospheres*, 103(D23):31203–31216, 1998. doi: 10.1029/98JD02651. [Page 164.]

I. Pison, L. Menut, and G. Bergametti. Inverse modeling of surface NO_x anthropogenic emission fluxes in the Paris area during the Air Pollution Over Paris Region (ESQUIF) campaign. *Journal of Geophysical Research: Atmospheres*, 112(D24), 2007. doi: 10.1029/2007JD008871. [Page 34.]

J. R. Pitt, G. Allen, S. J. B. Bauguitte, M. W. Gallagher, J. D. Lee, W. Drysdale, B. Nelson, A. J. Manning, and P. I. Palmer. Assessing London CO_2, CH_4 and CO emissions using aircraft measurements and dispersion modelling. *Atmospheric Chemistry and Physics*, 19(13):8931–8945, 2019. doi: 10.5194/acp-19-8931-2019. [Pages 33 and 34.]

I. B. Pollack, B. M. Lerner, and T. B. Ryerson. Evaluation of ultraviolet light-emitting diodes for detection of atmospheric NO_2 by photolysis-chemiluminescence. *Journal of Atmospheric Chemistry*, 65(2-3):111–125, 2010. doi: 10.1007/s10874-011-9184-3. [Pages 51 and 52.]

R. J. Pope, M. P. Chipperfield, S. R. Arnold, N. Glatthor, W. Feng, S. S. Dhomse, B. J. Kerridge, B. G. Latter, and R. Siddans. Influence of the wintertime North Atlantic Oscillation on European tropospheric composition: an observational and modelling study. *Atmospheric Chemistry and Physics*, 18(11):8389–8408, 2018. doi: 10.5194/acp-18-8389-2018. [Pages 28 and 155.]

J. Qi, B. Zheng, M. Li, F. Yu, C. Chen, F. Liu, X. Zhou, J. Yuan, Q. Zhang, and K. He. A high-resolution air pollutants emission inventory in 2013 for the Beijing-Tianjin-Hebei region, China. *Atmospheric Environment*, 170:156–168, 2017. doi: 10.1016/j.atmosenv.2017.09.039. [Pages 32 and 126.]

F. Raes and J. H. Seinfeld. New directions: Climate change and air pollution abatement: A bumpy road. *Atmospheric Environment*, 43(32):5132–5133, 2009. doi: 10.1016/j.atmosenv.2009.06.001. [Page 25.]

P. Rantala, L. Järvi, R. Taipale, T. K. Laurila, J. Patokoski, M. K. Kajos, M. Kurppa, S. Haapanala, E. Siivola, T. Petäjä, T. M. Ruuskanen, and J. Rinne. Anthropogenic and biogenic influence on VOC fluxes at an urban background site in Helsinki, Finland. *Atmospheric Chemistry and Physics*, 16(12):7981–8007, 2016. doi: 10.5194/acp-16-7981-2016. [Page 144.]

C. Reed, M. J. Evans, P. Di Carlo, J. D. Lee, and L. J. Carpenter. Interferences in photolytic NO_2 measurements: explanation for an apparent missing oxidant? *Atmospheric Chemistry and Physics*, 16(7):4707–4724, 2016. doi: 10.5194/acp-16-4707-2016. [Pages 52 and 53.]

C. Reed, M. J. Evans, L. R. Crilley, W. J. Bloss, T. Sherwen, K. A. Read, J. D. Lee, and L. J. Carpenter. Evidence for renoxification in the tropical marine boundary layer. *Atmospheric Chemistry and Physics*, 17(6):4081–4092, 2017. doi: 10.5194/acp-17-4081-2017. [Pages 38 and 50.]

J. Robson, R. Sutton, K. Lohmann, D. Smith, and M. D. Palmer. Causes of the rapid warming of the North Atlantic Ocean in the mid-1990s. *Journal of Climate*, 25(12): 4116–4134, 2012. doi: 10.1175/JCLI-D-11-00443.1. [Page 154.]

J. Robson, R. T. Sutton, A. Archibald, F. Cooper, M. Christensen, L. J. Gray, N. P. Holliday, C. Macintosh, M. McMillan, B. Moat, M. Russo, R. Tilling, K. Carslaw, D. Desbruyères, O. Embury, D. L. Feltham, D. P. Grosvenor, S. Josey, B. King, A. Lewis, G. D. McCarthy, C. Merchant, A. L. New, C. H. O'Reilly, S. M. Osprey, K. Read, A. Scaife, A. Shepherd, B. Sinha, D. Smeed, D. Smith, A. Ridout, T. Woollings, and M. Yang. Recent multivariate changes in the North Atlantic climate system, with a focus on 2005–2016. *International Journal of Climatology*, 38 (14):5050–5076, 2018. doi: 10.1002/joc.5815. [Pages 154, 155, and 156.]

T. Ryerson, E. Williams, and F. Fehsenfeld. An efficient photolysis system for fast-response NO_2 measurements. *Journal of Geophysical Research: Atmospheres*, 105 (D21):26447–26461, 2000. doi: 10.1029/2000JD900389. [Page 51.]

Y. Sadanaga, Y. Fukumori, T. Kobashi, M. Nagata, N. Takenaka, and H. Bandow. Development of a selective light-emitting diode photolytic NO_2 converter for continuously measuring NO_2 in the atmosphere. *Analytical Chemistry*, 82(22):9234–9239, 2010. doi: 10.1021/ac101703z. [Page 51.]

E. Saikawa, H. Kim, M. Zhong, A. Avramov, Y. Zhao, G. Janssens-Maenhout, J.-I. Kurokawa, Z. Klimont, F. Wagner, and V. Naik. Comparison of emissions inventories of anthropogenic air pollutants and greenhouse gases in China. *Atmospheric*

Chemistry and Physics, 17(10):6393, 2017. doi: 10.5194/acp-17-6393-2017. [Page 114.]

B. Samset, M. Sand, C. Smith, S. Bauer, P. Forster, J. Fuglestvedt, S. Osprey, and C.-F. Schleussner. Climate impacts from a removal of anthropogenic aerosol emissions. *Geophysical Research Letters*, 45(2):1020–1029, 2018. doi: 10.1002/2017GL076079. [Page 25.]

U. Schumann, D. W. Fahey, M. Wendisch, and J.-L. Brenguier. Introduction to airborne measurements of the earth atmosphere and surface. In A. Kokhanovsky, M. Wendisch, and J.-L. Brenguier, editors, *Airborne Measurements for Environmental Research*, chapter 1, pages 1–5. John Wiley & Sons, Ltd, 2013. doi: 10.1002/9783527653218.ch1. [Page 156.]

E. A. G. Schuur, A. D. McGuire, C. Schädel, G. Grosse, J. W. Harden, D. J. Hayes, G. Hugelius, C. D. Koven, P. Kuhry, D. M. Lawrence, S. M. Natali, D. Olefeldt, V. E. Romanovsky, K. Schaefer, M. R. Turetsky, C. C. Treat, and J. E. Vonk. Climate change and the permafrost carbon feedback. *Nature*, 520(7546):171–179, 2015. doi: 10.1038/nature14338. [Page 23.]

J. H. Seinfeld and S. N. Pandis. *Atmospheric chemistry and physics: from air pollution to climate change*. John Wiley & Sons, Hoboken, New Jersey, 2nd edition, 2006. ISBN 978-0471720188. [Page 27.]

J. H. Seinfeld, C. Bretherton, K. S. Carslaw, H. Coe, P. J. DeMott, E. J. Dunlea, G. Feingold, S. Ghan, A. B. Guenther, R. Kahn, I. Kraucunas, S. M. Kreidenweis, M. J. Molina, A. Nenes, J. E. Penner, K. A. Prather, V. Ramanathan, V. Ramaswamy, P. J. Rasch, A. R. Ravishankara, D. Rosenfeld, G. Stephens, and R. Wood. Improving our fundamental understanding of the role of aerosol-cloud interactions in the climate system. *Proceedings of the National Academy of Sciences*, 113(21):5781–5790, 2016. doi: 10.1073/pnas.1514043113. [Page 25.]

G. Shaddick, M. Thomas, P. Mudu, G. Ruggeri, and S. Gumy. Half the world's population are exposed to increasing air pollution. *npj Climate and Atmospheric Science*, 3(1):1–5, 2020. doi: 10.1038/s41612-020-0124-2. [Page 22.]

Z. Shi, T. Vu, S. Kotthaus, R. M. Harrison, S. Grimmond, S. Yue, T. Zhu, J. Lee, Y. Han, M. Demuzere, R. E. Dunmore, L. Ren, D. Liu, Y. Wang, O. Wild, J. Allan, W. J. Acton, J. Barlow, B. Barratt, D. Beddows, W. J. Bloss, G. Calzolai, D. Carruthers, D. C. Carslaw, Q. Chan, L. Chatzidiakou, Y. Chen, L. Crilley, H. Coe, T. Dai, R. Doherty, F. Duan, P. Fu, B. Ge, M. Ge, D. Guan, J. F. Hamilton, K. He, M. Heal, D. Heard, C. N. Hewitt, M. Hollaway, M. Hu, D. Ji, X. Jiang, R. Jones, M. Kalberer, F. J. Kelly, L. Kramer, B. Langford, C. Lin, A. C. Lewis, J. Li, W. Li, H. Liu, J. Liu, M. Loh, K. Lu, F. Lucarelli, G. Mann, G. McFiggans, M. R. Miller, G. Mills, P. Monk, E. Nemitz, F. O'Connor, B. Ouyang, P. I. Palmer, C. Percival, O. Popoola, C. Reeves, A. R. Rickard, L. Shao, G. Shi, D. Spracklen, D. Stevenson, Y. Sun, Z. Sun, S. Tao, S. Tong, Q. Wang, W. Wang, X. Wang, X. Wang, Z. Wang, L. Wei, L. Whalley, X. Wu, Z. Wu, P. Xie, F. Yang, Q. Zhang, Y. Zhang, Y. Zhang, and M. Zheng. Introduction to the special issue "In-depth study of air pollution sources and processes within Beijing and its surrounding region (APHH-Beijing)". *Atmospheric Chemistry and Physics*, 19(11):7519–7546, 2019. doi: 10.5194/acp-19-7519-2019. [Pages 74 and 115.]

D. Shindell and C. J. Smith. Climate and air-quality benefits of a realistic phase-out of fossil fuels. *Nature*, 573(7774):408–411, 2019. doi: 10.1038/s41586-019-1554-z. [Page 25.]

S. Sillman. The use of NO_y, H_2O_2, and HNO_3 as indicators for ozone-NO_x-hydrocarbon sensitivity in urban locations. *Journal of Geophysical Research: Atmospheres*, 100(D7):14175–14188, 1995. doi: 10.1029/94JD02953. [Page 97.]

B. Silver, C. Reddington, S. Arnold, and D. Spracklen. Substantial changes in air pollution across China during 2015–2017. *Environmental Research Letters*, 13(11): 114012, 2018. doi: 10.1088/1748-9326/aae718. [Pages 71 and 72.]

K. R. Smith, P. M. Edwards, M. J. Evans, J. D. Lee, M. D. Shaw, F. Squires, S. Wilde, and A. C. Lewis. Clustering approaches to improve the performance of low cost air pollution sensors. *Faraday Discussions*, 200:621–637, 2017. doi: 10.1039/C7FD00020K. [Page 49.]

M. T. Smith. Advances in understanding benzene health effects and susceptibility. *An-*

nual Review of Public Health, 31:133–148, 2010. doi: 10.1146/annurev.publhealth.012809.103646. [Page 31.]

S. J. Smith, J. van Aardenne, Z. Klimont, R. J. Andres, A. Volke, and S. Delgado Arias. Anthropogenic sulfur dioxide emissions: 1850–2005. *Atmospheric Chemistry and Physics*, 11(3):1101–1116, 2011. doi: 10.5194/acp-11-1101-2011. [Page 31.]

H. Sodemann, M. Pommier, S. R. Arnold, S. A. Monks, K. Stebel, J. F. Burkhart, J. W. Hair, G. S. Diskin, C. Clerbaux, P.-F. Coheur, D. Hurtmans, H. Schlager, A.-M. Blechschmidt, J. E. Kristjánsson, and A. Stohl. Episodes of cross-polar transport in the Arctic troposphere during July 2008 as seen from models, satellite, and aircraft observations. *Atmospheric Chemistry and Physics*, 11(8):3631–3651, 2011. doi: 10.5194/acp-11-3631-2011. [Page 39.]

D. Starkenburg, S. Metzger, G. J. Fochesatto, J. G. Alfieri, R. Gens, A. Prakash, and J. Cristobal. Assessment of despiking methods for turbulence data in micrometeorology. *Journal of Atmospheric and Oceanic Technology*, 33(9):2001–2013, 2016. doi: 10.1175/jtech-d-15-0154.1. [Page 118.]

A. F. Stein, R. R. Draxler, G. D. Rolph, B. J. B. Stunder, M. D. Cohen, and F. Ngan. NOAA's HYSPLIT Atmospheric Transport and Dispersion Modeling System. *Bulletin of the American Meteorological Society*, 96(12):2059–2077, 2016. doi: 10.1175/BAMS-D-14-00110.1. [Page 89.]

J. R. Stetter and J. Li. Amperometric gas sensors–a review. *Chemical Reviews*, 108 (2):352–366, 2008. doi: 10.1021/cr0681039. [Page 49.]

T. F. Stocker, D. Qin, G.-K. Plattner, M. Tignor, S. K. Allen, J. Boschung, A. Nauels, Y. Xia, V. Bex, and P. M. Midgley. *IPCC 2013: Climate Change 2013. The Physical Science Basis. Contribution of Working Group I to the Fifth Assessment Report of the Intergovernmental Panel on Climate Change*. Cambridge University Press, Cambridge, United Kingdom and New York, NY, USA, 2013. [Pages 23, 25, and 153.]

W. R. Stockwell, C. V. Lawson, E. Saunders, and W. S. Goliff. A review of tropo-

spheric atmospheric chemistry and gas-phase chemical mechanisms for air quality modeling. *Atmosphere*, 3(1):1–32, 2012. doi: 10.3390/atmos3010001. [Page 40.]

A. Stohl, C. Forster, S. Eckhardt, N. Spichtinger, H. Huntrieser, J. Heland, H. Schlager, S. Wilhelm, F. Arnold, and O. Cooper. A backward modeling study of intercontinental pollution transport using aircraft measurements. *Journal of Geophysical Research: Atmospheres*, 108(D12), 2003. doi: 10.1029/2002JD002862. [Page 39.]

D. Stone, L. K. Whalley, and D. E. Heard. Tropospheric OH and HO2 radicals: field measurements and model comparisons. 41:6348–6404, 2012. doi: 10.1039/C2CS35140D. [Page 104.]

V. Strand, M. Svartengren, S. Rak, C. Barck, and G. Bylin. Repeated exposure to an ambient level of NO_2 enhances asthmatic response to a nonsymptomatic allergen dose. *European Respiratory Journal*, 12(1):6–12, 1998. doi: 10.1183/09031936.98.12010006. [Page 114.]

Y. Sun, L. Wang, Y. Wang, L. Quan, and L. Zirui. In situ measurements of SO_2, NO_x, NO_y, and O_3 in Beijing, China during August 2008. *Science of The Total Environment*, 409(5):933–940, 2011. doi: 10.1016/j.scitotenv.2010.11.007. [Pages 97 and 98.]

R. T. Sutton, G. D. McCarthy, J. Robson, B. Sinha, A. T. Archibald, and L. J. Gray. Atlantic Multidecadal Variability and the U.K. ACSIS program. *Bulletin of the American Meteorological Society*, 99(2):415–425, 2018. doi: 10.1175/BAMS-D-16-0266.1. [Pages 153 and 158.]

Z. Tan, K. Lu, M. Jiang, R. Su, H. Wang, S. Lou, Q. Fu, C. Zhai, Q. Tan, D. Yue, D. Chen, Z. Wang, S. Xie, L. Zeng, and Y. Zhang. Daytime atmospheric oxidation capacity in four Chinese megacities during the photochemically polluted season: a case study based on box model simulation. *Atmospheric Chemistry and Physics*, 19 (6):3493–3513, 2019. doi: 10.5194/acp-19-3493-2019. [Page 98.]

Y. J. Tham, Z. Wang, Q. Li, H. Yun, W. Wang, X. Wang, L. Xue, K. Lu, N. Ma, B. Bohn, X. Li, S. Kecorius, J. Größ, M. Shao, A. Wiedensohler, Y. Zhang, and T. Wang. Significant concentrations of nitryl chloride sustained in the morning:

investigations of the causes and impacts on ozone production in a polluted region of northern China. *Atmospheric Chemistry and Physics*, 16(23):14959–14977, 2016. doi: 10.5194/acp-16-14959-2016. [Page 108.]

P. Thorsheim. Interpreting the London Fog Disaster of 1952. In E. M. Dupuis, editor, *Smoke and Mirrors: The Politics and Culture of Air Pollution*, pages 154–169. NYU Press, New York, 2004. ISBN 9780814719602. [Page 31.]

S. Tiwari, A. Dahiya, and N. Kumar. Investigation into relationships among NO, NO_2, NO_x, O_3, and CO at an urban background site in Delhi, India. *Atmospheric Research*, 157:119–126, 2015. doi: 10.1016/j.atmosres.2015.01.008. [Page 36.]

M. Trainer, D. D. Parrish, M. P. Buhr, R. B. Norton, F. C. Fehsenfeld, K. G. Anlauf, J. W. Bottenheim, Y. Z. Tang, H. A. Wiebe, J. M. Roberts, R. L. Tanner, L. Newman, V. C. Bowersox, J. F. Meagher, K. J. Olszyna, M. O. Rodgers, T. Wang, H. Berresheim, D. K. L, and U. K. Roychowdhury. Correlation of ozone with NO_y in photochemically aged air. *Journal of Geophysical Research: Atmospheres*, 98 (D2):2917–2925, 1993. doi: 10.1029/92JD01910. [Pages 94 and 97.]

W. S. Tunnicliffe, P. S. Burge, and J. G. Ayres. Effect of domestic concentrations of nitrogen dioxide on airway responses to inhaled allergen in asthmatic patients. *Lancet*, 344(8939):1733–1736, 1994. doi: 10.1016/S0140-6736(94)92886-X. [Page 114.]

K. Turnbull, B. Johnson, F. Marenco, J. Haywood, A. Minikin, B. Weinzierl, H. Schlager, U. Schumann, S. Leadbetter, and A. Woolley. A case study of observations of volcanic ash from the eyjafjallajökull eruption: 1. In situ airborne observations. *Journal of Geophysical Research: Atmospheres*, 117(D20):D00U12, 2012. doi: 10.1029/2011JD016688. [Page 157.]

A. J. Turner, C. Frankenberg, and E. A. Kort. Interpreting contemporary trends in atmospheric methane. *Proceedings of the National Academy of Sciences*, 116(8): 2805–2813, 2019. doi: 10.1073/pnas.1814297116. [Page 156.]

UN Environment Programme. Clean air as a human right, 2019. URL `https://www.unenvironment.org/news-and-stories/story/clean-air-human-right`. Last access: 03 August 2020. [Page 22.]

United Nations' Department Of Economic and Social Affairs: Population Division. The world's cities in 2016 - data booklet, 2016. [Pages 69 and 113.]

United Nations, Department of Economic and Social Affairs, Population Division. World urbanization prospects: The 2018 revision, 2019. URL `https://www.un.org/development/desa/pd/sites/www.un.org.development.desa.pd/files/files/documents/2020/Jan/un_2018_wup_report.pdf`. Last access: 25 July 2020. [Page 69.]

United Nations Framework Convention on Climate Change. Decision 1/CP.21, Paris Agreement, document FCCC/CP/2015/10/Add.1, 2015. [Page 23.]

M. Val Martin, R. Honrath, R. C. Owen, G. Pfister, P. Fialho, and F. Barata. Significant enhancements of nitrogen oxides, black carbon, and ozone in the North Atlantic lower free troposphere resulting from North American boreal wildfires. *Journal of Geophysical Research: Atmospheres*, 111(D23), 2006. doi: 10.1029/2006JD007530. [Page 30.]

M. Val Martin, R. Honrath, R. Owen, and Q. Li. Seasonal variation of nitrogen oxides in the central North Atlantic lower free troposphere. *Journal of Geophysical Research: Atmospheres*, 113(D17):D17307, 2008. doi: 10.1029/2007JD009688. [Pages 155, 168, 176, and 194.]

A. Valach, B. Langford, E. Nemitz, A. R. MacKenzie, and C. N. P. Hewitt. Seasonal and diurnal trends in concentrations and fluxes of volatile organic compounds in central London. *Atmospheric Chemistry and Physics*, 15(14):7777–7796, 2015. doi: 10.5194/acp-15-7777-2015. [Pages 114 and 144.]

A. R. Vaughan, J. D. Lee, P. K. Misztal, S. Metzger, M. D. Shaw, A. C. Lewis, R. M. Purvis, D. C. Carslaw, A. H. Goldstein, C. N. Hewitt, B. Davison, S. D. Beevers, and T. G. Karl. Spatially resolved flux measurements of NO_x from London suggest significantly higher emissions than predicted by inventories. *Faraday Discussions*, 189:455–472, 2016. doi: 10.1039/c5fd00170f. [Pages 33, 114, and 133.]

A. R. Vaughan, J. D. Lee, M. D. Shaw, P. K. Misztal, S. Metzger, M. Vieno, B. Davison, T. G. Karl, L. J. Carpenter, A. C. Lewis, R. M. Purvis, A. H. Goldstein, and C. N.

Hewitt. VOC emission rates over London and South East England obtained by airborne eddy covariance. *Faraday Discussions*, 200:599–620, 2017. doi: 10.1039/c7fd00002b. [Page 144.]

E. Velasco, B. Lamb, S. Pressley, E. Allwine, H. Westberg, B. Jobson, M. Alexander, P. Prazeller, L. Molina, and M. Molina. Flux measurements of volatile organic compounds from an urban landscape. *Geophysical Research Letters*, 32(20):L20802, 2005. doi: 10.1029/2005GL023356. [Page 144.]

E. Velasco, S. Pressley, R. Grivicke, E. Allwine, T. Coons, W. Foster, B. T. Jobson, H. Westberg, R. Ramos, F. Hernández, L. T. Molina, and B. Lamb. Eddy covariance flux measurements of pollutant gases in urban Mexico City. *Atmospheric Chemistry and Physics*, 9(19):7325–7342, 2009. doi: 10.5194/acp-9-7325-2009. [Pages 33 and 144.]

W. W. Verstraeten, J. L. Neu, J. E. Williams, K. W. Bowman, J. R. Worden, and K. F. Boersma. Rapid increases in tropospheric ozone production and export from China. *Nature Geoscience*, 8(9):690–695, 2015. doi: 10.1038/ngeo2493. [Page 72.]

A. Volz and D. Kley. A resonance-fluorescence instrument for the in-situ measurement of atmospheric carbon monoxide. *Journal of Atmospheric Chemistry*, 2(4):345–357, 1985. doi: 10.1007/BF00130747. [Pages 57 and 58.]

E. von Schneidemesser, P. S. Monks, and C. Plass-Duelmer. Global comparison of VOC and CO observations in urban areas. *Atmospheric Environment*, 44(39):5053–5064, 2010. doi: 10.1016/j.atmosenv.2010.09.010. [Page 133.]

E. von Schneidemesser, P. S. Monks, J. D. Allan, L. Bruhwiler, P. Forster, D. Fowler, A. Lauer, W. T. Morgan, P. Paasonen, M. Righi, K. Sindelarova, and M. A. Sutton. Chemistry and the Linkages between Air Quality and Climate Change. *Chemical Reviews*, 115(10):3856–3897, 2015. doi: 10.1021/acs.chemrev.5b00089. [Page 30.]

J. Wang, B. Ge, and Z. Wang. Ozone production efficiency in highly polluted environments. *Current Pollution Reports*, 4(3):198–207, 2018a. doi: 10.1007/s40726-018-0093-9. [Page 97.]

P. Wang, N. Elansky, Y. M. Timofeev, G. Wang, G. Golitsyn, M. Makarova, V. Rakitin, Y. Shtabkin, A. Skorokhod, E. Grechko, E. Fokeeva, A. Safronov, L. Ran, and W. T. Long-term trends of carbon monoxide total columnar amount in urban areas and background regions: Ground-and satellite-based spectroscopic measurements. *Advances in Atmospheric Sciences*, 35(7):785–795, 2018b. doi: 10.1007/s00376-017-6327-8. [Page 147.]

S. Wang, M. Zhao, J. Xing, Y. Wu, Y. Zhou, Y. Lei, K. He, L. Fu, and J. Hao. Quantifying the air pollutants emission reduction during the 2008 Olympic Games in Beijing. *Environmental Science & Technology*, 44(7):2490–2496, 2010a. doi: 10.1021/es9028167. [Page 26.]

S. X. Wang, M. Zhao, J. Xing, Y. Wu, Y. Zhou, Y. Lei, K. B. He, L. X. Fu, and J. M. Hao. Quantifying the air pollutants emission reduction during the 2008 Olympic Games in Beijing. *Environmental Science & Technology*, 44(7):2490–2496, 2010b. doi: 10.1021/es9028167. [Page 147.]

X. Wang, W. Chen, D. Chen, Z. Wu, and Q. Fan. Long-term trends of fine particulate matter and chemical composition in the Pearl River Delta Economic Zone (PRDEZ), China. *Frontiers of Environmental Science & Engineering*, 10(1):53–62, 2016. doi: 10.1007/s11783-014-0728-z. [Page 71.]

R. P. Wayne. *Chemistry of atmospheres – An introduction to the chemistry of the atmospheres of earth, the planets, and their satellites*. Clarendon Press, Oxford, UK, 2nd edition, 1991. ISBN 9780198503750. [Pages 27 and 35.]

E. K. Webb, G. I. Pearman, and R. Leuning. Correction of flux measurements for density effects due to heat and water vapour transfer. *Quarterly Journal of the Royal Meteorological Society*, 106(447):85–100, 1980. doi: 10.1002/qj.49710644707. [Page 120.]

L. K. Whalley, M. A. Blitz, M. Desservettaz, P. W. Seakins, and D. E. Heard. Reporting the sensitivity of laser-induced fluorescence instruments used for HO_2 detection to an interference from RO_2 radicals and introducing a novel approach that enables HO_2 and certain RO_2 types to be selectively measured. *Atmospheric Measurement Techniques*, 6(12):3425–3440, 2013. doi: 10.5194/amt-6-3425-2013. [Page 105.]

L. K. Whalley, D. Stone, R. Dunmore, J. Hamilton, J. R. Hopkins, J. D. Lee, A. C. Lewis, P. Williams, J. Kleffmann, S. Laufs, R. Woodward-Massey, and D. E. Heard. Understanding in situ ozone production in the summertime through radical observations and modelling studies during the Clean air for London project (ClearfLo). *Atmospheric Chemistry and Physics*, 18(4):2547–2571, 2018. doi: 10.5194/acp-18-2547-2018. [Page 105.]

E. J. Williams, K. Baumann, J. M. Roberts, S. B. Bertman, R. B. Norton, F. C. Fehsenfeld, S. R. Springston, L. J. Nunnermacker, L. Newman, K. Olszyna, J. Meagher, B. Hartsell, E. Edgerton, J. R. Pearson, and M. O. Rodgers. Intercomparison of ground-based NO_y measurement techniques. *Journal of Geophysical Research: Atmospheres*, 103(D17):22261–22280, 1998. doi: 10.1029/98JD00074. [Page 47.]

WMO. WDCGG Data summary No. 42: GAW Data, Volume IV-Greenhouse Gases and Other Atmospheric Gases, 2018. URL `https://gaw.kishou.go.jp/publications/summary`. Last access: 03 August 2020. [Page 39.]

T. Woollings, J. M. Gregory, J. G. Pinto, M. Reyers, and D. J. Brayshaw. Response of the North Atlantic storm track to climate change shaped by ocean–atmosphere coupling. 5(5):313–317, 2012. doi: 10.1038/ngeo1438. [Page 153.]

World Bank. World development indicators online database, 2020. URL `https://data.worldbank.org/`. Last access: 31 July 2020. [Page 69.]

World Health Organization. *Air quality guidelines: global update 2005. Particulate matter, ozone, nitrogen dioxide, and sulfur dioxide*. World Health Organization, Geneva, Switzerland, 2006. ISBN 9289021926. [Page 22.]

World Health Organization. *Ambient air pollution: A global assessment of exposure and burden of disease*. World Health Organization, Geneva, Switzerland, 2016. ISBN 9789241511353. [Page 21.]

World Health Organization. WHO global ambient air quality database (update 2018), 2018. URL `https://www.who.int/airpollution/data/cities/en/`. Last Access: 1 August 2020. [Page 22.]

World Meteorological Organization. Guide to instruments and methods of observation, Volume I –measurement of meteorological variables, 2018. URL https://library.wmo.int/doc_num.php?explnum_id=10179. Last accessed: 23 July 2020. [Page 60.]

X. Wu, R. C. Nethery, B. M. Sabath, D. Braun, and F. Dominici. Exposure to air pollution and COVID-19 mortality in the United States. *medRxiv*, 2020. doi: 10.1101/2020.04.05.20054502. [Page 19.]

J. Xu, J. Z. Ma, X. L. Zhang, X. B. Xu, X. F. Xu, W. L. Lin, Y. Wang, W. Meng, and Z. Q. Ma. Measurements of ozone and its precursors in Beijing during summertime: impact of urban plumes on ozone pollution in downwind rural areas. *Atmospheric Chemistry and Physics Discussions*, 11(23):12241–12252, 2011. doi: 10.5194/acp-11-12241-2011. [Page 28.]

W. Xu, W. Song, Y. Y. Zhang, X. J. Liu, L. Zhang, Y. H. Zhao, D. Y. Liu, A. H. Tang, D. W. Yang, D. D. Wang, Z. Wen, Y. P. Pan, D. Fowler, J. L. Collett, J. W. Erisman, K. Goulding, Y. Li, and F. S. Zhang. Air quality improvement in a megacity: implications from 2015 Beijing Parade Blue pollution control actions. *Atmospheric Chemistry and Physics*, 17(1):31–46, 2017. doi: 10.5194/acp-17-31-2017. [Page 73.]

T. Xue, Y. Zheng, D. Tong, B. Zheng, X. Li, T. Zhu, and Q. Zhang. Spatiotemporal continuous estimates of $PM_{2.5}$ concentrations in China, 2000–2016: A machine learning method with inputs from satellites, chemical transport model, and ground observations. *Environment International*, 123:345–357, 2019. doi: 10.1016/j.envint.2018.11.075. [Page 70.]

M. A. Yamasoe, B. Sauvage, V. Thouret, P. Nédélec, E. L. Flochmoen, and B. Barret. Analysis of tropospheric ozone and carbon monoxide profiles over South America based on MOZAIC/IAGOS database and model simulations. *Tellus B: Chemical and Physical Meteorology*, 67(1):27884, 2015. doi: 10.3402/tellusb.v67.27884. [Page 194.]

Z. Yang, H. Wang, Z. Shao, and R. Muncrief. Review of Beijing's comprehensive motor vehicle emission control programs, 2015. URL

https://theicct.org/publications/review-beijings-comprehensive-motor-vehicle-emission-control-programs. Last access: 10 July 2020. [Pages 130 and 133.]

C. X. Ye, X. L. Zhou, D. Pu, J. Stutz, J. Festa, M. Spolaor, C. Tsai, C. Cantrell, R. L. Mauldin, T. Campos, A. Weinheimer, R. S. Hornbrook, E. C. Apel, A. Guenther, L. Kaser, B. Yuan, T. Karl, J. Haggerty, S. Hall, K. Ullmann, J. N. Smith, J. Ortega, and C. Knote. Rapid cycling of reactive nitrogen in the marine boundary layer. *Nature*, 532(7600):489–491, 2016. doi: 10.1038/nature17195. [Page 38.]

Y. Yin, F. Chevallier, P. Ciais, G. Broquet, A. Fortems-Cheiney, I. Pison, and M. Saunois. Decadal trends in global CO emissions as seen by MOPITT. *Atmospheric Chemistry and Physics*, 15(23):13433–13451, 2015. doi: 10.5194/acp-15-13433-2015. [Page 31.]

R. J. Yokelson, I. R. Burling, J. B. Gilman, C. Warneke, C. E. Stockwell, J. de Gouw, S. K. Akagi, S. P. Urbanski, P. Veres, J. M. Roberts, W. C. Kuster, J. Reardon, D. W. T. Griffith, T. J. Johnson, S. Hosseini, J. W. Miller, D. R. Cocker III, H. Jung, and D. R. Weise. Coupling field and laboratory measurements to estimate the emission factors of identified and unidentified trace gases for prescribed fires. *Atmospheric Chemistry and Physics*, 13(1):89–116, 2013. doi: 10.5194/acp-13-89-2013. [Page 175.]

B. Zhang, R. Owen, J. Perlinger, D. Helmig, M. Val Martín, L. Kramer, L. Mazzoleni, and C. Mazzoleni. Ten-year chemical signatures associated with long-range transport observed in the free troposphere over the central North Atlantic. *Elementa Science of the Anthropocene*, 5(8):8, 2017. doi: 10.1525/elementa.194. [Pages 155, 176, 179, and 183.]

Q. Zhang, D. G. Streets, K. He, Y. Wang, A. Richter, J. P. Burrows, I. Uno, C. J. Jang, D. Chen, Z. Yao, and Y. Lei. NO_x emission trends for China, 1995–2004: The view from the ground and the view from space. *Journal of Geophysical Research: Atmospheres*, 112(D22), 2007. doi: 10.1029/2007jd008684. [Page 71.]

Q. Zhang, K. He, and H. Huo. Cleaning China's air. *Nature*, 484(7393):161–162, 2012. doi: 10.1038/484161a. [Page 70.]

Y. Zhao, L. P. Qiu, R. Y. Xu, F. J. Xie, Q. Zhang, Y. Y. Yu, C. P. Nielsen, H. X. Qin, H. K. Wang, X. C. Wu, W. Q. Li, and J. Zhang. Advantages of a city-scale emission inventory for urban air quality research and policy: the case of Nanjing, a typical industrial city in the Yangtze River Delta, China. *Atmospheric Chemistry and Physics*, 15(21):12623–12644, 2015. doi: 10.5194/acp-15-12623-2015. [Page 32.]

Y. Zhao, Y. D. Zhou, L. P. Qiu, and J. Zhang. Quantifying the uncertainties of China's emission inventory for industrial sources: From national to provincial and city scales. *Atmospheric Environment*, 165:207–221, 2017. doi: 10.1016/j.atmosenv.2017.06.045. [Page 115.]

B. Zheng, Q. Zhang, D. Tong, C. Chen, C. Hong, M. Li, G. Geng, Y. Lei, H. Huo, and K. He. Resolution dependence of uncertainties in gridded emission inventories: a case study in Hebei, China. *Atmospheric Chemistry and Physics*, 17(2):921–933, 2017. doi: 10.5194/acp-17-921-2017. [Pages 33, 126, 148, and 152.]

B. Zheng, F. Chevallier, P. Ciais, Y. Yin, M. N. Deeter, H. M. Worden, Y. Wang, Q. Zhang, and K. He. Rapid decline in carbon monoxide emissions and export from East Asia between years 2005 and 2016. *Environmental Research Letters*, 13(4):044007, 2018. [Pages 71 and 147.]

B. Zheng, F. Chevallier, Y. Yin, P. Ciais, A. Fortems-Cheiney, M. N. Deeter, R. J. Parker, Y. Wang, H. M. Worden, and Y. Zhao. Global atmospheric carbon monoxide budget 2000–2017 inferred from multi-species atmospheric inversions. *Earth System Science Data*, 11(3):1411–1436, 2019. doi: 10.5194/essd-11-1411-2019. [Page 31.]

G. J. Zheng, F. K. Duan, H. Su, Y. L. Ma, Y. Cheng, B. Zheng, Q. Zhang, T. Huang, T. Kimoto, D. Chang, U. Poeschl, Y. F. Cheng, and K. B. He. Exploring the severe winter haze in Beijing: the impact of synoptic weather, regional transport and heterogeneous reactions. *Atmospheric Chemistry and Physics*, 15(6):2969–2983, 2015. doi: 10.5194/acp-15-2969-2015. [Page 26.]

C. Zhou, S. Li, and S. Wang. Examining the impacts of urban form on air pollution in developing countries: A case study of China's megacities. *International Journal of Environmental Research and Public Health*, 15(8):1565, 2018a. [Page 72.]

W. Zhou, J. Zhao, B. Ouyang, A. Mehra, W. Xu, Y. Wang, T. J. Bannan, S. D. Worrall, M. Priestley, A. Bacak, Q. Chen, C. Xie, Q. Wang, J. Wang, W. Du, Y. Zhang, X. Ge, P. Ye, J. D. Lee, P. Fu, Z. Wang, D. Worsnop, R. Jones, C. J. Percival, H. Coe, and Y. Sun. Production of N_2O_5 and $ClNO_2$ in summer in urban Beijing, China. *Atmospheric Chemistry and Physics*, 18(16):11581–11597, 2018b. doi: 10.5194/acp-18-11581-2018. [Page 109.]

X. L. Zhou, H. L. Gao, Y. He, G. Huang, S. B. Bertman, K. Civerolo, and J. Schwab. Nitric acid photolysis on surfaces in low-NO_x environments: Significant atmospheric implications. *Geophysical Research Letters*, 30(23), 2003. doi: 10.1029/2003gl018620. [Page 38.]

P. J. Ziemann and R. Atkinson. Kinetics, products, and mechanisms of secondary organic aerosol formation. *Chemical Society Reviews*, 41(19):6582–6605, 2012. doi: 10.1039/C2CS35122F. [Page 25.]